LUND UNIVERSITY

# Solid Oxide Fuel Cell Modeling at the Cell Scale - Focusing on Species, Heat, Charge and Momentum Transport as well as the Reaction Kinetics and Effects

Andersson, Martin

*DOI:*
10.13140/RG.2.2.12858.59846

2011

Link to publication

*Citation for published version (APA):*
Andersson, M. (2011). *Solid Oxide Fuel Cell Modeling at the Cell Scale - Focusing on Species, Heat, Charge and Momentum Transport as well as the Reaction Kinetics and Effects*. [Doctoral Thesis (compilation), Heat Transfer]. Lund University. https://doi.org/10.13140/RG.2.2.12858.59846

*Total number of authors:*
1

**General rights**
Unless other specific re-use rights are stated the following general rights apply:
Copyright and moral rights for the publications made accessible in the public portal are retained by the authors and/or other copyright owners and it is a condition of accessing publications that users recognise and abide by the legal requirements associated with these rights.
• Users may download and print one copy of any publication from the public portal for the purpose of private study or research.
• You may not further distribute the material or use it for any profit-making activity or commercial gain
• You may freely distribute the URL identifying the publication in the public portal

Read more about Creative commons licenses: https://creativecommons.org/licenses/

**Take down policy**
If you believe that this document breaches copyright please contact us providing details, and we will remove access to the work immediately and investigate your claim.

LUND UNIVERSITY

PO Box 117
221 00 Lund
+46 46-222 00 00

Download date: 30. Apr. 2026

# Solid Oxide Fuel Cell Modeling at the Cell Scale

## - Focusing on Species, Heat, Charge and Momentum Transport as well as the Reaction Kinetics and Effects

LUND UNIVERSITY

av / by

**Karl Martin Johan Andersson**

AKADEMISK AVHANDLING / DOCTORAL DISSERATION

som för avläggande av teknologie doktorsexamen vid tekniska fakulteten, Lunds universitet, kommer att offentligen försvaras i hörsal B, M-huset, Ole Römers väg 1, Lund, fredagen den 9:e december 2011, kl. 10:15. Fakultetsopponent: Dr Steven Beale, National Research Council, Kanada.

which by due permission of the Faculty of Engineering at Lund University, will be publicly defended on Friday 9th of December 2011, at 10:15 in lecture hall B in the M-building, Ole Römers väg 1, Lund, for the degree of Doctor of Philosophy in Engineering. Faculty opponent: Dr Steven Beale, National Research Council, Canada.

| Organization | Document name |
|---|---|
| LUND UNIVERSITY<br>Division of Heat Transfer<br>Department of Energy Sciences<br>Faculty of Engineering | DOCTORAL DISSERTATION |
| | Date of issue<br>2011-12-09 |
| | Sponsoring organization<br>Swedish Research Council (Vetenskapsrådet, VR)<br>European Research Council (ERC)<br>Swedish Research Links (Sida) |
| Author(s)<br>Martin Andersson | |


Title and subtitle

Solid Oxide Fuel Cell Modeling at the Cell Scale
-Focusing on Species, Heat, Charge and Momentum Transport as well as the Reaction Kinetics and Effects


Abstract

Fuel cells are electrochemical devices that directly transform chemical energy into electricity. They are promising for future energy systems, since they are energy efficient, able to use renewable fuels and, when hydrogen is used as fuel, there are no direct emissions of greenhouse gases. Various improvements are made during the recent years, however the technology is still in the early phases of commercialisation.

Fully coupled computational fluid dynamics (CFD) approaches based on the finite element method (with the software COMSOL Multiphysics) in two-dimensions are developed, in several steps, to describe an intermediate temperature SOFC single cell. Governing equations covering heat, species, momentum, ion and electron transport are implemented and coupled to kinetics describing internal reforming and electrochemical reactions. Both ordinary and Knudsen diffusion are considered for the gas species transport. For the heat transport a local temperature equilibrium approach is compared to a local temperature non-equilibrium approach, considering the solid- and gas-phases. The Darcy-Brinkman equation enables continuous pressure and velocity fields over the electrode/gas channel interfaces. The electrochemical reaction model is extended from zero-dimension (with only an average value defined) in the early models, to one-dimension covering the variation in current density along the flow direction. Finally a two-dimensional approach including the current density distribution, both along the flow direction and through the electrolyte-electrodes, is developed. The model relies on experimental data from a standard cell developed at Ningbo Institute of Material Technology & Engineering (NIMTE) in China.

The anode microscopic structure and catalytic characteristics have a major impact on the internal reforming reaction rates and also on the cell performance. The large difference between the different activation energies and reaction kinetics found in the open literature may be due to the fact that several parameters probably have a significance influence on the reaction rate. Heat is generated due to ohmic, activation and concentration polarizations within the electrolyte and electrodes as well as change of entropy in the cathodic electrochemical reactions. Heat is consumed due to the change of entropy in the anodic electrochemical reactions and the steam reforming reactions within the anode. The activation polarizations in the electrodes and the ohmic polarization due to ion transport in the YSZ material are found to be the major part of the polarizations. The activation polarization is the most significant and as the electrochemical model is extended from one- to two-dimensions, the activation polarization within the cathode becomes smaller than the one within the anode. This difference might be explained by different current density per (active TPB) area and variable area-to-volume-ratios for the electrochemical reactions within the anode and cathode, respectively. The current density and the activation polarization are the highest at the electrolyte-electrode interface and decreases rapidly within the electrodes as the distance from the interface increases. However, the ohmic polarization by ion transfer increases for the positions away from the interface.



Key words: SOFC, anode-supported, modeling, CFD, charge/species/heat/momentum transport, electrochemical/internal reforming reactions, TPB, area-to-volume ratio, COMSOL Multiphysics

Classification system and/or index termes (if any):

| Supplementary bibliographical information: | Language<br>English |
|---|---|
| ISSN and key title:<br>0282-1990 | ISBN<br>978-91-7473-180-4 |

| Recipient's notes | Number of pages | Price |
|---|---|---|
| | Security classification | |



Distribution by (name and address) Martin Andersson, Dept. Energy Sciences, Lund University, Sweden

I, the undersigned, being the copyright owner of the abstract of the above-mentioned dissertation, hereby grant to all reference sources permission to publish and disseminate the abstract of the above-mentioned dissertation.

Signature _____ Date 2011-11-02

DOKUMENTDATABLAD enl SIS 61 41 21

# Solid Oxide Fuel Cell Modeling at the Cell Scale

## - Focusing on Species, Heat, Charge and Momentum Transport as well as the Reaction Kinetics and Effects

LUND UNIVERSITY

**Karl Martin Johan Andersson**

Dissertation for the degree of Doctor of Philosophy in Engineering.

ISBN 978-91-7473-180-4
ISSN 0282-1990
ISRN LUTMDN/TMHP--11/1084--SE

Copyright © Karl Martin Johan Andersson, 2011

Division of Heat Transfer
Department of Energy Sciences
Faculty of Engineering (LTH)
Lund University
Box 118, SE-221 00, Lund, Sweden

# Abstract

Fuel cells are electrochemical devices that directly transform chemical energy into electricity. They are promising for future energy systems, since they are energy efficient, able to use renewable fuels and, when hydrogen is used as fuel, there are no direct emissions of greenhouse gases. Various improvements are made during the recent years, however the technology is still in the early phases of commercialisation.

Fully coupled computational fluid dynamics (CFD) approaches based on the finite element method (with the software COMSOL Multiphysics) in two-dimensions are developed, in several steps, to describe an intermediate temperature SOFC single cell. Governing equations covering heat, gas-phase species, momentum, ion and electron transport are implemented and coupled to kinetics describing internal reforming and electrochemical reactions. Both ordinary and Knudsen diffusion are considered for the gas-phase species transport. For the heat transport a local temperature equilibrium approach is compared to a local temperature non-equilibrium approach, considering the solid- and gas-phases. The Darcy-Brinkman equation enables continuous pressure and velocity fields over the electrode/gas channel interfaces. The electrochemical reaction model is extended from zero-dimension (with only an average value defined) in the early models, to one-dimension covering the variation in current density along the flow direction. Finally a two-dimensional approach including the current density distribution, both along the flow direction and through the electrolyte-electrodes, is developed. The model relies on experimental data from a standard cell developed at Ningbo Institute of Material Technology & Engineering (NIMTE) in China.

The anode microscopic structure and catalytic characteristics have a major impact on the internal reforming reaction rates and also on the cell performance. The large difference between the different activation energies and reaction kinetics found in the open literature may be due to the fact that several parameters probably have a significance influence on the reaction rate. Heat is generated due to ohmic, activation and concentration polarizations within the electrolyte and electrodes as well as change of entropy in the cathodic electrochemical reactions. Heat is consumed due to the change of entropy in the anodic electrochemical reactions and the steam reforming reactions within the anode. The activation polarizations in the electrodes and the ohmic polarization due to ion transport in the YSZ material are found to be the major part of the polarizations. The activation polarization is the most significant and as the electrochemical model is extended from one- to two-dimensions, the activation polarization within the cathode becomes smaller than the one within the anode. This difference might be explained by different current density per (active TPB) area and variable area-to-volume-ratios for the electrochemical reactions within the anode and cathode, respectively. The current density and the activation polarization are the highest at the electrolyte-electrode interface and decreases rapidly within the electrodes as the distance from the interface increases. However, the ohmic polarization by ion transfer increases for the positions away from the interface.

Keywords: *SOFC, anode-supported, modeling, CFD, charge/species/heat/momentum transport, electrochemical/internal reforming reactions, TPB, area-to-volume ratio, COMSOL Multiphysics*

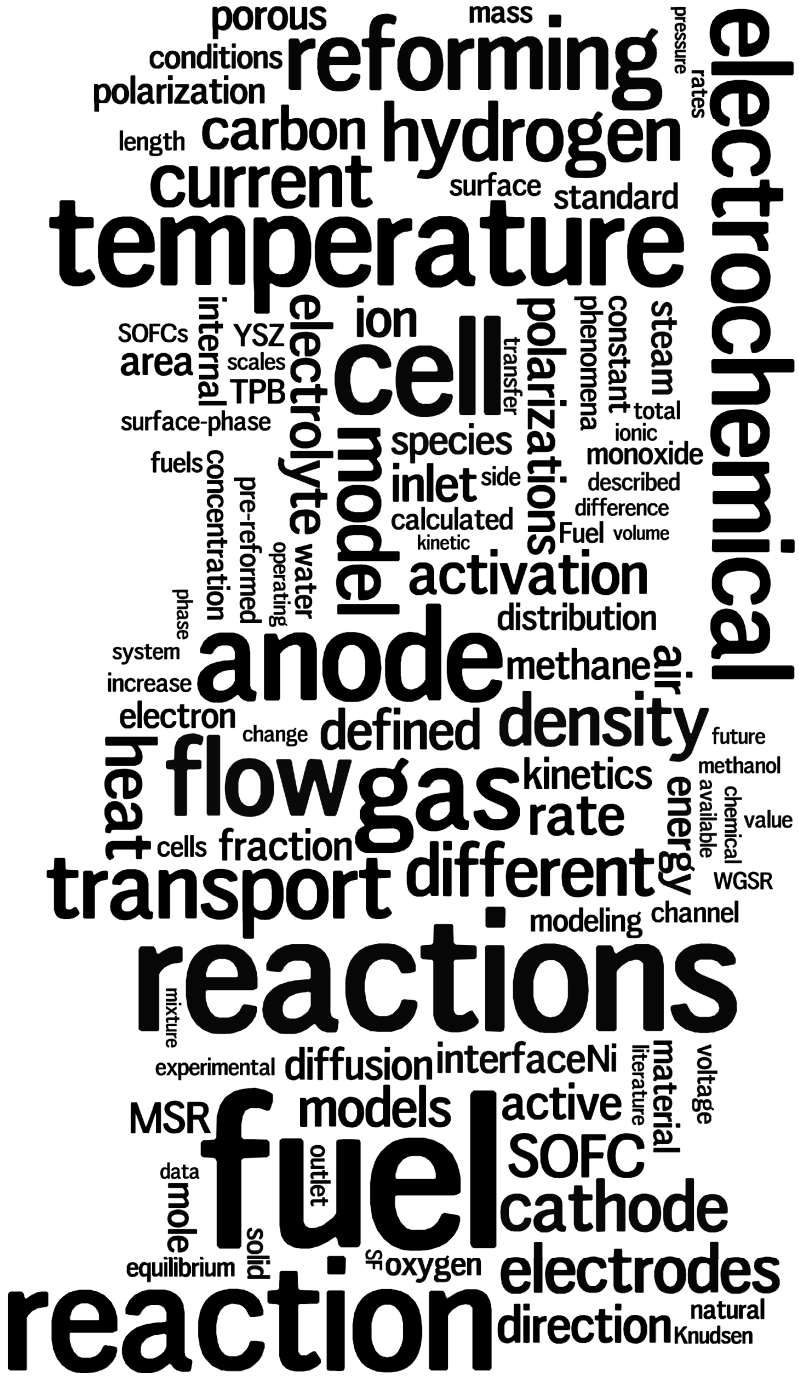
porous
mass
pressure
conditions
reforming
electrochemical
polarization
rates
length
carbon
hydrogen
current
surface
standard
temperature
internal
electrolyte
ion
cell
polarizations
steam
SOFCs
YSZ
constant
phenomena
area
scales
transfer
TPB
total
surface-phase
ionic
species
monoxide
fuels
concentration
pre-reformed
inlet
side
described
difference
calculated
Fuel
volume
kinetic
water
operating
model
activation
phase
distribution
anode
system
methane
air
increase
electron
change
defined
density
future
heat
flow
gas
kinetics
methanol
energy
chemical
available
rate
value
cells
fraction
different
WGSR
transport
modeling
channel
reactions
mixture
experimental
diffusion
interface
Ni
material
literature
voltage
MSR
models
active
fuel
SOFC
data
outlet
cathode
mole
solid
equilibrium
oxygen
electrodes
reaction
direction
natural
Knudsen

# Populärvetenskaplig beskrivning på svenska

## Bränslecellen uppfanns redan 1838, det kommersiella genombrottet dröjde till 2007, den framtida potentialen är mycket lovande

Domedagsprofetior angående växthuseffektens betydelse för livet på jorden når oss via media allt oftare. Bränsleceller är mycket lovande för ett framtida miljövänligt samhälle. Hög energieffektivitet och inga utsläpp av koldioxid, kväveoxider eller hälsoskadliga partiklar är några av fördelarna. Ett minskat behov av olja kan leda till ett minskat beroende av oberäkneliga oljestater och på sikt till en fredligare värld.

**Bränslecellens utveckling**
Bränslecellen är ingen ny uppfinning, idén kommer från år 1838 och Christian Friedrich Schönbein (verksam vid universitet i Basel) och William Robert Grove (verksam vid Royal Insitution of Great Britain). Det dröjde dock fram till 1950-talet innan kompletta bränslecellssystem var konstruerade. Anledningen till att utvecklingen var långsam till en början kan till stor del förklaras med tillgången till billig olja. Bränsleceller blev mer allmänt kända då de användes som kraftkälla i det amerikanska rymdprogrammet Apollo. Forskningen har ökat mycket under senare år på grund av ökade bränslepriser och diskussionen kring växthuseffektens påverkan på jordens klimat.

**Hur fungerar en bränslecell?**
Den enklaste formen av en bränslecell bygger på att syre och väte reagerar med varandra och bildar vatten. En bränslecell är uppbyggd av en anod, en katod och en elektrolyt. En anod är den del i en elektrolytisk cell som är förbunden med strömkällans positiva pol, och katoden är sammanbunden med dess negativa pol. Elektrolyten kan liknas vid ett membran. Det gasformiga bränslet transporteras till anoden där det reagerar i elektrokemiska reaktioner med syrejoner. Syrejonerna produceras i katoden där syre reagerar med elektroner till jonform. Syrejonerna transporteras igenom elektrolyten för att nå bränslet i anoden. Elektronerna släpps inte igenom elektrolyten, vilket gör att en spänning uppstår. Den givna beskrivningen gäller för vad som sker i en fastoxidbränslecell, men också övriga typer av bränsleceller är uppbyggda enligt motsvarande principer.

Fastoxidbränsleceller har en hög arbetstemperatur, elektrolyten, bestående av en fastoxid, är utformad för att endast släppa igenom syrejoner som transporteras från katoden till anoden.

Skillnaden mellan olika typer av bränsleceller är främst vilken typ av elektrolyt som används och bränslecellens arbetstemperatur.

Bränsleceller producerar elektricitet och värme direkt från kemiska reaktioner mellan bränsle och luft. Vilket bränsle som kan användas beror på vilken typ av bränslecell. När ren vätgas eller biogas används blir det inga nettoutsläpp av koldioxid, hälsoskadliga partiklar eller kväveoxider om produktionen av bränsle är ren. Processen är på så sätt helt miljövänlig och koldioxidneutral.

## Liten som en ärta till stor som ett kraftverk

Den framtida potentialen för bränsleceller är mycket stor eftersom de kan byggas i många olika storlekar. Mycket små för att ersätta ett batteri, små för att generera el till kringutrustning i en bil eller lastbil, stora för att ersätta motorn i en personbil och mycket stora i form av ett kraftvärmeverk. De största hindren för en kommersialisering i stor skala är tillverkningskostnaden, livslängden och saknaden av en infrastruktur för vätgas och biogas/ naturgas.

## Fred på jorden?

En ökad användning av bränsleceller kan leda till en ökad lokal bränsleproduktion, och därmed ett minskat beroende från import av olja och naturgas från länder där politisk instabilitet hör till vardagen. Dispyter angående rättigheter till oljeproduktion har resulterat i flera krig på senare år som kriget mellan Iran och Irak, Kuwaitkriget och Irakkriget. En ökad användning av effektiva energisystem, där bränsleceller är en viktig nyckelkomponent, kan vara viktigt för skapandet av en fredligare värld.

## Den egna forskningen

För fastoxidbränsleceller där arbetstemperaturen är mellan 600 och 1000 °C är det möjligt att använda sig av mer komplexa bränslen jämfört med vätgas, som exempelvis naturgas, biogas, metanol, etanol eller diesel. Då sker en omvandling av bränslet, antingen i en egen enhet som bränslet får passera innan det kommer till bränslecellen, eller inne i bränslecellens anod. Det material som vanligtvis används i anoden har visat sig vara lämpligt för katalytisk omvandling av naturgas och biogas till vätgas och kolmonoxid, vilka kan användas som bränsle i de elektrokemiska reaktionerna med syrejoner som sker i bränslecellens anod.

Forskningen inom forskargruppen i Lund har visat på fördelar med att omvandla biogas eller naturgas inne i bränslecellen. Värme som kommer från de elektrokemiska reaktionerna kan användas inne i bränslecellen för att driva omvandlingen till vätgas och kolmonoxid. Den totala effektiviteten ökar samtidigt som de totala temperaturskillnaderna minskar. Resultaten kan på sikt leda till en minskad produktionskostnad och en ökad livslängd.

Bränslecellens elektrokemiska reaktioner sker i anoden och katoden, huvuddelen av reaktionerna sker inom en tjocklek av endast 2,4 mikrometer i katoden och 6,2 mikrometer i anoden. I min forskning undersöks hur ytan för dessa reaktioner kan utökas och hur transporten av syrejoner kan underlättas. En större tillgänglig aktiv yta för elektrokemiska reaktioner möjliggör en högre strömtäthet. Den egenutvecklade modellen är validerad mot experimentella data från NIMTE (Ningbo Institute of Material Technology and Engineering) i Kina.

## Hur långt har utvecklingen kommit?

Bränsleceller anses vara i kommersiell tillverkning från och med år 2007. Produktion i stor skala har startat för ett antal nischmarknader inom rymdprogrammen, för militära ändamål och som reservkraft för till exempel sjukhus eller mobilmaster. Inom några år kommer sannolikt

bränslecellssystem att vara mer vanliga inom fordonsindustrin. Det är en enorm marknad som hägrar och marknadens i dag mest effektiva bränslecellsdriva bil är tre gånger så hög verkningsgrad som en vanlig bensinmotor. En ökad forskning och utveckling på bränsleceller kommer att leda till en ökad ekonomisk tillväxt.

## Framtida möjligheter

Volvo lastvagnar och Delphi utvecklar båda bränslecellssystem, som de hoppas kunna introducera på marknaden år 2012 eller 2013. Det kan nämnas att Toyota förväntar sig en dubblerad verkningsgrad om bränsleceller ersätter dagens förbränningsmotorer i bilar. Marknaden för bränsleceller förväntas växa kraftigt i takt med att tillverkningskostnaden minskar, verkningsgraden och livslängden ökar. De största konkurrenterna till bränsleceller är ett lågt pris på olja samt bristen på ett väl utvecklat system för säker lagring och transport av ett gasformigt bränsle. Vid användning av en extra enhet för omvandling av till exempel diesel ökar systemkostnaderna. Bränsleceller är beroende av batterier för att kunna leverera elektricitet när systemet startas upp samt för att möjliggöra drift vid en för bränslecellen optimal belastning.

I takt med att tillverkningskostnaderna sjunker och/eller bränslepriserna stiger ökar antalet områden där bränsleceller blir mer prisvärda jämfört med nuvarande teknologier så som batterier, motorer eller kraftverk. Den internationella energimyndigheten (IEA) förutspår att vätgas motsvarande 15 procent av dagens råoljeproduktion kommer att användas i bränsleceller för fordon år 2050. IEA förutspår vidare en installerad effekt motsvarande mer än den nuvarande effekten från kärnkraft i hela världen för stationära bränslecellssystem år 2050. För att uppnå denna stora betydelse måste tillverkningskostnaden sjunka och livslängden öka.

## Sammanfattningsvis

Problemen och utmaningarna med dagens energisystem är både globala och lokala med utsläpp av bland annat koldioxid, hälsoskadliga partiklar och kväveoxider. Man vet att det finns en begränsad mängd av fossila bränslen och det diskuteras hur länge mänskligheten kan fortsätta att utvinna olja i samma takt som idag. Möjligheten av en ren, miljövänlig och energieffektiv bränsleanvändning driver utvecklingen av bränsleceller och bränslecellssystem framåt i ett allt snabbare tempo. Det som kommer att bestämma tillväxten inom bränslecellsområdet är hur snabbt tillverkningskostnaden kan sänkas, livslängden ökas samt utvecklingen av oljepriset.

Den aktuella forskningen är finansierad av den svenska staten via Vetenskapsrådet och Sida samt av Europeiska forskningsrådet.

# Acknowledgments

This work has been carried out at the Division of Heat Transfer, Department of Energy Sciences, Faculty of Engineering, Lund University, Sweden.

I would like to express great appreciation to my supervisors Professor Jinliang Yuan and Professor Bengt Sundén, for allowing me a lot of freedom in my work, many discussions and a lot of support and guidance during the last 4 ½ years.

My deep appreciation goes to Hedvig Paradis for a fruitful, developing and friendly cooperation during the last 2 ½ years. Thanks goes to Munir Khan, Maria Navasa and Erik Johansson for support and inspiring discussions about fuel cells and modeling.

Many thanks go to Professor Wei Guo Wang at Ningbo Institute of Material Technology and Engineering-Chinese Academy of Sciences (NIMTE-CAS), China, for inviting me to a 3 months research visit. Dr. Ting Shuai Li and Dr. Tao Chen, both at NIMTE during autumn 2010, are acknowledged for introducing me to the experimental SOFC research.

The current work is financially supported by the Swedish Research Council (Vetenskapsrådet, VR), the European Research Council (ERC) and the Swedish Research Links (Sida).

Scholarships enabling participation and presentations in various scientific conferences are gratefully acknowledged, such as Sigfrid och Walborg Nordkvist Foundation (2008), Ångpanneföreningens Research Foundation (2009, 2010 and 2011) and Bengt Ingeströms Scholarship Foundation (2011). The Chinese Academy of Engineering (CAE) and the Royal Swedish Academy of Engineering Sciences (IVA) supported a three month research visit to NIMTE-CAS in Ningbo, China, during autumn 2010.

# List of Publications

This dissertation is based on the following papers which will be referred to by their roman numerals in the text:

I. **M. Andersson**, J. Yuan, B. Sundén, *Review on Modeling Development for Multiscale Chemical Reactions Coupled Transport Phenomena in SOFCs,* J. Applied Energy, **87**, pp. 1461-1476, 2010.

II. **M. Andersson**, J. Yuan, B. Sundén, W.G. Wang, *LTNE Approach and Simulation for Anode-Supported SOFCs*, ASME FuelCell2009-85054, in: Proceedings of the 7th International Fuel Cell Science, Engineering & Technology Conference, Newport Beach, California, USA, 2009.

III. **M. Andersson**, H. Paradis, J. Yuan, B. Sundén, *Modeling Analysis of Different Renewable Fuels in an Anode Supported SOFC*, ASME J. Fuel Cell Science and Technology, **8**, 031013, 2011.

IV. H. Paradis, **M. Andersson** J. Yuan, B. Sundén, *CFD Modeling: Different Kinetic Approaches for Internal Reforming Reactions in an Anode-Supported SOFC*, ASME J. Fuel Cell Science and Technology, **8**, 031014, 2011.

V. **M. Andersson**, X. Lu, J. Yuan, B. Sundén, *Analysis of Microscopic Anode Structure Effects on an Anode-Supported SOFC Including Knudsen Diffusion*, Proceeding of the 219th ECS Meeting in Montreal - Twelfth International Symposium on Solid Oxide Fuel Cells (SOFC-XII), S.C Singhal, K. Eguchi (eds), ECS Transactions, **35**, pp. 1799-1809, Canada, 2011.

VI. **M. Andersson**, H. Paradis, J. Yuan, B. Sundén, *Review of Catalyst Materials and Catalytic Steam Reforming Reactions in SOFC Anodes*, Int. J. Energy Research, 2011 (Available online, DOI: 10.1002/er.1875).

VII. **M. Andersson**, J. Yuan, B. Sundén, T.S. Li, W.G. Wang, *Modeling Validation and Simulation of an Anode Supported SOFC including Mass and Heat Transport, Fluid Flow and Chemical Reactions*, ASME ESFuelCell2011-54006, in: Proceedings of the ASME 9th International Fuel Cell Science, Engineering & Technology Conference, Washington, DC, USA, 2011.

VIII. **M. Andersson**, J. Yuan, B. Sundén, *SOFC Modeling Considering Electrochemical Reactions at the Active Three Phase Boundaries*, Int. J. Heat and Mass Transfer, 2011 (Accepted, DOI: 10.1016/j.ijheatmasstransfer.2011.10.032).

**My contribution to the listed papers**

Papers I, II, III, V, VI VII and VIII are for the majority my own work.

Paper IV is based on a MSc thesis that I supervised. Additionally I developed the basic model that was used and further developed in this paper.

**Other related publications by the author:**

1. **M. Andersson** J. Yuan, B. Sundén, *Chemical Reacting Transport Phenomena and Multiscale Models for SOFCs*, in: Proceedings of the Heat Transfer 2008, B. Sundén, C.A. Brebbia (eds), WIT Transactions on Engineering Sciences, **61**, pp. 69-79, WIT Press, UK, 2008.
2. J. Yuan, G. Yang, **M. Andersson** B. Sundén, *Analysis of Chemical Reacting Heat Transfer in SOFCs*, in: Proceedings of the 5th European Thermal Sciences Conference, Eindhoven, Netherlands, 2008.
3. J. Yuan, G. Yang, **M. Andersson**, B. Sundén, *CFD Approach for Chemical Reaction Coupled Heat Transfer in SOFC Channels*, in: Proceedings of the 7th International Symposium on Heat Transfer, ISHT7, Beijing, China, 2008.
4. **M. Andersson**, *SOFC Modeling Considering Mass and Heat Transfer, Fluid Flow with Internal Reforming Reactions*, Licentiate Thesis, ISRN LUTMDN/TMHP-09/7063-SE, Department of Energy Sciences, Lund University, Sweden, 2009.
5. **M. Andersson**, J. Yuan, B. Sundén, *SOFC Modeling Considering Internal Reforming by a Global Kinetics Approach*, in: Proceeding of the 216th ECS Meeting in Vienna -Eleventh International Symposium on Solid Oxide Fuel Cells (SOFC-XI), S.C Singhal, H. Yokokawa (eds), ECS Transactions, **25**, pp. 1201-1210, Austria, 2009.
6. **M. Andersson**, H. Paradis, J. Yuan, B. Sundén, *Modeling Analysis of Different Renewable Fuels in an Anode Supported SOFC*, ASME FuelCell2010-33044, in: Proceedings of the ASME 8th International Fuel Cell Science, Engineering & Technology Conference, Brooklyn, New York, USA, 2010.
7. H. Fridriksson, B. Sundén, J. Yuan, **M. Andersson**, *Study on Catalytic Reactions in Solid Oxide Fuel Cells with Comparison to Gas Phase Reactions in Internal Combustion Engines*, ASME FuelCell2010-33276, in: Proceedings of the ASME 8th International Fuel Cell Science, Engineering & Technology Conference, Brooklyn, New York, USA, 2010.
8. H. Paradis, **M. Andersson**, J. Yuan, B. Sundén, *CFD Modeling Considering Different Kinetic Models for Internal Reforming Reactions in an Anode-Supported SOFC*, ASME FuelCell2010-33045, in: Proceedings of the ASME 8th International Fuel Cell Science, Engineering & Technology Conference, Brooklyn, New York, USA, 2010.
9. **M. Andersson**, H. Paradis, J. Yuan, B. Sundén, *Catalyst Materials and Catalytic Steam Reforming Reactions in SOFC Anodes*, in: Proceedings of the International Green Energy Conference, Waterloo, Ontario, Canada 2010.
10. H. Paradis, **M. Andersson** J. Yuan, B. Sundén, *Comparative Analysis of Different Renewable Fuels for Potential Utilization in SOFCs*, in: Proceedings of the International Green Energy Conference, Waterloo, Ontario, Canada, 2010.
11. H. Paradis, **M. Andersson**, J. Yuan, B. Sundén, *Simulation of Alternative Fuels for Potential Utilization in Solid Oxide Fuel Cells*, Int. J. Energy Research, **35**, pp. 1107-1117, 2011.
12. H. Paradis, **M. Andersson**, J. Yuan, B. Sundén, *The Kinetics Effect in SOFCs on Heat and Mass Transfer Limitations: Interparticle, Interphase, and Intraparticle Transport*, ASME ESFuelCell2011-54015, in: Proceedings of the ASME 9th International Fuel Cell Science, Engineering & Technology Conference, Washington, DC, USA, 2011.
13. **M. Andersson**, J. Yuan, B. Sundén, *SOFC Modeling Considering Electrochemical Reactions at the TPBs*, in: Proceedings of the International Conference on Power and Energy Engineering (CPEE/CET2011-20962), Shanghai, China, 2011.

# Table of Contents

**Abstract** ..... **i**

**Populärvetenskaplig beskrivning på svenska** ..... **iii**

**Acknowledgments** ..... **vii**

**List of Publications** ..... **ix**

**Table of Contents** ..... **xi**

**Nomenclature** ..... **xiii**

**1 Introduction** ..... **1**
1.1 Background ..... 1
1.2 Objectives ..... 2
1.3 Methodology ..... 3
1.4 Outline of the thesis ..... 3

**2 Fuel Cells, Transport Processes and Chemical Reactions** ..... **5**
2.1 Introduction to fuel cells ..... 5
2.1.1 Early development ..... 7
2.1.2 Future fuel cell expectations and potential ..... 8
2.2 Solid Oxide Fuel Cells ..... 9
2.2.1 Alternative fuels ..... 11
2.3 Transport phenomena in SOFCs ..... 12
2.3.1 Gas-phase species transport ..... 13
2.3.2 Momentum transport ..... 14
2.3.3 Heat transport ..... 15
2.3.4 Ion and electron transport ..... 16
2.4 Internal reforming reactions ..... 19
2.4.1 Global reforming reaction kinetics ..... 21
2.4.2 Elementary multi-step reaction kinetics ..... 23
2.5 Electrochemical reactions ..... 28
2.5.1 Polarizations ..... 30
2.6 Micro and macroscale phenomena and analysis methods ..... 31
2.6.1 How far can SOFC modeling reach? ..... 33

**3 CFD Model Development - Governing Equations for Transport Processes and Chemical Reactions** ..... **35**
3.1 Gas-phase species transport ..... 36
3.2 Momentum transport ..... 37

3.3 Heat transport ..... 38
3.3.1 Local temperature equilibrium (LTE) ..... 38
3.3.2 Local temperature non-equilibrium (LTNE) ..... 39
3.3.3 Heat consumption and generation within the cell ..... 39
3.4 Ion and electron transport ..... 40
3.5 Electrochemical reactions ..... 41
3.6 Internal reforming reactions ..... 42

**4 Solution Methods and Model Validation ..... 43**
4.1 Solution methods ..... 43
4.2 Validation of the one-dimensional electrochemical model ..... 44

**5 Results and Discussion ..... 47**
5.1 Basic model with only hydrogen as fuel (paper II) ..... 47
5.2 Extended models including internal reforming reactions of hydrocarbon fuels (papers III and IV) ..... 49
5.3 Knudsen diffusion (paper V) ..... 54
5.4 One-dimensional electrochemical model and validation (paper VII) ..... 56
5.5 Two-dimensional electrochemical model with charge transport (paper VIII) ..... 58

**6 Conclusions ..... 63**

**7 Future Work ..... 65**

**8 References ..... 67**

# Nomenclature

| | |
|---|---|
| $A_i$ | pre-exponential factor, units vary depending on participating species |
| $a_k$ | species dependent parameter in the specific heat calculation |
| $AV$ | surface area to volume ratio, $m^2/m^3$ |
| $b_k$ | species dependent parameter in the dynamic viscosity calculation |
| $c_p$ | specific heat at constant pressure, J/(kg·K) |
| $c_k$ | species dependent parameter in the thermal conductivity calculation |
| $c_j$ | concentration, mol/m³ |
| $D_{ij}$ | diffusion coefficient, $m^2/s$ |
| $D_i^T$ | thermal diffusion coefficient, kg/(m·s) |
| $E$ | actual voltage, V |
| $E_a$ | activation energy, J/mol |
| $E^0$ | theoretical (reversible) voltage before partial pressure consideration, V |
| $E_b$ | classical electronic energy barrier of adsorption, J/mol |
| $E_{eq,e}$ | equilibrium voltage for the electrodes, V |
| $E^{OCV}$ | open circuit voltage or theoretical voltage after partial pressure consideration (before consideration of polarizations), V |
| $\mathbf{F}$ | volume force vector, $N/m^3$ |
| f | empirical factor for electrochemical validation ($A_{active}/A_{interface}$), - |
| F | Faraday constant, 96485 C/mol |
| $\Delta G$ | change of Gibbs free energy of reactions, J/mol |
| $h$ | Planck constant, J/s; thickness of anode active zone, m |
| $h_{s,g}$ | heat transfer coefficient, $W/(m^2 \cdot K)$ |
| $h_v$ | volumetric heat transfer coefficient, $W/(m^3 \cdot K)$ |
| $\Delta H$ | enthalpy change of reactions, J/mol |
| $i_a$ | current density (per area), $A/m^2$ |
| $i_v$ | current density (per volume), $A/m^3$ |
| $i^*$ | empirical parameter in the electrochemical model, units vary depending on assumed rate limiting step |
| $i_0$ | exchange current density, $A/m^2$ |
| $k$ | thermal conductivity, W/(m·K) |
| $k_b$ | Boltzmann's constant, J/K |
| $K_{eq}$ | equilibrium constant, units vary depending on participating species |
| $k_i$ | reaction rate constant, units vary depending on participating species |
| $l_{ij}$ | characteristic length, Å |
| $l_{TPB}$ | three phase boundary length, m |

| | |
|---|---|
| $M$ | molecular weight, kg/mol |
| $n$ | number of species (in the gas-phase species transport governing equation), - |
| $n_e$ | number of electrons transferred per reaction, - |
| $n_{H2}$ | moles of $H_2$ generated in the reforming reactions per mole of fuel, - |
| $n_i$ | temperature exponent fraction in the reaction rate, - |
| $N_{sites}$ | standard-state number of binding sites per adsorbate, - |
| $p$ | pressure, Pa or atm |
| $Q$ | source term (heat), $W/m^3$; total partition function, - |
| R | gas constant, 8.314 J/(mol·K) |
| $R_{ads}$ | total number of adsorbate reactants, - |
| $r_e$ | effective pore radius, m |
| $r_i$ | chemical reaction rate, $mol/(m^3 \cdot s)$ or $mol/(m^2 \cdot s)$ |
| $R_{ohm}$ | electrolyte specific-area ohmic resistance, $\Omega/m^2$ |
| $R_{tot}$ | the total number of reactants participating in reactions, - |
| $S_i$ | source term (species), $kg/(m^3 \cdot s)$ |
| $\Delta S_i$ | entropy change of reaction, J/(K·mol) |
| $t$ | transport distance within a specific component, m |
| $T$ | temperature, K |
| $\vec{u}$ | velocity vector, m/s |
| $V$ | volume fraction, - |
| $w_j$ | mass fraction of species j, kg/kg |
| x, y | coordinate system, m |
| $x_j$ | mole fraction of species j, mol/mol |

**Greek symbols**

| | |
|---|---|
| β | transfer coefficient in the Butler-Volmer equation, - |
| $\beta_F$ | Forchheimer coefficient, $kg/m^4$ |
| $\gamma_k$ | sticking coefficient, - |
| $\Gamma_{tot}$ | total surface site density, $mol/m^2$ |
| $\varepsilon$ | porosity, - |
| $\varepsilon_{ki}$ | parameter covering the coverage dependency of rate constant, J/mol |
| $\eta$ | polarizations or over-potential, V |
| $\theta_k$ | surface coverage, - |
| $\kappa$ | permeability, $m^2$ |
| $\mu$ | dynamic viscosity, Pa·s |
| $\mu_{ki}$ | parameter modeling the coverage dependency of rate constant, - |
| $\rho$ | density, $kg/m^3$ |
| $\sigma$ | ionic/electronic conductivity, $\Omega^{-1}m^{-1}$ |
| $\sigma_j$ | co-ordination number, - |
| $\tau$ | tortuosity, - |
| $\phi$ | potential, V |
| $\Psi$ | viscous stress tensor, $N/m^2$ |

| | |
|---|---|
| $\Omega_D$ | diffusion collision integral, - |

**Subscripts and Superscripts**

| | |
|---|---|
| - | reverse reaction |
| * | surface-phase species (bound to the catalyst) |
| a | anode |
| act | activation polarization |
| c | cathode |
| conc | concentration polarization |
| e | electrochemical reactions, electrode ( $e \in \{a, c\}$ ) |
| eff | effective |
| el | electrolyte |
| g | gas-phase |
| i | gas-phase species i, reaction i |
| j | gas-phase species j |
| k | surface-phase species k |
| K | Knudsen diffusion |
| l | electrolyte material |
| m | reaction order of methane (in the MSR) |
| MSR | methane steam reforming reaction |
| n | reaction order of water (in the MSR) |
| ohm | ohmic polarization |
| ref | reforming reactions, $ref \in \{MSR, WGSR, ATR, SR\}$ |
| s | solid-phase, electrode material |
| tot | total |

**Abbreviations**

| | |
|---|---|
| AFC | alkaline fuel cell |
| APU | auxiliary power unit |
| ATR | autothermal reforming |
| CAE | Chinese Academy of Engineering |
| CAS | Chinese Academy of Sciences |
| CFD | computational fluid dynamics |
| CM | continuum methods |
| DFT | density functional theory |
| DIR | direct internal reforming |
| DMFC | direct methanol fuel cell |
| ERC | European Research Council |
| FC | fuel cell |
| FDM | finite difference method |
| FEM | finite element method |
| FIB-SEM | focused ion beam-scanning electron microscopy |
| FVM | finite volume method |
| HRC | heterogeneous reaction mechanism |

| | |
|---|---|
| IEA | International Energy Agency |
| IIR | indirect internal reforming |
| IR | internal reforming |
| IT | intermediate temperature |
| IVA | Kungliga Ingenjörsvetenskapsakademien (Royal Swedish Academy of Engineering Sciences) |
| LBM | lattice Boltzmann method |
| LHV | lower heating value |
| LTE | local temperature equilibrium |
| LTNE | local temperature non-equilibrium |
| MC | Monte Carlo |
| MCFC | molten carbonate fuel cell |
| MD | molecular dynamics |
| MSR | methane steam reforming reaction |
| NIMTE | Ningbo Institute of Material Technology & Engineering, China |
| PAFC | phosphoric acid fuel cell |
| PEMFC | polymer electrolyte membrane fuel cell |
| POX | partial oxidation |
| PWC | point-wise coupling methodology |
| SC | steam-to-carbon ratio |
| SF | steam-to-fuel ratio |
| SOFC | solid oxide fuel cell |
| SR | steam reforming |
| TPB | three-phase boundary |
| VR | Vetenskapsrådet (Swedish Research Council) |
| WGSR | water-gas shift reaction |
| WTP | willingness to pay |
| ¥ | Japanese Yen |

**Chemical**

| | |
|---|---|
| $C_2H_5OH$ | ethanol |
| CGO | gadolinium doped cerium oxide |
| $CH_3OCH_3$ | di-metyl-ether (DME) |
| $CH_3OH$ | methanol |
| $CH_4$ | methane (gas-phase) |
| $C_nH_mO_z$ | biomass with $n$ moles of carbon, $m$ moles of hydrogen and $z$ moles of oxygen |
| CO | carbon monoxide (gas-phase) |
| Co | cobalt |
| $CO_2$ | carbon dioxide (gas-phase) |
| $CO_3^{2-}$ | carbonate ion |
| COS | carbonyl sulfide |
| Cu | copper |
| $e^-$ | electron |

| | |
|---|---|
| Fe | iron |
| $H^+$ | proton |
| $H_2$ | hydrogen (gas-phase) |
| $H_2O$ | water/steam (gas-phase) |
| $H_2S$ | hydrogen sulfide |
| La | lanthanum |
| LSCF | $[La,Sr][Co,Fe]O_3$ |
| LSM | strontium doped lanthanum manganite |
| $N_2$ | nitrogen (gas-phase) |
| $NH_3$ | ammonia |
| Ni | nickel |
| Ni(111) | Ni terrace (catalytically active, and stable facet on Ni crystallites) |
| NiO | nickel oxide |
| $O_0^X$ | lattice oxygen |
| $O_2$ | oxygen (gas-phase) |
| $O^{2-}$ | oxygen ion |
| $OH^-$ | hydroxyl ion |
| S | sulfur |
| Sc | scandium |
| Sr | strontium |
| $V_o^{\bullet\bullet}$ | oxygen vacancy |
| YSZ | yttria-stabilized zirconia |

# 1 Introduction

This work is based on various research projects supported by the Swedish Research Council (Vetenskapsrådet, VR), the European Research Council (ERC) and the Swedish Research Links (Sida). It contains modeling and analysis of heat, momentum, gas-phase species, ion and electron transport, as well as electrochemical and internal reforming reactions inside intermediate temperature anode-supported solid oxide fuel cells (SOFCs). A basic cell scale model that uses a hydrogen/steam mixture as fuel is developed (paper II), and further extended to include/cover:

1) Kinetics for internal reforming reactions of hydrocarbon fuels (papers III and IV).
2) Knudsen diffusion to describe the collision effects between the gas molecules and the pore walls (paper V).
3) Extension of the electrochemical model from 0D (papers II, III, IV and V) to 1D, along the flow direction, (paper VII). Also the ion transport in the electrodes is accounted (with the ion transport factor) in paper VII.
4) Validation of the developed model with experimental data (paper VII).
5) A 2D (along the flow direction and through the electrodes and electrolyte) electrochemical model accounting for a realistic ion and electron transport path in the electrodes (paper VIII).

## 1.1 Background

The fuel cell potential is enormous, however the cell/system production and the fuel cost (comparative to competing technologies) must be decreased and the life time increased before becoming an important part in the energy systems. There is a need for multi-physics and- scale SOFC models, as most existing models do not consider species, heat, momentum, ion and electron transport as well as chemical reactions (electrochemical and internal reforming) simultaneously. Strong coupling between the mentioned phenomena makes multi-physics SOFC modeling promising for optimizing the design and decreasing the production cost. The internal reforming and electrochemical reaction rates are dependent on the local microscopic structure, temperature and the gas-phase concentrations. The local temperature depends on the reaction rates, the flow rates of the air and fuel streams, the gas-phase concentrations as well as the different polarizations. The gas-phase concentration distribution depends on the temperature, the flow rates of the air and fuel streams as well as the reactions in the electrode porous structure. The ion and electron distributions are affected by the local temperature, the gas-phase concentrations and also the porous material structure. The different polarizations depend on temperature, gas-phase concentrations and porous material structure/design. The above mentioned relationships between the physical parameters/phenomena within a fuel cell show the importance of the couplings between them, i.e., the reason why computational fluid

dynamics (CFD) calculations are necessary and needed to understand the physical phenomena within fuel cells and for improving the fuel cell overall performance, with the overall purpose to reduce the cost and promote commercialization.

Before designing and developing a model, it is important to specify what one wants to know, how accurate and why. The choice of computational methods must come from a clear understanding of physical and chemical phenomena. It is also needed to be aware of what approximations being made and which ones being significant (can for example be investigated with parameter studies). Research of the physical phenomena is based on different scales: micro-, meso- and macroscales. The particle size in SOFC functional materials is in the sub-micron scale, and the three-phase boundary (TPB) structure/design is in the nanoscale. The morphology and properties of these scales are important for the performance of the fuel cell, since they control how much of the Gibbs free energy being available for the reactions. It means that the sciences at a microscopic scale are critical to the performance at a macroscopic (system) scale. A robust model and multi-scale analysis should consider those microscopic details as well as macroscale processes.

It has been concluded in this work that most of the polarizations within the cells are generated due to activation polarization in the electrodes as well as ionic resistance in the electrolyte and electrodes. The knowledge related to these findings is expected to increase when the developed model is further extended to include more detailed microscale phenomena within the electrodes and electrolyte. The reforming and electrochemical reactions depend strongly on the catalyst distribution in terms of particle size and various transport processes.

## 1.2 Objectives

The overall aim of this thesis is to analyze heat, gas-phase species, momentum, ion and electron transport as well as electrochemical and internal reforming reactions in SOFCs, in order to enhance the understanding of complex physical phenomena occurring inside the cell and the couplings between them, and in the long run enable to increase the efficiency, decrease the production cost and to promote the fuel cell commercialization. A basic model is developed to enable the prediction of concentration- and temperature distributions, having only hydrogen as fuel. This model is further extended in several steps to also include the mixture of carbon monoxide, carbon dioxide and methane as the fuel stream, involving internal reforming reactions, Knudsen diffusion, variations in current density along the flow direction as well as ion and electron transport within the electrolyte and electrodes. The objectives may be formulated in more details as given below:

- Through literature studies, the state-of-the-art CFD modeling has been reviewed including heat, species, momentum, ion and electron transport as well as internal reforming and electrochemical reactions within SOFCs. Modeling methods concerning physical phenomena at different scales and the integration between the different scales are identified.
- To develop CFD models in the cell scale concerning gas-phase species, heat, momentum, electron and ion transport.
- To investigate the effect of internal reforming reactions on temperature and concentrations, as well as to identify possible fuels for external and internal reforming reactions for SOFCs.

- To include kinetics for electrochemical reactions within the electrodes and to identify where the most significant polarizations occur, and how to reduce them.
- To study the characteristics and influence of ion and electron transport paths within the electrodes.
- To validate the developed model with experimental data.

## 1.3 Methodology

A literature review is conducted to find out what methods have been developed to model SOFCs, according to length scales. Coupling between different methods and length scales, i.e., multiscale modeling is outlined. SOFC microscale models correspond in many cases to the atom or molecular level. The Finite Element Method (FEM) and Finite Volume Method (FVM) are used to model SOFCs at the macroscale level. Multiscale modeling is a promising tool for fuel cell research. COMSOL Multiphysics, based on the FEM, as well as FLUENT, based on the FVM, are examples of commercial codes for analysis of different physical models at different scales. Multiscale modeling increases the understanding for detailed transport phenomena, and can be used to make a correct decision on the specific design and control of operating conditions. The tortuosity, which is an important parameter for characterization of fluid flow through the porous media in many macroscale models, is used in this work to describe microscale phenomena at the macroscale considering gas-phase species, ion and electron transport.

Models that describe physical (gas-phase species, heat, ionic, electronic and momentum) phenomena inside an anode-supported SOFC are developed, in COMSOL Multiphysics, to deeply understand the effect of design and operating parameters. A two-dimensional CFD approach is applied. This work focuses on the effect of operating temperature, oxygen and fuel utilizations, reaction kinetics for internal reforming reactions, ion transport within the electrodes and electrolyte, electron transport within the electrodes, ordinary and Knudsen diffusion as well as different polarizations. The considered cell includes interconnects, air and fuel channels, anode, cathode and electrolyte. Temperature dependent physical properties are taken into account as well. The temperature distribution in the solid- and gas-phase are calculated separately, based on the local temperature non-equilibrium (LTNE) approach for most of the models. The basic model is extended in several steps to study the effects of internal reforming reactions, Knudsen diffusion and ion transport within the electrodes and electrolyte and electron transport in the electrodes. The electrochemical reactions are in the early models defined as interface conditions in the transport equations, compared to the later models where the implementation considers source terms.

The developed model relies on the experimental data from a standard cell developed at Ningbo Institute of Material Technology & Engineering (NIMTE), in China. The single cell sample has dimensions of $5 \cdot 5.8$ cm$^2$, with an active area of $4 \cdot 4$ cm$^2$. A testing house is used, where the cell temperature is kept constant at 750 °C. Voltage probes are placed on the surface of the anode- and cathode support.

## 1.4 Outline of the thesis

The overview of the thesis is presented in chapter 1. Chapter 2 contains a literature survey, where early fuel cell development, future potential, different types of fuel cells, different

transport processes that take place inside a fuel cell, kinetic approaches covering internal reforming and electrochemical reactions as well as integration of phenomena occurring at different scales are presented. The developed mathematical models are introduced in chapter 3, with a breakdown to gas-phase species, momentum, heat, ion and electron transport as well as electrochemical and internal reforming reactions. The solution methods and the model validation are presented in chapter 4. The results and discussion are introduced in chapter 5 and the related conclusions in chapter 6. The ideas for future work are outlined in chapter 7.

# 2 Fuel Cells, Transport Processes and Chemical Reactions

In this chapter a short introduction to fuel cells is given. A description of the early development by C. F. Schönbein and W. R. Grove, as well as the future potential is presented. Basic information about fuel cell technology, with focus on SOFCs, is described. An introduction will be given to different transport phenomena occurring inside SOFCs as well as internal reforming and electrochemical reaction kinetics. Finally fuel cell modeling and integration between the different scales are outlined.

## 2.1 Introduction to fuel cells

Fuel cells directly convert the free energy of a chemical reactant to electrical energy and heat. This is different from a conventional thermal power plant, where the fuel is oxidized in a combustion process combined with a conversion process (thermal-mechanical-electrical energy), that takes place after the combustion [1]. If pure hydrogen is used, no pollution of air and environment occurs at all, because the output from the fuel cells is electricity, heat and water. Fuel cells do not store energy as batteries do [2]. A fuel cell consists of two electrodes: one anode for fuel and one cathode for oxidant. The electrodes are separated by the electrolyte and connected into an electrically conducting circuit. A gas or liquid flow, as the fuel or oxidant, is transported to a specific electrode, which should be permeable via a porous structure. Unit cells are organized together into stacks [3]. Different fuel cell types and their characteristics are summarized in Table 1.

The fuel cell is not a new invention, because the electrochemical process was discovered already in 1838-39 [4]. Among various types of fuel cells (FCs), the SOFC has attained significant interests because of its high efficiency and low emissions of pollutants to the environment. High temperature operation offers many advantages, such as high electrochemical reaction rate, flexibility of using various fuels and toleration of impurities (examples are given in Table 1) [5]. The creation of strategic niche markets and search for early market niches are of a vital importance for the further development [4].

The ideal amount of energy that can be converted into electrical energy can be described by the Gibbs free energy change of a chemical reaction ($\Delta G$) [3]:

$$\Delta G = -n_e \cdot \mathrm{F} \cdot E^{OCV} \tag{1}$$

where $n_e$ is the number of electrons involved in the reaction, F the Faraday constant and $E^{OCV}$ the open circuit voltage or the voltage of the cell for thermodynamic equilibrium in the absence of current flow.

*Table 1. Fuel Cell types and their characteristics [3,4].*

| | AFC | PAFC | PEMFC | SOFC | MCFC |
|---|---|---|---|---|---|
| **Electrolyte** | Alkaline - potassium hydroxide | Phosphoric acid | Polymer membrane | Ceramic membrane | Molten carbonate |
| **Mobile ion** | $OH^-$ | $H^+$ | $H^+$ | $O^{2-}$ | $CO_3^{2-}$ |
| **Producing water at** | Anode | Cathode | Cathode | Anode | Anode |
| **Operating temperature** | 50-200 °C | ~220 °C | 70-100 °C | 500-1000 °C | ~650 °C |
| **Current densities [A/cm$^2$]** | 0.1-0.4 | 0.15-0.4 | 0.4-0.9 | 0.3-1.0 | 0.1-0.2 |
| **Voltage interval [V]** | 0.85-0.6 | 0.8-0.6 | 0.75-0.6 | 0.95-0.6 | 0.95-0.75 |
| **Stack Efficiency (LHV) [%]** | 45-60 | 45-65 | 40-70 | 45-75 | 50-65 |
| **Typical Applications & Power Output** | Space power 1-15 kW Niche vehicles 20 kW | Stationary 200 kW | Vehicles 100 kW Stationary 1-10 kW Portables < 1.5 kW | Stationary 5-200 kW APUs ~5 kW | Large stationary 200 kW-MW |
| **Fuel** | $H_2$ | $H_2$ | $H_2$ | $CH_4$, $H_2$ | $CH_4$, $H_2$ |
| **Interconnect** | Metal | Graphite | Carbon or Metal | Stainless steel or Ni | Ni ceramic or Steel |
| **Electrodes** | Transition metals | Carbon | Carbon | Perovskite & Perovskite/ metal cerment | Ni & NiO |
| **Catalyst** | Pt | Pt | Pt | Ni (Electrode material) | Ni (Electrode material) |
| **Product Heat Management** | Process gas +electrolyte circulation | Process gas +liquid cooling medium or steam generation | Process gas + liquid cooling medium | Internal reforming + process gas | Internal reforming + process gas |
| **$H_2$** | Fuel | Fuel | Fuel | Fuel | Fuel |
| **CO** | Poison | Poison | Poison | Fuel | Fuel |
| **$CH_4$** | Poison | Dilutent | Dilutent | Fuel (after reforming) | Dilutent |
| **$CO_2$ & $H_2O$** | Poison | Dilutent | Dilutent | Dilutent | Dilutent |
| **S ($H_2S$ & COS)** | Poison | Poison | ? | Poison | Poison |

### 2.1.1 Early development

The principle behind fuel cells dates back to 1838 when the Swiss-German scientist Christian Friedrich Schönbein (professor at Basel University) tried to prove that currents were not a result of two substances coming into *"mere contact"* with each other, instead the current were caused by a *"chemical action"*. This finding was submitted on February 18th, 1838 and published in *"The London and Edinburgh Philosophical Magazine and Journal of Science",* 1838 [6]. In 1839 he published a conclusion based on experiments on platinum wire, and how it could become polarized or depolarized depending on the surroundings. Fluids, separated by a membrane, were tested, with different gases dissolved in each compartment. No current was obtained when gold or silver wires were used. It was concluded that *"the chemical combination of oxygen and hydrogen in acidulated (or common) water is brought about by the presence of platina in the same manner as that metal determines the chemical union of gaseous oxygen and hydrogen"* [7].

Not only Schönbein worked on the principle behind fuel cells, Sir William Robert Grove (Royal Institution of Great Britain) performed experiments with a set-up, where two platinum electrodes were halfway submerged into a beaker of aqueous sulfuric acid and tubes were inverted over each of the electrodes, one containing oxygen gas and one containing hydrogen. The description of the experiments was submitted on December 14th, 1838 and published in the *"Philosophical Magazine and Journal of Science"*, 1839 [8]. As the tubes were lowered, the electrolyte was displaced by the gases, leaving only a thin coating of the acid solution on the electrode. A galvanometer indicated a flow of electrons between the two electrodes. The current decreased after some time, but could be restored by renewing the electrolyte layer. Grove concluded in 1842 [9] that the reaction rate was dependent on the *"surface of action",* i.e., the area of contact between the gas reactant and a layer of liquid electrolyte thin enough to allow the gas to diffuse to the solid electrolyte. Platinum particles deposited on a solid platinum electrode were used to increase the surface area. Grove's goal of electrolyzing water into hydrogen and oxygen was achieved with 26 cells connected in electrical series. Grove was counted according to Chen [10] as the fuel cell inventor. The first fuel cell was called a "gaseous voltaic battery".

The SOFC was developed in 1937 by Baur and Preis [11] for a need of more manageable electrolytes. Davtyan evolved (in 1946) the Molten Carbonate Fuel Cell (MCFC) with the goal of using coal as fuel and a solid ionic conductor was used as electrolyte and the working temperature was 700 °C. Davtyan is not only the inventor of the MCFC, he also developed a fuel cell with alkaline electrolyte and a low working temperature in atmospheric pressure, i.e., the Alkaline Fuel Cell (AFC). It should be mentioned that AFCs were used in the Apollo space program to supply electricity for life support, guidance and communications for the modules and also water support for the two weeks missions on the moon. Kodesch and Marko evolved the Direct Methanol Fuel Cell (DMFC) in 1951 using carbon electrodes. Fuels such as aldehyde (formaldehyde) and alcohols (methanol and ethanol) could be used. The Polymer Electrolyte Membrane Fuel Cell (PEMFC) was developed, by General Electric in 1960, to avoid the problem with sealing and circulating a liquid alkaline electrolyte (in AFCs). The Phosphoric Acid Fuel Cell (PAFC) was evolved to use reformed natural gas as fuel in the TARGET program (Team to Advance Research for Gas Energy Transformation), a research program sponsored by mostly American gas companies. This program was initiated in 1967 and a demonstration on a working fuel cell operating on natural gas took place in 1975 [10]. It can be concluded that the development of new fuel cell types have been motivated by avoiding problems with existing types.

### 2.1.2 Future fuel cell expectations and potential

The International Energy Agency (IEA), based in Paris, has concluded in many reports that fuel cells will be a key component in a future sustainable energy system. Fuel cell systems including niche applications or a market where fuel cells bring an added value are already competitive, compared to other energy systems. A high energy content per weight was the key point in the American space program and the low noise is the key factor for the fuel cell development related to military applications. About 80 percent of the energy resources traded today is of fossil origin (coal, oil and natural gas). These resources are limited and the fossil energy resource will sooner or later be depleted, starting with oil. Many of the energy conversion technologies used today are energy inefficient, compared to fuel cells [4]. The IEA made predictions and prognoses for the future fuel cell potential, for example, in [12].

A new technology, such as the fuel cell, is usually introduced into the market in niches where the new and non-traditional characteristic of the technology provides sufficient added value to compensate for the high (capital) cost [4]. During recent years, there have been increasing interests to use fuel cells as auxiliary power unites (APUs) in on-board applications, for example in luxury passenger vehicles, police vehicles, contractor trucks, specialized utility trucks, recreational vehicles, refrigeration vehicles, and heavy trucks, military vehicles, tourist- and leisure boats, manly due to a higher energy efficiency comparing to existing technologies [13]. In a short term, on-board hydrogen production makes it possible to use current fuel refilling system. Gasoline, kerosene or diesel can still be used as fuel and only one fuel storage system is then needed on-board the vehicle. The vehicle industry is known to be conservative regarding fuels and usage of diesel or gasoline as fuel will promote the fuel cell commercialization. In these cases the hydrocarbon fuel will then be reformed in an on-board pre-reformer to hydrogen. FC APUs can be considered as a good transition state to reach the aim of hydrogen economy in vehicle applications. Systems containing SOFC as well as PEM APUs are possible, the later one can be designed from a few hundred Watts for yachts, up to more than 10 kW for the heavy trucks [13,14].

*Table 2. Willingness To Pay (WTP) for different FC niche markets [4].*

| Niche Market | WTP (€/kW) | Main added value |
|---|---|---|
| **Space applications** | ~30 000 | High gravimetric density |
| **Military applications** | 3000-7000 | Low noise |
| **APUs** | 1000-2000 | Low stand-by losses |
| **Portable applications** | 500-2000 | Grid independence and high volumetric energy density |
| **Combined heat and power** | 500-1200 | High efficiency and low emissions |
| **Buses** | 200-300 | Zero local emissions and resource flexibility |
| **Cars** | 50-150 | Zero local emissions and resource flexibility |

Fuel cells have in general a higher fuel conversion efficiency, compared to existing technologies and the willingness to pay (WTP) will be increased from increasing energy prices and less availability of (fossil) fuels. Note that the WTP differs for different energy markets around the world, depending on fuel prices, infrastructure (for example available access for natural gas), governmental subsidies and competing technologies. The estimated target cost (in 2008), for

different fuel cell niche markets, can be seen in Table 2. The target costs can be compared to a current (2011) price of € 29,000-32,000 (¥ 3.2-3.5 million) for a 700 W electricity ENE-FARM system to be used for private homes (in Japan), including a hot water unit and a burner. It is expected that FC system for private home in US or in Europe needs a higher power. The Japanese government gives currently subsidiaries of 40 %. There is an aim of a price in 2015 of € 4500-6400 (¥ 0.5-0.7 million) for a similar system [15]. The above mentioned Japanese prices can be compared to the WTP in Table 2, which is significantly lower. It should be noted that the target of fuel cells replacing the main engine in a standard car will only be reached in a far future, since the average car is used not more than an hour a day and the cost for the increased fuel conversion efficiency will not be economically reasonable, compared to for example the diesel engines.

## 2.2 Solid Oxide Fuel Cells

SOFCs can work with a variety of fuels, e.g., hydrogen, carbon monoxide, methane and combinations of these [16]. Also fuels with longer carbon chains are possible, however they need to be pre-reformed outside the anode, as further discussed in chapter 2.2.1. Oxygen is reduced in the cathode, eqn (2) and the oxygen ions are transported through the electrolyte, but the electrons are prevented to pass through the electrolyte. The anodic electrochemical reactions are defined in eqns (3)-(4). Note that the participation of methane in electrochemical reactions at the anodic TPB is negligible, instead it is catalytically converted in the methane steam reforming reaction (MSR), eqn (5), externally or within the anode, into carbon monoxide and hydrogen, which are used as fuel in electrochemical reactions [17,18]. Carbon monoxide can be oxidized in the electrochemical reaction, eqn (4), but can also react in the water-gas shift reaction (WGSR), eqn (6). The reactions described here are the overall ones, more detailed reaction mechanisms are discussed in chapters 2.4-2.5. Hybrid concept involving a combination of a gas turbine and a fuel cell can be developed with high conversion efficiency [3]. Also the hybrid systems with batteries are promising, because the fuel cell can be operated with an optimized load, i.e., the fuel conversion efficiency can be increased and the start-up time can also be reduced [19].

$$O_2 + 4e^- \Leftrightarrow 2O^{2-} \tag{2}$$

$$2H_2 + 2O^{2-} \Leftrightarrow 2H_2O + 4e^- \tag{3}$$

$$2CO + 2O^{2-} \Leftrightarrow 2CO_2 + 4e^- \tag{4}$$

$$CH_4 + H_2O \Leftrightarrow 3H_2 + CO \qquad \text{(MSR)} \tag{5}$$

$$CO + H_2O \Leftrightarrow H_2 + CO_2 \qquad \text{(WGSR)} \tag{6}$$

SOFCs have in general either planar or tubular configurations. Planar SOFC configurations consist of alternating flat plates of a trilayer anode-electrolyte-cathode and interconnects, as seen in Figure 1, where also the global scale internal reforming (eqns (5)-(6)) and electrochemical (eqns (2)-(4)) reactions are presented. The planar design needs sealing material to seal the edges of the cell and avoid fuel leakage and air mixing. The glass ceramics and glass are suitable, because they are compatible with the other components at the SOFC working temperature [20]. A tubular SOFC is composed of two electrodes that are sandwiching an electrolyte layer. For

conventional tubular fuel cells the air flows inside the tube and the fuel on the outside. Tubular fuel cells can be stacked either electrically in series or in parallel [21]. Tubular and Planar SOFCs can be either electrolyte-, anode- or cathode supported. An electrolyte-supported SOFC has thin electrodes (~50 μm), and a thick electrolyte (more than 100 μm). An electrolyte-supported SOFC works preferably at a temperature around 1000 °C [22], and according to Wang *et al.* [23] is defined as the 1st generation SOFC.

In an electrode-supported SOFC either the anode (anode-supported) or the cathode (cathode-supported) is thick enough to serve as the supporting substrate for the cell, normally between 0.3 and 1.5 mm. Reducing the operating temperature to an intermediate range, 600-800 °C (IT), will cause an increase of both ohmic- and activation polarizations in the electrodes. This requires development of highly active electrolyte materials that has low polarizations [24]. Electrode-supported design makes it possible to have a very thin electrolyte (as thin as 10 μm, [25]), i.e., the resistive loss (due to ion transport) from the electrolyte is significantly reduced [23]. SOFCs working at those temperatures are classified as the 2nd generation SOFCs [23]. The electrolyte contains normally yttria-stabilized zirconia (YSZ), the cathode strontium doped lanthanum manganite (LSM)/YSZ and the anode nickel (Ni)/YSZ [1,23].

The SOFC research in the last years has been focused on lowering the operating temperature, with the aim of an operating temperature in the range of 300-600 °C [7]. Positive aspects of the development in this direction are that the start-up and shut-down time decreases, design and materials requirement are simplified, corrosion rates significantly reduced and the stack lifetime prolonged. Metallic material, for example, stainless steel (=low cost), can be used for interconnects and construction materials. This reduces the construction cost and increase the stability of the fuel cells [26,27]. Wang *et al.* [23] expect the YSZ to be doped with Sc (scandium) in the electrolyte to increase the ionic conductivity, Gd doped $CeO_2$ (CGO) to replace YSZ/LBM at the cathodic TPB and [La,Sr][Co,Fe]$O_3$ (LSCF)/CGO to replace LSM at the cathode support layer in the 3rd generation SOFCs.

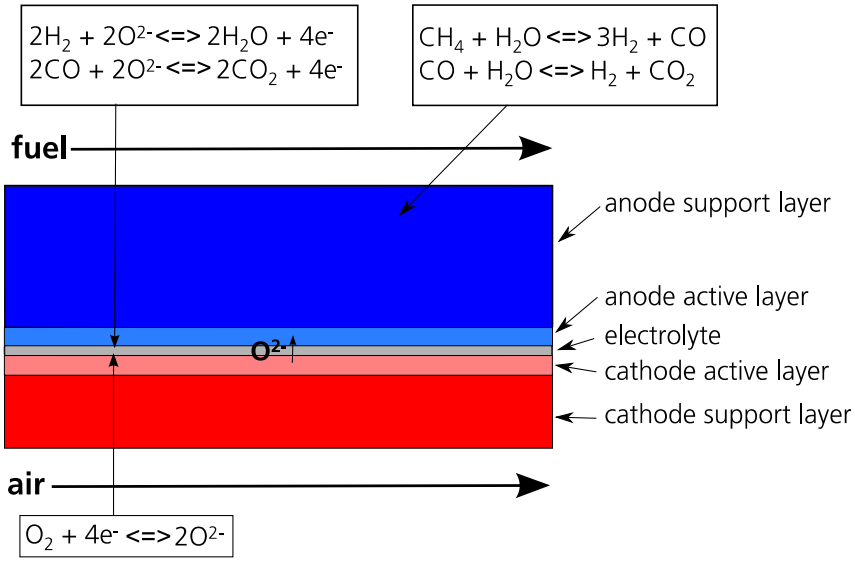


*Figure 1. Planar SOFC structure.*

### 2.2.1 Alternative fuels

Using alternative fuels (other than hydrogen) gives SOFCs a major advantage because pure hydrogen is highly flammable and volatile which makes it problematic to handle. Hydrogen has also a low density, which makes storing costly. It should be mentioned that pure hydrogen is expensive to obtain because it has to be extracted from other sources, most commonly natural gas. Like hydrogen, methanol and ethanol are useful energy carriers rather than primary fuels (such as natural gas, coal or oil) through gasification or chemical synthesis reforming processes. The characteristics of these alcohol-based fuels are very similar to conventional liquid fuels (propane, butane and diesel) and can be readily handled, stored and transported [28]. The emissions of carbon dioxide do not have to be an issue, when they are produced in a renewable manner, because the net effect on the emissions will be zero [29].

Methanol is interesting due to its availability, high specific energy as well as easy storage and transportation. Ethanol is also a promising candidate because it is readily produced from renewable resources. Moreover, ethanol has extra advantages, in terms of power density, non toxicity, transportation and storage. However, because of incomplete oxidization, the ethanol processing reactions consist of more complicated multi-step reaction mechanism and involve a number of adsorbed intermediates and byproducts. Biomass can be converted into biogas (mainly methane and carbon dioxide), usually by anaerobic breakdown in the absence of oxygen [30].

The net reaction of methanol, ethanol and dimethyl ether (DME) to hydrogen and carbon monoxide are described in eqns (7)-(9), respectively. The produced carbon monoxide reacts further with steam to hydrogen and carbon dioxide by the WGSR, eqn (6) [28]. The enthalpy change ($\Delta H$) of the steam reforming reactions for hydrocarbons with a short carbon chain can be seen in Table 3. Note that it is assumed that the fuels are reformed all the way to hydrogen and carbon dioxide. Ethanol consumes the most heat per mole of fuel. However, when considering that reforming of the different fuels generates a different amount of hydrogen to be used in electrochemical reactions ($n_{H2}$), the most required heat per mole of generated hydrogen is by reforming methane. Globally all heat needed for the reforming reactions is generated within the cell, thanks to the electrochemical reactions. Also ammonia is possible as fuel according to Ni *et al.* [31] and the reforming reaction is shown in eqn (10). In comparison to the steam reforming in eqns (5)-(6) and (8)-(9), dry reforming reactions are also possible, and presented for ethanol in eqn (11) [32] and for methane in eqn (12) [33].

$$CH_3OH \Leftrightarrow 2H_2 + CO \tag{7}$$

$$C_2H_5OH + H_2O \Leftrightarrow 4H_2 + 2CO \tag{8}$$

$$CH_3OCH_3 + H_2O \Leftrightarrow 4H_2 + 2CO \tag{9}$$

$$2NH_3 \Leftrightarrow N_2 + 3H_2 \tag{10}$$

$$C_2H_5OH + CO_2 \Leftrightarrow 3H_2 + 3CO \tag{11}$$

$$CH_4 + CO_2 \Leftrightarrow 2H_2 + 2CO \tag{12}$$

*Table 3. Enthalpy change of the steam reforming reactions for different fuels suitable for SOFCs [28].*

| **Fuel** | $\sum \Delta H$ ***(kJ/mol)*** | $\sum \Delta H / n_{H_2}$ ***(kJ/mol/per mole of $H_2$ generated)*** |
|---|---|---|
| **Carbon monoxide (CO)** | +41.4 | +41.4 |
| **Methane ($CH_4$)** | −165 | −41.2 |
| **Methanol ($CH_3OH$)** | −49.4 | −16.5 |
| **DME ($CH_3OCH_3$)** | −121 | −20.2 |
| **Ethanol ($C_2H_5OH$)** | −173 | −28.8 |

Also hydrocarbons with longer carbon chains (from renewable or fossil origin) can be used as raw energy within a fuel cell system for hydrogen production. External reforming is necessary, to avoid carbon deposition within the anode, as further discussed in chapter 2.4. Equation (13) states the ideal reforming reaction, where the only products are pure hydrogen and carbon dioxide. In reality within a (fuel cell) reformer, there are several ordinary reforming reactions: steam reforming (SR) and partial oxidation (POX), mainly depending on the amount of oxygen and steam available as well as the temperature. The SR, eqn (14), is effective for hydrogen production and largely exothermic. In POX, eqn (15), the fuel is partially burned with a substoichiometric amount of air. An ATR (autothermal reforming) system contains one reactor with SR and one with POX. It should be noted that, if sufficient amount of heat is available, SR gives most hydrogen per amount of raw fuel. However, the conversion of complex hydrocarbons may be more difficult in terms of thermal management, because it is largely endothermic, compared to POX [30].

$$C_nH_mO_z + yO_2 + 2\cdot(n-y-0.5\cdot z)\cdot H_2O \Leftrightarrow nCO_2 + 2\cdot(n-y-0.5\cdot z+0.25\cdot m)\cdot H_2 \quad \text{(ATR)} \quad (13)$$

$$C_nH_mO_z + 2\cdot(n-z)\cdot H_2O \Leftrightarrow nCO + 2\cdot(n-z+0.5\cdot m)\cdot H_2 \quad \text{(SR)} \quad (14)$$

$$C_nH_mO_z + 0.5\cdot(n-z)\cdot O_2 \Leftrightarrow nCO + 0.5\cdot m\cdot H_2 \quad \text{(POX)} \quad (15)$$

## 2.3 Transport phenomena in SOFCs

Species transport in the porous electrodes occurs in the gas-phase, integrated with the chemical reforming reactions at the solid active surfaces. The electrodes are porous and species transfer is dominated by gas diffusion [34]. The electrolyte has two functions: to transport oxygen ions from the cathode to the anode and to block electron and gas flow between the anode and cathode [17]. The flow of electrons (electronic charge) through external circuit balances the flow of ions (ionic charge) through the electrolyte and electrical power is produced [35]. The interconnect can be assumed to be impermeable for gases. Electron transport needs to be considered because the current from the SOFC is collected [22]. The amount of fuel transported to the active surfaces for electrochemical reactions are governed by different parameters, such as porous microstructure, gas consumption, pressure gradient between the fuel flow duct and the porous anode and the inlet conditions [36]. The supply of the reactants can be the rate limiting step, because the gas molecule diffusion coefficient is much smaller than for

ions. The charge-transfer chemistry at the anodic TPB proceeds on the basis of the fuel concentration, such as hydrogen or carbon monoxide. The concentration of the fuel gases, $CH_4$, CO and $H_2$, decreases along the length of the fuel channel while the concentration increases for $H_2O$ and $CO_2$, due to electrochemical and internal reforming reactions. As a result the current density decrease, as the fuel concentration becomes low. However, this is compensated by an increased temperature, along the main flow direction [16].

### 2.3.1 Gas-phase species transport

In the porous material, there are two kinds of gas-phase species diffusion mechanisms: molecular and Knudsen diffusions. The molecular diffusion (collisions between gas molecules) is significant in the case of large pores, whose size is much bigger than the mean free path of the diffusion gas molecules. The Knudsen diffusion is important when the mean free path is of the same order or bigger than the pore size, and the molecules collide with the solid walls more often than with other molecules. At the SOFC operating temperature, the mean free path of these gas components is about 0.2-0.5 μm [37,38]. The molecular diffusion coefficients ($D_{ij}$), for a multi-component gas mixture system, can be calculated as [39]:

$$D_{ij} = \frac{2.66 \cdot 10^{-8} \cdot T^{3/2}}{p \cdot M_{ij}^{1/2} \cdot l_{ij}^2 \cdot \Omega_D} \tag{16}$$

$$M_{ij} = \frac{2}{\frac{1}{M_i} + \frac{1}{M_j}} \tag{17}$$

where $l_{ij}$ is the characteristic length, $p$ the pressure, $T$ the temperature, $M_{ij}$ the molecular mass for species $i$ and $j$, and $\Omega_D$ the diffusion collision integral.

In the porous media, there is a reduced void volume and an increased diffusion length based on the local microstructures, and the coefficients are usually corrected by porosity ($\varepsilon$) and tortuosity ($\tau$) [37,40,41]. Different approaches can be found in the literature [41]:

$$D_{ij,eff} = \varepsilon^{\tau} \cdot D_{ij} \tag{18}$$

$$D_{ij,eff} = \frac{\varepsilon}{\tau} \cdot D_{ij} \tag{19}$$

where $D_{ij,eff}$ represents the effective diffusion coefficient in the porous medium. Tortuosity is an important parameter for characterization of fluid flow through the porous media in many macroscale models. It is normally considered as a geometric parameter, but it was originally introduced as a kinematic property, equal to the relative average length of the flow path of a fluid particle from one side of a porous structure to the other side. If a suitable model is developed for the porous medium microscopic structures, then the tortuosity becomes a geometric property. Frequently in the literature, tortuosity is treated as a fitting property (used for the validation purposes), i.e., the tortuosity should then not be seen as a kinematic- or geometric property. One way to overcome these limitations is to apply the lattice Boltzmann

method (LBM) to simulate gas flow in the porous media. It should be noted that LBMs do not require pressure-velocity decoupling or solution of a large system of algebraic equations [42].

The Knudsen diffusion coefficient of the gas component i with the component j in a gas mixture, $D_{K,ij}$, can be calculated based on the free molecule flow theory [40,43]:

$$D_{K,ij} = \frac{2}{3} \cdot r_e \cdot \sqrt{\frac{8 \cdot \mathrm{R} \cdot T}{\pi \cdot M_{ij}}} \tag{20}$$

where R is the gas constant and $r_e$ the effective radius of the pores. The effective diffusion coefficient, covering both the ordinary and the Knudsen diffusion, is further extended as [40]:

$$D_{eff,ij} = \frac{\varepsilon}{\tau} \cdot \left( \frac{D_{ij} \cdot D_{K,ij}}{D_{ij} + D_{K,ij}} \right) \tag{21}$$

### *2.3.2 Momentum transport*

The governing equations for momentum transport is normally the Navier-Stokes equations in the fuel channels and the Darcy equation for the porous electrodes [36,40]. The physics of laminar and turbulent incompressible flow are well described by the Navier-Stokes equation, and it is common practice to assume laminar flow for fuel cell gas channels due to the low velocities, which decreases the computational cost significantly [41]. The Darcy equation describes the balance between the force from the pressure gradient and the frictional resistance from the (porous) solid material. It should be noted that the Darcy equation expresses the flow in the porous structure well away from the walls. It is found that the conditions at the fuel and air channel-electrode interfaces are not well described by either the Darcy or the Navier-Stokes equations. The Darcy-Brinkman equation is developed to enable continuous velocity and pressure fields, i.e., the fluid and the porous region is treated as a single domain [44,45].

The density ($\rho_g$) for the participating gases is calculated, according to the ideal gas law [45]:

$$\rho_g = \frac{p \cdot \sum x_j \cdot M_j}{\mathrm{R} \cdot T} \tag{22}$$

where $x_j$ is the mole fraction of gas-phase species *j*. The dynamic viscosities ($\mu_j$) for each participating species in the gas-phase, as well as for the mixture, are evaluated as [46]:

$$\mu_j = \sum_{k=1}^{7} \mathrm{b_k} \cdot \left( \frac{T}{1000} \right)^k \tag{23}$$

$$\mu_g = \sum_i x_j \cdot \mu_j \tag{24}$$

where $b_k$ is the species dependent parameter and "*k*" stands for the number of species dependent parameters in the equation and index *g* is the gas-phase. The mole fraction averaging approach (eqn. (24)) might not be the most accurate equation for the dynamic viscosity of gas-phase mixtures present in SOFCs. The difference between different expressions covering the dynamic viscosity of gas-phase mixtures is discussed in Todd and Young [46].

### 2.3.3 Heat transport

The heat transfer inside SOFCs includes various aspects such as convective heat transfer between the solid surfaces and the gas streams, conductive heat transfer in the solid and the porous structures [47]. Radiative heat transfer occurs, for example, within the electrode-electrolyte structure, as surface-to-surface radiation in the air and fuel channels as well as from the stack to the surrounding environment. It should be noted that modeling concerning radiative transfer includes several challenges such as the complexity of the governing equations, which depends on many independent variables, and the non-linearity of the governing equations. The accuracy is limited to the extent of which radiative properties are known and experimental studies in this area are still rare [48]. Further analysis of heat radiation is outside of the scope of this work, but it is interesting for future studies.

The heat generation/consumption occurs due to electrochemical reactions and the related polarizations [47], and because of internal reforming reactions of hydrocarbons in the porous anode [49]. Accurate temperature prediction within SOFCs is essential for predicting and optimizing the overall cell performance as well as avoiding thermo-mechanical degradation [50].

A very common assumption in SOFC modeling is to assume local thermal equilibrium (LTE) [40,50,51]. However, some typical conditions found in the porous SOFC electrodes bring this assumption into question: (**1**) very low Reynolds number flow, (**2**) presence of volumetric heat generation and (**3**) large difference in thermal conductivity between the gas- and solid-phases. A local temperature non-equilibrium (LTNE) approach was developed by Damm and Fedorov [50] to predict and model the temperature difference between the solid- and gas-phases within the porous electrodes. A parameter study, covering the surface area and the heat transfer coefficient (between the gases and the solid walls, is conducted for the conditions applied in paper II and the results (temperature difference between the solid- and gas-phases) are shown in Table 4. It is concluded that the temperature difference between the gas- and the solid-phase is very small. Both the LTE and the LTNE approaches are implemented in chapter 3.3.

*Table 4. LTNE parameter study for the temperature difference between the solid and the gas-phase.*

| | Anode | | Cathode | |
|---|---|---|---|---|
| | **average** | **maximum** | **Average** | **maximum** |
| **Basic case [K]** | $9.8 \cdot 10^{-6}$ | 0.014 | $5.5 \cdot 10^{-4}$ | 0.067 |
| $\boldsymbol{AV_{tot}} \cdot$ **10 [K]** | $1.1 \cdot 10^{-6}$ | $1.4 \cdot 10^{-3}$ | $6.0 \cdot 10^{-5}$ | $7.6 \cdot 10^{-3}$ |
| $\boldsymbol{AV_{tot}}$ **/ 10 [K]** | $5.8 \cdot 10^{-5}$ | 0.13 | $5.2 \cdot 10^{-3}$ | 0.34 |
| $\boldsymbol{h_{sg,ch}} \cdot$ **2 [K]** | $9.8 \cdot 10^{-6}$ | 0.014 | $5.4 \cdot 10^{-5}$ | 0.065 |
| $\boldsymbol{h_{sg,ch}}$ **/ 2 [K]** | $9.8 \cdot 10^{-6}$ | 0.015 | $5.5 \cdot 10^{-4}$ | 0.069 |

*where $AV_{tot}$ is the total surface area to volume ratio and $h_{sg,ch}$ the heat transfer coefficient at the channel walls.*

The specific heat ($c_p$) for each gas-phase species and the fluid mixture is calculated as [46]:

$$c_{p,j} = \frac{\sum_{k=1}^{7} \mathrm{a_k} \cdot \left(\frac{T}{1000}\right)^k}{M_j} \tag{25}$$

$$c_{p,g} = \sum_i w_j \cdot c_{p,j} \tag{26}$$

where $w$ is the mass fraction and $\mathrm{a_k}$ the species dependent parameter (extracted from [46]).

The thermal conductivity ($k$) for each species of the gas-phase, as well as for the mixture, is defined as [46]:

$$k_j = 0.01 \cdot \sum_{k=1}^{7} \mathrm{c_k} \cdot \left(\frac{T}{1000}\right)^k \tag{27}$$

$$k_g = \sum_i x_j \cdot k_j \tag{28}$$

where $\mathrm{c_k}$ is the species dependent parameter (extracted from [46]). The mole fraction averaging method (eqn (28)) is not the most accurate expression for the thermal conductivity of gas-phase mixtures present in SOFCs [46]. Implementation of correlations with a better agreement to experimental data can be interesting for future studies. The effective values of the thermal conductivity ($k_{eff}$) in the porous electrodes can, when a LTE approach is applied, be specified as [40]:

$$k_{eff} = \varepsilon \cdot k_g + (1-\varepsilon) \cdot k_s \tag{29}$$

where index $s$ is the solid-phase.

### *2.3.4 Ion and electron transport*

The ion and electron transport is driven by a potential difference. The electrochemical reactions occurring within SOFCs are explained in chapter 2.5. The electromotive force ($E^{OCV}$) is determined by the difference in thermodynamic potentials of the electrode reactions [3,52]. When a hydrogen-steam mixture is presented as fuel at the anodic TPB and air at the cathodic TPB, the electromotive force can be calculated by the standard Nernst equation [3,52]:

$$E_{H_2/O_2}^{OCV} = E_{H_2/O_2}^{0} - \frac{\mathrm{R} \cdot T}{2 \cdot \mathrm{F}} \cdot \ln\left(\frac{p_{H_2O}}{p_{H_2}\sqrt{p_{O_2}}}\right) \tag{30}$$

$$E_{H_2/O_2}^{0} = 1.253 - 2.4516 \cdot 10^{-4} \cdot T \tag{31}$$

where $E^0$ is the theoretical (reversible) voltage before partial pressure consideration and $p_i$ the partial pressure at the TPB, in atm. It should be noted that eqns (30)-(31) are developed for a pure hydrogen-steam mixture. The electromotive force for carbon monoxide or methane as fuel is presented in eqns (32)-(33), respectively. $E^0$ for carbon monoxide decreases with increased temperature, but it is not temperature dependent for methane, due to a constant mole number for both the products and the reactants. $E^0$ for methane and carbon monoxide can be found in [53].

$$E_{CO/O_2}^{OCV} = E_{CO/O_2}^{0} - \frac{\mathrm{R}\cdot T}{2\cdot \mathrm{F}}\cdot \ln\left(\frac{p_{CO_2}}{p_{CO}\sqrt{p_{O_2}}}\right) \tag{32}$$

$$E_{CH_4/O_2}^{OCV} = E_{CH_4/O_2}^{0} - \frac{\mathrm{R}\cdot T}{8\cdot \mathrm{F}}\cdot \ln\left(\frac{p_{CO_2}\cdot {p_{H_2O}}^2}{p_{CH_4}\cdot {p_{O_2}}^2}\right) \tag{33}$$

Due to the internal resistance and the different polarizations, the actual voltage ($E$) becomes less than the ideal one, and is expressed as [3,52]:

$$E = E^{OCV} - \eta_{act} - \eta_{ohm} - \eta_{conc} \tag{34}$$

where $\eta$ is the polarization or over-potential. The activation polarizations, in the anode and cathode, are defined as [45]:

$$\eta_{act,a} = \phi_s - \phi_l - E_{eq,a} \tag{35}$$

$$\eta_{act,c} = \phi_s - \phi_l - E_{eq,c} \tag{36}$$

where $\phi$ is the potential, $E_{eq,e}$ is the equilibrium voltage for the electrodes, the index $a$ stands for the anode, $c$ for the cathode, $l$ for the electrolyte (YSZ) material, $s$ for the electrode materials (Ni or LSM). If the current is known, the activation polarizations are instead calculated as [54]:

$$\eta_{act,e} = \frac{2\cdot \mathrm{R}\cdot T}{n_e\cdot \mathrm{F}}\sinh^{-1}\left(\frac{i_{a,e}}{2\cdot i_{0,e}}\right) \tag{37}$$

where $i_{0,e}$ the exchange current density and $i_{a,e}$ is the current density (per area). The exchange current densities are calculated as described in chapter 3.5 (eqn (86)).

The concentration polarizations ($\eta_{conc}$) are, when only hydrogen is considered as the electrochemical active fuel, calculated by [52]:

$$\eta_{conc,a} = \frac{\mathrm{R}\cdot T}{n_{e,a}\cdot \mathrm{F}}\cdot \ln\left(\frac{p_{H_2O,TPB}\cdot p_{H_2,b}}{p_{H_2,TPB}\cdot p_{H_2O,b}}\right) \tag{38}$$

$$\eta_{conc,c} = \frac{\mathrm{R} \cdot T}{n_{e,c} \cdot \mathrm{F}} \cdot \ln\left(\frac{p_{O_2,b}}{p_{O_2,TPB}}\right) \tag{39}$$

where the index *b* stands for the interface between the gas channel and the electrode.

The ohmic polarizations ($\eta_{ohmc}$) can be calculated as [52]:

$$\eta_{ohm} = R_{ohm} \cdot i_{a,e} \tag{40}$$

$$R_{ohm} = \frac{t_{l,a}}{\sigma_{l,a}} + \frac{t_{s,a}}{\sigma_{s,a}} + \frac{t_{l,el}}{\sigma_{l,el}} + \frac{t_{l,c}}{\sigma_{l,c}} + \frac{t_{s,c}}{\sigma_{s,c}} \tag{41}$$

where $R_{ohm}$ is the electrolyte specific-area ohmic resistance, *t* the transport distance for ions and electrons in the specific component, respectively, and index *el* stands for the electrolyte. Note that defining *t* to the component thickness in the electrodes underestimates the ionic/electronic resistance. The electronic conductivities in the anode ($\sigma_{s,a}$) and the cathode ($\sigma_{s,c}$), and ionic conductivity in the YSZ ($\sigma_{l,el}$) can be calculated as [55,56]:

$$\sigma_{s,c} = \frac{4.2 \cdot 10^7}{T} \cdot \exp\left(\frac{-1200}{T}\right) \tag{42}$$

$$\sigma_{l,el} = 3.34 \cdot 10^4 \cdot \exp\left(\frac{-10300}{T}\right) \tag{43}$$

$$\sigma_{s,a} = \frac{9.5 \cdot 10^7}{T} \cdot \exp\left(\frac{-1150}{T}\right) \tag{44}$$

The actual length that ions and electrons are transported in the electrodes increases because of the real/functional material compositions and their micro structures. This is accounted for by using the structure-dependent tortuosities and volume fractions (eqns (45)-(47)), but can also be implemented directly as *t* in eqn (41). A discussion about the use of the tortuosity in modeling is found in chapter 2.3.1. The effective ionic- and electronic conductivity in the electrodes are defined as [57]:

$$\sigma_{l,e,YSZ} = \sigma_{l,e} \cdot \frac{V_{YSZ,e}}{\tau_{YSZ,e}} \tag{45}$$

$$\sigma_{s,a,Ni} = \sigma_{s,a} \cdot \frac{V_{Ni,a}}{\tau_{Ni,a}} \tag{46}$$

$$\sigma_{s,c,LSM} = \sigma_{s,c} \cdot \frac{V_{LSM,c}}{\tau_{LSM,c}} \tag{47}$$

where $V$ is the volume fraction for the specific materials. Kanno *et al.* calculated (by LBM) the tortuosity and the values between 7 and 17 are found for Ni and between 6 and 14 for YSZ, respectively [57]. Iwai *et al.* evaluated the tortuosity statistically with the random walk process of nonsorbing particles as well as with the LBM, and the values between 6.91 and 29.46 were found for Ni and between 9.84 and 27.89 for YSZ, respectively, depending slightly on the evaluation methods, but mostly on the direction (x, y and z) [18]. Vivet *et al.* [58] calculated the tortuosity in the range of 3.04 and 6.24 for Ni, and between 1.79 and 2.10 for YSZ, respectively.

## 2.4 Internal reforming reactions

Reforming reactions enable the conversion of hydrocarbons, such as methane, methanol or ethanol, into hydrogen and carbon monoxide, which can be used as fuel in the electrochemical reactions. The reforming reactions (eqns (5)-(15)) in SOFC systems can be conducted both externally and internally. The external reforming (ER), such as the pre-reforming in a SOFC system, means that the reformer is placed outside the cell, which is possible for all types of fuel cells. The internal reforming (IR) means that the reforming reactions occur within the cell. A sketch of the Ni/YSZ structure (within an anode) is shown in Figure 2, where the intermediate reactions occur at the Ni surfaces. The intermediate species in Figure 2 are those presented by Janardhanan and Deutschmann [19], among others. The IR can be direct or indirect. In the direct internal reforming (DIR) approach, the reforming processes occur together with electrochemical reactions within the anode. In the indirect internal reforming (IIR) approach the reforming reactions appear in a reformer (within the cell) in close contact with the anode where the exothermic electrochemical reactions take place. The IR reactions decrease the requirement for cell cooling (less surplus of air). Less steam is needed and finally it offers advantages with respect to the system capital cost. Up to half of the heat produced by the oxidation reaction can be "consumed" by the MSR (eqn (5)). This improves the system electrical efficiency [49,59].

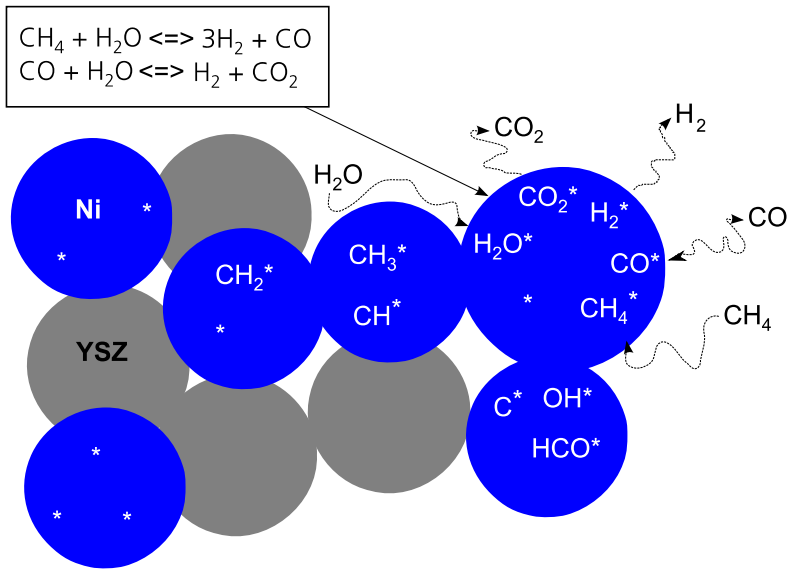


*Figure 2. The internal reforming reactions at the Ni surfaces within the anode.*

The direct use of hydrocarbon fuels can lead to that the catalyst is rapidly deactivated by sulfur poisoning and also carbon formation on the traditional SOFC anodes may occur [25,32]. Some fuels, for example syngas from coal gasification, contain sulfur. The irreversible anode damage is caused by the adsorption of sulfur on the TPB, due to melted nickel sulfides [25]. Various methods for sulfur removal can be applied, such as high temperature desulfurisation, where organic sulfur compounds are reduced to hydrogen sulfite and the corresponding hydrocarbon, passing a cobalt or molybdenum catalyst supported on alumina, compared to adsorption methods that can be applied for smaller SOFC systems [60]. Li *et al.* [25] found that the extent of $H_2S$ poisoning increases with a decrease of temperature and/or current density or an increased voltage. It was also concluded that the sulfide or sulfur at the anode TPB can not be completely removed at lower operating temperatures and current densities. It was proven that a relatively high current density can help to achieve cell performance recovery.

The probability for carbon deposition depends on the steam and fuel compositions as well as the operating temperature. The fuel gas composition in the fuel mixture are normally described as steam-to-fuel (SF) or as steam-to-carbon ratio (SC). In SC the $CO_2$ is included in denominator but it is not included in SF [61]. Carbon monoxide disproportionates, eqn (48), due to the catalysis of nickel, when the fuel cell is using for example some coal syngases, which leads to carbon deposition on the nickel surfaces if not sufficient amount of steam is available. It can be noted that the disproportionation reaction is exothermic. Carbon deposition can also occur due to the CO reduction, eqn (49). The SOFC anode is deactivated by increasing the polarization resistance, blocking active sites and reducing the porosity [62].

$$2CO \Leftrightarrow CO_2 + C \tag{48}$$

$$CO + H_2 \Leftrightarrow C + H_2O \tag{49}$$

Methane and methanol can with an appropriate steam content be directly fed to Ni/YSZ anode without the problem of carbon formation. Cimenti and Hill [32] performed thermodynamical analyzes to investigate the amount of steam, which needs to be available to avoid carbon deposition. For the steam reforming of methanol an SF of 0.228 at 973 K and 0.060 at 1073 K is enough, compared to 1.583 at 973 K and 1.125 at 1073 K for steam reforming of ethanol. Note that for ethanol and methane the SF decreases within the anode close to the inlet because of the reforming reactions (each mole of methane requires two moles of steam and each mole of ethanol needs three moles of steam for complete reforming reaction), i.e., the SF for the inlet fuel needs to be higher than the thermodynamically minimum requirement. The steam reforming can be compared to the dry reforming, where one mole of methanol requires 0.641 mol of carbon dioxide at 973 K and 0.072 mol at 1073 K to avoid carbon deposition. For ethanol (eqn (11)) 3.20 mol of carbon dioxide at 973 K and 1.35 mol at 1073 K are needed to avoid carbon deposition. For the fuels with a longer carbon chain, a pre-reformer (with a catalyst less sensitive to carbon formation than Ni/YSZ) should be included in the fuel cell system [61]. The risk of carbon deposition can be decreased if a pre-reforming is carried out upstream the cell, or changes can be made to the anode structure [63]:

- Complete or partial replacement of doped zirconia with doped ceria or ceria-zirconia possessing a higher lattice oxygen reactivity/mobility. This can be combined with complete or partial replacement of Ni by Cu.
- Replacement of doped zirconia by complex perovskites with their doping by active metals in the steam reforming reaction.

- Complete or partial replacement of Ni by precious metals in cermets with complex perovskites or doped zirconia as oxide phases.

In a conventional SOFC (with nickel mole fraction of 0.50 and operating temperature of 800-1000 °C) the endothermic reaction is very fast. This can result in a temperature drop at the inlet of the stack, where the MSR is fast. The temperature gradient results in thermal tensions, which in the worst case causes mechanical failure of the cells [49]. The problem of the tensions and big temperature gradients close to the inlet could be solved with different approaches:

- Reducing the operating temperature to an intermediate range to reduce the steam-reforming reaction rates [64].
- Recycling part of the anode gas to obtain dilution of the fuel. The rate of reforming reactions decreases, due to the decreased fuel concentration. A 50 percent recycling results in enough steam for reforming reactions and the cost for a separate water supply is saved [49].
- The anode material can be designed with the aim of a decreased steam reforming activity, i.e., a higher activation energy or a decreased available active area [49].

In a case where the reforming reactions occur within the porous anode, the Le Chatelier's principle tells that the equilibrium constant for the MSR increases as the temperature increases, because this reaction is endothermic. An increased equilibrium constant means that the equilibrium proceeds further to the right. The WGSR is exothermic and its equilibrium constant decreases as the temperature increase. An increased pressure causes the MSR equilibrium shifting to the side with fewer moles of gas, i.e., the equilibrium constant is decreased. For the WGSR the pressure has no effect on the equilibrium constant. Note that the MSR does normally not reach the equilibrium conditions within an SOFC, compared to the WGSR that is normally assumed to be in equilibrium. The reaction rates can be described with the simplified global expressions as well as the detailed expressions for surface-phase chemical reactions, as discussed in the following subchapters.

### *2.4.1 Global reforming reaction kinetics*

Several kinetic expressions dealing with the MSR are available in the literature. The reaction order varies significantly between the schemes, in terms of the orders of methane and water (*m* and *n* in eqn (50)). The reaction order of methane (*m*) varies between 0.85 and 1.4. For water both negative and positive values for the reaction order (*n*) exist. However, it has been shown that all these findings could be correct for the chosen operating conditions of the experiments. A small SC gives positive reaction order of water. SC in the order of 2 yields the reaction orders of water close to zero, and high SC gives negative values [65]. Experimental work has shown that it is possible to change the MSR orders by modifying the anode, for example *m* increased from 0.85 to 1.4 and *n* decreased from –0,35 to –0,8 when new catalytic compounds are added to the Ni-YSZ anode, in Aguiar *et al.* [64]. It is worthwhile to note that the reaction orders (*m* and *n*) usually originate from fitting experimental data to a kinetic expression.

$$r_{MSR} = A_{MSR} \cdot x_{CH_4}^{m} \cdot x_{H_2O}^{n} \cdot p_{tot}^{2} \cdot \exp\left(\frac{-E_{a,MSR}}{\mathrm{R} \cdot T}\right) \tag{50}$$

where $r_{MSR}$ is the MSR rate, $E_a$ the activation energy and $A$ the pre-exponential factor. Normally the unit for the MSR rate is in mol/(s·m$^2$), and can then be converted to mol/(s·m$^3$) after multiplying it with the active surface area to volume ratio available for the MSR ($AV_{MSR}$, in m$^2$/m$^3$). The range for the $AV_{MSR}$ (related to catalytic kinetic reactions) varies in the literature between $1 \cdot 10^5$ m$^2$/m$^3$ [66] and $2.2 \cdot 10^6$ m$^2$/m$^3$ [67] for SOFC anodes. The $AV_{MSR}$ can be compared to the $AV_{tot}$, that reaches $1 \cdot 10^8$ m$^2$/m$^3$ for Ni/YSZ material developed for SOFC anodes (with a nickel content of 50 %, surface area of 27 m$^2$/g and a power density of 3.75 g/cm$^3$ [68]). On the other hand the surface area [69] reaches 162-112 m$^2$/g for the materials containing 13-40 mole-% Ni or NiO. Note that not all the surfaces are available for the catalytic reactions, due to the distribution of catalyst, dead pores and mass transfer limitations among others. An $AV_{MSR}$ of $2.2 \cdot 10^6$ m$^2$/m$^3$ is applied in most of this work, which corresponds to 2.2 percent of the total Ni/YSZ surface area to volume ratio, when compared to the $AV_{tot}$ in Aruna *et al.* [68]. Vivet *et al.* [58] used the focused ion beam-scanning electron microscopy (FIB-SEM) to obtain a 3D reconstruction of a Ni/YSZ anode and the total Ni surface is $2.33 \cdot 10^6$ m$^2$/m$^3$, where $1.18 \cdot 10^6$ m$^2$/m$^3$ is exposed to the porous-phase. The kinetic expression for the MSR in eqn (50) is of Arrhenius type, and can be compared to an expression of the Langmuir-Hinshelwood type [70], in eqn (51), and an expression of the equilibrium approach [65] in eqn (52).

$$r_{MSR,Lang} = A_{MSR} \cdot \frac{x_{CH_4} \cdot x_{H_2O} \cdot K_{CH_4} \cdot K_{H_2O} \cdot p_{tot}^2}{\left(1 + x_{CH_4} \cdot K_{CH_4} \cdot p_{tot} + x_{H_2O} \cdot K_{H_2O} \cdot p_{tot}\right)^2} \tag{51}$$

$$r_{MSR,eq} = A_{MSR} \cdot x_{CH_4} \cdot x_{H_2O} \cdot p_{tot}^2 \cdot \left(1 - \frac{x_{CO} \cdot x_{H_2}^3 \cdot p_{tot}^2}{K_{eq,MSR} \cdot x_{CH_4} \cdot x_{H_2O}}\right) \tag{52}$$

where $K_{eq,MSR}$ is the temperature dependent equilibrium constant for the MSR. The reaction orders in eqn (52) are the same as the molar proportions for the respective gas-phase species in the global chemical reaction (i.e., 1 for both methane and water for the forward reaction, and 3 for hydrogen and 1 for carbon monoxide for the backward reaction).

An Arrhenius type reaction rate consists of three parts, the partial pressures (or total pressure and mole fractions), the pre-exponential factor and the activation energy. These parameters differ quite a lot in the literature among different research works. The pre-exponential factor describes the number of collisions between the molecules within the reactions and the exponential expression with the activation energy describes the probability for the reaction to occur. As the activation energy increases, the catalytic reaction becomes less probable. The activation energy is based on the catalytic characteristics, such as the chemical compositions. Even though the activation energy may be high, which leads to a decrease in the reaction rate, the overall reaction rate can still be fast due to the pre-exponential value. The pre-exponential factors depend strongly on both the temperature and properties of the anode material. It is possible to change the reaction rate, either by changing the particle size of the active catalysts or the porous structure, i.e., active catalytic area ($AV_{MSR}$). The large difference between the activation energies found in the literature, [65,67,71-74] suggests that more parameters have significant influence on the reaction rate. It should be mentioned that when kinetic expressions are created often the just mentioned parameters are used as fitting parameters for the validation.

Various approaches for defining the WGSR (eqn (6)) can be found in literature:

- Global catalytic reaction mechanism that considers the reaction in the anode only [40,75].
- Global catalytic (equilibrium) reaction mechanism that considers reaction in the anode and in the fuel channel [67]. Note that Klein *et al.* [67] assumes the same kinetics for the reaction within both the anode and the gas channel.
- A more advanced reaction mechanism that includes the catalytic surface-phase reaction kinetics for the MSR, WGSR and the Boudouard reactions can be found in [19,76], among others.

The WGSR kinetics can be expressed as [75]:

$$r_{WGSR} = k_{WGSR} \cdot \left( x_{H_2O} \cdot x_{CO} \cdot p_{tot}^2 - \frac{x_{H_2} \cdot x_{CO_2} \cdot p_{tot}^2}{K_{eq,WGSR}} \right) \tag{53}$$

$$k_{WGSR} = 0.0171 \cdot \exp\left( \frac{-103 \cdot 10^3}{\mathrm{R} \cdot T} \right) \tag{54}$$

$$K_{eq,WGSR} = \exp\left( -0.2935 \cdot Z^3 + 0.6351 \cdot Z^2 + 4.1788 \cdot Z + 0.3169 \right) \tag{55}$$

$$Z = \frac{1000}{T} - 1 \tag{56}$$

where $k$ is the rate constant and $K_{eq}$ the equilibrium constant.

### *2.4.2 Elementary multi-step reaction kinetics*

An SOFC anode is normally fabricated as a porous metal-ceramic composite, where the open voids, ceramic and metal phases occupy roughly one third of the total volume each. The characteristic pore dimensions are in the order of 1 μm [77]. The electrochemical reactions in the SOFC electrodes are strongly connected to the surface-phase chemistry and the catalytic reforming reactions. Significant disparities are seen, in the rate constants and expressions, the activation energies, the involved reaction pathways, the rate-limiting steps and the intermediate species, between different numerical studies in literature on the catalytic reforming activity on Ni-YSZ [78,79]. The surface coverage can be calculated with for example a mean-field approach, where it is assumed that the surface state can be described with average quantities, such as surface coverage, thermodynamic and kinetic adsorbation properties. The surface-phase species are coupled to the gas-phase species via desorption and adsorption reactions. The surface-phase species are also participating in the reactions among themselves [79]. It is found that the catalytic nickel sites for conversion of methane and the sites for electrochemical reactions are not the same [80]. Knowledge of the catalytic reaction mechanism considering steam reforming of hydrocarbons is regarded as a key factor for designing an anode material with a high efficiency and a long life length [81]. The CO* formation as well as the $CH_4$(g) adsorption have been suggested as the rate limiting steps. According to Jones *et al.* [82] the rate limiting step changes from CO* formation to $CH_4$(g) adsorption as the operating temperature is increased.

A multi-step heterogeneous reaction mechanism (HCR) for the Ni/YSZ catalysts has originally been developed by Hecht *et al.* [83]. This mechanism consists of 21 reversible reactions, involving 6 gas-phase species and 12 surface-phase adsorbed species. The mechanism is elementary in nature and covers the global aspects of the MSR, the WGSR and the Bouduard reactions as well as the surface-carbon coverages. A simplified sketch of this reaction mechanism can be seen in Figure 3. Most of the expressions are expressed in the Arrhenius rate form and depend on the surface coverage. This scheme is validated by the experiments by Hecht *et al.* [83], considering a porous Ni-YSZ anode only, i.e., there is no electric current withdrawn from the system. The experiments were designed to measure the extent of the reforming processes under the conditions well away from equilibrium conditions. Pure steam reforming and pure dry reforming with carbon dioxide as well as a combination of these were included in the validation. Note that this mechanism is not validated on the conditions where coking occurs [83]. The HCR developed by Hecht *et al.* [83] was extended by Janardhanan and Deutschmann [19] to describe a larger temperature range between 220 and 1700 °C (compared to a constant temperature of 800 °C). However, the same chemical reaction schemes were applied.

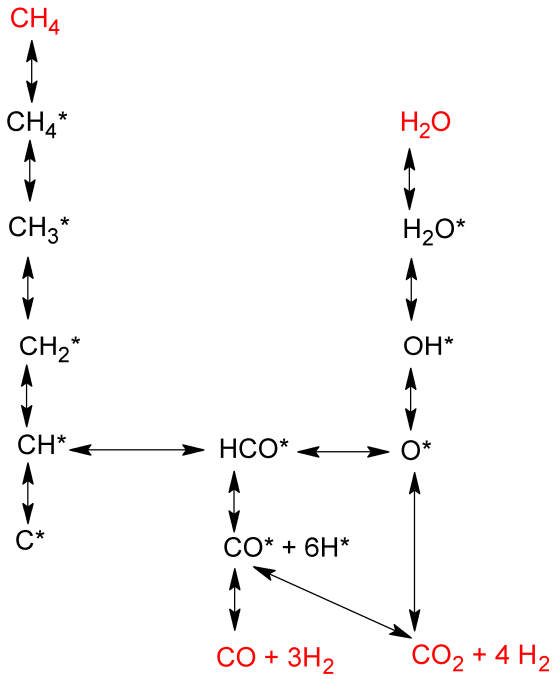


*Figure 3. Simplified sketch of the catalytic MSR and WGSR mechanism proposed by Hecht et al. [83] and Janardhanan and Deutschmann [19] among others. Note that the generation and consumption of H*, O* and OH* in each reaction step are not explicitly shown in the figure. The gas reactants and products are marked with red color.*

Blaylock *et al.* [84] investigated the different reaction pathways and the kinetics of the MSR over the Ni(111) surfaces, in order to develop a comprehensive ab initio microkinetic model. The Ni(111) surface is sometimes also referred as Ni terrace, known to be catalytically active, and it is the most stable facet on Ni crystallites. The reaction scheme consists of 7 gas-phase species, 18 surface-phase adsorbed ones and 36 reversible reactions. A simplified sketch of this

reaction scheme can be found in Figure 4. Besides the Ni terrace also the step sites catalyze the MSR, i.e., a model that considers only the Ni terrace underestimates the reforming reaction rate. The reaction path associated with the steps has a low activation barrier and the one associated with terraces has a higher activation barrier. It is found that there are many more active terrace sites compared to the active step sites at the TPB. The graphite formation occurs at the step sites. It is possible to add different additives that block different step sites and certainly decreases the probability for graphite formation. An optimized catalyst will have just enough additives that graphite formation is effectively blocked, while the fast "channel" reaction can still proceed [85].

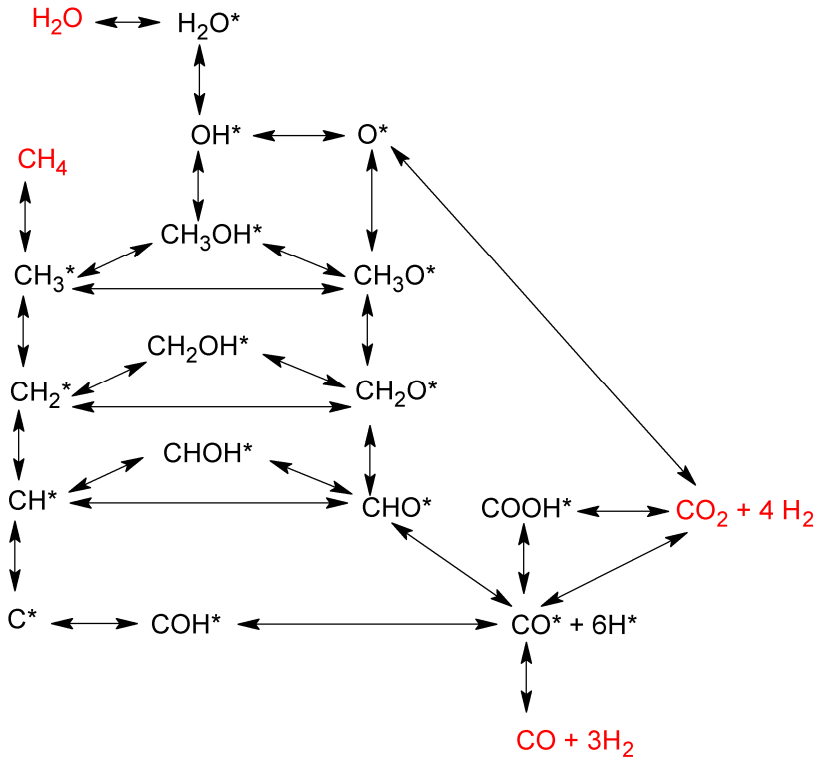


*Figure 4. Simplified sketch of the catalytic reforming reaction mechanism proposed by Blaylock et al. [84]. Note that the generation and consumption of H*, O* and OH* in each reaction step are not explicitly shown in the figure. The gas reactants and products are marked with red color.*

The reaction mechanism from Hecht *et al.* [83] in Figure 3 and the one from Blaylock *et al.* [84] in Figure 4 differ concerning the number of the intermediate adsorbed surface-phase species. The later approach with a larger number of the adsorbed surface-phase species contains obviously more reaction steps. For instance, the first reaction step in Hecht *et al.* contains the adsorption of $CH_4$(g) to $CH_4$*, compared to the adsorption of $CH_4$(g) to $CH_3$* + H* in the scheme presented in [84]. It should be noted that extra intermediate species are involved in [84].

For the scheme in [84] 87 % of the total reaction flux is predicted to involve the reaction of CH* with one oxygen containing species. It is worth to note that CHO* is formed from CH* and O*, and decomposed later to form CO* and H*. This single reaction path corresponds to approximately 56 % of the total reaction flux. The formation of CHOH* from OH* and CH*, with a subsequent reaction to COH*, is the second-most-active pathway and corresponds to 31 % of the total reaction flux. On the other hand, the reaction of $CH_2$* with either OH* or O* involves 12 % of the total flux.

**Microkinetic models**

A great deal of information is available for Ni as the reforming catalyst, because it has been commonly used for catalysis in the chemical industry. For SOFC anodes the ceramic oxygen-ion conductor YSZ itself also has catalytic activity for the partial oxidation. A kinetic model can be constructed by combining thermochemical values for each species with computed activation energies and the transition-state properties. The forward rate coefficients are described either as a surface-phase reaction rate coefficient or an adsorption reaction. The original kinetic data is often taken from a variety of different catalysis studies which makes the mechanism not thermodynamically consistent. Therefore some of the original kinetic parameters are often modified to ensure the overall consistency concerning the enthalpy and the entropy. This approach permits the computation of the reverse reaction rate coefficients, which in turn are dependent on the forward reaction rate coefficients [83].

For the surface-phase and the desorption reactions, often the Arrhenius form is applied for the reaction rate constants, at least for small or moderate variations of the temperature for the reactions [86]. The reaction rate constant ($k_i$) in a generalized modification of an Arrhenius type equation including the species coverage can be expressed as [19]:

$$k_i = A_i \cdot T^{n_i} \cdot \exp\left(\frac{-E_{a,i}}{\mathrm{R} \cdot T}\right) \prod_{k=1}^{K_g+K_s} \theta_k^{\mu_{ki}} \cdot \exp\left(\frac{-\varepsilon_{ki} \cdot \theta_k}{\mathrm{R} \cdot T}\right) \tag{57}$$

where $n_i$ the temperature exponent fraction. To describe the coverage dependece, $\mu_{ki}$ and $\varepsilon_{ki}$ are introduced as the parameters for the surface-phase species $k$ and the reaction $i$. The species molar production rate depends on the surface-phase species concentration which is sometimes expressed as the surface coverage $\theta_k$. The relation between the surface coverage and the surface-phase concentration is expressed as [87]:

$$\theta_k = \frac{c_j \cdot \sigma_j}{\Gamma_{tot}} \tag{58}$$

where $\sigma_j$ is the co-ordination number (number of sites required for a species for adsorption), $c_j$ the concentration and $\Gamma_{tot}$ the total surface site density. The reaction rate constant for a surface-phase reaction can also be written as [84]:

$$k_i = \left(\frac{k_b \cdot T}{h}\right) \cdot \left(\frac{Q^{TS} \cdot \left(Q'_{slab}\right)^{R_{tot}-1}}{\prod_{r=1}^{R_{tot}} Q_r}\right) \cdot v \frac{N_{sites}^{0\,R_{tot}-1}}{C_T^{R_{ads}-1}} \cdot \exp\left(\frac{-E_b}{\mathrm{R} \cdot T}\right) \tag{59}$$

where $k_b$ is the Boltzmann constant, $h$ the Planck constant, $Q$ the total partition function, $R_{tot}$ the total number of reactants participating in the reactions, $R_{ads}$ the total number of adsorbate reactants, $N_{sites}$ the standard-state number of binding sites per adsorbate and $E_b$ the classical electronic energy barrier of the adsorption.

Non-activated adsorption is calculated using the kinetic theory of the gases by assuming the sticking coefficient to be equal to the fraction of vacant sites. The forward reaction rate constant can be presented for the non-activated adsorption as [84]:

$$k_i = \sqrt{\frac{k_b \cdot T}{2 \cdot \pi \cdot M_k}} \tag{60}$$

Hecht *et al.* [83], Janardhanan and Deutschmann [19] as well as Hofmann *et al.* [76] were, for the adsorption reactions, applying an approach with the sticking coefficient instead of the approach in eqn (57). The forward reaction rate constants including the sticking coefficient ($\gamma_k$) for the non-activated adsorption reaction can be expressed as:

$$k_i = \frac{\gamma_k}{(\Gamma_{tot})^m} \cdot \sqrt{\frac{\mathrm{R} \cdot T}{2 \cdot \pi \cdot M_k}} \tag{61}$$

For the activated adsorption and for the surface-phase reactions, the transition-state theory can be applied to obtain the reaction rate coefficients for the forward reactions. The forward reaction rate constant for the activated molecular adsorption is then written as [84]:

$$k_i = \left(\frac{k_b \cdot T}{h}\right) \cdot \left(\frac{Q^{TS}}{Q_{gas} \cdot Q_{slab}}\right) \cdot \left(\frac{\mathrm{R} \cdot T}{p_{tot}}\right) \cdot \Gamma_{tot} \cdot \exp\left(\frac{-E_b}{\mathrm{R} \cdot T}\right) \tag{62}$$

The construction of a kinetic model needs to be performed for the relationship between the standard free energy change of an elementary reaction step and the equilibrium. When the equilibrium constant ($K_{eq,i}$) and the forward reaction rate constant are known, the reverse reaction rate constant can be expressed as [86]:

$$k_{-1,i} = \frac{k_i}{K_{eq,i}} \tag{63}$$

where $K_{eq,i}$ is defined as [86]:

$$K_{eq,i} = \exp\left(-\frac{\Delta G_i}{\mathrm{R} \cdot T}\right) = \exp\left(-\frac{\Delta H_i - T \cdot \Delta S_i}{\mathrm{R} \cdot T}\right) \tag{64}$$

where $\Delta S$ is the entropy change due to chemical reaction. It should be noted that the principle of reversibility should be used with some caution. The mechanism for the reactions can be

reversible for a given set of concentrations, temperature and pressure, but may not be valid for other conditions. The reaction may proceed through the same steps in the forward and the backward reactions but the rate of the individual steps may differ by several orders of magnitude [86].

## 2.5 Electrochemical reactions

Electrochemical reactions occur at the TPBs, i.e., the region where the ionic (YSZ), electronic (Ni or LSM) and gas-phase meet, as shown in Figure 5. Ions migrate in the YSZ material (from the cathodic TPB to the anodic TPB), conduction of electrons occurs in the electronic-phase (Ni or LSM) and transport of gas molecules takes place in the open voids within the electrodes. A larger TPB area gives more reaction sites (=lower activation polarization in the electrodes) [34]. Note that the TPB needs to be connected to the rest of the domain, i.e., the pores need to be connected through the surrounding pore network to the fuel/air stream, the Ni- or LSM-phase must be connected to the current collector and the YSZ-phase in the electrodes to the YSZ electrolyte for electrochemical reactions to proceed [88]. Vivet *et al.* [58] used the FIB-SEM to obtain a 3D reconstruction and the total (anodic) TPB length is calculated to $7.4 \cdot 10^{12}$ $m/m^3$.

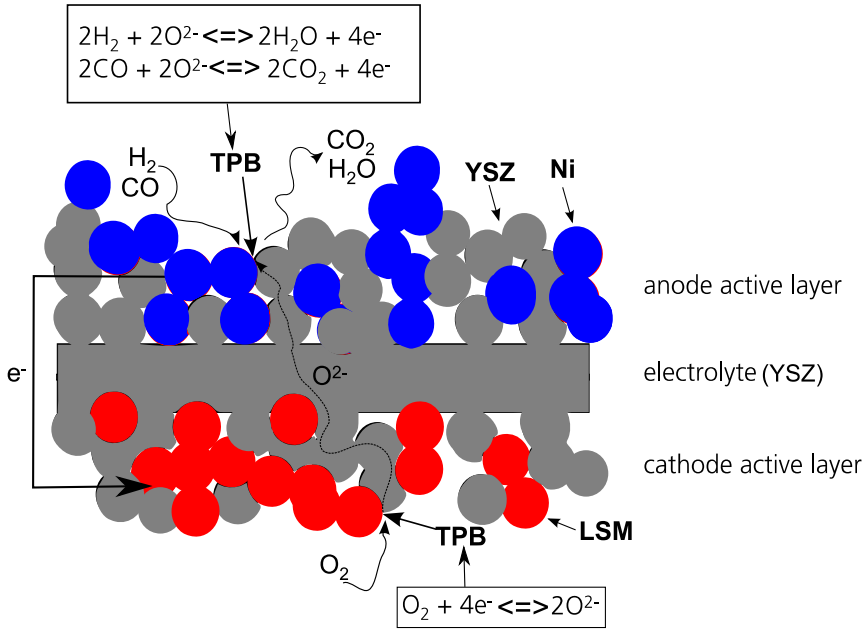


*Figure 5. The electrochemical reactions at the anodic and cathodic TPBs.*

The total gas pressure is lower close to the TPBs, compared to other parts of the cathode because of the consumption of oxygen molecules at the TPBs. This gradient makes the transport of oxygen from the channel towards the electrolyte easier. The TPB area or length in the electrodes depends on the particle diameter. A reduction of the particle diameter increases the TPB area, at the same time the Knudsen diffusivity and the flow permeability are reduced. Nam

and Jeon [34] found that most of the electrochemical reactions occur within 10 μm (from the electrolyte interface) for the anode and 50 μm for the cathode when the mean particle diameter is 1 μm [34]. The thickness of the active TPB zone is also discussed in chapter 5.5.

The charge-transfer processes are the ones of the least understood aspects of fuel cell chemistry [88,89]. It is expected that understanding the mechanism of the surface-phase reactions that occur close to the anode TPB is important for the future advances of the SOFC development [89]. Most models in the literature assume a single global charge-transfer reaction, leading to the Butler-Volmer equation, as further discussed in chapter 3.5. Adsorption/desorption, surface diffusion, the formation of hydroxyl and a charge-transfer reaction are all found to be feasible rate-limiting steps in an SOFC (anode) model [88]. Lee *et al.* [88] used a five step elementary reaction mechanism for the electrochemical reactions.

$$H_2(g) + 2(Ni) \Leftrightarrow 2H(Ni) \tag{65}$$

$$H(Ni) + O^{2-}(YSZ) \Leftrightarrow (Ni) + OH^{-}(YSZ) + e^{-} \tag{66}$$

$$H(Ni) + OH^{-}(YSZ) \Leftrightarrow (Ni) + H_2O(YSZ) + e^{-} \tag{67}$$

$$H_2O(YSZ) \Leftrightarrow H_2O(g) + (YSZ) \tag{68}$$

$$O_0^X(YSZ) + (YSZ) \Leftrightarrow O^{2-}(YSZ) + V_0^{\bullet\bullet}(YSZ) \tag{69}$$

where hydrogen is assumed to be adsorbed only at the nickel *(Ni)* surfaces and other surface-phase species at the YSZ surfaces.

*Table 5. Exchange current density in Butler-Volmer equation when assuming different rate-limiting conditions for the anode electrochemical reactions [88].*

| **Rate-limiting reaction** | **Exchange current density ($i_0$)** | **Hydrogen adsorption ($i^*_{H_2}$)** |
|---|---|---|
| **Eqn (65)** | $i_0 = i^*_{H_2} \cdot \left(p_{H_2}\right)$ | $2 \cdot \mathrm{F} \cdot l_{TPB} \dfrac{\gamma_i}{\sqrt{2 \cdot \pi \cdot \mathrm{R} \cdot T \cdot M_{H_2}}}$ |
| **Eqn (66)** | $i_0 = i^*_{H_2} \dfrac{p_{H_2O}^{1/4} \cdot \left(K_{\mathrm{eq},65} \cdot p_{H_2}\right)^{1/4}}{1 + \left(K_{\mathrm{eq},65} \cdot p_{H_2}\right)^{1/2}}$ | $\dfrac{2 \cdot \mathrm{F} \cdot l_{TPB} \cdot K_{\mathrm{eq},69}^{1/4} \cdot k_{66,a}^{3/4} \cdot k_{66,c}^{1/4}}{\left(K_{\mathrm{eq},67} \cdot K_{\mathrm{eq},68}\right)^{1/4}}$ |
| **Eqn (67)** | $i_0 = i^*_{H_2} \dfrac{p_{H_2O}^{3/4} \cdot \left(K_{eq,65} \cdot p_{H_2}\right)^{1/4}}{1 + \left(K_{eq,65} \cdot p_{H_2}\right)^{1/2}}$ | $2 \cdot \mathrm{F} \cdot l_{TPB} \cdot k_{67,c} \cdot \left(K_{\mathrm{eq},67} \cdot K_{\mathrm{eq},66}\right)^{1/4} \left(\dfrac{K_{\mathrm{eq},69}}{K_{\mathrm{eq},68}}\right)^{3/4}$ |
| **Eqn (68)** | $i_0 = i^*_{H_2} \cdot \left(p_{H_2O}\right)$ | $2 \cdot \mathrm{F} \cdot l_{TPB} \cdot K_{\mathrm{eq},69} \cdot k_{68,b}$ |

*where i* is an empirical parameter in the electrochemical model and $l_{TPB}$ the TPB length.*

Various interactions appear between (**1**) adsorbed atomic hydrogen *H(Ni)*, an empty surface site (Ni) and an electron $e^-$ *(Ni)*, (**2**) a lattice oxygen $O_0^X$(YSZ) and an oxygen vacancy $V_0^{\bullet\bullet}$*(YSZ)* within the YSZ electrolyte, and (**3**) hydroxyl ion $OH^-$*(YSZ)*, water $H_2O$*(YSZ)*, oxygen ion $O^{2-}$*(YSZ)* and empty *YSZ* sites, as considered in this electrochemical reaction mechanism (eqns (65)-(69)). The exchange current density depends on the assumption of which equation is the rate limiting one, as shown in Table 5. Note that different expressions can be obtained, based on the dependence on the partial pressure of the products and reactants, anodic or cathodic reaction coefficient ($k_a$ or $k_c$) and the equilibrium constants ($K_{eq}$) for the respective reactions. Determination of the actual rate-limiting reactions among eqns (65)-(68) requires a very careful analysis and fitting of experimental data to the different theoretical derivations. Also the anodic and cathodic charge-transfer coefficients in the Butler-Volmer equation depend on the assumption of the rate-limiting equations [88].

Vogler *et al.* [89] studied the electrochemical hydrogen oxidation reaction at the nickel/YSZ anode, and considered eqns (65)-(69) but also the YSZ surface-phase reaction between water and oxygen ions, the Ni surface-phase reaction for water and hydroxyl ions, and five additional charge-transfer reactions. This scheme is based on elementary physics and chemical processes (without the assumption of a specific rate-determining step). This scheme is compared with experiments and applied to determine the anode performance, to estimate the pre-exponential factors and the activation energies. Only the forward-rate coefficients from the experimental and the literature data are used and then the reverse-rate constants are calculated according to thermodynamic consistency. Seven possible different combinations of one or two elementary charge-transfer reactions are investigated and compared to the experimental data. They concluded that the hydrogen spillover mechanisms (eqn (67) together with eqn (70)) have the best agreement with experimental data.

$$H(Ni) + O^{2-}(YSZ) \Leftrightarrow (Ni) + OH^-(YSZ) + e^- \tag{70}$$

### 2.5.1 Polarizations

The influence of polarizations/potential differences varies depending on cell structure/design and operating conditions. The potentials vary along the flow direction and they are affected by for example the local temperature as well as the local hydrogen and oxygen concentrations. It is concluded in Sohn *et al.* [90] that for an intermediate temperature SOFC with a co flow configuration, the activation polarization is dominant in the cathode near the fuel and air inlets, and in the anode near the outlets. Also the counter flow configuration is investigated and the variation in cathodic activation overpotential is smaller, compared to the co flow configuration. For both the co flow and the counter flow configurations the activation polarization in the cathode is dominating at lower current densities and the activation polarization in the anode at higher ones. The dominance of the anode activation polarization at high current densities is explained by the depletion of hydrogen according to a high fuel utilization [90]. The influence from ionic polarizations depends mostly on the ionic conductivity within the electrolyte and the electrolyte thickness, where a decreased thickness means a decreased ohmic polarization. When the concentration of fuel or oxidant reaches zero at the TPB, the concentration overpotentials increases and the voltage reach zero [91]. Bessler *et al.* [79] studied an electrode-supported SOFC and found that the polarizations within the cathode are small compared to the one within the anode or electrolyte. Xiao *et al.* [92] investigated an anode-supported SOFC with a Ni/YSZ anode and a LSM cathode and concluded that the cathodic polarizations decrease with increasing temperature, but the anodic polarization increases with increasing temperature.

Expressions concerning the activation, concentration and ionic polarizations are specified in chapter 2.3.4.

## 2.6 Micro and macroscale phenomena and analysis methods

Multi-physics phenomena can often be described with a set of partial differential equations at the different length scales. The coupled partial differential equations can be solved simultaneously or separately in the physical domains for corresponding physical phenomena. Fuel cell operation depends on complex interaction between multi-physics such as momentum, species, heat, ion and electron transport as well as (electro-) chemical reactions [93]. Instantaneous flow around individual moving particles can be calculated in microscale models, which corresponds in many cases to the atom or molecular level as thermo- or fluid dynamics and detailed chemical reactions are studied. The microscale does not need to be as small as the size of the molecules. A mesoscale model corresponds to a larger scale than a particle but a smaller one than the device or the global flow field, and the flow field is divided into a number of small cells, but not as small as the particle size. Macroscale models match to the global flow field or the overall cell performance, Microscale modeling is in general more related to theoretical knowledge compared to macroscale modeling that is more related to validation and empirical data. Empirical parameters for the macroscale models could be based on the results from micro- or mesoscale models [17], for example the tortuosity is implemented in this work. Different methods have been developed to describe different scales, as explained in paper I.

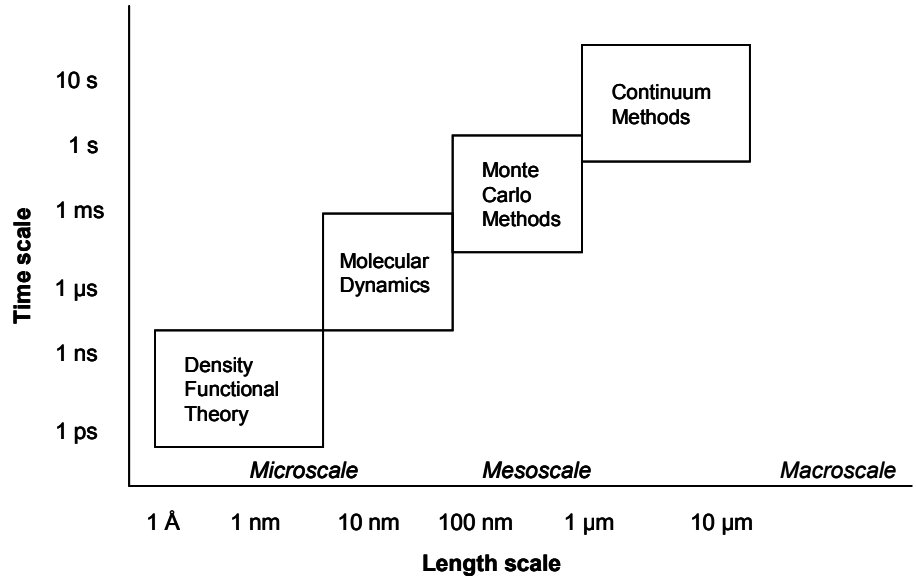


*Figure 6. Characteristic time and length scales for various methods [94].*

An SOFC can be described by different length scales: system scale (~$10^{2}$ m), component scale (~$10^{1}$ m), material aspect at the fuel cell/constituent (~$10^{-2}$ m), flow/diffusion morphologies (~$10^{-3}$ m), material structure/interface (~$10^{-6}$ m), and functional material levels (~$10^{-9}$ m). Not

only proper length scales are necessary to describe various parts of an SOFC, also different time scales need to be considered. For example, cell charging and cathode gas thermal diffusion are in $10^{-3}$ s, convective transport is in $10^{-1}$ s, cell heating and anode streamwise thermal diffusion are in $10^{3}$ s and cathode streamwise thermal diffusion is in $10^{4}$ s [5]. A general relation between time- and length scales with proper modeling methods can be seen in Figure 6, where Density Functional Theory (DFT) and Molecular Dynamics (MD) correspond to the microscale and Monte Carlo (MC) to the mesoscale. Continuum Methods (CM) with a length scale bigger than 10 μm is suitable to the macroscale.

Two basic integration approaches can be found: hierarchical method, and hybrid/cocurrent method. The hierarchical modeling starts at higher resolution (smaller scale) and the properties are extracted and used as input to the upper level. The hierarchical methods are today the most developed methods for multiscale modeling. Hybrid approaches can be used to describe various regions of the material with the appropriate time and length scale resolutions. The hybrid methods that permit cocurrent simulations are promising for the future development, because only one calculation needs to be performed. However, it requires more computational power than the hierarchical methods [95].

As an example a general hybrid molecular-continuum strategy, i.e., the point-wise coupling methodology (PWC) was presented by Asproulis *et al.* [96]. The solution in the entire domain is advanced through the continuum solver and the atomistic models are utilized to: (**1**) calculate transport properties (such as viscosity for the non-Newtonian fluids and thermal conductivity), (**2**) provide accurate boundary condition (such as temperature, slip velocity and tangential stress) and (**3**) substitute constitutive relations for the pressure, among others. The MD solver is applied to calculate macroscopic quantities at selected points in time and space for the prevailing continuum conditions. The transport of information from the molecular to the continuum model is less complicated compared to the opposite direction, but it is crucial for the accuracy and efficiency of the hybrid scheme. The calculations of the macroscopic variables are performed through averaging the corresponding microscopic properties. The PWC effectively avoids performing MC simulations for nearly identical continuum states, meaning a significant reduction in computational time [96].

Khaleel *et al.* [97] developed a multiscale approach, where the microscale electrochemistry model (LBM) calculates the performance of the porous electrode material based on the detailed material structures at the micro level, distribution of the reaction surfaces, and transport of oxygen ions through the material. The microscale electrochemistry modeling is used to calculate the overall fuel cell current-voltage relation, which is then used as input to the macroscale calculations, where the current density, cell voltage and heat production are calculated.

Bove *et al.* [98] established a macroscale black-box model, using the equations that are generally used for microscale models. The main problem with this approach is that the gas composition variation along the flow direction is neglected, the effect of fuel utilization variations can not be estimated and the cell voltage is underestimated. The advantages are that the calculations are less time consuming compared to microscale modeling, and contain more information describing microscale phenomena compared to other macroscale models.

Cheng *et al.* [99] introduced multiscale concepts, but they did not mention how the different scales interact with each other. It is frequently stated in the literature that data or property constants can be obtained from the smaller scales and then used in a larger scale model. However, information about the methodology of this coupling is rare [17,19,95].

### 2.6.1 How far can SOFC modeling reach?

There are still many unresolved issues in fuel cell modeling. The exchange current density is used to calculate the activation polarization and depends on the catalyst for the electrochemical reactions. One problem is that the data in literature is not identical or well explained. Further study of the mechanisms behind the activation polarization is important for the further development [100]. Normally only hydrogen is considered as electrochemical active fuel. However, also carbon monoxide and methane participates in the electrochemical reactions. The coupling of several simulations participating electrochemical fuels is still rare in SOFC modeling.

The macroscale modeling has gained a lot of success during the last years in understanding complex phenomena occurring during FC operation and it has been possible to improve the FC design. However, the microstructure of the porous electrodes is normally not included in the model, the porosity and the tortuosity are, for macroscale models, normally treated as fitting parameters, as described in chapter 3.1. Fuel cell modeling can be significantly improved if detailed submodels being not too expensive (in computational time) are included in a general model. A challenge for the future is to develop approaches for multiscale and multiphysics modeling considering coupling of fluid flow, heat, (gas- and solid-phase) species and charge transport, electrochemical kinetics as well as reforming kinetics (when hydrocarbon fuels are used). It has been found that the reaction kinetics for the reforming reactions require rigorous studies, even several heterogeneous reaction mechanisms have been developed. It should be noted that they did not match each other very well [100].

A grand challenge for future SOFC modeling development is the concept of an inverse coupled multiphysics modeling, where the nano-structured material design is calculated from the defined system requirements, instead of material and other engineering specifications. The activation- and diffusion-related polarizations depend strongly on the nano-structure of the cathode and anode materials, and are good examples for application of this potential approach [101].

# 3 CFD Model Development - Governing Equations for Transport Processes and Chemical Reactions

CFD models for anode-supported SOFCs, in 2D, are developed and implemented in the commercial software, COMSOL Multiphysics. The equations for momentum, gas-phase species, ion (only in paper VIII), electron (only in paper VIII) and heat transport are solved simultaneously. The geometry for papers II, III, IV and V are based on data available in the open literature [91] while papers VII and VIII are based on a standard cell (Figure 7) by NIMTE, as defined in Table 6. A sketch of the model can be seen in Figure 8, note that it is not to scale.

*Table 6. Cell geometry.*

| Cell Component | Parameters (in II, III, IV, V) | Parameters (in VII, VIII) |
|---|---|---|
| **Cell length** | 0.4 m (II) / 0.1 m | 0.1 m |
| **Fuel channel height** | 1 mm | 1 mm |
| **Air channel height** | 1 mm | 1 mm |
| **Anode thickness** | 500 μm | 415 μm |
| **Cathode thickness** | 50 μm | 70 μm |
| **Electrolyte thickness** | 20 μm | 10 μm |
| **Interconnect thickness** | 500 μm | 300 μm |

The NIMTE standard cell consists of a 400 μm thick Ni (40 %)/YSZ (60 %) anode substrate and additionally an active anodic layer of 15 μm, where the electrochemical reactions occur. The electrolyte is a 10 μm thick layer of YSZ. The cathode consists of a 20 μm thick active layer of LSM/YSZ and a buffer layer of 50 μm LSM. Note that the anode active- and support layers have the same material composition, and the interface may not be very distinct, to be compared to the cathode, where the active and support layers have different compositions. It is a fact that a fine porous microstructure with a high surface area may lead to a decreased mechanical strength. Because the TPB, does not extend too far from the anode-electrolyte interface, a graded porosity can be used to maximize the length of the TPB in the active region. The high mechanical strength is maintained for the rest of the anode which is used primarily as the cell support and for internal reforming reactions, when hydrocarbons are supplied as fuels.

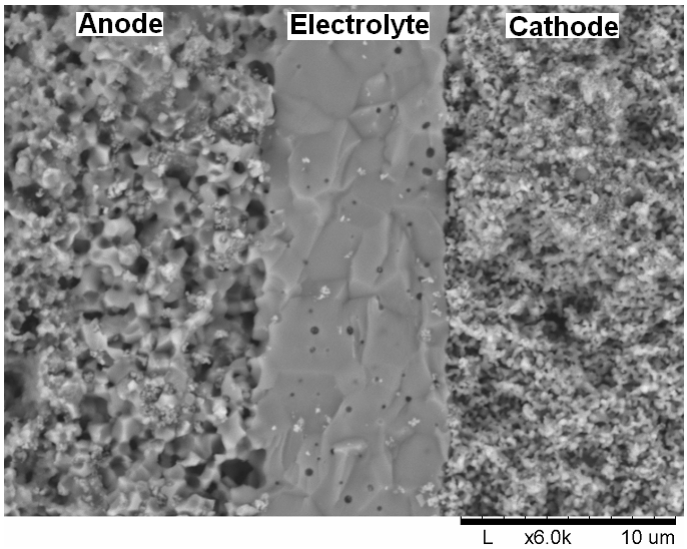


*Figure 7. A SEM image of a tested SOFC cross section, with (from left to right) anode active layer, electrolyte and cathode active layer.*

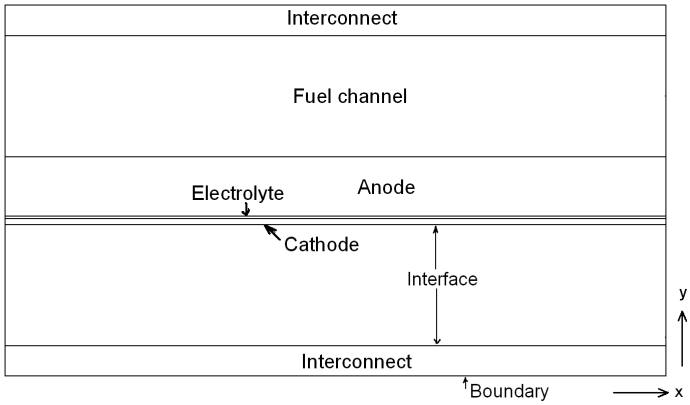


*Figure 8. Sketch of an anode-supported SOFC, not to scale.*

## 3.1 Gas-phase species transport

Equation (71) is used to describe species transport phenomena for each gas-phase component inside the cell and solved for the fuel- and air channels and the respective electrodes [102]:

$$-\nabla\left(\rho_g \cdot w_i \sum^{n} D_{eff,ij} \cdot \nabla x_j\right) + \left(\left(x_j - w_j\right)\frac{\nabla p}{p} \cdot \left(\nabla \bullet \vec{u}\right)\right) - \nabla\left(D_i^T \cdot \frac{\nabla T}{T}\right) + \rho_g \cdot \vec{u} \cdot \nabla w_j = S_i \qquad (71)$$

where $\vec{u}$ the velocity vector, $n$ the number of species and $D_i^T$ the thermal diffusion coefficient. $S_i$ refers to the source term by the chemical reactions (internal reforming as well as

electrochemical reactions). The reaction rates for internal reforming reactions (papers III, IV, V, VII and VIII) are specified in chapter 3.6, and for electrochemical reactions (paper VIII) in chapter 3.5. It should be noted that the electrochemical reactions in papers II, III, IV, V and VII are implemented as interface conditions, as described further in the respective papers. The models in papers II, III and IV, consider only molecular (ordinary) diffusion, and developments are made in paper V to include Knudsen diffusion (also included in papers VII and VIII). The equations for both molecular and Knudsen diffusion are defined in chapter 2.3.1. The effective diffusion coefficients are implemented according to eqn (19).

The air inlet is defined as oxygen and nitrogen ($x_{O2} : x_{N2} = 0.208 : 0.792$). The model in paper II contains only hydrogen and water and the fuel inlet is specified with a hydrogen mass fraction of 0.90. For papers IV, V, VII and VIII the fuel inlet conditions (mole fractions) are defined as 30 % pre-reformed natural gas, as specified by IEA: $x_{H2} : x_{CH4} : x_{CO} : x_{H2O} : x_{CO2} = 0.2626 : 0.171 : 0.0294 : 0.4934 : 0.0436$ [65]. The model in papers VII and VIII includes also one case with only hydrogen and water, with a hydrogen mole fraction of 0.90, i.e., the same conditions as for the experiments used for the validation. The fuel inlet conditions are varied in a parameter study in paper III to investigate the impact from different pre-reformed renewable fuels. The fuel and gas channel outlets are, for all the models, defined as convective flux boundaries.

## 3.2 Momentum transport

The Darcy-Brinkman equation, eqn (72), is introduced and solved for the gas flow in the fuel and air channels, and in the porous materials simultaneously (as discussed in chapter 2.3.2) [44,45]:

$$\frac{\rho_g}{\varepsilon}\cdot\left(\nabla\bullet\vec{u}\right)\cdot\frac{\vec{u}}{\varepsilon}-\nabla\left[-p+\frac{\mu_g}{\varepsilon}\left\{\Psi-\frac{2}{3}\left(\nabla\bullet\vec{u}\right)\right\}\right]+\left(\frac{\mu_g}{\kappa}+\beta_F\left|\vec{u}\right|+\nabla\left(\rho_g\cdot\vec{u}\right)\cdot\vec{u}\right)=\mathbf{F} \qquad (72)$$

where $\mathbf{F}$ is the volume force vector, $\kappa$ the permeability of the porous medium ($1.76\cdot10^{-11}$ m$^2$ [22]), $\Psi$ the viscous stress tensor and $\beta_F$ the Forchheimer coefficient (includes the microscopic inertial effects). The densities and the dynamic viscosity are calculated as described in chapter 2.3.2. The momentum equation in the air and fuel channels reduces to eqn (73) [45]:

$$\rho_g\cdot\left(\nabla\bullet\vec{u}\right)\cdot\vec{u}-\nabla\left[-p+\mu_g\cdot\left\{\Psi-\frac{2}{3}\cdot\left(\nabla\bullet\vec{u}\right)\right\}\right]=\mathbf{F} \qquad (73)$$

The gas inlet velocities are defined as a laminar flow profile, and the average values are based on the fuel- and oxygen utilizations. The utilizations of fuel and oxygen are defined to 80 % and 20 %, respectively, for the standard cases in papers II, III, IV and V. The models in papers VII and VIII define the utilizations to 70 % and 18 %, respectively, as used in experiments concerning the standard cell at NIMTE. Note that the air and fuel utilizations are not kept constant in the parameter studies performed in the different papers. The fuel utilizations are evaluated by comparing the fuel gas content at the inlet and at the outlet, where each mole of methane corresponds to 4 moles of hydrogen and each mole of carbon monoxide corresponds to 1 mole of hydrogen. At the outlet the pressure (1 atm) is fixed for all the developed models.

## 3.3 Heat transport

An LTE approach is applied in paper VIII, i.e., the temperature is assumed to be locally the same for the gas- and solid-phases (within the electrodes), to reduce the calculation time and also based on the minor temperature difference between the gas- and the solid-phase, as concluded in chapter 2.3.3.

The temperature distribution is in papers II, III, IV, V and VII calculated separately for the gas-phase (in air and fuel channels and electrodes) and for the solid-phase (interconnects, electrodes and electrolyte), according to the LTNE approach, in chapter 3.3.2. Heat is then transferred between the phases at the channel walls and in the porous electrodes.

### *3.3.1 Local temperature equilibrium (LTE)*

The governing equation for the temperature distribution (within all the subdomains) is according to the LTE approach defined as [102]:

$$\rho_g \cdot \varepsilon \cdot c_{p,g} \cdot \vec{u} \cdot \nabla T = \nabla \bullet \left( k_{eff} \nabla T \right) + Q \tag{74}$$

The source term (Q) is defined in eqns (78)-(81). The overall governing equation for heat transport, eqn (74), reduces to pure heat conduction in the electrolyte and in the interconnector (eqn (75)). Note that the porosity equals one in the air and fuel channels. The inlet gas temperature is defined by the operating temperature and is also varied in the parameter studies. The outlets are defined as convective flux boundaries for all the models. The boundaries at the top and the bottom of the cell are defined as symmetry boundaries, because it is assumed that the cell is surrounded by other ones with identical temperature distribution. Looking at the stack scale, there might be significant heat losses due to thermal radiation and it is suggested to include these phenomena in future studies.

The gas-phase values of the thermal conductivity and the specific heat are defined in chapter 2.3.3. The conductivity and the density for the solid materials in the different subdomains are outlined in Table 7. The values for the electrodes from [87] for the density are valid for a porosity of 0.35. Higher values are expected as the porosity is decreased to 0.30 in papers VII and VIII and lower values are expected as it is increased to 0.50, as in papers II, III, IV and V. However, the impact within the model is found to be negligible.

*Table 7. Solid Material Parameters.*

| | **Thermal conductivity, $k_s$ (W/(m·K)) [103]** | **Density, $\rho_s$ (kg/m$^3$) [87]** |
|---|---|---|
| **Anode (Ni/YSZ)** | 11 | 3310 |
| **Cathode (LSM/YSZ)** | 6 | 3030 |
| **Electrolyte (YSZ)** | 2.7 | 5160 |
| **Interconnect (stainless steel)** | 6 | 3030 |

### 3.3.2 Local temperature non-equilibrium (LTNE)

The general heat conduction equation is applied to calculate the temperature distribution for the solid materials in the electrolyte, the interconnect and the electrodes [102]:

$$\nabla \bullet \left(-k_s \cdot \nabla T_s\right) = Q_s \tag{75}$$

The heat source ($Q_s$) includes heat transfer between the solid- and gas-phases, and heat generation because of ohmic polarization. Heat generation due to electrochemical reactions are simplified and defined as interface conditions (in papers II, III, IV, V and VII), such as for gas-phase species transport, as discussed earlier. The temperature distribution for the gas mixtures in the fuel and air channels and in the porous electrodes is calculated as [102]:

$$\nabla \bullet \left(-k_g \cdot \nabla T_g\right) = Q_g - \rho_g \cdot \varepsilon \cdot c_{p,g} \cdot \vec{u} \cdot \nabla T_g \tag{76}$$

in which $Q_g$ is the heat transfer between the gas- and solid-phases and heat consumption due to internal reforming reactions. The values of the thermal conductivity and the specific heat are defined in chapter 2.3.3. The characteristics of the solid materials in the different subdomains are outlined in Table 7.

The heat transfer between the gas- and solid-phase, in the electrodes, depends on the temperature difference and the particle surface area to volume ratio as [104]:

$$Q = h_v \cdot \left(T_g - T_s\right) = AV_{tot} \cdot h_{s,g,por} \cdot \left(T_g - T_s\right) \tag{77}$$

in which $h_v$ is the volumetric heat transfer coefficient, $h_{s,g,por}$ the heat transfer coefficient (as described in [50]) and $AV_{tot}$ the surface area to volume ratio available for heat transfer. It is assumed that all surface area is available for heat transfer between the gas molecules and the pore walls. The heat flux between the electrodes/interconnect and gas channels are specified at two channel walls, located opposite to each other, with a constant Nusselt number (4.094) from [105], based on the fully developed flow for a square duct (the aspect ratio is 1 for both channels). The inlet, outlet and symmetry conditions for the LTNE approach are the same as for the LTE approach above.

### 3.3.3 Heat consumption and generation within the cell

The heat consumption/generation because of internal reforming reactions is implemented in eqn (78). The change of enthalpy ($\Delta H$) is defined in Table 3 (chapter 2.2.1), the MSR rate in chapter 3.6 and the WGSR rate in chapter 2.4.1.

$$Q_{ref} = r_{MSR} \cdot \Delta H_{MSR} + r_{WGSR} \cdot \Delta H_{WGSR} \tag{78}$$

The heat generation because of ionic and electronic ohmic polarization is calculated as [56]:

$$Q_{h,ohm} = \sum \frac{i_{a,l}^2}{\sigma_l} + \sum \frac{i_{a,s}^2}{\sigma_s} \tag{79}$$

where $\sigma$ is the ionic/electronic conductivity, i.e., heat is generated due to electronic transfer resistance in Ni or LSM, and due to ionic transport resistance in YSZ. The electron transport in the electrodes as well as ion transport in the electrodes and in the electrolyte are considered in the model in paper VIII only, while the simplified approach is applied in papers II, III, IV, V and VII, where only ion transport in the electrolyte and electron transport in the electrodes are included.

The heat generation due to the activation and the concentration polarizations are (in paper VIII) defined as eqn (80) [56]. Note that papers II, III, IV, V and VII contain simplified models for the electrochemical reactions, i.e., heat generation due to polarizations and electrochemical reactions is implemented as interface conditions, i.e., eqns (80)-(81) are not implemented as source terms.

$$Q_{act+conc} = -\left(\eta_{act,e} + \eta_{conc,e}\right) \cdot i_{v,e} \tag{80}$$

where $i_{v,e}$ is the current density (per volume). The amount of heat generated (within the cathode side)/consumed (within the anode side) because of the change of entropy in electrochemical reactions is defined as [106]:

$$Q_e = -\Delta S_e \frac{T \cdot i_{v,e}}{n_e \cdot \mathrm{F}} \tag{81}$$

The entropy change due to reaction ($\Delta S_e$) is, in paper VIII, calculated from the data in [107] for the anode and the cathode TPBs, respectively. It should be mentioned that a simplified approach with a total entropy change (for eqns (2)-(3)) and as an assumption half of the heat generation in each electrode is implemented in the models presented in papers II, III, IV, V and VII.

## 3.4 Ion and electron transport

The potential difference between the anode and the cathode current collectors corresponds to the total cell voltage, as introduced in chapter 2.3.4. The governing equations for ion and electron transport (in paper VIII) are implemented as [45]:

$$i_{v,l} = \nabla \bullet \left(-\sigma_l \nabla \phi_l\right) \tag{82}$$

$$i_{v,s} = \nabla \bullet \left(-\sigma_s \nabla \phi_s\right) \tag{83}$$

The potential ($\phi$) at the anode current collector is set to zero and the one at the cathode current collector as the cell operating voltage (0.7 V in this study). All other boundaries and interfaces are electrically insulated. An operating voltage of 0.7 V is also applied in paper VII, to compare with the implementation of an average current density in papers II, III, IV and V. Equations (30)-(31) (defined in chapter 2.3.4) are employed to calculate the electromotive force, i.e., it is assumed that methane and carbon monoxide fully react with the steam and only $H_2$ participates in the electrochemical reactions. For the case of a mixture of pre-reformed natural gas

($H_2/H_2O/CH_4/CO/CO_2$) presented, the Nernst equation may not be the most applicable expression.

The electronic conductivities ($\sigma_s$) in the anode and the cathode, and ionic conductivity ($\sigma_l$) in the electrolyte material are defined in chapter 2.3.4 (eqns (42)-(44)). The effective ionic- and electronic conductivity is defined in eqns (45)-(47), by including tortuosity and material volume fractions for ion and electron transport within the anode and the cathode. For this work the following microstructure related parameters in Table 8 are employed for the electrodes. It is worthwhile to note that there is a minor transport of oxygen ions in Ni material and of electrons in YSZ material [58].

*Table 8. Microstructure properties for the porous electrodes.*

| | $V_{YSZ}$ | $V_{Ni}$ or $V_{LSM}$ | $\varepsilon_{por}$ | $\tau_s$ | $\tau_l$ |
|---|---|---|---|---|---|
| **Anode** | 0.42 | 0.28 | 0.30 | 10 | 10 |
| **Cathode** | 0.42 | 0.28 | 0.30 | 10 | 10 |

## 3.5 Electrochemical reactions

The electrochemical reactions are implemented by an averaged value (0D) at the electrode-electrolyte interface in papers II, III, IV and V, by a locally varied one (1D along the flow direction) in paper VII and by a 2D-approach (along the flow direction as well as through the electrode and electrolytes) and in paper VIII. Electrochemical reactions occur at the TPBs as discussed in chapter 2.5. The global cathodic electrochemical reaction is shown in eqn (2) and the anodic one in eqn (3). The current density (per unit volume) in the anode as well as in the cathode is calculated by the Butler-Volmer equation [108]:

$$i_{v,e} = AV_e \cdot i_{0,e}\left\{\exp\left(\beta\frac{n_e \cdot \mathrm{F} \cdot \eta_{act,e}}{\mathrm{R} \cdot T}\right) - \exp\left(-(1-\beta)\frac{n_e \cdot \mathrm{F} \cdot \eta_{act,e}}{\mathrm{R} \cdot T}\right)\right\} \tag{84}$$

where $AV_e$ is the electrochemical active area to volume ratio (the values for the anode and cathode are presented in chapter 5.5) and β the transfer coefficient, usually assumed to be 0.5. The Butler-Volmer equation can then be expressed as [52,91,108]:

$$i_{v,e} = AV_e \cdot 2 \cdot i_{0,e} \cdot \sinh\left(\frac{n_e \cdot \mathrm{F} \cdot \eta_{act,e}}{2 \cdot \mathrm{R} \cdot T}\right) \tag{85}$$

$$i_{0,e} = \frac{R \cdot T}{n_e \cdot F} A_{i,e} \cdot \exp\left(\frac{-E_a}{\mathrm{R} \cdot T}\right) \tag{86}$$

The pre-exponential factor ($A_{i,e}$) in eqn (86) is $2.35 \cdot 10^{11}\ \Omega^{-1}\mathrm{m}^{-2}$ for the cathode and $6.54 \cdot 10^{11}\ \Omega^{-1}\mathrm{m}^{-2}$ for the anode, respectively [52,91]. An activation energy ($E_a$) of 137 kJ/mol for the cathode and 140 kJ/mol for the anode are used by Patcharavorachot *et al.* [52] and Aguiar *et al.* [91] while the values between 110 and 140 kJ/mol for the anode and between 130 and 190 kJ/mol for the cathode appear in various works available in the open literature

[22,76,109-112]. Note that the Butler-Volmer equation is calculated per area in papers II, III, IV and V (implemented as an interface condition at the electrode-electrolyte interface), compared to paper VIII, implemented above, where it is calculated per volume and implemented as a source term within the electrodes. In the earlier papers (II, III, IV and V), the current is known (defined to a constant value), instead the activation polarizations are calculated with the Butler-Volmer equation.

## 3.6 Internal reforming reactions

Sufficient activity for the reforming reactions is provided inside the SOFC anode [55]. The reaction kinetics from Klein *et al.* [67] for the MSR, (eqn (87), accounting for the active area to volume ratio), and the one from Haberman and Young [75] for the WGSR (eqns (53)-(56)) are used to calculate the reaction rates in papers III, V, VII and VIII. The WGSR kinetics from [75] is also applied in paper IV. Klein *et al.* [67] refer to early experiments considering the MSR rate on a Ni/YSZ anode performed at the Research Centre Jülich [113].

There are several other kinetic models in the literature for the MSR, with examples presented in eqns (88)-(90) [70,72-74]. It is worth noting that both Achenbach & Riensche's [72,73] (eqn (88)) together with Leinfelder's [74] (eqn (89)) kinetics are an Arrhenius kinetics reaction rate type, while Dreschers kinetics [70] (eqn (90)) is a Langmuir-Hinshelwood type. They are selected, for a parameter study in paper IV, on the basis of the different order of the reactant dependence and the broad range of the activation energy. The kinetic differences depend on how the experimental configuration is set up, the material compositions and operating conditions are selected. Equation (88) is a combination of the one by Achenbach & Riensche [72] and the study of Achenbach [73], in which the reaction order of methane is unity and water has no catalytic effect on the reaction, i.e., it is a simplified equation [72,73]. Note that Leinfelder [74] found a positive reaction order of water while Achenbach & Riensche [72,73] identified a reaction order of zero.

$$\begin{aligned} r_{MSR,Klein} &= AV_{MSR} \cdot 943 \cdot \exp\left(\frac{-225 \cdot 10^3}{\mathrm{R} \cdot T}\right) \cdot x_{CH_4} \cdot x_{H_2O} \cdot p_{tot}^2 \\ &- AV_{MSR} \cdot 7.74 \cdot 10^{-9} \cdot \exp\left(\frac{-1.93 \cdot 10^3}{\mathrm{R} \cdot T}\right) \cdot x_{CO} \cdot x_{H_2}^3 \cdot p_{tot}^4 \end{aligned} \tag{87}$$

$$r_{MSR,AchRie} = AV_{MSR} \cdot 4274 \cdot \exp\left(\frac{-82 \cdot 10^3}{\mathrm{R} \cdot T}\right) \cdot x_{CH_4} \cdot p_{tot} \tag{88}$$

$$r_{MSR,Lei} = AV_{MSR} \cdot 30.8 \cdot 10^{10} \cdot \exp\left(\frac{-205 \cdot 10^3}{\mathrm{R} \cdot T}\right) \cdot x_{CH_4} \cdot x_{H_2O} \cdot p_{tot}^2 \tag{89}$$

$$r_{MSR,Dre} = AV_{MSR} \cdot \frac{288.52 \cdot \exp\left(\frac{-11 \cdot 10^3}{\mathrm{R} \cdot T}\right) \cdot x_{CH_4} \cdot x_{H_2O} \cdot p_{tot}^2}{1 + 16.0 \cdot x_{CH_4} \cdot p_{tot} + 0.143 \cdot x_{H_2O} \cdot p_{tot} \cdot \exp\left(\frac{39 \cdot 10^3}{\mathrm{R} \cdot T}\right)} \tag{90}$$

# 4 Solution Methods and Model Validation

## 4.1 Solution methods

In most cases the governing equations are numerically solved in COMSOL Multiphysics (version 3.5) using a stationary solver with a direct (UMFPACK) linear solver system. The relative tolerance was limited to $10^{-6}$ and applied to a convergence criterion based on a weighted Euclidean norm for the estimated relative error. Grid independence was, for the model described in paper II, achieved at $30 \cdot 10^3$ elements (Figure 9), after which the change in the maximum temperature was less than 0.1 %, the change in maximum velocity less than 1 %, the change in oxygen consumption less than 0.1 % and the change in hydrogen consumption less than 1 % (compared with the ones predicted by $53 \cdot 10^3$ elements). The cell geometry parameters are defined in chapter 3 (Table 6). When gas-phase species transport equations for methane, carbon monoxide and carbon dioxide are solved, the mesh size within the anode is decreased, to capture internal reforming reactions and effects on transport phenomena. Also a segregated solver is implemented for most models to decrease the calculation time.

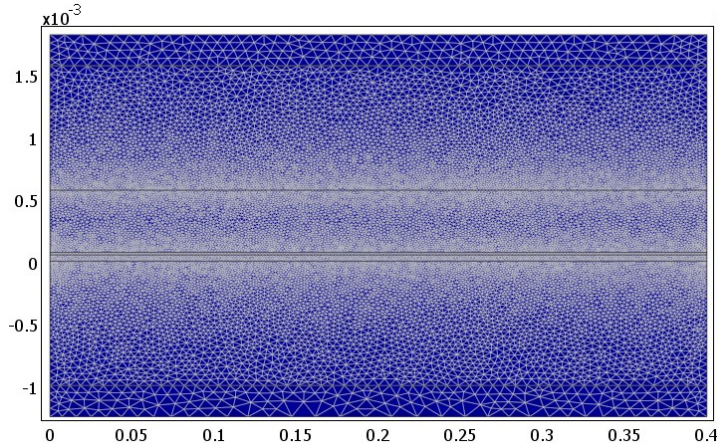


*Figure 9. SOFC geometry and mehsing for the basic case.*

A grid independence study is further performed for the model presented in paper VIII, when the governing equations are numerically solved in a new version of COMSOL Multiphysics (version 4.1:0.185) using a stationary segregated solver with a direct (MUMPS) linear solver system. The governing equations are segregated in 5 different groups: **(1)** velocity field, pressure

distribution and pressure corrections, **(2)** temperature distribution, **(3)** ion and electron distribution,**(4)** gas-phase species distribution on the air side ($O_2/N_2$) and **(5)** gas-phase species distribution on the fuel side ($H_2/H_2O/CH_4/CO/CO_2$). The segregated solver solves for $2.29 \cdot 10^6$ degrees of freedom. Grid independence was achieved at $0.716 \cdot 10^6$ elements, after which the change in the maximum temperature is less than 0.08 %, in the maximum air velocity less than 0.36 %, in the minimum oxygen mole fraction less than 0.25 %, in the minimum hydrogen mole fraction less than 0.35 %, in the methane conversion less than 0.22 % and in the maximum current density at the inlet less than 0.07 % (compared with the predictions by $1.18 \cdot 10^6$ elements). It should be noted that the mesh is finest close to the electrode-electrolyte interface and coarsest for the air- and fuel channels and for the interconnects. The reason for such a mesh arrangement is mainly due to the charge-transfer and electrochemical reactions (affecting the governing transport equations for ion, electron, gas-phase species, heat and momentum) appearing only in the regions close to the electrode-electrolyte interface.

## 4.2 Validation of the one-dimensional electrochemical model

Numerical results of any SOFC model are only approximations of real performance and the validation is an important and necessary step in the development of reliable and accurate computational models. A range of validity should be evaluated and can be established by comparing the developed model with experimental data. It should be noted that CFD models ideally make it possible to reduce the amount of experimental tests needed for cell development. Our models in papers VII and VIII rely on the experimental data from a standard cell developed at NIMTE.

For the experiments a fuel flow rate of 800 sccm (standard cubic centimeters per minute) and an air flow rate of 2000 sccm are used. The single cell sample has dimensions of $5 \cdot 5.8$ cm$^2$, with an active area of $4 \cdot 4$ cm$^2$. An alumina testing house is used, where the cell temperature is kept constant during the tests, i.e., 750 °C for this case. Voltage probes are placed on the surface of the anode- and cathode support. It should be noted that the model is assumed isothermal during the validation, to agree with the experimental conditions.

The electrochemical reactions, within the anode as well as within the cathode, occur at the TPBs, i.e., the sites which are connected to ionic-, electronic- as well as gas-phase. The reaction rate decreases drastically as the distance from the electrolyte-electrode interface increases [114-115], and this is also discussed in chapter 5. Two approaches are available to describe the electrochemical reactions in a CFD model, either as a source term (volume), or as an interface condition (cross-sectional area, x- and z-directions). When the concept with the source term is applied, the active thickness of the anode (h) and the active area for electrochemical reactions per volume ($AV_{active}$) need to be defined, as seen in Figure 10**.** In a real SOFC electrode is it tricky to define "h", since the reaction rates decreases rapidly for positions far away form the electrode-electrolyte interface. However "h" is needed to compare the 1D electrochemical approach with the 2D one. For the concept with the interface condition, as applied in paper VII, the empirical electrochemical reaction factor "f" is introduced. It is calculated by validating a theoretical model with the experiments. It can be described as the catalytically active area available for electrochemical reactions ($A_{active}$) divided by the x-z cross sectional area ($A_{interface}$). To compare the two concepts, f (-) = $A_{active}/A_{interface}$ and $AV_{active}$ (m$^2$/m$^3$) = $A_{active}/(A_{interface} \cdot h)$). Note that the governing transport equations are not solved for the z-direction, but it is important for calculating the electrochemical properties.

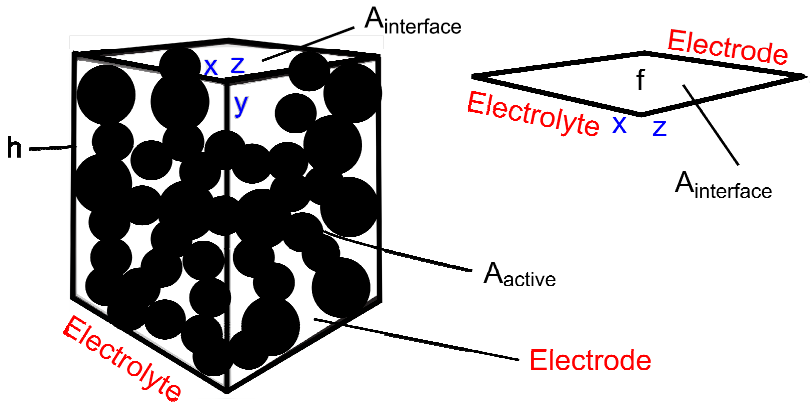


*Figure 10. Sketch over the concepts (source term, to the left, and interface condition, to the right) to define active area for the electrochemical reactions.*

The test results from the NIMTE standard cell experiments are presented in Figure 11. The cell testing was conducted at 750 °C. It is assumed that the temperature is constant within the cell, because the cell is placed in a heated oven. In Figure 11 the geometric dimensions and the active area available for electrochemical reactions are updated, in which f is 0.60. The agreement is not very good at high currents, where the model predicts higher currents compared to the experiments. The agreement between the modeling and experimental results is improved, when the ion transport factor is implemented, i.e. the ohmic polarization is increased (by a factor of two) to consider that the electrochemical reactions take place in a region away from the electrode-electrolyte interface. This ion transport factor is ignored in our previous model because charge transport equations are not included. The agreement between the experiments and the model is better, as seen in Figure 11, when f is 0.88. Note that the agreement is especially good when the voltage varies between 0.6 and 1.0 V (0.7 V is used in the validated model).

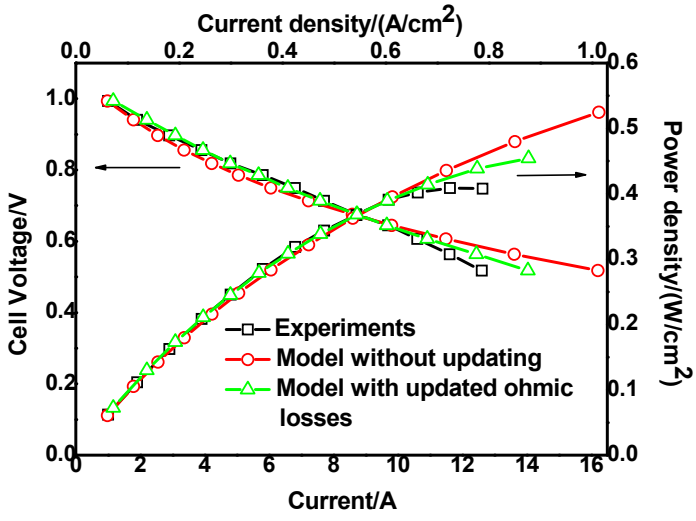


*Figure 11. Comparison between the measured and predicted performance of single SOFC cell.*

# 5 Results and Discussion

The cell geometries for the different models are defined in Table 6 (chapter 3) and the solid material parameters (thermal conductivity and density) can be found in Table 7 (chapter 3.3). The fuel and air inlet concentrations are specified in chapter 3.1, and the fuel and air utilizations in chapter 3.2. The Butler-Volmer equation for electrochemical reactions is defined in chapter 3.5 and the kinetics related to internal reforming reactions (valid for chapters 5.2-5.5) is explained in chapter 3.6. Co flow is applied, except for a parameter study in chapter 5.1, when counter flow is also considered.

## 5.1 Basic model with only hydrogen as fuel (paper II)

The basic model includes the governing equations for heat, gas-phase species and momentum transport. The fuel stream includes only hydrogen and steam, and the current density is averaged to 0D, i.e., the voltage varies along the flow direction.

The temperature increases along the x-direction (the main flow direction), as seen in Figure 12. Heat is generated because of the change of entropy by electrochemical reactions and due to activation, ohmic and concentration polarizations within the cell. The predicted temperature difference in the y-direction inside the air channel occurs because the convective heat flux is bigger compared to the fuel channel and due to the relatively larger flow rate. For this case, the difference between the inlet and outlet temperature is high because of a relatively high cell length (0.4 m, compared to 0.1 m for the other cases in chapters 5.2-5.5), the lack of heat consumption (for example due to the MSR) as well as a high fuel and oxygen utilizations.

The polarizations along the main flow direction are presented in Figure 13. It is found that the ohmic polarizations in the electrodes due to electron transport (not presented in the figure) as well as the concentration polarizations are negligible, compared to the activation polarizations within the electrodes and the ohmic polarization in the electrolyte (due to ion transport). The activation- and ohmic polarizations decrease along the flow direction, as temperature increase (see Figure 12). It is found that the activation polarization is more temperature dependent than the ohmic polarization. In this model the current density is defined as a constant (average) value, i.e., the temperature as well as the hydrogen and oxygen concentrations are not considered locally for evaluation of the current density distribution. This limitation is released in the models presented in chapters 5.4-5.5.

A simulation is also conducted to study the effect of counter flow, i.e., the air enters into the fuel cell from one side (x=0.4 m) and the fuel from the opposite side (x=0), see Figure 14. Both the air and fuel gases enter the cell at 1000 K. The fuel gas is cooled down by the air flow along the channel and the outlet temperature for the fuel gas stream is found to be close to the inlet temperature of the air flow. As the fuel gas stream enters into the cell it is quickly heated up to a temperature close to the outlet temperature of the air flow, and as expected this large

temperature gradient may cause material problems. It is recommended for counter flow to keep the inlet temperature of the fuel stream as close as possible to the outlet temperature of the air stream. Both the temperature gradient inside the cell and the maximum temperature are bigger for a counter flow design, compared to the basic case (Figure 12). When a more complex fuel mixture and internal reforming reactions are added (as in the following chapters), a high temperature close to the fuel inlet can be favorable if high reforming reaction rates are required.

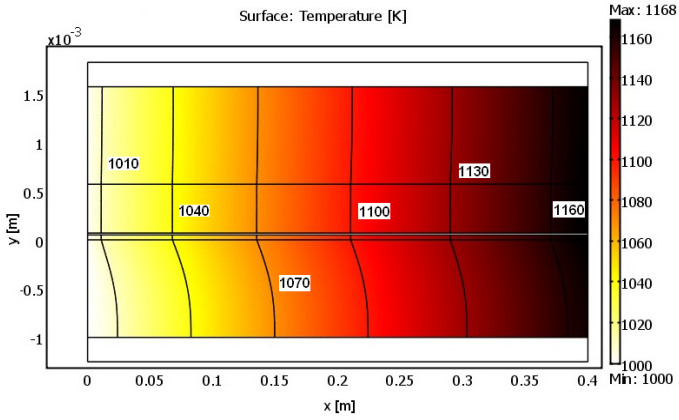


*Figure 12. Temperature distribution for co flow.*

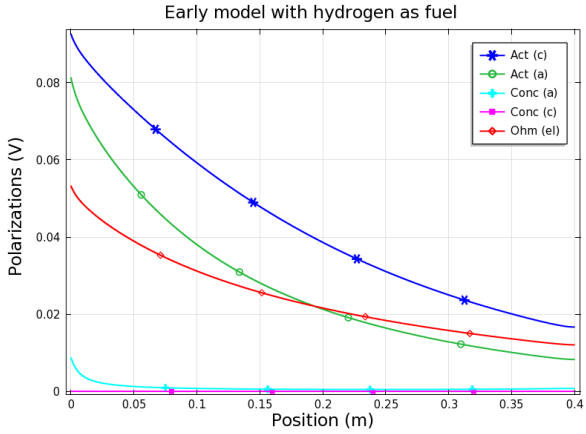


*Figure 13. Polarizations along the flow direction for co flow.*

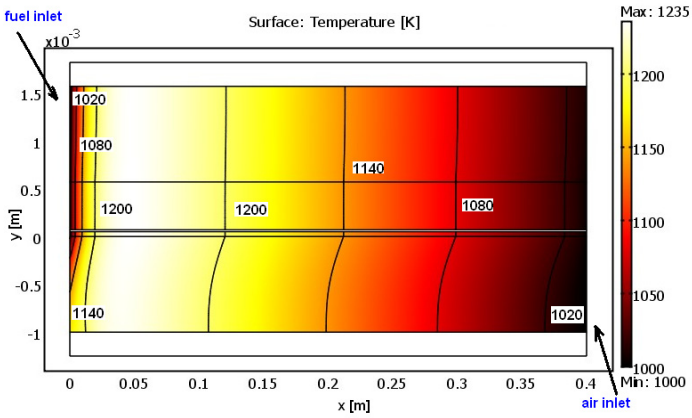


*Figure 14. The temperature distribution predicted for a counter flow.*

## 5.2 Extended models including internal reforming reactions of hydrocarbon fuels (papers III and IV)

The investigation performed in this part concerns biogas, pre-reformed- methanol, ethanol, and natural gas. The inlet mole fractions are specified in Table 9. The mole fractions based on initial SFs of 3 and 5 for methanol and ethanol are calculated from the experiments performed by Laosiripojana and Assabumrungrat [61]. It should be noted that the SF values in [61] corresponds to the parameters before the pre-reformer. After the pre-reforming of ethanol, the fuel mixture contains some ethylene and ethane. To simplify the calculation and because of the lack of kinetic data for the reforming of ethylene and ethane on Ni/YSZ catalyst, these concentrations are assumed to be methane. For the case of biogas, a small fraction of hydrogen is added to enable electrochemical reactions close to the inlet as well, and steam is added to avoid carbon deposition and to participate in the reforming reactions. The fuel composition for 30 % pre-reformed natural gas is defined by IEA [65] and is frequently used in literature, and also as the fuel inlet composition in chapters 5.3-5.5.

*Table 9. Fuel gas mole fractions at the cell inlet and related SF values.*

| | SF before reformer | SF before fuel cell | $H_2$ | CO | $CO_2$ | $CH_4$ | $H_2O$ |
|---|---|---|---|---|---|---|---|
| **Methanol** | 3 | 1.36 | 0.270 | 0.115 | 0.051 | 0.017 | 0.547 |
| **Methanol** | 5 | 1.90 | 0.247 | 0.072 | 0.042 | 0.011 | 0.628 |
| **Ethanol** | 3 | 0.66 | 0.359 | 0.114 | 0.030 | 0.112 | 0.385 |
| **Ethanol** | 5 | 1.04 | 0.312 | 0.081 | 0.036 | 0.080 | 0.491 |
| **Biogas steam mixture** | n/a | 0.87 | 0.03 | 0 | 0.27 | 0.36 | 0.34 |
| **30 % pre-reformed natural gas** | n/a | 1.07 | 0.263 | 0.0294 | 0.0436 | 0.171 | 0.493 |

The predicted temperature distribution for the case of pre-reformed methanol with an initial SF of 1.36 before the fuel steam enters fuel cell (and an SF of 3 before the reformer) can be seen in Figure 15. Increased SF means a slightly decreased temperature rise, due to a higher flow rate in the fuel channel, as presented in paper III. Note that the cooling from the air flow is significant, compared to the fuel flow. The temperature distribution for the case with pre-reformed natural gas is shown in Figure 16. This case contains more methane compared to that of pre-reformed methanol. A higher fraction of methane means a decreased temperature rise, due to heat consumption in the MSR. The overall temperature increase decreases compared to the model with only hydrogen as fuel (chapter 5.1), because of heat consumption from the MSR and because of a decreased cell length.

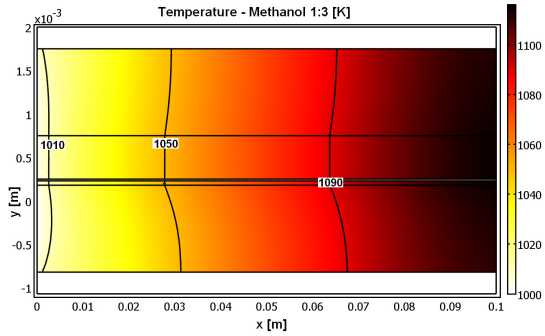


*Figure 15. Temperature distribution predicted for pre-reformed methanol (SF=1.36).*

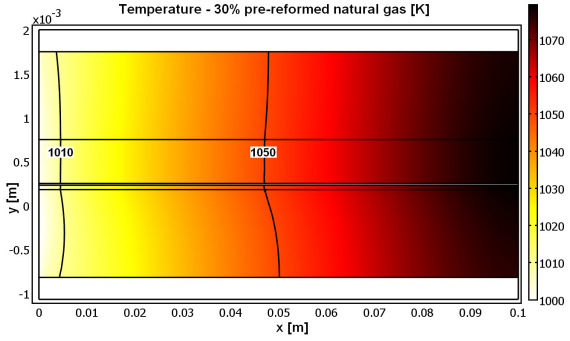


*Figure 16. Temperature distribution predicted for 30 % pre-reformed natural gas (SF=1.07).*

The predicted mole fractions for the participating gas-phase species in the fuel channel along the flow direction for the case with pre-reformed methanol (SF=1.36) and with 30 % pre-reformed natural gas are shown in Figure 17 and Figure 18, respectively. Hydrogen is consumed and water is generated (due to electrochemical reactions) along the flow direction. There is a consumption of water as carbon monoxide and methane are reformed. The mole fraction of carbon monoxide depends on the WGSR, which is normally assumed to be in equilibrium, as discussed in chapter 2.4.1. The hydrogen production depends mostly on the MSR rate, which depends on the activation energy, $AV_{MSR}$, local temperature and gas-phase species concentrations, as outlined in chapters 2.4.1 and 2.4.2. Note that the total amount of molecules (within the fuel

cell) increases as the MSR proceeds to the right. The case with pre-reformed methanol contains initially a relatively high fraction of carbon monoxide and the WGSR rate is fast (due to conditions far from equilibrium), which gives an initial increase of hydrogen and an initial decrease of water. The higher initial fraction of methane in the case with pre-reformed natural gas gives a lower outlet fraction of water (consumed both in the MSR and in the WGSR). There is some methane left in the outlet fuel stream for the case with natural gas, due to the high activation energy in the Klein kinetics applied in this study.

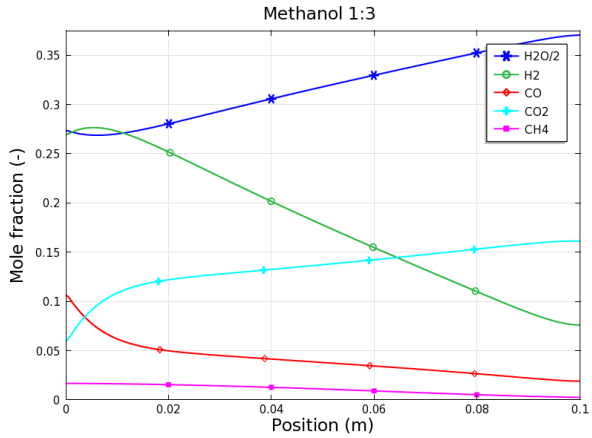


*Figure 17. Mole fraction of the fuel gas-phase species in the fuel channel along the flow direction for pre-reformed methanol (SF=1.36). Note that the scales on the y-axis are different and the value should be multiplied with 2 for water.*

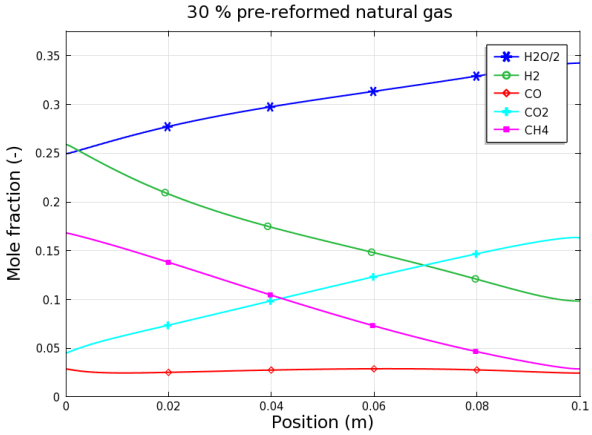


*Figure 18. Mole fraction of the gas-phase species in the fuel channel along the flow direction for 30 %-pre reformed natural gas (SF=1.07). Note that the scales on the y-axis are different as explained in Figure 17.*

The MSR rate in the anode for the case with pre-reformed methanol (SF=1.36) is shown in Figure 19. The fuel contains initially very little methane. This gives a low initial MSR rate,

which increases as the temperature is increased, and decreases as the concentration of methane decreases. The impact from the backward reaction rate, due to the consumption of carbon monoxide and hydrogen, is found to be neglible. As shown in Figure 20, high reaction rates for the WGSR are obtained when the inlet concentrations are far from equilibrium conditions in terms of temperature and concentrations, for example for the case with pre-reformed methanol (SF=1.36).

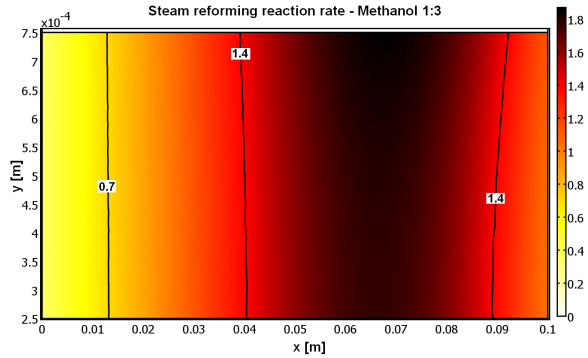


*Figure 19. MSR rate (in mol/(m$^3$s)) within the anode for pre-reformed methanol (SF=1.36).*

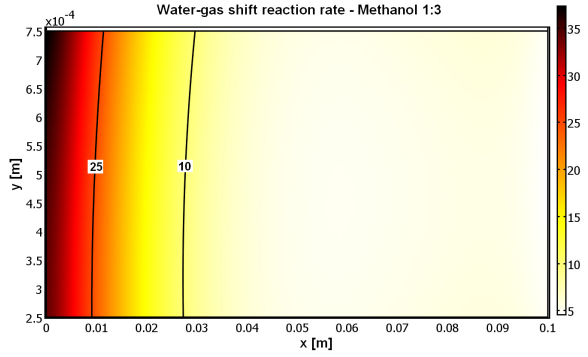


*Figure 20. WGSR rate (in mol/(m$^3$s)) within the anode for pre-reformed methanol (SF=1.36).*

In this section three different kinetic models, found in the open literature and presented in chapter 3.6, are applied and compared concerning the MSR kinetics within SOFCs. The fuel inlet composition is defined as 30 % pre-reformed natural gas. The reaction rates for both the MSR (Rr) and the WGSR (Rs) along the flow direction are plotted in Figure 21 and Figure 22, for Leinfelder's and Drescher's kinetics, respectively. It should be clearly noted that the reaction rates are only plotted for the entrance region, (0-0.01 m). Close to the inlet where the concentration of methane is high, the reaction rate for the MSR is high, because of the relatively low activation energy (both for Leinfelder and for Drescher), compared to the Klein kinetics employed above and in chapters 5.3-5.5 [67]. As shown in the figures, the reaction rates for the MSR (Rr) and the WGSR (Rs) are for Drescher's kinetics much faster than those for Leinfelder's kinetics, and consequently also compared to the Klein kinetics. Furthermore, more

hydrogen is produced when steam is generated in the electrochemical reactions, due to the fact that the WGSR is in equilibrium, as discussed in chapter 2.4.1. The large differences between the MSR kinetics show that the different kinetic models need to be evaluated on a more detailed level as they cannot correctly explain the complex surface-phase reactions by just a few empirical parameters, such as the activation energy. To fully understand the effect and dependence of the parameters, microscale modeling and/or more experimental investigations are needed. To draw confirmatory conclusions from modeling work, it is important to reveal the difference of the kinetic models from experimental work carried out on SOFC, not from a fuel reformer.

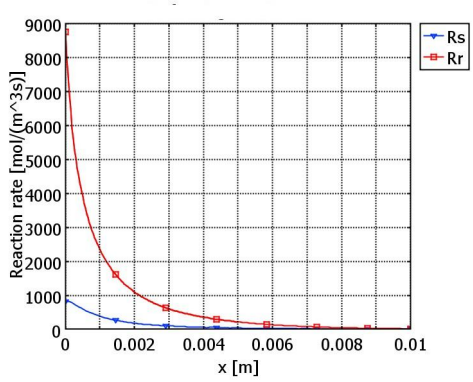


*Figure 21. Reforming reaction rate [mol/(m$^3$s)] for the entrance region (till 0.01m) in the anode along the flow direction for Leinfelder's kinetics.*

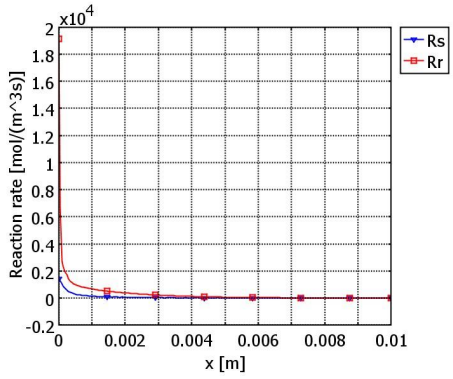


*Figure 22. Reforming reaction rate [mol/(m$^3$s)] for the entrance region (till 0.01m) in the anode along the flow direction for Drescher's kinetics.*

The effect on mole fraction distribution of the different gas-phase species is similar for both Achenbach & Riensche's (eqn (88)) and Leinfelder's (eqn (89)) kinetics and therefore only the mole fraction distribution by Leinfelder's kinetics is presented here in Figure 23. Methane reacts with steam at the surface of the Ni-catalyst in the anode which leads to production of carbon monoxide and hydrogen. The hydrogen is consumed at the TPBs for the electrochemical reactions. As shown in Figure 24, the prediction by Drescher's (eqn (90)) kinetics shows that the maximum mole fraction of hydrogen is bigger and obtained in a shorter distance from the inlet. The big differences in the reaction rates are due to the significantly different activation

energies and pre-exponential factors, as discussed in chapter 2.4.1. Both Leinfelder's and Drescher's kinetics are fast although the Drescher one, expressed by a Langmuir-Hinshelwood type, differs slightly more from the others. It deserves to be pointed out that Drescher's kinetics includes both positive and negative orders of the partial pressure of methane and water, as well as two different activation energies for the denominator and the numerator, which can have some effect on the reaction rates and other parameters.

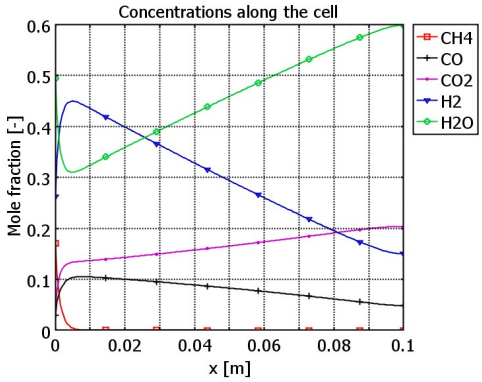


*Figure 23. Mole fraction of the gas-phases species in the fuel channel along the flow direction for Leinfelder's kinetics.*

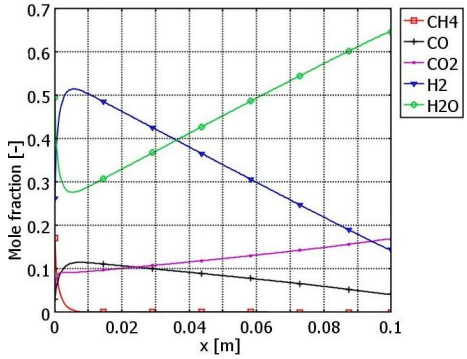


*Figure 24. Mole fraction of the gas-phase species in the fuel channel along the flow direction for Drescher's kinetics.*

## 5.3 Knudsen diffusion (paper V)

For the model described in chapters 5.1-5.2 only the ordinary diffusion, i.e., the collisions between the gas molecules themselves are considered. In this chapter (and for chapters 5.4-5.5 as well) the collisions between the molecules and the pore walls are also included, as defined in chapter 2.3.1. The fuel concentrations in this chapter are defined as 30 % pre-reformed natural gas (introduced in chapter 3.1). There is an obvious change of mole fraction distributions through the anode (y-direction) when Knudsen diffusion is considered in the model, as seen in Figure 25, compared to Figure 26 when only ordinary diffusion is considered. For the model without Knudsen diffusion, the changes in mole fractions through the anode are very small. As

Knudsen diffusion is included the transport resistance through the anode is significantly increased and the difference between the mole fractions at the anode-electrolyte interface and the ones at the anode-fuel channel interface is large. The consumption of methane and carbon monoxide in the MSR and WGSR result in a decreasing mole fraction as the distance to the fuel channel increases. Hydrogen is consumed at the TPB where the lowest faction is found, compared to water that is generated at the TPB, where it has its highest fraction. Carbon dioxide is produced within the anode and the fraction is lowest at the fuel channel interface. A lower fraction of hydrogen and a higher fraction of water at the TPB, compared to the model without Knudsen diffusion, give a decreased open circuit voltage and also higher concentration polarizations. The size of pores is at the same order as the gas mean free path, i.e., there are extra resistance in the porous material and the Knudsen diffusion may play an important role. Taking Knudsen diffusion into account is reasonable and necessary.

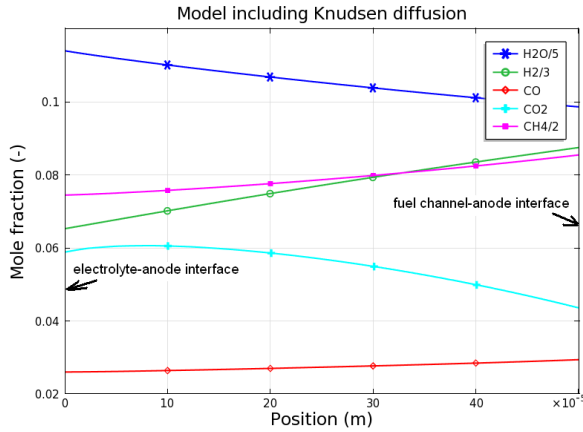


*Figure 25. Mole fraction distribution through the anode (y-direction) at the inlet as Knudsen diffusion is implemented in the model. Note that the scales on the y-axis are different and the value should be multiplied with 5, 3 and 2 for water, hydrogen and methane, respectively.*

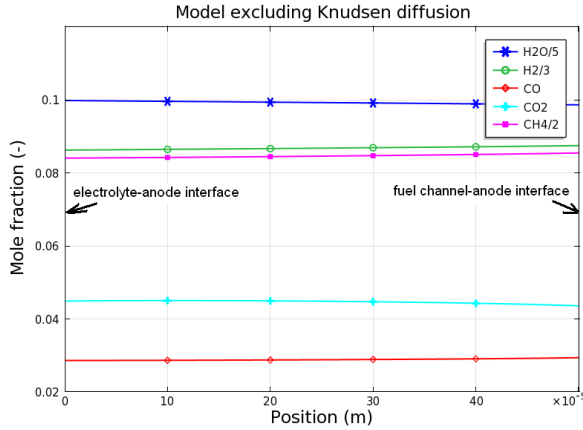


*Figure 26. Mole fraction distribution through the anode (y-direction) at the inlet if Knudsen diffusion is not included in the model. Note that the scales on the y-axis are different as explained in Figure 25.*

## 5.4 One-dimensional electrochemical model and validation (paper VII)

In this chapter my model is validated using experimental data from NIMTE, and also extended to evaluate the variable current density at the electrolyte-electrode interface along the flow direction (1D).

As a first step, the hydrogen-steam mixture ($x_{H2}$ : $x_{H2O}$ = 0.90 : 0.10) is applied, i.e., at the conditions similar to the experiments. The anode current density along the flow direction is presented in Figure 27, compared to earlier models where only an average value (0D) is implemented. The current density increases along the main flow direction as the temperature rises and this increase eases as the mole fraction of hydrogen within the anode decreases. A future step could adjust the parameter values for the active area, porosity and/or particle size along the flow direction to adequate the current density. The different polarizations within the cell are presented in Figure 28. It is found that the activation polarization corresponds to a majority of the polarizations and is larger in the cathode compared to the anode. The polarization because of the concentration differences is small. In earlier models (Figure 13) only an averaged current density is defined, compared to this model where a constant voltage is defined instead. The total polarizations decrease along the flow direction as the ideal voltage decrease, due to the temperature increase as well as the decrease in concentration of hydrogen in the fuel channel and oxygen in the air channel. An ion transport factor is implemented (as a part of the validation and described in chapter 4) to include the full distance the ions need to be transported from the anodic TPB to the cathodic TBP, i.e., the ion transport in the cathode and anode are also considered. This approach is further extended in chapter 5.5, where the electrochemical reactions are implemented as source terms instead of interface conditions.

The inlet fuel concentrations are further modified and defined as 30 % pre-reformed natural gas, as also for chapters 5.2-5.3 and 5.5. The anode current density along the flow direction (Figure 29) increases initially as the temperature increases and decreases as the mole fraction of hydrogen reduces. Note that the current density is significantly reduced for this case (the average reaches 2350 A/m$^2$), compared to the case with a hydrogen-steam mixture in Figure 27 (where the average is 4300 A/m$^2$). The current densities in Figure 27 and Figure 29 can be compared to the earlier models, where the same average value (3000 A/m$^2$) is used for both cases with a hydrogen-steam mixture (chapter 5.1) and more complex compositions such as the 30 % pre-reformed natural gas (chapters 5.2-5.3). It should be mentioned that it is assumed that the methane and carbon monoxide are completely reformed to hydrogen before the electrochemical reactions, only hydrogen and water are considered for the anodic ideal voltage calculation (as discussed in chapter 2.3.4). The polarizations occurring in this case are presented in Figure 30. The ideal voltage is lower for the case with pre-reformed natural gas compared to the case with only hydrogen and steam (Figure 28), because the mole fraction of hydrogen is lower and the mole fraction of steam is higher (to avoid carbon deposition within the anode). This gives a lower value of the total polarizations, because the cell voltage is defined as the same constant value of 0.7 V. The same trend for the other polarizations is found, except for the anode concentration polarization, where a lower fraction of hydrogen gives higher polarizations.

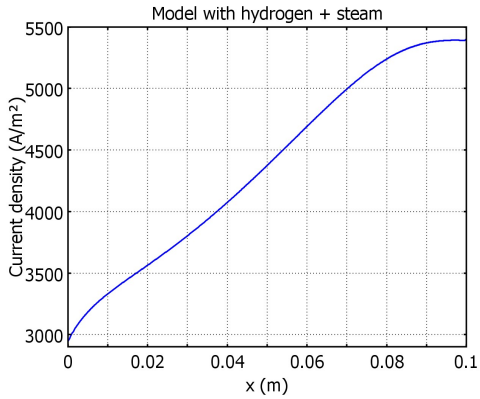


*Figure 27. Current density distribution predicted along the flow direction with hydrogen and steam mixture in the fuel stream.*

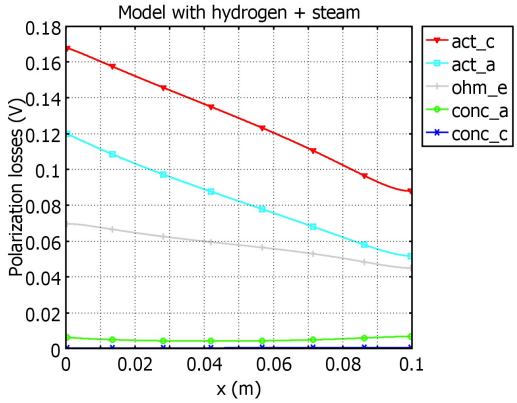


*Figure 28. Prediction of different polarizations along the flow direction with hydrogen and steam mixture in the fuel stream.*

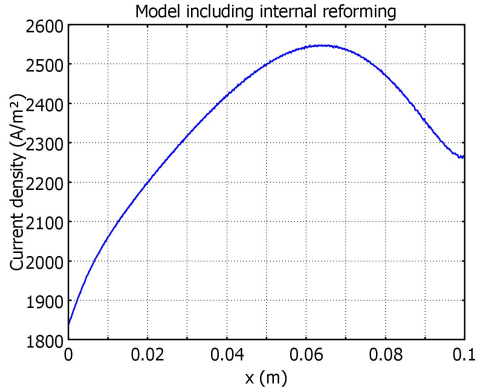


*Figure 29. Current density distribution along the flow direction for the model with natural gas in the fuel stream.*

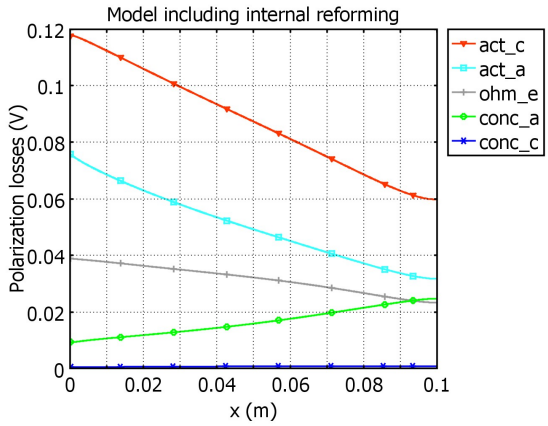


*Figure 30. Different polarizations along the flow direction for the model with natural gas in the fuel stream.*

## 5.5 Two-dimensional electrochemical model with charge transport (paper VIII)

In this chapter the governing equations for ion and electron transport are included, i.e., the electrochemical model is extended to 2D (along the flow direction and the cross section normal to the flow direction through the electrodes and electrolyte), to include ion current density distribution in the electrolyte and electrodes, and electron current density distribution in the electrodes. A standard case is introduced, where the fuel utilization is 70 %, the oxygen utilization is 18 %, the inlet temperature is 1010 K and the inlet fuel is defined as 30 % pre-reformed natural gas.

The ion current density along the y-direction (i.e., the cross-section normal to the flow direction) is shown in Figure 31 at inlet and outlet. For the standard case the current density distribution shows a similar behavior at inlet and outlet, because the decrease of ideal voltage due to the temperature increase and the consumption of fuel and oxygen are compensated by an increase of the current density as the cell temperature is increased. It can be seen that the current density gradients are steeper on the cathode side, than on the anode side. In this model the volume fractions of the solid materials and pores as well as the tortuosities are accounted for, to better describe the realistic transport distances for ions and electrons within the anode and the cathode. The electrochemical reactions occur within a few micrometers close to the electrode-electrolyte interface, as shown in Figure 31. It is found that the electrochemical reaction zone is only 2.4 μm deep, into the active region from the interface, in the cathode, and 6.2 μm in the anode. This zone is defined as where the ion current density is higher than 300 A/m², i.e., around 10 % of the maximum value at the inlet for the standard case. The depth of the electrochemically active reaction zones is quite small compared to the designed active layers with a finer structure and a higher surface area than the ones in the buffer layers. As mentioned above, for the NIMTE standard cell, the thickness of the active layers is 20 μm and 15 μm for the cathode and the anode, respectively.

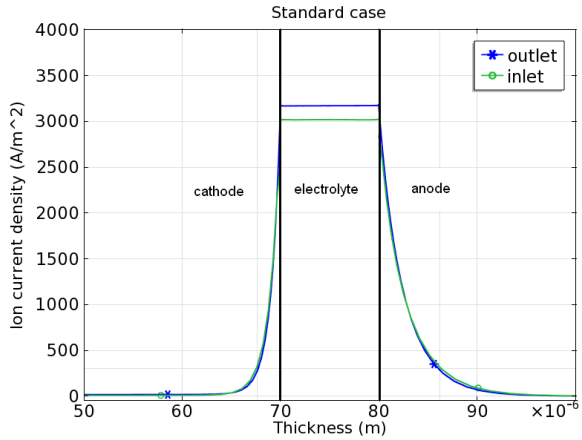


*Figure 31. Profile of ion current density (A/m$^2$). Note that for the anode and cathode, only the parts (20 μm) closest to the electrolyte interface are highlighted in the figure and the "zero" is assigned at the air channel-cathode interface.*

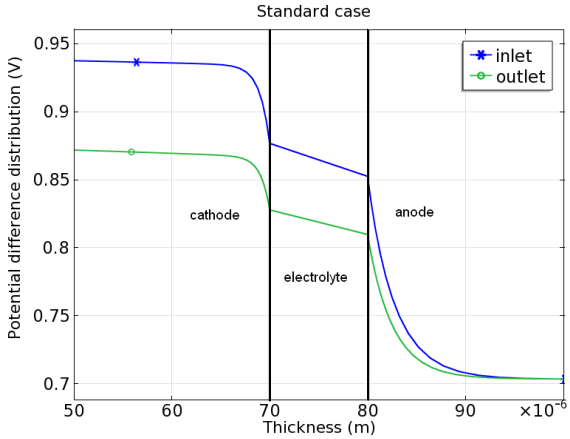


*Figure 32. Potential difference distribution..*

The profile of potential difference is shown in Figure 32 for the positions close to the inlet and the outlet. The ideal voltage decreases along the flow direction due to both the temperature increase and the consumption of fuel and oxygen. It can be revealed from Figure 32 that around 60 % of the polarizations occur in the anode, 10 % in the electrolyte and 30 % in the cathode, i.e., any efforts to improve the fuel cell performance should be focused on decreasing the activation polarization or improving the volumetric current density on the anode side. These findings are different compared to our previous predictions (chapters 5.1-5.4), where the electrochemical reactions are defined at the electrode-electrolyte interfaces only (i.e., ionic resistance within the electrodes are neglected) and the cathodic activation polarization dominates over the anodic one. The ion transport in the anode and cathode are partly included in chapter 5.4 with the concept of the ion transport factor and the electrochemical reactions defined as interface conditions. The difference, in polarizations compared to previous models, might be partially due to a larger active TPB $AV_e$ applied on the cathodic side ($2.6 \cdot 10^6$ m$^2$/m$^3$)

compared to the anode side ($1.3 \cdot 10^5$ $m^2/m^3$). This makes the electrochemical reaction zone thinner within the cathode. As a result the current density per active TPB area is lower in the cathode (1400 $A/m^2$ as a maximum value at the interface), compared to the anode (9400 $A/m^2$). This gives lower activation polarizations on the cathode side. However the current density per unit volume is higher on the cathode side ($3.6 \cdot 10^9$ $A/m^3$ as a maximum value at the interface), compared to the anode side ($1.5 \cdot 10^9$ $A/m^3$). Note that the different $AV_e$, within the anode and cathode, appear from the validation implementing the expressions for exchange current density used by Patcharavorachot *et al.* [52] and Aguiar *et al.* [91]. Implementing different expressions for the exchange current density may result in other values for $AV_e$.

The activation polarizations along the flow direction (x-direction) within the anode and the cathode for the standard case are shown in Figure 33. These can be compared with the ones predicted by our previous model (Figure 30 in chapter 5.4), where the electrochemical reactions as well as the activation and concentration polarization are defined as interface conditions at the electrode-electrolyte interfaces. For both models, the cell voltage is defined to 0.7 V and a similar trend is found, i.e., the total polarization decreases along the flow direction (as the temperature increases) and the activation polarizations dominate, compared to the ohmic and the concentration polarizations. However, in this study, the activation polarization on the anode side is bigger than that on the cathode side, partially due to the different $AV_e$ implemented, as discussed in the previous paragraph. This effect was not included when the electrochemical reactions were defined at the electrode-electrolyte interface in our earlier models (chapters 5.1-5.4). The activation polarization distributions represent the biggest difference between the models. It should be noted that in the current model, the current density per active area and the activation polarization are highest at the electrode-electrolyte interface and decreases rapidly within the electrodes as the distance to the interface increases. On the other hand, the ohmic polarization for the ion transfer increase, within the electrodes, at positions away from the interface. The couplings between the different polarizations are defined in chapter 2.3.4. Also the variation in the ionic polarization through the electrolytes (y-direction in the model) was neglected in the previous models. This comparison clearly shows that the impact of including the detailed charge-transfer reactions and polarizations is significant, despite that a few micrometer thin reaction zone appeared in both anode and the cathode.

As a parameter study, the inlet temperature is increased by 25 K (to 1035 K) to investigate its influence on the cell performance. The fuel and air flow rates are kept constant, i.e., the fuel and air utilizations vary, as compared to the standard case above. The ion current density (in Figure 34) increases as the inlet temperature increases, with a maximum value of around 3950 $A/m^2$ at the inlet and 3750 $A/m^2$ at the outlet. For the standard case the maximum value is around 3000 $A/m^2$ at the inlet and 3200 $A/m^2$ at the outlet. The increase in ion current density is due to the decreased polarizations and the increased hydrogen concentration, mostly from the MSR by an initially higher hydrogen production. The lower ion current density at the outlet, compared to that at the inlet, is because of a lower concentration of hydrogen at the outlet. The depth of the electrochemically active zones increases slightly to 2.5 μm and 6.3 μm for the cathode and anode, respectively. The corresponding values are 2.4 μm and 6.2 μm for the standard case. It should be noted that the reaction zone is slightly thicker at the inlet compared to the one at the outlet, and the values mentioned here are the averaged ones. The fuel utilization reaches 85 % for this case, compared to 70 % for the standard case.

Normally the air flow rate is adjusted to make sure that the cell receives sufficient cooling to keep a specific temperature. The air flow rate is, in this study, reduced by 20 % to examine the impact on the cell performance. Decreased air flow rates mean decreased cooling and may cause a higher outlet temperature. The ion current density close to the outlet increases (with a

maximum value of around 3600 A/m²), as shown in Figure 35, mainly due to an increased outlet temperature, compared to the standard case (with a maximum value of 3200 A/m²) in Figure 31. It should be mentioned that the current density at the inlet is the same as for the standard case. Also the depth of the electrochemically active zones is the same as for the standard case, i.e., 2.4 µm and 6.2 µm for the cathode and anode, respectively. The fuel utilization reaches 75 %, compared to 70 % for the standard case. The increase in fuel utilization is due to a higher methane conversion, because the temperature within the cell is increased. The outlet concentrations of hydrogen and carbon monoxide are similar to the standard case. The air utilization equals 23 % compared to 18 % for the standard case.

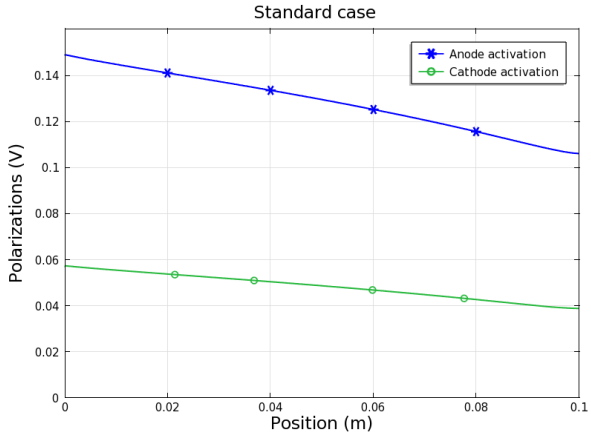


*Figure 33. Activation polarization along the flow direction in the anode and cathode.*

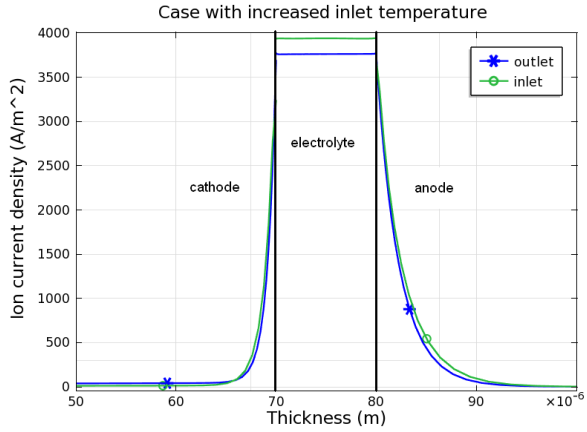


*Figure 34. Ion current density (A/m$^2$) for the case with increased inlet temperatures (1035 K).*

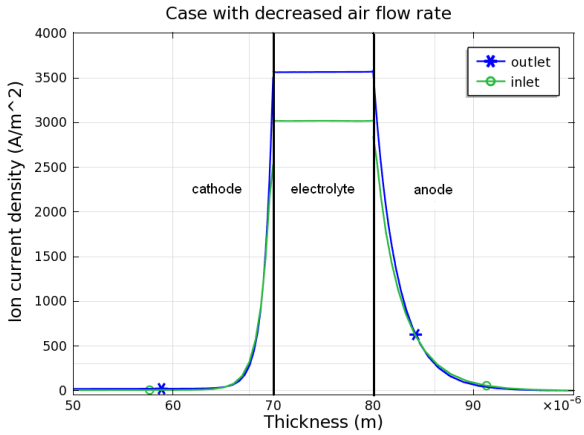


*Figure 35. Ion current density (A/m$^2$) for the case with a decreased air flow rate.*

The ionic tortuosities within the anode and the cathode are, for a parameter study, decreased from 10 for the standard case to 5 to investigate the influence on the cell performance. The electrochemical reaction zones increase to 3.8 µm on the cathode side and 9.5 µm on the anode side (as shown in Figure 36). For the standard case these are 2.4 µm and 6.2 µm, respectively. In other words, the total active area available for the electrochemical reactions increases (since the $AV_e$ is the same). A higher ionic tortuosity means an increased ionic resistance in the electrode. The maximum current density at the inlet is about 4050 A/m², compared to 3000 A/m² for the standard case (Figure 31), and at the outlet 3500 A/m² (compared to 3200 A/m²). The current density at the outlet is lower than at the inlet, because the fuel utilization increases to 82 % (compared to 70 % for the standard case) and the mole fraction of hydrogen is lower close to the outlet (the minimum value reaches 0.06 compared to 0.12 for the standard case).

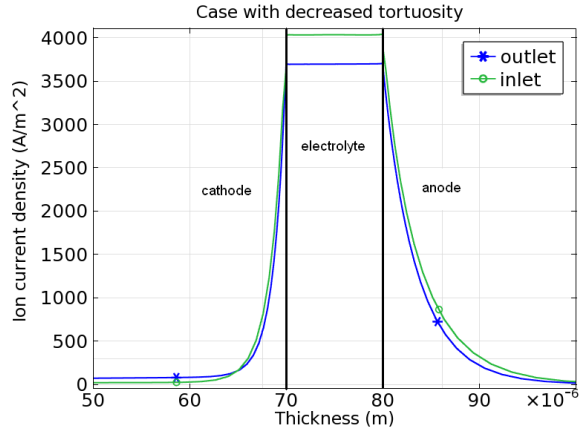


*Figure 36. Ion current density (A/m$^2$) for the case with decreased ionic tortuosity.*

# 6 Conclusions

The fuel cell is not a new invention, since the principle dates back to 1838. However the fuel cell technology is approaching the commercial phase, the potential for the future is enormous and fuel cells can be key components in a future sustainable energy system. To achieve this, the production cost must be decreased and the life length, the resistance to contaminants as well as the understanding of the physical phenomena occurring within the cell must be increased. When hydrogen or other suitable renewable fuels are used as fuel, there are no net emissions of greenhouse gases.

CFD approaches (with the finite element model and the software COMSOL Multiphysics) are developed and implemented to analyze various chemical and physical phenomena, which take place inside a single cell anode-supported SOFC. Equations for gas-phase species, heat, momentum, ion and electron transport are solved simultaneously by coupling with kinetic expressions for electrochemical and internal reforming reactions appearing in various domains. The Darcy-Brinkman equation enables continuous pressure and velocity fields over the electrode-gas channel interfaces. Correlations for a more realistic description of the transport of ions and electrons within the anode and the cathode are included. The ion/electron transport pathways are evaluated by accounting for volume fractions of the specific materials- and pores, as well as ionic/electronic tortuosities. The model relies on experimental data from a standard cell developed at Ningbo Institute of Material Technology & Engineering (NIMTE) in China.

Understanding of the MSR and catalyst materials structure is expected to be of significant importance for further SOFC development. The reforming reaction rates are either described by a global kinetics approach or by a more detailed approach describing elementary surface-phase reactions kinetics. It is found that the reaction orders and the activation energies vary significantly between the different global models presented in the open literature. Different mechanisms considering the elementary surface-phase kinetics are available, but there is a disagreement considering the involved pathways, intermediate species and rate-limiting reactions. Microscale modeling as well as further experimental investigations are required to increase the knowledge related to the surface-phase reforming reactions within SOFC anodes.

The governing equation for gas-phase species transport accounts for both ordinary diffusion (collisions between gas molecules themselves) and Knudsen diffusion (collisions between gas molecules and the pore walls). There is an obvious change of concentration distribution within the anode, due to the extra resistance in the porous materials because the size of pores is at the same order as the mean free path, i.e., the Knudsen diffusion plays an important role within SOFC anodes. Thinner anodes reduces the diffusion length and transport resistance, however the active surface area for the MSR is simultaneously reduced.

Both LTNE and LTE approaches are developed and it is found that, for the specific design and operating conditions applied in this work, the temperature difference between the gas- and the solid-phases within the porous electrodes is neglible. Heat is generated due to ohmic, activation

and concentration polarizations within the electrolyte and electrodes as well as change of entropy in the cathodic electrochemical reactions. Heat is consumed due to the change of entropy in the anodic electrochemical reactions and in the internal steam reforming reactions within the anode. The heat, which is generated within the cell, can also be used for external reforming reactions and pre-heating of the fuel and air flows outside the cell. It is revealed that for the counter flow design the inlet temperature of the fuel stream needs to be close to the outlet temperature of the air stream to avoid too high temperature gradients close to the fuel stream inlet. The cell current density can be increased by increasing the operating temperature. However, a too high maximum temperature or temperature gradient decreases the cell life time. An increased air flow can reduce the temperature increase, and as a result a higher current density can be withdrawn from the cell, with a constant voltage. If the air flow is increased some extra energy is externally needed for the air-pump and a bigger heat exchanger area for the pre-heating is required.

The electrochemical model is extended from zero-dimension (with only an average value defined) in the early models, to one-dimension covering the current density variation along the flow direction. Finally a two-dimensional approach including the current density distribution, along the flow direction and through the electrolyte-electrodes, is developed and coupled to the governing equations for heat, gas-phase species, momentum and charge transport. The activation polarization is the most significant among the different polarizations. As the electrochemical model is extended from one- to two-dimension, the activation polarization within the cathode becomes less important than the one within the anode. This difference might be explained by different current density per (active TPB) area and variable area-to-volume-ratios for the electrochemical reactions within the anode and cathode, respectively. This work reveals that the electrochemical reactions occur within only a few micro meters from the electrode-electrolyte interface, for instance, for the two-dimensional electrochemical model (standard case) 90 % of the electrochemical reactions occur within 2.4 μm in the cathode and 6.2 μm in anode from the electrode-electrolyte interface. The predicted current density gradient is steeper on the cathode side, compared to the anode side, and it is found that around 60 % of the polarizations occur in the anode, 10 % in the electrolyte and 30 % in the cathode. The current density and the activation polarization are highest at the electrolyte-electrode interface and decreases rapidly within the electrodes as the distance from the interface increases. However, ohmic polarization by ion transfer increases for the positions away from the interface.

# 7 Future Work

The fuel cell is not a new invention, because its principle dates back to 1838. However, the fuel cell technology is approaching the commercial phase, the potential for the future is enormous and the fuel cell can be a key component in a future sustainable energy system. To achieve this, the production cost must be decreased and the life length must be increased. The needed improvements will be accelerated from mass production requirements. One way to decrease the cost and also increase the life time is to increase the understanding of multiscale transport- and reaction phenomena within the cell.

Fuel cell operation depends on the complex interactions between multi-physics such as fluid flow, species, heat, ion and electron transport, as well as electrochemical and internal reforming reactions. Coupling of these phenomena, i.e., multiscale modeling is promising for future fuel cell research. Micro- and macroscale physical phenomena and chemical reactions could be captured in details. The implementation of ion transport in the electrolyte and the YSZ materials, and electron transport in the electrodes in this work reveals the importance of an understanding of the detailed phenomena occurring at the TPB. Further development of the couplings between the microscale phenomena at the TPB and the macroscale cell scale model is promising for an increased exchange current density per area and also an increased total area.

The models, described in this thesis, consider hydrogen, water, methane, carbon monoxide and carbon dioxide in the fuel stream. It is of interest to include other fuels, such as methanol and ethanol or hydrocarbons with longer carbon chains as well, in terms of kinetics considering an extended amount of reforming reactions and the effects on transport processes. It is assumed that carbon monoxide is reformed before it participates in any electrochemical reaction, and it is not considered in the ideal voltage evaluation. It is expected that lifting these limitations will give an increased knowledge concerning the processes at the TPBs. The reforming and the electrochemical reaction rates are dependent on the temperature, the concentrations, the type and the amount of catalyst available. It is expected that a model including the catalytic surface-phase reactions (instead of global kinetics expressions used in this thesis) will be valuable for future fuel cell development, in terms of optimized active surface areas with a decreased activation energies, i.e., faster reaction rates and an increased active area for the electrochemical as well as internal reforming reactions. The radiative heat transfer within the cell or from the cell/stack to the surroundings is not included in the models presented in this work, but might be reasonable for future studies. The thermal conductivity and dynamic viscosity covering gas-phase mixtures are implemented by mole fraction averaging. Implementation of more accurate expressions may be interesting for an extension of the model.

The validation described in this work is isothermal and only hydrogen and steam on the fuel side are included. An extended experimental study, which also includes the temperature variation along the flow direction and/or the effects of methane, carbon monoxide and carbon dioxide, and even of fuels, such as methanol, ethanol, or any fuel with a longer carbon chain, will increase the scientific value of the model validation.

# 8 References


[1] Li P.W., Schaefer L., Chyu M.K., Multiple Transport Processes in Solid Oxide Fuel Cells, Chapter 1 in Sundén B., Faghri M. (eds), Transport Phenomena in Fuel Cells, WIT Press, ISBN 9781853128400, UK, 2005.

[2] Yuan J., Faghri M., Sundén B., On Heat and Mass Transfer Phenomena in PEMFC and SOFC and Modelling Approaches, Chapter 4 in Sundén B., Faghri M. (eds), Transport Phenomena in Fuel Cells, WIT Press, ISBN 9781853128400, UK, 2005.

[3] Fuel Cell Handbook (the seventh edition), EG&G Technical Services Inc., U.S. Department of Energy, Morgantown, Virginia, USA, 2004.

[4] Saxe M., Bringing Fuel Cells to Reality and Reality to Fuel Cells, Doctoral Thesis, Department of Chemical Sciences and Engineering, Royal Institute of Technology, ISBN 9789174151084, Sweden, 2008.

[5] Kemm M., Dynamic Solid Oxide Fuel Cell Modelling for Non-steady State Simulation of System Applications, Doctoral Thesis, Department of Energy Sciences, Lund University, ISBN 9162869817, Sweden, 2006.

[6] Schönbein C.F., Further Experiments on the Current Electricity Excited by Chemical Tendencies, Independent of Ordinary Chemical Action, *The London and Edinburgh Philosophical Magazine and Journal of Science*, **12**, pp. 311-317, 1838.

[7] Schönbein C.F., On the Voltaic Polarization of certain Solid and Fluid Substances, *The London and Edinburgh Philosophical Magazine and Journal of Science*, **14**, pp. 43-45, 1839.

[8] Grove W.R, On Voltaic Series and the Combination of Gases by Platinum, *The London and Edinburgh Philosophical Magazine and Journal of Science*, **14**, pp. 127-130, 1839.

[9] Grove W.R, On a Gaseous Voltaic Battery, *The London, Edinburgh and Dublin Philosophical Magazine and Journal of Science*, **21**, pp. 417-420, 1842.

[10] Chen E., History, Chapter 2 in Hoogers G. (ed.), Fuel Cell Technology Handbook, CRC Press LLC, ISBN 9780849308772, USA, 2003.

[11] Baur E., Preis H., Über Brennstoff-Ketten mit Festleitern (in German), About Fuel-Chains with Fixed Ladders (title translated to English), *Z. Elektrochemie und angewandte physikalische Chemie*, **43**, pp. 727-732, 1937.

[12] Prospects for Hydrogen and Fuel Cells, International Energy Agency, OECD Publiching, ISBN 9789264109575, Paris, France, 2005.

[13] Aicher T., Lenz B., Gschnell F., Groos U., Federici F., Caprile L., Parodi L., Fuel Processors for Fuel Cell APU Applications, *J. Power Sources*, **154**, pp. 503-508, 2006.

[14] Cutillo A., Specchia S., Antonini M., Saracco G., Specchia V., Diesel Fuel Processor for PEM Fuel Cells: Two Possible Alternatives (ATR versus SR), *J. Power Sources*, **154**, pp. 379-385, 2006.

[15] Jannash A.-K., Möjlighet och Potential för Bränslecellssystem för Energiförsörjning i Byggnader (in Swedish) Possibilities and Potential Concerning Fuel Cell Systems for Energy Supplies in Buildings (title translated to English), Catator AB, Lund, Sweden, 2011.

[16] Zhu H., Kee R., Janardhanan V., Deutschmann O., Goodwin D., Modeling Elementary Heterogeneous Chemistry and Electrochemistry in Solid-Oxide Fuel Cells, *J. Electrochem. Soc.*, **152**, pp. A2427-A2440, 2005.

[17] Gooenough J.B., Huang Y., Alternative Anode Materials for Solid Oxide Fuel Cells, *J. Power Sources*, **173**, pp. 1-10, 2007.

[18] Ni M., Leung M.K.H., Leung D.Y.C., Micro-Scale Modeling of Solid Oxide Fuel Cells with Micro-structurally Grades Electrodes, *J. Power Sources*, **168**, pp. 369-378, 2007.

[19] Janardhanan V., Deutschmann O., CFD Analysis of a Solid Oxide Fuel Cell with Internal Reforming: Coupled Interactions of Transport, Heterogeneous Catalysis and Electrochemical Processes**,** *J. Power Sources*, **162**, pp. 1192-1202, 2006.

[20] Kumar V., Arora A., Pandey O.P., Singh K., Studies on Thermal and Structural Properties of Glasses as Sealants for Solid Oxide Fuel Cells, *Int. J. Hydrogen Energy*, **33**, pp. 434-438, 2008.

[21] Suzuki K., Iwai H., Nishino T., Electrochemical and Thermo-Fluid Modelling of a Tubular Solid Oxide Fuel Cell with Accompanying Indirect Internal Fuel Reforming, Chapter 3 in Sundén B., Faghri M. (eds), Transport Phenomena in Fuel Cells, WIT Press, ISBN 9781853128400, UK, 2005.

[22] Kakac S., Pramuanjaroenkij A., Zhou X.Y., A Review of Numerical Modeling of Solid Oxide Fuel Cells, *I. J. Hydrogen Energy*, **32**, pp. 761-786, 2007.

[23] Wang W.G. Guan W.B., Li H.M., Xue Y.J., Wang J.X., Wu Y.N., Wang J., Liu K., SOFC Research and Development at NIMTE, *Proceedings of the 8th European Fuel Cell Forum*, Lucerne, Switzerland, 2008.

[24] Inagaki T., Nishiwaki F., Knaou J., Yamasaki S., Hosoi K., Miyazawa T., Yamanda M., Komada N., Demonstration of High Efficiency Intermediate-Temperature Soild Oxide Fuel Cell Based on Lanthanium Gallate Electrolyte, *J. Alloys and Compounds*, **408-412**, pp. 512-517, 2006.

[25] Li T.S., Wang W.G., Chen T., Miao H., Xu C., Hydrogen Sulfide Poisoning in Solid Oxide Fuel Cells under Accelerated Testing Conditions, *J. Power Sources*, **195**, pp. 7025-7032, 2010.

[26] Liu Q.L., Khor K.A., Chan S.H., High Performance Low-Temperature Solid Oxide Fuel Cell with Novel BSCF Cathode, *J. Power Sources*, **161**, pp. 123-128, 2006.

[27] Suzuki T., Yamaguchi T., Fujishiro Y., Awano M., Fabrication and Characterization of Micro Tubular SOFCs for Operation in the Intermediate Temperature, *J. Power Sources*, **160**, pp. 73-77, 2006.

[28] Cocco D., Tola V., Use of Alternative Hydrogen Energy Carriers in SOFC-MGT Hybrid Power Plants, *En. Con. Man.*, **50**, pp. 1040-1048, 2009.

[29] Mignard D., Pritchard C., On the Use of Electrolytic Hydrogen from Variable Renewable Energies for the Enhanced Conversion of Biomass to Fuels, *Chem. Eng. Research and Design*, **86**, pp. 473-487, 2008.

[30] Xuan J., Leung M.K.H., Leung D.Y.C., Ni M., A Review of Biomass-derived Fuel Processors for Fuel Cell Systems, *Renewable and Sustainable Energy Reviews*, **13**, pp. 1301-1313, 2009.

[31] Ni M., Leung M.K.H, Leung D.Y.C., Ammonia-Fed Solid Oxide Fuel Cells for Power Generation - A Review, *Int. J. Energy Res.*, **33**, pp. 943-959, 2009.

[32] Cimenti M., Hill J.M., Thermodynamic Analysis of Solid Oxide Fuel Cells Operated with Methanol and Ethanol under Direct Utilization, Steam Reforming, Dry Reforming or Partial Oxidation Conditions, *J. Power Sources*, **186**, pp. 377-384, 2009.

[33] Laosiripojana N., Sutthisripok W., Assabumrungrat S., Synthesis Gas Production from Dry Reforming of Methane over $CeO_2$ Doped Ni/$Al_2O_3$: Influence of the Doping Ceria on the Resistance toward Carbon Formation, *Chem. Eng.*, **112**, pp. 13-22, 2005.

[34] Nam J.H., Jeon D.H., A Comprehensive Micro-scale Model for Transport and Reaction in Intermediate Temperature Solid Oxide Fuel Cells, *Electrochim. Acta*, **51**, pp. 3446-3460, 2006.

[35] Haile S.M., Fuel Cell Materials and Components, *Acta Mater.*, **51**, pp. 1981-2000, 2003.

[36] Yuan J., Sundén B., Analysis of Chemically Reacting Transport Phenomena in an Anode Duct of Intermediate Temperature SOFCs, *ASME J. Fuel Cell Sci. Technol.*, **3**, pp. 687-701, 2006.

[37] Janardhanan V.M., Heuveline V., Deutschmann O., Three-Phase Boundary Length in Solid-Oxide Fuel Cells: A Mathematical Model, *J. Power Sources*, **178**, pp. 368-372, 2008.

[38] Murzin D.Y., Salmi T., Catalytic Kinetics, Elsevier Science, ISBN 9780444516053, the Netherlands, 2005.

[39] Reid R.C., Prausnitz J.M., Poling B.E., The Properties of Gases & Liquids, Fourth Edition, R.R. Donnelley & Sons Company, ISBN 9780070517998, USA, 1986.

[40] Yuan J., Huang Y., Sundén B., Wang W.G., Analysis of Parameter Effects on Chemical Reaction Coupled Transport Phenomena in SOFC Anodes, *Heat Mass Transfer*, **45**, pp. 471-484, 2009.

[41] Bove R., Ubertini S., Modeling Solid Oxide Fuel Cell Operation: Approaches, Techniques and Results, *J. Power Sources*, **159**, pp. 543-559, 2006.

[42] Asinari P., Quaglia M.C., von Sakovsky M.R., Kasula B.V., Direct Numerical Calculation of the Kinematic Tortuosity of Reactive Mixture Flow in the Anode Layer of Solid Oxide Fuel Cells by the Lattice Boltzmann Method, *J. Power Sources,* **170**, pp. 359-375, 2007.

[43] Cayan N., Pakalapati S., Elizalde-Blancas F., Celik I., On Modeling Multi-Component Diffusion Inside the Porous Anode of Solid Oxide Fuel Cells using Fick's Model, *J. Power Sources*, **192**, pp. 467-474, 2009.

[44] le Bars M., Grae Worster M., Interfacial Conditions Between a Pure Fluid and a Porous Medium: Implications for Binary Alloy Solidification, *J. Fluid Mech.*, **550**, pp.149-173, 2006.

[45] COMSOL Multiphysics 4.1 user guide, Stockholm, Sweden, 2010.

[46] Todd B., Young J.B., Thermodynamic and Transport Properties of Gases for Use in Solid Oxide Fuel Cell Modeling, *J. Power Sources*, **110**, pp. 186-200, 2002.

[47] Lister S., Djilali N., Two-Phase Transport in Porous Gas Diffusion Electrodes, Chapter 5 in Sundén B., Faghri M. (eds), Transport Phenomena in Fuel Cells, WIT Press, ISBN 9781853128400, UK, 2005.

[48] Damm D.L., Fedorov A.G., Radiation heat transfer in SOFC Materials and Components, *J. Power Sources*, **143**, pp. 158-165, 2005.

[49] Boder M., Dittmeyer R., Catalytic Modification of Conventional SOFC Anodes with a View to Reducing Their Activity for Direct Internal Reforming of Natural Gas, *J. Power Sources*, **155**, pp. 13-22, 2006.

[50] Damm D.L., Fedorov A.G., Local Thermal Non-Equilibrium Effects in Porous Electrodes of the Hydrogen Fueled SOFC, *J. Power Sources*, **159**, pp. 1153-1157, 2006.

[51] Pramuanjaroenkij A., Kakac S., Zhou X.Y., Mathematical Analysis of Planar Solid Oxide Fuel Cells, *Int. J. Hydrogen Energy*, **33**, pp. 2547-2565, 2008.

[52] Patcharavorachot Y., Arpornwichanop A., Chuachuebsuk A., Electrochemical Study of a Planar Solid Oxide Fuel Cell: Role of Support Structures, *J. Power Sources*, **177**, pp. 254-261, 2008.

[53] Winkler W., Nehter P., Thermodynamics of Fuel Cells, *Fuel Cells and Hydrogen Energy*, **1**, pp. 15-50, 2008.

[54] Chan S.H., Low C.F., Ding O.L., Energy and Exergy Analysis of Simple Solid-Oxide Fuel-Cell Power Systems, *J. Power Sources*, **103**, pp. 188-200, 2002

[55] Ferguson J.R., Fiard J.M., Herbin R., Three Dimensional Numerical Simulation for Various Geometries of Solid Oxide Fuel Cells, *J. Power Sources*, **58**, pp. 109-122, 1996.

[56] Hajimolana S.A., Hussain M.A., Daud W.M.A.W., Soroush M., Shamiri A., Mathematical Modeling of Solid Oxide Fuel Cells: A Review, *Renewable and Sustainable Energy Reviews*, **15**, pp. 1893-1917, 2011.

[57] Kanno D., Shikazono N., Takagi N., Matsuzaki K., Kasagi N., Evaluation of SOFC Anode Polarization Simulation Using Three-Dimensional Microstructures Reconstructed by FIB Tomography, *Electrochim. Acta*, **56**, pp. 4015-4021, 2011.

[58] Vivet N., Chupin S., Estrade E., Piquero T., Pommier P.L., Rochais D., Bruneton E., 3D Microstructure Characterization of a Solid Oxide Fuel Cell Anode Reconstructed by Focused Ion Beam Tomography, *J. Power Sources*, **196**, pp. 7541-7549, 2011.

[59] Dokmaingam P., Assabumrungrat S., Soottitantawat A., Laosiripojana N., Modelling of Tubular-Designed Solid Oxide Fuel Cell with Indirect Internal Reforming Operation Fed by Different Primary Fuels, *J. Power Sources*, **195**, pp. 69-78, 2010.

[60] Ormerod R.M., Fuels and Fuel Processing, Chapter 12 in Singhal S.C., Kendall K. (eds), High-Temperature Solid Oxide Fuel Cells: Fundamentals, Design and Applications, Elsevier, ISBN 9781856173872, 2003.

[61] Laosiripojana N., Assabumrungrat S., Catalytic Steam Reforming of Methane, Methanol and Ethanol over Ni/YSZ: The Possible Use of these Fuels in Internal Reforming SOFC, *J. Power Sources*, **163**, pp. 943-951, 2007.

[62] Miao H., Wang W.G., Li T.S., Chen T., Sun S.S., Xu C., Effects of Coal Syngas Major Compositions on Ni/YSZ Anode-Supported Solid Oxide Fuel Cells, *J. Power Sources*, **195**, pp. 2230-2235, 2010.

[63] Sadykov V.A., Mezentseva N.V., Bunina R.V., Alikina G.M., Lukashevich A.I., Kharlamova T.S., Rogov V.A., Zaikovskii V.I., Ishchenko A.V., Krieger T.A., Bobrenok O.F., Smirnova A., Irvine J., Vasylyev O.D., Effect of Complex Oxide Promoters and Pd on Activity and Stability of Ni/YSZ (ScSZ) Cermets as Anode Materials for IT SOFC, *Catalysis Today*, **131**, pp. 226-237, 2008.

[64] Aguiar P., Adjiman C.S., Brandon N.P., Anode-Supported Intermediate-Temperature Direct Internal Reforming Solid Oxide Fuel Cell: II. Model-Based Dynamic Performance and Control, *J. Power Sources*, **147**, pp.136-147, 2005.

[65] Nagel F., Schildhauer T., Biollaz S., Stucki S., Charge, Mass and Heat Transfer Interactions in Solid Oxide Fuel Cells Operated with Different Fuel Gases - A Sensitivity Analysis, *J. Power Sources*, **184**, pp. 129-142, 2008.

[66] Danilov V.A, Tade M.O., A CFD-Based Model of a Planar SOFC for Anode Flow Field Design, *Int. J. Hydrogen Energy*, **34**, pp. 8998-9006, 2009.

[67] Klein J.-M., Bultel Y., Georges S., Pons M., Modeling of a SOFC Fuelled by Methane: From Direct Internal Reforming of Gradual Internal Reforming, *Chem. Eng. Sci.*, **62**, pp. 1636-1649, 2007.

[68] Aruna S.T., Muthuraman M., Patil K.C., Synthesis and Properties of Ni-YSZ Cermet: Anode Materials for Solid Oxide Fuel Cells, *Solid State Ionics*, **111**, pp. 45-51, 1998.

[69] Mamak M., Coombs N., Ozin G.A., Practical Solid Oxide Fuel Cells with Anodes derived From Self-Assembeled Mesoporous-NiO-YSZ, *Chem. Commun.*, **20**, pp. 2300-2301, 2002.

[70] Drescher I., Kinetik der Methane-Dampf-Reformierung (in German), Kinetics of the Methane Steam Reforming (title translated to English), Doctoral Thesis, Research Institute Jülich, Germany, 1999.

[71] Drescher I., Lehnert W., Meusinger J., Structural Properties of SOFC Anodes and Reactivity, *Electrochim. Acta*, **43**, pp 3059-3068, 1998.

[72] Achenbach E., Riensche E., Methane/Steam Reforming Kinetics for Solid Oxide Fuel Cells, *J. Power Sources*, **52**, pp. 283-288, 1994.

[73] Achenbach E. Three-Dimensional and Time-Dependent Simulation of a Planar Solid Oxide Fuel Cell Stack, *J. Power Sources*, **49**, pp. 333-348, 1994.

[74] Leinfelder R., Reaktionskinetische Untersuchungen zur Methan-Dampf-Reformierung und Shift-Reaktion an Anoden Oxidkeramischer Brennstoffzellen (in German), Kinetic Studies on The Reaction of the Methane Steam Reforming and the Shift Reaction at Solid Oxide Fuel Cells Anodes (title translated to English), Doctoral Thesis, Faculty of Engineering, University of Erlangen-Nürnberg, Germany, 2004.

[75] Haberman B.A., Young J.B., Three-Dimensional Simulation of Chemically Reacting Gas Flows in the Porous Support Structure of an Integrated-Planar Solid Oxide Fuel Cell, *Int. J. Heat Mass Transfer*, **47**, pp. 3617-3629, 2004.

[76] Hofmann P., Panopoulos K.D., Fryda L.E., Kakaras E., Comparison between Two Methane Reforming Models Applied to a Quasi-Two-Dimensional Planar Solid Oxide Fuel Cell Model, *Energy*, **34**, pp. 2151-2157, 2008.

[77] Marrero-López D., Ruiz-Morales J.C., Peña-Martínez J., Canales-Vázquez J., Núñez P., Preparation of Thin Layer Material with Macroporous Microstructure for SOFC Applications, *J. Solid State Chemistry*, **181**, pp. 685-692, 2008.

[78] King D., Strohm J., Wang X., Roh H.-S., Wang C., Chin Y.-H., Wang Y., Lin Y., Rozmiarek R., Singh P., Effect on Nickel Microstructure on Methane Steam Reforming Activity of Ni-YSZ Cermet Anode Catalyst, *J. Catalysis*, **258**, pp. 356-365, 2008.

[79] Bessler W.G., Gewies S., Vogler M., A New Framework for Physically Based Modeling of Solid Oxide Fuel Cells, *Electrochim. Acta*, **53** pp. 1782-1800, 2007.

[80] Rosterup-Nielsen J.R., Hansen J.B., Helveg S., Christiansen N., Jannasch A.-K., Sites for Catalysis and Electrochemistry in Solid Oxide Fuel Cell (SOFC) Anode, *Appl. Phys.*, **A85**, pp. 427-430, 2006.

[81] Molenda J., Swierczek K., Zajac W., Functional Materials for the IT-SOFC, *J. Power Sources*, **173**, pp. 657-670, 2007.

[82] Jones G., Jakobsen J.G., Shim S.S., Kleis J., Andersson M.P., Rossmeisl J., Abild-Pedersen F., Bligaard T., Helveg S., Hinnemann B., Rostrup-Nielsen J.R., Chorkendorff I., Sehested J, Nørskov J.K., First Principles Calculations and Experimental Insight Into Methane Steam Reforming Over Transition Metal Catalysts, *J. Catalysis*, **259**, pp. 147-160, 2008.

[83] Hecht E., Gupta G., Zhu H., Dean A., Kee R., Maier L., Deutschmann O., Methane Reforming Kinetics within a Ni-YSZ SOFC Anode Support, *Applied Catalysis A: General,* **295**, pp. 40-51, 2005.

[84] Blaylock D., Ogura W.T., Green W.H., Beran G.J.O., Computational Investigation of Thermochemistry and Kinetics of Steam Methane Reforming on Ni(111) under Realistic Conditions, *J. Phys. Chem. C*, **113**, pp. 4898-4908, 2009.

[85] Bengaard H.S., Nørskov J.K., Sehested J., Clausen B.S., Nielsen L.P., Molenbroek A.M., Rostrup-Nielsen J.R., Steam Reforming and Graphite Formation on Ni Catalysts, *J. Catalysis*, **209**, pp. 265-384, 2002.

[86] Stoltze P., Microkinetic Simulation of Catalytic Reactions, *Progress in Surface Science*, **65**, pp. 65-150, 2000.

[87] Janardhanan V.M., Heuveline V., Deutschmann O., Performance Analysis of a SOFC Under Direct Internal Reforming Conditions, *J. Power Sources*, **172**, pp. 296-307, 2007.

[88] Lee W.Y., Wee D., Ghoniem A.F., An Improved One-Dimensional Membrane-Electrolyte Assembly Model to Predict the Performance of Solid Oxide Fuel Cell Including the Limiting Current Density, *J. Power Sources*, **186**, pp. 417-427, 2009.

[89] Vogler M., Bieberle-Hütter A., Gauckler L., Warnatz J., Bessler W.G., Modelling Study of Surface Reactions, Diffusion, and Spillover at a Ni/YSZ Patterned Anode, *J. Electrochem. Soc.*, **156**, B663-B672, 2009.

[90] Sohn S., Nam J.H., Jeon D.H., Kim C.-J., A Micro/Macroscale Model for Intermediate Temperature Solid Oxide Fuel Cells with Prescribed Fully-Developed Axial Velocity Profile in Gas Channels, *Int. J. Hydrogen Energy*, **35**, pp. 11890-11907, 2010.

[91] Aguiar P., Adjiman C.S., Brandon N.P., Anode-Supported Intermediate Temperature Direct Internal Reforming Solid Oxide Fuel Cell. I: Model-Based Steady-State Performance, *J. Power Sources*, **138**, pp. 120-136, 2004.

[92] Xiao H., Reitz T.L., Rottmayer M.A., Polarization Measurements of Anode-Supported Solid Oxide Fuel Cells Studied by Incorporation of a Reference Electrode, *J. Power Sources*, **183**, pp. 46-54, 2008.

[93] Dennis B.H., Han Z., Jin W., Wang B.P., Xu L., Aapro T., Ptchelintsev A., Reinikainen T., Multi-Physics Simulation Strategies with Applications to Fuel Cell Modeling, *Proceedings of the 7th. Int. Conf. on Thermal, Mechanical and Multiphysics Simulation and Experiments in Micro-Electronics and Micro-Systems, EuroSimE,* Como, Italy, 2006.

[94] Karakasidis T., Charitidis C., Multiscale Modelling in Nanomaterials Scince, *Mater. Sci. Eng.*, **C27**, pp. 1082-1089, 2007.

[95] Frayret C., Villesuzanne A., Pouchard M., Matar S., Density Functional Theory Calculations on Microscopic Aspects of Oxygen Diffusion in Ceria-Based Materials, *I. J. Quantum Chemistry*, **101**, pp. 826-839, 2005.

[96] Asproulis N., Kalweit M., Drikakis D., Hybrid Molecular-Continuum Methods for Micro- and Nanoscale Liquid Flows, *Proceedings of the 2nd Micro and Nano Flows Conference*, West London, UK, 2009.

[97] Khaleel M.A., Rector D.R., Lin Z., Johnson K., Recknagle K., Multiscale Electrochemistry Modeling of Solid Oxide Fuel Cells, *Int. J. Multiscale Comp. Eng.*, **3,** pp. 33-47, 2005.

[98] Bove R., Lunghi P., Sammes N.M., SOFC Mathematical Model for Systems Simulation. Part One: From a Micro-Detailed to Macro-Black-Box Model, *Int. J. Hydrogen Energy,* **30**, pp. 181-187, 2005.

[99] Cheng C.H., Chang Y.W., Hong C.W., Multiscale Parametric Studies on the Transport Phenomenon of a Solid Oxide Fuel Cell, *ASME J. Fuel Cell Sci. Technol.*, **2**, pp. 219-225, 2005.

[100] Faghri A., Guo Z., Challenges and Opportunities of Thermal Management Issues Related to Fuel Cell Technology and Modeling, *Int. J. Heat Mass Transfer*, **48**, pp. 3891-3920, 2005.

[101] Reifsnider K., Huang X., Ju G., Solasi R., Multi-scale Modeling Approaches for Functional Nano-Composite Materials, *J. Mater. Sci.*, **41**, pp. 6751-6759, 2006.

[102] COMSOL Multiphysics 3.5 user guide, Stockholm, Sweden, 2008.

[103] Iwata M., Hikosaka, T., Morita M., Iwanari T., Ito K.,Onda K., Esaki Y., Sakaki Y., Nagata S., Performance Analysis of Planar-Type Unit SOFC considering Current and Temperature Distributions, *Solid State Ionics*, **132**, pp. 297-308, 2000.

[104] Chao C.H., Hwang A.J.J., Predictions of Phase Temperatures in a Porous Cathode of Polymer Electrolyte Fuel Cells using a Two-Equation Model, *J. Power Sources*, **160**, pp. 1122-1130, 2006.

[105] Shah R.K., London A.L., Laminar Flow Forced Convection in Ducts. Academic Press, ISBN 9780120200511, London, UK, 1978.

[106] Kulikovsky A.A., A Simple Equation for Temperature Gradient in a Planar SOFC Stack, *Int. J. Hydrogen Energy*, **35,** pp. 308-312, 2010.

[107] Bessler W.G., Warnatz J., Goodwin D.G., The Influence of Equilibrium Potential on the Hydrogen Oxidation Kinetics of SOFC Anodes, *Solid State Ionics*, **177**, pp. 3371-3383, 2007.

[108] Chan S.H., Khor K.A., Xia Z.T., A Complete Polarization Model of a Solid Oxide Fuel Cell and its Sensitivity to Change of Cell Component Thickness, *J. Power Sources*, **93**, pp. 130-140, 2001.

[109] Akhtar N., Decent S.P., Kendall K., Numerical Modelling of Methane-Powered Micro-Tubular, Single-Chamber Solid Oxide Fuel Cell, *J. Power Sources* ,**195**, pp. 7796-7807, 2010.

[110] Shi Y., Cai N., Li C., Bao C., Croiset E., Qian J., Hu Q., Wang S., Modeling of an Anode-Supported Ni-YSZ|Ni-ScSZ|ScSZ|LSM-ScSZ Multiple Layers SOFC Cell Part I. Experiments, Model Development and Validation, *J. Power Sources*, **172**, pp. 235-245,2007.

[111] Akkaya A.V., Electrochemical Model for Performance Analysis of a Tubular SOFC, I*nt. J. Energy Research*, **31**, pp. 79-98, 2007.

[112] Konno A., Iwai H., Inuyama K., Kuroyanagi A., Saito M., Yoshida H., Kodani K., Yoshikata K., Mesoscale-Structure Control at Anode/Electrolyte Interface in Solid Oxide Fuel Cell, *J. Power Sources*, **196**, pp. 98-109, 2011.

[113] Lehnert W., Meusinger J., Thom F., Modelling of Gas Transport Phenomena in SOFC Anodes, *J. Power Sources*, **87**, pp. 57-63, 2000.

[114] Suwanwarangkul R., Croiset E., Fowler M.W., Douglas P.L., Entchev E., Douglas M.A., Performance comparison of Fick's, Dusty-gas and Stefan-Maxwell Models to Predict the Concentration Overpotential of a SOFC Anode, *J. Power Sources*, **122**, pp. 9-18, 2003.

[115] Tseronis K., Kookos I.K., Theodoropoulos C. Modeling Mass Transport in Solid Oxide Fuel Cell Anodes: A Case for a Multidimensional Dusty Gas-Based Model, *Chem. Eng. Sci.*, **63**, pp. 5626-5638, 2006.

# Paper I

This paper has been published in:

*J. Applied Energy,*
Vol. 87, pp. 1461-1476, 2010.

© 2010 Elsevier.

Applied Energy 87 (2010) 1461–1476

Contents lists available at ScienceDirect

Applied Energy

journal homepage: www.elsevier.com/locate/apenergy

# Review on modeling development for multiscale chemical reactions coupled transport phenomena in solid oxide fuel cells

Martin Andersson, Jinliang Yuan *, Bengt Sundén

*Department of Energy Sciences, Lund University, SE-221 00 Lund, Sweden*

ARTICLE INFO

*Article history:*
Received 20 October 2009
Received in revised form 9 November 2009
Accepted 12 November 2009
Available online 16 December 2009

*Keywords:*
SOFC
Multiscale modeling
Review
Chemical reaction
Transport phenomena

ABSTRACT

A literature study is performed to compile the state-of-the-art, as well as future potential, in SOFC modeling. Principles behind various transport processes such as mass, heat, momentum and charge as well as for electrochemical and internal reforming reactions are described. A deeper investigation is made to find out potentials and challenges using a multiscale approach to model solid oxide fuel cells (SOFCs) and combine the accuracy at microscale with the calculation speed at macroscale to design SOFCs, based on a clear understanding of transport phenomena, chemical reactions and functional requirements. Suitable methods are studied to model SOFCs covering various length scales. Coupling methods between different approaches and length scales by multiscale models are outlined. Multiscale modeling increases the understanding for detailed transport phenomena, and can be used to make a correct decision on the specific design and control of operating conditions. It is expected that the development and production costs will be decreased and the energy efficiency be increased (reducing running cost) as the understanding of complex physical phenomena increases. It is concluded that the connection between numerical modeling and experiments is too rare and also that material parameters in most cases are valid only for standard materials and not for the actual SOFC component microstructures.

© 2009 Elsevier Ltd. All rights reserved.

**Contents**

1. Introduction . . . 1463
2. Transport phenomena mechanisms . . . 1463
   2.1. Mass transport . . . 1464
      2.1.1. Knudsen diffusion . . . 1464
   2.2. Momentum transport . . . 1465
   2.3. Heat transport . . . 1465
      2.3.1. Local temperature non-equilibrium (LTNE) approach . . . 1466
      2.3.2. Thermal radiation . . . 1466
   2.4. Charge transport . . . 1466
   2.5. Interaction issues . . . 1467
3. Microcatalytic reaction mechanisms . . . 1467
   3.1. Electrochemical reactions . . . 1467
   3.2. Internal reforming reactions . . . 1468
      3.2.1. Global reforming reaction kinetics . . . 1469
      3.2.2. Elementary surface reaction kinetics . . . 1470
4. Multiscale SOFC modeling development . . . 1471
   4.1. Micro-, meso- and macroscale approaches . . . 1471
      4.1.1. SOFC modeling at microscale . . . 1471
      4.1.2. SOFC modeling at mesoscale . . . 1472
      4.1.3. SOFC modeling at macroscale . . . 1472
      4.1.4. SOFC modeling integration issues . . . 1472

* Corresponding author. Tel.: +46 46 222 4813.
*E-mail addresses:* martin.andersson@energy.lth.se (M. Andersson), jinliang. yuan@energy.lth.se (J. Yuan), bengt.sunden@energy.lth.se (B. Sundén).

0306-2619/$ - see front matter © 2009 Elsevier Ltd. All rights reserved.
doi:10.1016/j.apenergy.2009.11.013

4.2. Validation. . . . 1473
4.3. State-of-the-art in multiscale SOFC modeling. . . . 1473
4.3.1. How far can SOFC modeling reach? . . . 1474
5. Conclusions. . . . 1474
Acknowledgement . . . 1475
References . . . 1475

**Nomenclature**

| | |
|---|---|
| $A$ | active surface area, $cm^2$ |
| $c_p$ | specific heat capacity at constant pressure, J/(kg K) |
| $Da$ | Darcy number, dimensionless |
| $D$ | diffusion coefficient, $m^2/s$ |
| $d_p$ | electrode particle diameter, m |
| $E$ | reversible electrochemical cell voltage, V |
| $E_a$ | activation energy, kJ/mol, |
| F | Faraday constant, 96485 C/mol |
| $F_{ij}$ | view factor, dimensionless |
| $h_{s,g}$ | heat transfer coefficient, $W/(m^2\ K)$ |
| $h_v$ | volume heat transfer coefficient, $W/(m^3\ K)$ |
| $i$ | current density, $A/cm^2$ |
| $i_0$ | exchange current density, $A/cm^2$ |
| $k$ | thermal conductivity, W/(m K) |
| $k_i$ | reaction rate constant, $mol/(m^3\ Pa^2\ s)$ |
| $k'$ | Boltzmann's constant, J/K |
| $k''$ | pre-exponential factor, $1/(\Omega\ m^2)$ |
| $K_e$ | equilibrium constant, $Pa^2$ or dimensionless |
| $l_{TPB}$ | length of the three-phase boundary, m |
| $M_i$ | molecular weight of species $i$, kg/mol |
| $n_e$ | number of electrons transferred per reaction, dimensionless |
| $Nu$ | Nusselt number, dimensionless |
| $p$ | pressure, Pa, bar |
| $q$ | heat flux, $W/m^2$ |
| $Q$ | source term (heat), $W/m^3$ |
| $r_i$ | chemical reaction rate, $mol/(m^3s)$, $mol/(m^2s)$ |
| $r'$ | average pore radius, m |
| R | gas constant, 8.314 J/(mol K) |
| $SA$ | surface area ratio, $m^2/m^3$ |
| $S_i$ | source term mass, $kg/(m^3s)$ |
| $T$ | temperature, K |
| $\mathbf{T}$ | viscous stress tensor, $N/m^2$ |
| $t$ | tortuosity, dimensionless |
| $u,v$ | velocity, m/s |
| $w_i$ | mass fraction of species $i$, kg/kg |
| $x_j$ | molar fraction of species $j$, mol/mol |

*Greek symbols*

| | |
|---|---|
| $\alpha$ | absorptivity, $m^2/mol$ |
| $\varepsilon$ | emissivity, dimensionless |
| $\varphi$ | porosity, dimensionless |
| $\eta$ | over-potential, V |
| $\kappa$ | permeability, $m^2$ |
| $\kappa_{dv}$ | deviation from thermodynamic equilibrium, Pa s |
| $\mu$ | dynamic viscosity, Pa s |
| $\rho$ | density, $kg/m^3$ |
| $\sigma$ | ionic/electronic conductivity, $\Omega^{-1}\ m^{-1}$ |
| $\phi$ | charge potential |

*Subscripts*

| | |
|---|---|
| $a$ | anode |
| $act$ | activation polarization |
| $c$ | cathode |
| $e$ | electrode, $e \in \{a, c\}$ |
| $el$ | electrolyte, electrons |
| $eff$ | effective |
| $f$ | fluid phase |
| $g$ | gas phase |
| $i$ | molecule $i$ |
| $io$ | ions |
| $j$ | molecule $j$ |
| $K$ | Knudsen diffusion |
| $r$ | steam reforming reaction |
| $por$ | porous media |
| $s$ | solid phase, water–gas shift reaction, catalytic site |

*Abbreviations*

| | |
|---|---|
| CFD | computational fluid dynamics |
| CM | continuum methods |
| DFT | Density Functional Theory |
| DGM | Dusty-Gas model |
| FC | fuel cell |
| FEM | finite element method |
| FM | Fick's model |
| FVM | finite volume method |
| HCR | heterogeneous reaction mechanism |
| HT | high temperature |
| IEA | International Energy Agency |
| IT | intermediate temperature |
| LBM | Lattice-Boltzmann method |
| LSM | strontium doped lanthanium manganite |
| LTE | local temperature equilibrium |
| LTNE | local temperature non-equilibrium |
| MC | Monte Carlo |
| MD | Molecular Dynamics |
| PWC | point-wise coupling methodology |
| SA | surface area |
| SMM | Stefan–Maxwell model |
| SOFC | solid oxide fuel cell |
| TPB | three-phase boundary |
| YSZ | yttria-stabilized zirconia |

*Chemical*

| | |
|---|---|
| $CH_4$ | methane |
| CO | carbon monoxide |
| $CO_2$ | carbon dioxide |
| $e^-$ | electron |
| $H_2$ | hydrogen |
| $H_2O$ | water |
| $N_2$ | nitrogen |
| $NH_3$ | ammonia |
| Ni | nickel |
| $O_0^X$ | lattice oxygen |
| $O_2$ | oxygen |
| $OH^-$ | hydroxyl ion |
| $V_0^{\cdot\cdot}$ | oxygen vacancy |

## 1. Introduction

Fuel cells directly convert the free energy of a chemical reactant to electrical energy and heat. This is different from a conventional thermal power plant, where the fuel is oxidized in a combustion process combined with a conversion process (thermal–mechanical–electrical energy), that takes place after the combustion [1]. If pure hydrogen is used, no pollution of air and environment occurs at all, because the output from the fuel cells is electricity, heat and water. Fuel cells do not store energy as batteries do [2]. A fuel cell consists of two electrodes: one anode for fuel and one cathode for oxidant. The electrodes are separated by the electrolyte and connected into an electrically conducting circuit. A gas or liquid, with fuel or oxidant, is transported to the electrode, which should be permeable via a porous structure. Unit cells are further organized together into stacks to supply the required electricity [3].

The solid oxide fuel cell (SOFC) electrolyte is non porous ceramic, normally $Y_2O_3$ stabilized $ZrO_2$ (YSZ). At an operating temperature between 600 and 1000 °C, the ceramic electrolyte becomes non-conductive for electrons, but conductive to oxygen ions. Cathodes are mostly made from electronically conducting oxides or mixed electronically conducting and ion-conduction ceramics. The anode consists normally of nickel/yttria stabilized zirconia (Ni/YSZ) cermet. SOFCs can be designed with planar, tubular or monolithic structures. The planar design is normally more compact, compared to the tubular design, i.e., a higher volume of specific power is achieved. Tubular and planar SOFCs can be either electrolyte-, anode-, cathode- or metal- supported. An electrolyte-supported SOFC has thin anode and cathode (~50 μm), and the thickness of the electrolyte is more than 100 μm. This design works preferably at temperatures around 1000 °C. In an electrode-supported SOFC either the anode (anode-supported) or the cathode (cathode-supported) is thick enough to serve as the supporting substrate for cell fabrication, normally between 0.3 and 1.5 mm. The electrolyte is in this configuration very thin, and the operating temperature can be reduced to an intermediate range [4].

The current trend is to decrease the operating temperature. Low temperature (LT)-SOFCs in the range of 300–600 °C is under development, the challenge is to increase the ionic conductivity in the electrolyte. Low temperatures make it possible to use cheaper materials throughout the fuel cell system. An approach with material development on the nanoscale is expected to be very promising [5].

As an alternative to the conventional SOFCs (SOFC-O) with electrolyte of YSZ, the concept of proton ceramic electrolyte (such as $BaCeO_3$ based ceramics) has been developed (SOFC-H). Complete fuel utilization is possible, since the water is produced in the cathode (instead of in the anode) and no dilution of the fuel occurs. Thermodynamic analysis has shown that a higher theoretical efficiency can be reached, compared to conventional SOFC-O [6].

The fuel cell is not a new invention, since the electrochemical process was discovered already in 1838–1839. The interest in fuel cells has been growing exponentially, which is evident from the amount of published scientific papers, after year 2000 [7]. Among various types of fuel cells (FCs), the SOFC has attained significant interest due to its high efficiency and low emissions of pollutants to the environment. High temperature operation offers many advantages, such as high electrochemical reaction rate, flexibility of using various fuels and toleration of impurities [8]. Fuel cell systems are still an immature technology in early phases of development, as can be noted due to lack of a dominant design, few commercial systems and a low market demand. The creation of strategic niche markets and search for early market niches are of a vital importance for the further development. It is expected that mass production will start when a dominant design is found, and then production cost will significantly decrease due to the economy of scale [7].

SOFCs can work with a variety of fuels, e.g., hydrogen, carbon monoxide, methane, ammonia and combinations of these [9,10]. Oxygen is reduced in the cathode (Eq. (1)). The oxygen ions are transported through the electrolyte, but the electrons are prevented to pass through the electrolyte. The electrochemical reactions (Eqs. (2) and (3)) take place at the anodic three-phase boundary (TPB). Methane needs to be reformed (Eq. (4)) before the electrochemical reactions [11]. Carbon monoxide can be oxidized in the electrochemical reaction (Eq. (3)) but can also react with water (Eq. (5)). Ammonia is converted to hydrogen (Eq. (6)). The reactions described here are the overall reactions, more detailed reaction mechanisms can be found in [11–12]. Note that methane and ammonia are not participating in the electrochemical reactions at the anodic TPB, methane is catalytically converted, within the anode, into carbon monoxide and hydrogen and ammonia into nitrogen and hydrogen. Hydrogen and carbon monoxide are used as fuel in the electrochemical reactions [10,12].

$$O_2 + 4e^- \iff 2O^{2-} \tag{1}$$

$$H_2 + O^{2-} \iff H_2O + 2e^- \tag{2}$$

$$CO + O^{2-} \iff CO_2 + 2e^- \tag{3}$$

$$CH_4 + H_2O \iff 3H_2 + CO \tag{4}$$

$$CO + H_2O \iff H_2 + CO_2 \tag{5}$$

$$2NH_3 \iff N_2 + 3H_2 \tag{6}$$

A literature review is conducted to find out what methods have been developed to model SOFCs, arranged according to length scales. The mechanisms behind the transport processes within SOFCs are outlined, in terms of momentum-, mass-, heat- and charge transport. Approaches to model electrochemical as well as internal reforming reactions are discussed in detail. Coupling between different methods, length scales and multiscale model integration are outlined. SOFC microscale models correspond in many cases to the atom or molecular level. The finite element method (FEM) and finite volume method (FVM) are used to model SOFCs at the macroscale level. Multiscale modeling is found to be a promising tool for fuel cell research. COMSOL Multiphysics, based on the FEM, as well as FLUENT, based on the FVM, are examples of commercial codes for analysis of coupling different physical models at different scales. Multiscale modeling increases the understanding for detailed transport phenomena, and can be used to make a correct decision on the specific design and control of operating conditions. Note that this paper reviews SOFC component and the cell models, and an introduction to SOFC stack and system models can be found in [13] and [14], respectively.

## 2. Transport phenomena mechanisms

SOFCs can be examined from different points of view: as an electrochemical generator in a viewpoint of electrochemical reactions at continuum level, as a heat and mass exchanger in a perspective of fluid dynamics and transport phenomena, or as a chemical reactor in viewpoints of chemical reactions depending on fuel composition and heat effects associated with the electrochemical conversion [4].

The amount of fuel gases transported to the active surface for the electrochemical reactions are governed by different parame-

ters, such as porous microstructure, gas consumption, pressure gradient between the fuel flow duct and porous anode, and inlet conditions [15]. The gas molecules diffuse to the three-phase boundary (TPB), where the electrochemical reactions take place. The supply of reactants can be the rate-limiting step, since the gas molecule diffusion coefficient is much smaller than that for ions. The charge transfer chemistry at the interface between the electrolyte and the anode proceeds on the basis of the hydrogen concentration. The hydrogen concentration depends on the transport within the porous anode and the heterogeneous reforming reaction chemistry. The concentration of the fuel gases, $CH_4$, CO and $H_2$, decreases along the length of the fuel channel while the concentration increases for $H_2O$ and $CO_2$. As a result the current density decreases along the fuel channel [16].

Two approaches for defining the electrochemical reactions can be found in the literature, either as source terms in the governing equations [17,18] or as interface conditions defined at the electrode/electrolyte interfaces [19–24]. Selection of either approach affects the momentum-, heat transfer- and mass transport equations. The approach defining interface conditions can be used, because the thickness of the active layer is sufficiently thin, compared to the thickness of the electrode [19–24]. The reason for using an approach where the electrochemical reactions are defined as source terms is that the reaction zone can be spread out into the electrode some distance away from the electrode/electrolyte interface [17].

For steady state problems, the boundary conditions can be defined with two types of spatial conditions, either as a "*Dirichlet boundary condition*", where the generic value at the boundary is a known and constant value or as a "*Neuman boundary condition*", where the derivates of the generic variable are known [25].

### 2.1. Mass transport

Mass transport in the electrodes occurs in the gas phase, integrated with the chemical reforming reactions at the solid active surface. The electrodes are porous and mass transfer is dominated by gas diffusion [16]. The interconnect can be assumed to be impermeable for gases. Electron transport effect on the mass transfer needs to be considered since the current is collected [4].

Fick's model is the simplest diffusion model used for dilute or binary systems [26]. In the literature the Stefan–Maxwell model is commonly used to calculate the diffusion in a multi-component system. In some references the Stefan–Maxwell model is combined with the Knudsen diffusion term (frequently called the Dusty-Gas model or extended Stefan–Maxwell equation) [18,20,27–30], to predict the collision effects between the gas molecules and the solid porous material. In other models this effect is neglected [16].

Dusty-Gas model (DGM), Ficks model (FM) and Stefan–Maxwell model (SMM) are developed in [19], in order to predict the concentration over-potential inside an SOFC anode. DGM and FM consider molecular diffusion, Knudsen diffusion and the effect of a finite pressure gradient. The flux ratio in DGM depends on the square-root of the gas molecular weight, but it does not for FM. Explicit analytical expressions describing fluxes can be used in FM. The SMM can be seen as a simpler model since it does not consider the Knudsen diffusion. DGM is the most appropriate model for $H_2$–$H_2O$ and CO–$CO_2$ system. However, it is only used when the operating current density is high. Ni et al. [12,31] studied the effect of microstructural grading on SOFC performance with a DGM to analyze the coupled phenomena of mass transfer and electrochemical reactions in the SOFC electrodes.

To account for the increased diffusion length due to the tortuous paths of real pores in the porous materials, different approaches can be found in the literature [25]:

$$D_{ij,eff} = \varphi^t \cdot D_{ij} \tag{7}$$

$$D_{ij,eff} = \frac{\varphi}{t} \cdot D_{ij} \tag{8}$$

where $D_{ij}$ is the Maxwell–Stefan binary diffusion coefficient, $D_{ij,eff}$ the effective Maxwell–Stefan binary diffusion coefficient in the porous medium, $\varphi$ the porosity and $t$ the tortuosity. Similar expressions can be found for molecular diffusion coefficients in porous materials [29,30]. Tortuosities up to the range of 10–17 can be found in the literature. These values are too high considering that the range for porous sintered ceramics is reported to be 2–10 [29].

The Maxwell–Stefan equation can be formulated as [32]:

$$\nabla\left(-\rho \cdot w_i \sum D_{ij,eff} \cdot \nabla x_j + (x_j - w_j)\frac{\nabla p}{p} \cdot u - D_i^T \cdot \frac{\nabla T}{T}\right) + \rho \cdot u \cdot \nabla w_j = S_i \tag{9}$$

$$x_j = \frac{w_j}{M_j} \cdot M \tag{10}$$

$$\sum_{i=1}^{n} w_i = 1 \tag{11}$$

where $w$ is the mass fraction, $x$ the mole fraction, $D_i^T$ the thermal diffusion coefficient and $S_i$ the source term due to chemical reactions. The effective diffusion coefficient ($D_{ij,eff}$) equals the molecular diffusion coefficient ($D_{ij}$) in the gas channels.

Mass or molar fractions need, for the inlet fuel- and air flows, to be defined at the cell level. The outlet conditions are usually defined as convective fluxes. The effects on mass transport from the electrochemical reactions are either defined as source terms in the governing equations or as interface conditions, as discussed previously [33].

For instance, Andersson [33] has developed a model considering fluid flow, mass- and heat transfer for a single cell IT-SOFC. The mole fraction of oxygen (Fig. 1) decreases along the flow direction in the air channel and the cathode. There is a concentration difference in the *y*-direction as well, that forces the flow towards the cathode/electrolyte interface. However, it is hard to recognize in the air channel as the cell length is 400 times bigger than the air channel height.

#### 2.1.1. Knudsen diffusion

For the porous material, molecular diffusion is predominant for the case with large pores, whose size is much bigger than the free path of the diffusion gas molecules [18], i.e., the Stefan–Maxwell model describes the transport processes with a satisfactory accu-

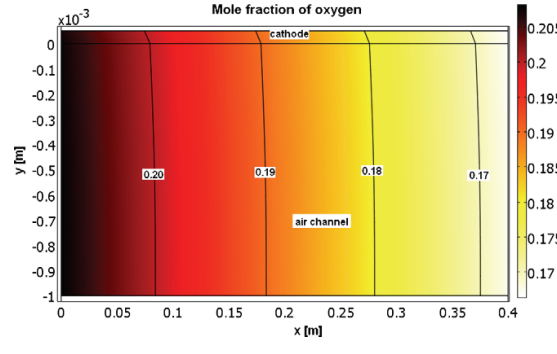


**Fig. 1.** Mole fraction of oxygen in the air channel and cathode for a single cell IT-SOFC [33].

racy. The Knudsen diffusion is used when the pores are small in comparison to the mean free path of the gas. In this case, molecules collide more often with the pore walls than with other molecules. The Knudsen diffusion coefficient can be calculated using a kinetic theory that relates the diameter of the pore and the mean free path of the gas according to [30]:

$$D_k = \frac{u \cdot r'}{6} \tag{12}$$

where $D_k$ is the Knudsen diffusion coefficient, $r'$ is the average pore radius and $u$ is the velocity of the gas molecules. If the pores are straight and circular, the diffusion coefficient of the component $i$ is [30]:

$$D_{ik} = 97.0 \cdot r' \cdot \sqrt{\frac{T}{M_i}} \tag{13}$$

where $D_{ik}$ is the Knudsen diffusion coefficient for molecule $i$, $T$ the temperature and $M_i$ the molecular weight. To calculate the average pore radius ($r'$), the surface area of the porous solid and the porosity are used [30]:

$$r' = \frac{2 \cdot \varphi}{SA \cdot \rho_B} \tag{14}$$

where SA is the surface area of the porous solid and $\rho_B$ the bulk density of the solid particle. It is possible to account for the tortuous path of the molecule, by calculating the effective Knudsen diffusion coefficient [30]:

$$D_{ik,eff} = D_{ik} \cdot \left(\frac{\varphi}{t}\right) \tag{15}$$

where $D_{ik,eff}$ is the effective Knudsen diffusion coefficient. Molecular diffusion and Knudsen diffusion may appear at the same time and can be calculated as [26,30]:

$$\frac{1}{D_{i,eff}} = \frac{1}{D_{ij,eff}} + \frac{1}{D_{ik,eff}} \tag{16}$$

### 2.2. Momentum transport

The fuel cell manifolds should be designed with the aim to achieve uniform fluid distribution between different unit cells and a stable stack operation. The flow field in a unit cell may be divided into three parts, inlet manifold, cell gas channels (fuel and air) and outlet manifold. The inlet manifold for a single cell is a part of the stack inlet manifold, the air (or fuel) is directed into the single cell and the excess is transported to the next cells. For a stack with a given number of single cells, the geometric parameters that are influential to the stack flow uniformity are: the height of the repeating unit cell, the height and length of the gas channels, the inlet manifold width and the outlet manifold width [34].

The effects of the geometric parameters on the stack flow uniformity are normally understandable in terms of their effects on the relative dominances between the pressure changes in the gas channels and manifolds. According to a study in [34], the fuel flow distribution is more uniform than the air flow distribution for a given stack, due to the fact that the fuel flow velocity is small or in the laminar region, with a small pressure change in the manifold. The results also show that the flow distribution for stacks with a large number of cells can be far from ideal conditions. It is revealed that the ratio between inlet and outlet manifold widths is a key parameter for the flow distribution, and the optimal ratio increases with the number of cells in the stack.

The gases flow inside the fuel cell components, such as in the air and fuel channels and to the porous electrodes. The physics of laminar and turbulent incompressible flow are well described by the Navier–Stokes equations. It is common practice to assume laminar flow for fuel cell gas channels due to the low velocities, which decreases the computational cost significantly [25]. The Darcy equation describes the balance in the porous electrodes between the force from the pressure gradient and the frictional resistance from the solid material. It should be noted that the Darcy equation expresses the flow in the porous structure well away from the walls. A traditional modeling approach for such a system consists of solving the Darcy's equation in the porous medium and the Navier–Stokes equations in the channels separately. The problem with such an approach is to define interfacial conditions at the interface between the two domains. It is hard to define this tangential velocity component. To avoid this problem the Darcy–Brinkman equation is introduced and solved for the gas flow in the fuel and air channels and in the porous media (electrodes) [20,32,35].

The Darcy–Brinkman equation (Eq. (17)) is transformed into the standard Navier–Stokes equation when ($\kappa \to \infty$) and ($\varepsilon_p = 1$), and into the Darcy equation as ($Da \to 0$). $Da$ is the Darcy number. The derivation of the Navier–Stokes equation and Darcy equation from Darcy–Brinkman equation can be found in [35].

$$\left(\frac{\mu}{\kappa} + \rho \cdot \nabla u\right) \cdot u - \nabla\left[-p + \frac{1}{\varphi}\{\mathbf{T} - (\lambda - \kappa_{dv})(\nabla u)\}\right] = \mathbf{F} \tag{17}$$

where $\mathbf{F}$ is the volume force vector, $\kappa$ the permeability of the porous medium, $\varphi$ the porosity, $\mu$ the dynamic viscosity, $u$ the velocity vector and $\mathbf{T}$ the viscous stress tensor ($\mathbf{T} = \nu(\nabla u + (\nabla u)^{\mathbf{T}})$). $\kappa_{dv}$ is the deviation from thermodynamic equilibrium. When this term is zero, the fluid particles are in equilibrium with their surroundings. $\lambda$ is the second viscosity and is, for gases, normally assumed as: $\lambda = -2/3\mu$ [36].

When a single cell is modeled, a velocity (profile) is defined at the air- and fuel channel inlets (frequently as a laminar flow profile) and pressure at the air- and fuel channel outlets. The effects from the electrochemical reactions are either defined as source terms in the governing equations or as interface conditions as discussed previously [33,37].

### 2.3. Heat transport

The heat transfer inside SOFCs includes various aspects such as convective heat transfer between the solid surfaces and the gas streams, conductive heat transfer in solid and porous structures. Heat generation occurs due to the electrochemical reactions at TPB between the electrolyte and electrodes [38], the current flow (ohmic polarization) and the internal reforming reactions of carbon monoxide at the porous anode and in the fuel channel [39]. The steam reforming reaction of methane in the porous anode is endothermic, and heat is then consumed [39]. Accurate temperature prediction distribution within SOFCs is essential for predicting and optimizing the overall cell performance as well as avoiding thermo-mechanical degradation [40]. Most of the heat within SOFCs is generated near the electrode/electrolyte interface and is dissipated by: (1) conduction in the solid matrix, (2) heat transfer from the solid to the gas phase by convection within the pores, and (3) advection of the gas through the micro-pores to the flow channel [40].

Effective transport parameters for the porous material need to be calculated when a local temperature equilibrium (LTE) approach (assumes the same temperature for gas- and solid phase) is used. The thermal conductivity ($k_{eff}$) and specific heat ($c_{p,eff}$) can be specified as [18]:

$$k_{eff} = \varphi \cdot k_f + (1 - \varphi) \cdot k_s \tag{18}$$

$$c_{p,eff} = \varphi \cdot c_{p,f} + (1 - \varphi) \cdot c_{p,s} \tag{19}$$

where $\varphi$ is the porosity, *eff* means effective, *s* solid and *f* fluid (gas) phase. The temperature distribution can be predicted by [32]:

$$\nabla(-k_{eff}\cdot\nabla T)=Q-\rho_{eff}\cdot c_{p,eff}\cdot u\cdot\nabla T \tag{20}$$

where $T$ is the temperature (same temperature is assumed for solid- and gas phase), and $Q$ the source term (due to the chemical- and the electrochemical reactions).

### 2.3.1. Local temperature non-equilibrium (LTNE) approach

A very common method in SOFC modeling is to employ LTE [18,26,40]. However, some typical conditions found in the porous SOFC electrodes bring this assumption into question: (1) very low Reynolds number flow, (2) presence of volumetric heat generation, and (3) large difference in thermal conductivities between the gas- and solid phases. A local temperature non-equilibrium (LTNE) approach is developed in [40] to predict the temperature difference between the solid- and gas phases within the porous electrodes. Heat is (according to the LTNE approach) transferred between the phases at the solid material surfaces in the porous electrodes. The general heat conduction equation is used to calculate the temperature distribution for the solid matrix in the porous electrodes [32]:

$$\nabla(-k_s\cdot\nabla T_s)=Q_s \tag{21}$$

where $k_s$ is the thermal conductivity of the solid, $T_s$ the temperature in the solid phase and $Q_s$ the heat source (heat transfer between the solid- and gas phases, the heat generation due to the ohmic polarization and due to the internal reforming reactions). The heat generation due to electrochemical reactions, concentration polarization and activation polarization can be defined either as a source term or as an interface condition. Note that part of the heat generation/consumption enters into the solid phase and the remaining part to the gas phase. Knowledge about this ratio is still pore. The temperature distribution for the gas mixtures in the fuel and air channels, and in the porous electrodes can be defined as [32]:

$$\nabla(-k_g\cdot\nabla T_g)=Q_g-\rho_g\cdot c_{p,g}\cdot u\cdot\nabla T_g \tag{22}$$

where $c_{p,g}$ is the gas phase heat capacity, $T_g$ the gas temperature and $Q_g$ the heat transfer between the gas- and solid phases and the heat generation that occurs in the gas phase. Because the Reynolds number is very low inside the porous electrodes, the heat transfer coefficient, $h_{s,g,por}$ (when spherical particles are assumed in the porous electrodes) can be calculated as [40]:

$$h_{s,g,por}=\frac{2\cdot k_g}{d_p} \tag{23}$$

where $d_p$ is the electrode particle diameter and $k_g$ the gas conductivity. The heat transfer between the gas- and solid phase depends on the temperature difference and the particle surface area as [41]:

$$Q_g=h_v\cdot(T_g-T_s)=SA\cdot h_{s,g,por}\cdot(T_g-T_s) \tag{24}$$

where $h_v$ is the volume heat transfer coefficient and *SA* the surface area ratio.

Most cell level models define the temperature at the air and fuel channel inlets and convective flux at the outlets. The boundaries at the top and bottom of the cells are (for a cell model) normally defined by symmetries, when the cell is assumed to be surrounded by other similar cells with the same temperature distribution [33].

For example, Andersson [33] uses a LTNE approach to calculate the temperature distribution for a single cell IT-SOFC. The temperature increases along the *x*-direction (the main flow direction), as seen in Fig. 2. The temperature difference in the *y*-direction inside the air channel occurs because the convective heat flux is bigger in the air channel (compared to the fuel channel) due to the relatively larger gas flow rate. It is revealed that the temperature difference between the phases is less than 1 K for the studied case (not shown here).

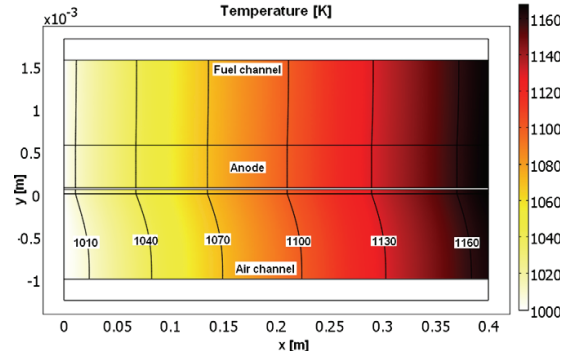


**Fig. 2.** Temperature for the gas phase in a single cell IT-SOFC [33].

### 2.3.2. Thermal radiation

SOFCs are operating at a high temperature and thus thermal radiation should be involved for an accurate heat balance. Heat exchange between the surfaces of the air and fuel channels, radiation between the surfaces of the channels and flowing gases (especially water and carbon dioxide) and radiation heat loss from the stack to the environment should be taken into account for effective thermal management of the fuel cell stack. The thermal radiation between the surfaces may be calculated as [42]:

$$q_i=\sum_{j=1}^{n}A_iF_{ij}k'(T_i^4-T_j^4) \tag{25}$$

where the radiation leaves surface $i$ as a result of its interaction with surface $j$, $T$ is the temperature (in Kelvin), $k'$ is the Bolzmann constant and $F$ is the view factor. The net rate between the channel surfaces (assumed to have blackbody conditions) and the channel gases can be expressed as [42]:

$$q_{net}=A_sk'(\varepsilon_gT_g^4-\alpha_gT_s^4) \tag{26}$$

where $A$ is the active surface area, $\varepsilon$ the emissivity and $\alpha$ the absorptivity.

## 2.4. Charge transport

The SOFC electrolyte has two functions: to transport oxide ions from the electrolyte to the anode and to block electron flow from the anode to the cathode [11]. The flow of electronic charges through external circuit balances the flow of the ionic charge through the electrolyte and electrical power is produced [43]. This transport can be described by considering the ion transport from the conservation of charge as [26]:

$$\nabla\cdot i=0=\nabla\cdot i_{io}+\nabla\cdot i_{el} \tag{27}$$

$$-i_{io}=\nabla\cdot i_{el} \tag{28}$$

$$i_{io}=-\sigma_{io}^{eff}\nabla\phi_{io} \tag{29}$$

Eq. (29) is Ohm's law, $i_{io}$ and $i_{el}$ are charge fluxes for ions and electrons, respectively, and $\varphi_{io}$ is the ionic potential in the electrolyte. The interfaces/boundaries can be defined as electric potential ($V=V_0$), electric isolation ($n\cdot i=0$) or ground conditions ($V=0$). The effects of the electrochemical reactions are either defined as source terms in the governing equations or as interface conditions

at the electrolyte/electrode interface, as previously discussed [32]. Bessler et al. [37] assume that the electrode component has a constant electric potential.

The Nernst potential is usually calculated as the sum of the potential differences across the anode and cathode [26]:

$$E = \Delta\phi_a + \Delta\phi_c \tag{30}$$

where $E$ is the reversible electrochemical cell voltage and $\phi$ the charge potential.

### 2.5. Interaction issues

The mass-, heat-, momentum- and charge transport and the chemical reactions are dependent on each other. The fluid properties and the flow field (momentum transport) depend on the temperature and the species concentrations. The (electro-) chemical reaction rates depend on temperature, species concentrations and available surface areas for catalytical reactions. The chemical reactions generate and consume heat, i.e., the temperature distribution depends on the chemical reaction rates, as well as on the solid and the gas properties (for example the heat capacity and the conductivity). All these dependences require that the governing equations are solved coupled [1].

## 3. Microcatalytic reaction mechanisms

### 3.1. Electrochemical reactions

Electrochemical reactions occur at the TPB, i.e., the region where the electrode, electrolyte and gas phase meet. Ions migrate in the ionic phase, conduction of electrons occurs in the electronic phase and transport of gas molecules takes place in the porous part of the electrodes. A larger TPB area gives more reaction sites (=lower activation polarization in the electrodes) [16]. Note that the TPB needs to be connected to the rest of the structure, i.e., the pores need to be connected through the surrounding pore network to the fuel/air stream, the nickel phase must be connected to the current collector and the YSZ phase to the bulk YSZ electrolyte [29].

The total pressure is lower close to TPB, compared to other parts of the cathode due to the consumption of oxygen molecules at TPBs. This gradient makes the transport of oxygen from the channel towards the electrolyte easier. The TPB area in the electrode depends on the particle diameter. A reduction of the particle diameter increases the TPB area, at the same time the Knudsen diffusivity and the flow permeability are reduced. In [16] it is found that most of the electrochemical reaction occurs within 10 μm (from the electrolyte interface) for the anode and 50 μm for the cathode when the mean particle diameter is 1 μm [16].

At the interface between the electrode and electrolyte the Bulter–Volmer equation can be used to calculate the volumetric current density [30]:

$$i = i_0\left\{\exp\left(\beta\cdot\frac{n_e\cdot \mathrm{F}\cdot\eta_{act,e}}{\mathrm{R}\cdot T}\right) - \exp\left(-(1-\beta)\frac{n_e\cdot \mathrm{F}\cdot\eta_{act,e}}{\mathrm{R}\cdot T}\right)\right\} \tag{31}$$

where F is the Faraday constant, R the ideal gas constant and $\beta$ the transfer coefficient, usually assumed to be 0.5. The Butler–Volmer equation can often be expressed as [30]:

$$i = 2\cdot i_0\cdot\sinh\left(\frac{n_e\cdot \mathrm{F}\cdot\eta_{act,e}}{2\cdot \mathrm{R}\cdot T}\right) \tag{32}$$

$$\eta_{act,e} = \frac{2\cdot \mathrm{R}\cdot T}{n_e\cdot \mathrm{F}}\sinh^{-1}\left(\frac{i_e}{2\cdot i_{0,e}}\right) \tag{33}$$

$$i_0 = \frac{\mathrm{R}\cdot T}{n_e\cdot F}k''_e\cdot\exp\left(\frac{-E_e}{\mathrm{R}\cdot T}\right) \tag{34}$$

where $i_0$ is the exchange current density, $k''$ the pre-exponential factor and $E$ the activation energy.

The charge transfer processes are ones of the least understood aspects of fuel cell chemistry [29,44]. It is expected that understanding the mechanism of the surface reactions that occur close to the anode TPB is important for the future advances of the SOFC development [44]. Most models in the literature assume a single global charge transfer reaction, leading to the Bulter–Volmer equation (Eq. (31)). Adsorption/desorption, surface diffusion, the formation of hydroxyl and a charge transfer reaction are all found to be feasible rate-limiting steps in an SOFC (anode) model [29].

A five elementary reaction mechanism for the electrochemical reactions used by Lee et al. [29], among others, reads:

$$\mathrm{H_2(g)} + 2(\mathrm{Ni}) \iff 2\mathrm{H(Ni)} \tag{35}$$

$$\mathrm{H(Ni)} + \mathrm{O_2(YSZ)} \iff (\mathrm{Ni}) + \mathrm{OH^-(YSZ)} + \mathrm{e^-(Ni)} \tag{36}$$

$$\mathrm{H(Ni)} + \mathrm{OH^-(YSZ)} \iff (\mathrm{Ni}) + \mathrm{H_2O(YSZ)} + \mathrm{e^-(Ni)} \tag{37}$$

$$\mathrm{H_2O(YSZ)} \iff \mathrm{H_2O(g)} + (\mathrm{YSZ}) \tag{38}$$

$$\mathrm{O_0^X(YSZ)} + (\mathrm{YSZ}) \iff \mathrm{O^{2-}(YSZ)} + V_0^{\cdot\cdot}(\mathrm{YSZ}) \tag{39}$$

Hydrogen is assumed to be adsorbed only at the nickel (Ni) surface and other surface species at the electrolyte surface (YSZ). Interactions between (1) adsorbed atomic hydrogen H(Ni), an empty surface site (Ni) and an electron $e^-$(Ni), (2) a lattice oxygen $O_0^X$(YSZ) and an oxygen vacancy, $V_0^{\cdot\cdot}$(YSZ) within the YSZ electrolyte, and (3) hydroxyl ion $OH^-$(YSZ), water $H_2O$(YSZ), oxygen ion $O^{2-}$(YSZ) and empty YSZ sites are considered in this reaction mechanism (Eqs. (35)–(39)). The expression for the exchange current density depends on the assumption of which equation is the rate-limiting one, as shown in Table 1. Note that different expressions can be obtained, based on the dependence on the partial pressure of the product and reactants, anodic or cathodic reaction coefficient ($k_a$ or $k_c$) and the equilibrium constants ($K$) for the respective reactions. Determination of the actual rate-limiting reactions among Eqs. (35)–(38) requires a very careful analysis and fitting of experimental data to the different theoretical derivations. Also the anodic and cathodic charge-transfer coefficients in the Butler–Volmer equation depends on the assumption of the rate-limiting equations. The hydrogen adsorption rate can be described as: $i^*_{H_2}\cdot p_{H_2}$, where $i^*_{H_2}$ can be seen as an adjustable parameter (connected to the exchange current density) to match the experimentally observed performance [29].

Vogler et al. [44] studied the electrochemical hydrogen oxidation reaction at nickel/YSZ anodes and considered Eqs. (35)–(39) but also the YSZ surface reaction between water and oxygen ions, Ni surface reaction for water and hydroxyl ions, and five additional charge transfer reactions. Their computational model is based on elementary physics and chemical processes (without the assumption of a specific rate-determining step). Models and experiments

**Table 1**
Exchange current density in Bulter–Volmer equation when assuming different rate-limiting conditions for the anode electrochemical reactions [29].

| Rate limiting reaction | Exchange current density ($i_0$) | Hydrogen adsorption ($i^*_{H_2}\cdot p_{H_2}$) |
|---|---|---|
| Eq. (35) | $i_0 = i^*_{H_2}(p_{H_2})$ | $2Fl_{TPB}\frac{S^0_i}{\sqrt{2\pi RTM_{H_2}}}\cdot p_{H_2}$ |
| Eq. (36) | $i_0 = i^*_{H_2}\frac{p_{H_2O}^{1/4}\left(K_{35}p_{H_2}\right)^{1/4}}{1+\left(K_{35}p_{H_2}\right)^{1/2}}$ | $\frac{2Fl_{TPB}K_{39}^{1/4}k_{36,a}^{3/4}k_{36,c}^{1/4}}{(K_{37}K_{38})^{1/4}}\cdot p_{H_2}$ |
| Eq. (37) | $i_0 = i^*_{H_2}\frac{p_{H_2O}^{3/4}\left(K_{35}p_{H_2}\right)^{1/4}}{1+\left(K_{35}p_{H_2}\right)^{1/2}}$ | $2Fl_{TPB}k_{37c}(K_{37}K_{36})^{1/4}\left(\frac{K_{39}}{K_{38}}\right)^{3/4}\cdot p_{H_2}$ |
| Eq. (38) | $i_0 = i^*_{H_2}(p_{H_2O})$ | $2Fl_{TPB}K_{39}k_{38b}\cdot p_{H_2}$ |

are compared to determine the anode performance and to estimate the pre-exponential factors and the activation energies. Only the forward-rate coefficients from the experimental and literature data are used and then the reverse-rate constants are calculated according to thermodynamic consistency. Seven possible different combinations of one or two elementary charge transfer reactions are investigated and compared to the experimental data. It is found that the hydrogen spillover mechanisms (Eq. (37) together with Eq. (40)) have best agreement with the experimental data. The calculated activation energy (using experimental data) is higher than expected. This may be explained by an unfavorable geometry at atomic scale.

$$H(Ni) + O^{2-}(YSZ) \iff (Ni) + OH^{-}(YSZ) + e^{-}(Ni) \quad (40)$$

A high TPB length (or area) is required for high electrochemical performance, and of crucial importance for the fuel cell performance. Janardhanan et al. [45] concluded that the maximum volume specific TPB length is achieved at 50% porosity (while other parameters are fixed). A mathematical model is developed in [45] based on porosity, particle diameter and volume fraction of the ionic- and electronic phase. The calculation can be based on both uniform and non-uniform particle size distributions.

Asinari et al. [46] uses the Lattice-Boltzmann method to construct a 3D microscopic topology, where the TPB area is calculated. Both the electron and the ion dynamics are included in the numerical model. In order to realize an electrochemical reaction the electron conducting cell (EEC) must be in contact with the electron sink, i.e., at least one connection path must exist between the EEC in question and the collection grid.

Martinez and Brouwer [47] have developed a Monte Carlo percolation model to be able to characterize the factors controlling the TPB formation within an SOFC electrode. The model considers ionic and electronic conductor, gas phase percolation, competition between percolation of gas and electronically conducting phases. It is found that physical processes such as sorbate transport significantly affect the TPB formation. It is also concluded that the TPB formation is most effective when the electronic volume fraction is quite low.

The contribution to the gas species distributions (in mol/($m^2$s)) by the electrochemical reactions is given as [25,27,48]:

$$r_{H_2} = \frac{-i}{2 \cdot F} \quad (41)$$

$$r_{H_2O} = \frac{i}{2 \cdot F} \quad (42)$$

$$r_{O_2} = \frac{-i}{4 \cdot F} \quad (43)$$

where $i$ is the current density and F the Faraday constant.

### 3.2. Internal reforming reactions

Internal reforming reactions inside SOFC porous anodes enable the conversion of hydrocarbon fuels (and water) into hydrogen and carbon monoxide, and further carbon monoxide (and water) to hydrogen. The heat, needed by the steam reforming reaction, is generated in the electrochemical reactions at the active surface (TPB) between the porous anode/electrolyte and cathode/electrolyte. A good heat transfer (in terms of short heat transfer distance between heat generation and consumption within the cell) can be achieved and the conversion efficiency is increased. Hydrogen and carbon monoxide can be oxidized as soon as they are produced by the reforming reactions, and steam produced by the electrochemical reaction (Eq. (2)) can be used in the reforming reactions (Eqs. (4) and (5)) [15,49].

The steam reforming of hydrocarbon fuels (Eqs. (4) and (5)) could either take place before the fuel cell stack (in an external pre-reformer) or inside the cell in the anode (internal reforming). A pre-reformer needs extra added steam, since it cannot use the steam generated in the electrochemical reactions. The internal steam reforming reaction takes place over ceramic-supported nickel catalysts and decreases the requirement for cell cooling (less surplus of air). Less steam is needed for the reforming reactions and finally it offers advantages with respect to the capital cost. Up to half of the heat produced by the oxidation reaction (exothermic) could be "consumed" by the steam reforming process. This would improve the system electrical efficiency [39].

The probability for carbon depositions depends on the steam/methane ratio. It has been well established that the key reactions occur over a surface layer of nickel atoms. If a layer of carbon is allowed to build up and attach to a nickel crystallite rapid catalyst breakdown can occur, due to the graphite formation. It should be noted that hydrocarbons with a longer coal chain than methane have a higher propensity for carbon deposition. To avoid the carbon deposition inside the SOFC anode pre-reforming have to be carried out before the fuel enters into the cell at a lower temperature at which carbon deposition does not occur [50].

In a conventional (high temperature (HT)) SOFC (with nickel content of about 50 vol.% and operating temperature about 1000 °C) the endothermic reaction is very fast. This can result in a temperature drop at the inlet of the stack. The temperature gradient results in thermal tensions, which in the worst case causes mechanical failure of the cells [39]. The problem of the tensions and big temperature gradients close to the inlet could be solved with different approaches:

(1) Lowering the operating temperature to an intermediate range to reduce the steam reforming reaction rates [51].
(2) Recycling a part of the anode gas to obtain a dilution of the fuel. The rate of reforming reactions decreases, due to decrease in fuel concentration. A 50% recycling results in sufficient steam for the reforming reactions and the cost for a separate water supply is saved [39].
(3) The anode material can be designed with the aim of a decreased steam reforming activity. Until now these new SOFC materials (such as iron or copper) have too low electronic conductivity to meet the real world requirements. When nickel is replaced during the fabrication process with for example iron, a less catalytic active anode regarding the reforming activity is constructed. This is in the short term a promising method, and this approach is based on well-established production processes. Other researches replace nickel with copper and the same effect has been reached [39].

The reforming reactions occur in the porous anode. The reaction rates can be described with simplified global expressions (Section 3.2.1) or detailed expressions for surface chemical reactions (Section 3.2.2). Some models in literature are compared in terms of internal reforming reaction mechanisms and involved gas species, as in Table 2. It is found that comparison with experimental data is rare. Most of the models [6,23,52–55] use an equilibrium approach both for the water–gas shift reaction and steam reforming reaction. For the steam reforming reaction a comparison of the kinetic expression with different dependences of water and methane is presented in this table. It is common to use an inlet concentration considering 30% pre-reformed natural gas, which is also specified as International Energy Agency (IEA) conditions [6,23,54–55]. The ratio of water to methane is varied, in [53], to study the effect of gradual vs. direct internal reforming reactions.

**Table 2**
Comparison of models considering internal reforming reactions.

| | Sanchez et al. [52] | Klein et al. [53] | Janardhanen and Deutschmann [27] | Nagel et al. [54] | Wang et al. [55] | Lehnert et al. [23] | Aguiar et al. [51] | Ni et al. [6] |
|---|---|---|---|---|---|---|---|---|
| *Fuel (inlet vol.%)* | | | | | | | | |
| $CH_4$ | 0.09 | [a] | 0.970 | 0.171 | 0.171 | 0.171 | 0.280 | 0.171 |
| CO | 0.07 | n/a | 0 | 0.029 | 0.029 | 0.029 | 0.005 | 0.029 |
| $CO_2$ | 0.22 | n/a | 0 | 0.044 | 0.044 | 0.044 | 0.030 | 0.044 |
| $H_2$ | 0.28 | n/a | 0 | 0.263 | 0.263 | 0.263 | 0.120 | 0.263 |
| $H_2O$ | 0.34 | [a] | 0.030 | 0.493 | 0.493 | 0.493 | 0.565 | 0.493 |
| *Equations* | | | | | | | | |
| Equilibrium reactions | X | X | | X | X | X | | X |
| Surface reactions | | | X | | | | | |
| $m$ (Eq. (44))[b] | 1/0.85 | n/a | n/a | 1/0.85/1 | n/a | n/a | 1/1/0.85/1.4 | n/a |
| $n$ (Eq. (44))[b] | 0/−0.35 | n/a | n/a | 0/−0.35/1 | n/a | n/a | −1.25/0/ −0.35/0.8 | n/a |
| *Comparison with exp. data* | | | | | | | | |
| *Yes* | | | X | | | | | |
| *No* | X | X | | X | X | X | X | X |

[a] The ratio of water to methane ($x_{H_2O}/x_{CH_4}$) is varied between 0.01 and 1.
[b] A comparison study between different equations for reaction rates, in the reference, is made when more than one value is presented [51–52,54].

### 3.2.1. Global reforming reaction kinetics

Methane can be converted to hydrogen and carbon monoxide inside the porous anode by the catalytic steam reforming. Carbon monoxide reacts further (inside the anode as well in the fuel channel) with steam to produce hydrogen and carbon dioxide according to the water–gas shift reaction [24,56]. The overall reactions can be written as Eqs. (4) and (5). Hydrogen reacts with oxygen ions at the anodic TPB and generates steam. As hydrogen is consumed and steam is generated, the water–gas shift reaction proceeds towards the right, i.e., more hydrogen is produced. The catalytic reforming reactions occurs at the surface of the porous structure inside the anode [55].

Several kinetic expressions considering the steam reforming reaction are developed in the literature. The reaction order varies significantly between the models, in terms of orders of methane and water ($m$ and $n$ in Eq. (44)), see Table 2 for typical values. The reaction order of methane ($m$) varies between 0.85 and 1.4. The highest difference in reaction orders is found for water ($n$), both negative and positive values exist, however, it has been shown that all these findings could be correct for the chosen operating conditions of the experiments. Small steam-to-carbon (SC) ratio gives positive reaction order of water. SC in the order of two yields the reaction orders of water close to zero, and high SC gives negative values [54]. Experimental work has shown that it is possible to change the steam reforming reaction orders by modifying the anode, for example $m$ increased from 0.85 to 1.4 and $n$ decreased from −0.35 to −0.8 when basic compounds are added in Ni–YSZ anode [51]. As seen in Table 2, comparison with experimental data is rare, but it is worth while to note that the reaction orders ($m$ and $n$) usually originate from fitting experimental data to a kinetic expression.

$$r_r = k \cdot p_{CH_4}^m \cdot p_{H_2O}^n \cdot \exp\left(\frac{-E_a}{R \cdot T}\right) \tag{44}$$

where $r_r$ is the reaction rate of steam reforming reaction (in mol/s/m), $p$ the partial pressure (in bar), R the ideal gas constant and $T$ the temperature. The reaction rate is converted to mol/s/m$^2$ after multiplying the reaction rate (mol/s/m) with the surface area ratio ($SA$). The kinetic expression (Eq. (44) can be compared to the equilibrium approach (Eq. (45)) [54].

$$r_{r,eq} = k \cdot p_{CH_4} \cdot p_{H_2O} \cdot \left(1 - \frac{p_{CO} \cdot p_{H_2}^3}{K_{e,STR} \cdot p_{CH_4} \cdot p_{H_2O}}\right) \tag{45}$$

where $K_e$ is the equilibrium constant. The reaction orders in Eq. (45) are the same as the molar proportions for the respective gas species in the global chemical reaction (1 for both methane and water for the forward reaction, and 3 for hydrogen and 1 for carbon monoxide for the backward reaction).

Different approaches for defining the water–gas shift reaction (Eq. (5)) can be found in literature: (1) Global reaction mechanism that considers reaction in the anode only [6,18]. (2) Global reaction mechanism that considers reaction in the anode and in the fuel channel [53,57]. (3) A more advanced reaction mechanism that includes catalytic surface reaction kinetics for steam reforming, water–gas shift reaction and the Boudouard mechanism can be found in [27,58]. It is frequently stated in literature [52–53,57] that the water–gas shift reaction should be considered to be in (or very close to) equilibrium state. When the equilibrium is assumed the reaction velocity can be expressed with an equilibrium-limited shift reaction rate expression, first order in carbon monoxide as [55]:

$$r_s = k_s \cdot p_{CO} \cdot \left(1 - \frac{p_{CO_2} \cdot p_{H_2}}{K_{e,s} \cdot p_{CO} \cdot p_{H_2O}}\right) \tag{46}$$

where $r_s$ is the reaction velocity of the water–gas shift reaction, $k_s$ the pre-exponential factor, $p_i$ partial pressure for the respective species and $K_{e,s}$ the temperature dependent equilibrium constant [55].

The concentration of the different gases in the anode (the steam reforming and the water–gas shift reactions) and fuel channel (the water–gas shift reaction) is changing as the above described reactions proceed:

$$r_{CH_4} = -r_r \tag{47}$$

$$r_{H_2} = 3 \cdot r_r + r_s \tag{48}$$

$$r_{CO} = r_r - r_s \tag{49}$$

$$r_{CO_2} = r_s \tag{50}$$

$$r_{H_2O} = -r_r - r_s \tag{51}$$

where $r_i$ is the reaction rate of species $i$. The catalytic steam reforming rate is expressed by $r_r$ and the water–gas shift reaction rate by $r_s$.

Andersson [33] uses a global approach to calculate internal reforming reactions for a single cell SOFC. The gas-phase tempera-

ture within the cell is presented in Fig. 3. The steam reforming reaction reduces the temperature close to the fuel channel inlet. The temperature is slightly lower on the air side (compared to the fuel side), due to a higher air flow rate. The initial temperature decrease is found to be 15 K in the anode, compared to 14 K in the cathode, 13 K in the fuel channel and 11 K in the air channel. For the case with higher operating temperature a higher reforming reaction rate is expected and also the temperature close to the inlet decreases faster. The mole fraction distribution of methane can be seen in Fig. 4. The concentration difference in the *y*-direction is due to the consumption of methane in the porous structure. Methane diffuses from the channel towards the porous anode. Note that the fuel channel length is 100 times bigger than the channel height.

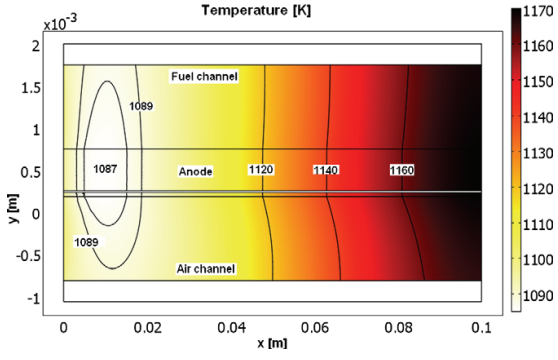


**Fig. 3.** Temperature distribution within the single cell (in the gas phase) when a global approach for internal reforming reactions is employed [33].

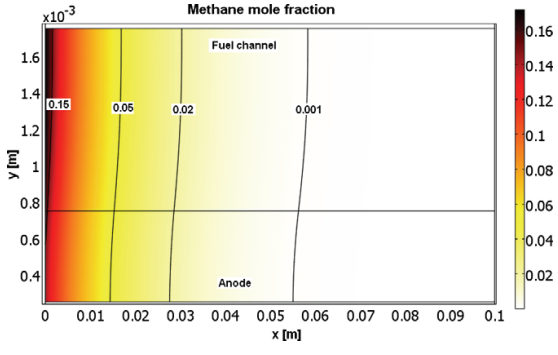


**Fig. 4.** The mole fraction of methane within the anode and fuel channel in Andersson's model [33].

### 3.2.2. Elementary surface reaction kinetics

Elementary-kinetic electrochemical modeling of SOFC electrodes is strongly connected to the heterogeneous catalysis and the surface chemistry (as shown in Figs. 5 and 6). Note that information considering the surface coverages are not available when the global approach is applied. Both for the anode and cathode there is (within the literature) a disagreement considering the involved reaction pathways, rate-limiting steps and intermediate species [37,59]. Elementary-kinetic models are normally limited to only the electroactive region, and couplings to transport models are still rare. The electroactive species occurring in the charge transfer reactions are surface-adsorbed intermediates. The surface coverage can be calculated with for example a mean-field approach, where it is assumed that the surface state can be described with average quantities, such as surface coverage, thermodynamic and kinetic adsorbate properties. The composition (segregation phenomena and impurities) and the detailed surface structure (steps, edges and terraces), occurring on the atomic scale, are then not further resolved, when using the mean-field approach. The surface concentration of the different species is normalized to the total concentration of available surface sites, yielding the dimensionless coverage. The surface species are coupled to the gas-phase species via desorption and adsorption reactions, and to bulk-phase species via surface/bulk exchange reactions. The surface species are also participating in the reactions among themselves [37].

An SOFC anode is normally fabricated as a porous metal–ceramic composite, where the gas, ceramic and metal phases occupy roughly 30% of the volume each, the characteristic pore dimensions are in the order of 1 μm [61]. Knowledge of the catalytic reaction mechanism considering reforming of hydrocarbons is counted as a key importance for designing an anode material with a high efficiency and a long life length [62].

Janardhanan and Deutschmann [63] have developed a multi-step heterogeneous reaction mechanism for Ni catalysts. The mechanism consists of 42 reactions, 6 gas-phase species and 12 surface adsorbed species. The mechanism is elementary in nature and covers the global aspects of the reforming, the water–gas shift and the Bouduard reactions. Most of the expressions are expressed in Arrhenius rate form and are dependent on the surface coverage.

Hofmann et al. [58] compare the heterogeneous reaction mechanism (HCR) from [48] with a simplified approach, where the

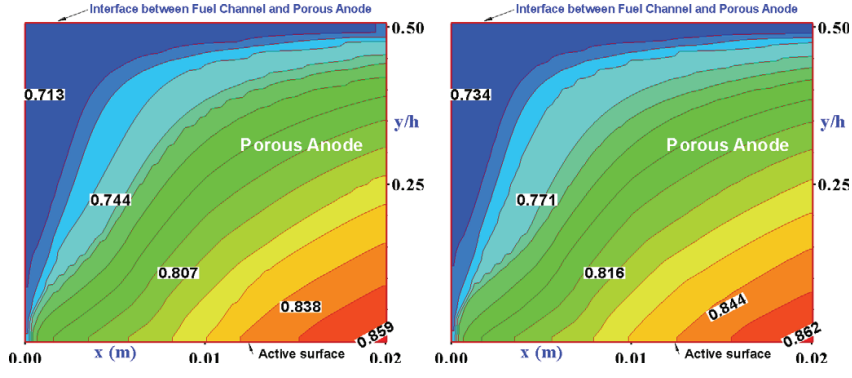


**Fig. 5.** Fraction of $Ni_s$ (empty catalytic sites) at 700 °C (left side) and 900 °C (right side) along main flow direction of an IT-SOFC anode [60].

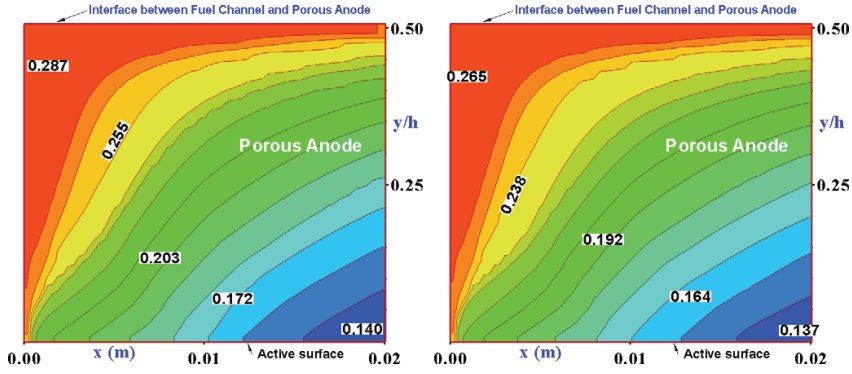


**Fig. 6.** Surface coverage of $H_s$ (hydrogen bound to the catalytic sites) at 700 °C (left side) and 900 °C (right side) along main flow direction of an IT-SOFC anode [60].

methane reforming is described according to a global kinetic approach and the water–gas shift reaction in equilibrium. The HCR model can be used to calculate the catalytic surface coverage. It is concluded that the HCR predicts a less steep methane consumption along the flow channel. Slower methane conversion means less hydrogen available throughout the cell. Also the temperature distribution is significantly affected by the steam reforming reaction, with a flatter temperature gradient for the HCR.

## 4. Multiscale SOFC modeling development

### 4.1. Micro-, meso- and macroscale approaches

An SOFC can be described by different length scales: system-scale ($\sim 10^2$ m), component scale ($\sim 10^1$ m), material aspect at the fuel cell/constituent ($\sim 10^{-2}$ m), flow/diffusion morphologies ($\sim 10^{-3}$ m), material structure/interface ($\sim 10^{-6}$ m, Monte Carlo (MC)- and continuum methods (CM) in Fig. 7), and functional material levels ($\sim 10^{-9}$ m, Density Functional Theory (DFT) and Molecular Dynamics (MD) in Fig. 7). Not only proper length scales are needed to describe various parts of an SOFC, also different time scales need to be considered. Cell charging and cathode gas thermal diffusion are in $10^{-3}$ s, convective transport is in $10^{-1}$ s, cell heating and anode streamwise thermal diffusion are in $10^3$ s and cathode streamwise thermal diffusion is in $10^4$ s [8]. A general relation between time- and length scales with proper modeling methods can be seen in Fig. 7, DFT and MD corresponds to the microscale, MC and CM to the mesoscale and methods with a length scales bigger than 10 μm (for example finite element method (FEM) and finite volume method (FVM)) to the macroscale. There are two basic approaches for interaction between the different modeling methods (i.e., multiscale modeling): (1) hierarchical methods and (2) hybrid or concurrent methods [64]. These approaches are further described in Section 4.1.4.

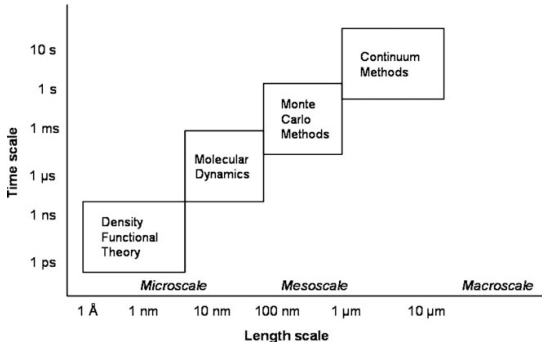


**Fig. 7.** Characteristic time and length scales for various methods [64].

Research of the physical phenomena is based on different levels of scales: micro-, meso- and macroscales. The microscale model corresponds in many cases to the atom or molecular level as thermo- or fluid dynamics and detailed chemical reactions are studied. The microscale does not need to be as small as the size of the molecules. A mesoscale model corresponds to a larger scale than a particle but a smaller one than the facility or the global flow field. Macroscale models match to the global flow field. Microscale modeling is in general more related to theoretical knowledge compared to macroscale modeling that is more related to empirical data. Empirical parameters for macroscale models could be based on the results from micro- or mesoscale models [12].

Instantaneous flow around individual moving particles can be calculated in microscale models. Flows corresponding to calculation cells, larger than particles but smaller than global flow fields, are calculated with mesoscale models. Trajectories of individual particles are calculated with particle motion equations for microscale modeling. The flow field is in mesoscale modeling divided into a number of small cells, but not as small as the particle size [12].

Different methods have been developed to describe different scales. Methods that can be used for SOFC modeling are listed in Table 3, based on micro-, meso- and macroscales.

#### 4.1.1. SOFC modeling at microscale

Frayret et al. [65] simulated microscopic aspects of oxygen diffusion in ceria-based materials in the ionic conductor with the DFT. This methodology is a good tool to study the connection between dopant ionic radius and diffusion at the atomistic scale. DFT is an "ab inito" method where the material properties are described by solutions of the Schrödinger equation. DFT models have a characteristic length scale of Å–nm and a time scale of ps–ns.

Cheng et al. [66] simulated the oxygen ion-hoping phenomenon inside a YSZ electrolyte with MD. MD can be used to model grain boundary structure, specific heat capacity and molecular structure. Systems up to $10^5$ atoms and a time scale of the order of ten ns can be modeled [67].

The Lattice-Boltzmann method (LBM) is used to model mass transport of gases inside the porous anode of an SOFC. The porous structure is based on scanning electron microscope (SEM) images, which are converted to digital form. Advantages of the LBM model

**Table 3**
Computational methods arranged after scales [12–15,17,36,64–72].

| Microscale | Mesoscale | Macroscale |
|---|---|---|
| Density Functional Theory (DFT) | Monte Carlo (MC) | Finite element method (FEM) |
| Quantum Chemistry (QC) | Brownian Dynamics (BD) | Finite volume method (FVM) |
| Lattice-Boltzmann method (LBM) | Dissipative Particle Dynamics (DPD) | Finite difference method (FDM) |
| Molecular Dynamics (MD) | | Spectral Methods (SM) |
| Mechanistic Models (MM) | | |

are that a detailed analysis of mass transfer can be carried out for the actual anode microstructure; this means that tortuosity is not used as a fitting parameter. LBM approach is according to an investigation in [68] accurate enough to model concentration polarization in 2D. By changing the number of void spaces present in the solid matrix the porosity in the LBM is varied.

More detailed information is needed about the kinetic, thermodynamic, and transport data of species and reactions, particular for the YSZ surface but also for other parts of the cell. This is achievable either with experiments from the surface science or with microscale theoretical approach, such as quantum chemical calculations with DFT and Molecular Dynamics calculations [44].

*4.1.2. SOFC modeling at mesoscale*

Modak and Lusk [67] applied kinetic MC to simulate the open-circuit voltage and electrical double layers of a doped electrolyte. Discrete time increments of various size are used to capture diffusion or adsorption in a single step. The physical property data generated by QC and MD can be utilized in the KMC model. Monte Carlo methods have a characteristic length scale of 100 nm–μm and a time scale of ms–s [15].

Huang et al. [69] employed COMSOL Multhiphysics to model the multhiphysics processes in the SOFC cathode–electrolyte interface considering the geometry and detailed distribution of the pores and the ionic conducting phase. The charge transfer rate, electron- and ion conduction are governed in a modeling domain extracted from actual materials encountered in the application. Note that FEM is developed for phenomena occurring in the macroscale. However Huang and coauthors are solving cathode electrochemical processes at mesoscale with COMSOL Multhiphysics.

*4.1.3. SOFC modeling at macroscale*

Cheng et al. [66] used the FEM and the commercial software COMSOL Multiphysics to solve the flow equations for macroscopic transport phenomena. Navier–Stokes equations are used to describe the flow conditions in the air and fuel channels and the Darcy law describes the flow conditions in the porous layer. FEM has a characteristic time scale of 1 s and above [65].

A clear relationship between the underlying physical conditions and numerical algorithm has made the FVM a popular method for commercial codes such as PHOENICS, FLUENT, CFX and STAR-CD [36]. Pasaogullari and Wang [70] as well as Autossier et al. [71] used FLUENT to solve the equations of momentum, mass, energy, multi-component species and electrochemical kinetics for an SOFC. Hussain et al. [17] employed the FVM to model the transport of multi-component species inside porous SOFC anodes.

Continuum electrochemical models are commonly used in many modeling studies, where the electrical current density, the cell voltage and the heat production are considered. The output voltage is normally expressed as the difference of the open-circuit voltage and the polarizations due to the electrical current generation. Continuum electrochemistry models can be used to determine effects of various designs and operating parameters on the generated power, maximum cell temperature, fuel conversion efficiency, stresses caused by temperature gradients and the effects of thermal expansions. The performance of a particular electrode under different operating conditions can be calculated, but sufficient information on how an electrode with different microstructure will perform cannot be calculated with the macroscale models. Chemical reactions and species transport characteristics (within the electrode) are affected by the microstructural parameters. Oxygen ion diffusion and surface diffusions are dependent on the available geometric paths through the structure. The reactive surface availability decides the surface chemical reaction rate. It can be concluded that the ability to model fuel cell characteristics at the microscale level is needed for the electrode design and optimization [72].

*4.1.4. SOFC modeling integration issues*

Multi-physical problems can often be described with a set of partial differential equations at different length scales. The coupled partial differential equations can be solved simultaneously in physical domains for corresponding physical phenomena. Fuel cell operation depends on complex interaction between multi-physics such as multi-phase fluid flow, mass transport, heat transfer and (electro-) chemical reactions [73]. Two basic integration approaches can be found: hierarchical method, and hybrid and cocurrent method. The hierarchical modeling starts at higher resolution (smaller scale) and properties are extracted and used as input to the next level method. The hierarchical methods are today the most developed methods for multiscale modeling [65]. Three different methods are used for hybrid approaches to describe various regions of the material with the appropriate time and length scale resolutions. The hybrid methods that permit cocurrent simulations are promising for the future development, since only one calculation needs to be performed, however, it requires more computational power compared to the hierarchical methods [65].

As an example a general hybrid molecular-continuum strategy, i.e., the point-wise coupling methodology (PWC) was presented in [74]. The solution in the entire domain is advanced through the continuum solver and the atomistic models are utilized to: (1) calculate transport properties (such as viscosity for the non-Newtonian fluids and thermal conductivity), (2) provide accurate boundary condition (such as temperature, slip velocity and tangential stress), and (3) substitute constitutive relations for the pressure among others. The MD solver is occupied to calculate macroscopic quantities at selected points in time and space for the prevailing continuum conditions. The transport of information from the molecular to the continuum model is less complicated compared to the opposite direction, however it is crucial for the accuracy and efficiency of the hybrid scheme. The calculation of the macroscopic variables are performed through averaging the corresponding microscopic properties. The PWC effectively avoids performing MC simulations for nearly identical continuum states, meaning a significant reduction in computational time [74].

The particle size in SOFCs is in the sub-micron scale, and the TPBs are in nanoscale. The morphology and properties of these scales are important for the performance of the fuel cell, since they control how much of the Gibbs free energy being available. It means that the sciences at nanoscale are critical to the performance at a system-scale. A robust design and multiscale analysis should consider those nano-details as well as macro system level [75].

Khaleel et al. [72] developed a multiscale approach, where the microscale electrochemistry model (Lattice-Boltzmann algorithm) calculates the performance of the porous electrode material based on material structure at the microstructure level, distribution of reaction surfaces, and transport of oxygen ions through the mate-

rial. The microscale electrochemistry modeling is used to calculate the overall fuel cell current–voltage relation, which is then used as input to the macroscale calculations (MARC software), where the current density, cell voltage and heat production are calculated.

Bove et al. [76] established a macroscale black-box model, using equations that are generally used for microscale models. The main problem with this approach is that the gas composition variation along the flow direction is neglected, the effect of fuel utilization variation cannot be estimated and the cell voltage is underestimated. The advantages is that the calculations are less time consuming compared to microscale modeling, and contains more information describing microscale phenomena compared to other macroscale models.

Cheng et al. [66] and Pasaogullari and Wang [70] introduced multiscale-concepts; however, they did not mention how the different scales interact with each other. It is frequently stated in the literature that data or property constants can be obtained from smaller scale and then used in a model made at a larger scale. However, information about the construction of this coupling is rare [27,64–65].

### 4.2. Validation

The numerical results of a computation are only an approximation of the real world conditions and considering that convergence is not sufficient, validation is a necessary step in the development of computational models [25,77]. A range of validity can be established between the developed model and experimental data. Models are usually validated by adjusting estimated physical prosperities values to reach certain agreement [78]. For example adjusting the reaction orders of methane and water in the methane steam reforming reaction according to experimental data is very common.

Microscale approaches, such as Lattice-Boltzamann (LB) method can be used to model multi-component gas transport in SOFCs. The diffusive flow in the porous electrodes can then be simulated without any empirical modification of diffusion coefficients, such as medium porosity and tortuosity. Validation of these microscale models are not required [79].

Tortuosity is an important parameter for characterization of fluid flow through porous media in many macroscale models. It is normally considered as a geometric parameter, however, it was originally introduced as a kinematic property, equal to the relative average length of the flow path of a fluid particle from one side of a porous structure to the other side. If a suitable model is developed for the porous medium, then the tortuosity becomes a geometric property. Frequently in the literature tortuosity is treated as a fitting property (used for validation purposes), i.e., the tortuosity should then not be seen as a kinematic- or geometric property [46].

Nicotella et al. [80] has developed a model considering mass and charge transport and electrochemical reactions in porous composite cathodes. A validation is performed to compare the experimental data on polarization resistance obtained by impedance spectroscopy on cathodes of different thicknesses with the simulations. It is concluded that the developed model can replicate the experimental results concerning the dependence of the polarization resistance on the cathode thicknesses, because non-uniform morphological properties are taken into account.

Peksen et al. [81] has developed a computational model (based on FVM) for SOFC pre-reformer considering fluid flow, heat transfer, chemical reacting species transport. Surface temperature measurements and species gas compositions are used for validation of the 3D model. Also experimental validation is performed using thermocouples and gas chromatography.

Suwanwarangkul et al. [19] modeled transport phenomena inside SOFC anodes. Fick's- Stefan–Maxwell- and Dusty-Gas models were compared. Experimental data from literature were used to compare the calculated concentration over-potential for $H_2$–$H_2O$–Ar and CO–$CO_2$ systems.

### 4.3. State-of-the-art in multiscale SOFC modeling

Mathematical models are central tools in examining and understanding effects of various operating parameters and designs, as well as promoting the SOFC development. Results from modeling can be used to select optimal operating conditions and to optimize the design. Numerical results obtained from commercial softwares show acceptable accuracy if compared with experimental data as well other modeling predictions [4].

The current state-of-the-art in SOFC modeling is to use computational fluid dynamics (CFD) to solve the transport equations and couple the solution to an electrochemical model. Some models found in the literature are compared in terms of methodology for the modeling, see Table 4. Most of the investigated models [15,17,20,22,24–26] use the finite volume method (FVM) for solving the governing equations. Most authors [15,17,22,24–26,33,82] include a parameter study to test their models, but comparison with experimental data is rare. Regarding the flow configuration co-, counter- as well as cross flow can be found in the literature. Note that it is not relevant to compare flow configurations for models at the component level.

Most authors [15,20,22,24,82] do not include material characteristics that are dependent on the temperature. However, Refs. [15,17,33] define the conductivity as temperature dependent, while the other material characteristic parameters are still defined at one temperature only. All investigated models include governing equations for mass transport, most of them [15,20,24–26,33,82] for momentum transport, some of them for energy [15,20,26,33] and ionic transport [17,22,24–26]. Pramuanjaroenkij et al. [26] included simultaneously the governing equations for mass-, energy-, momentum-, and ionic transport. Models are developed with different aims at component, cell or stack level, and calculations considering entire fuel cells system can also be found in the literature [83], however, is not reviewed in this study. Steady-state conditions are applied in a majority of the models developed so far [19].

The fuel cell is considered as a black box in zero-dimensional modeling. The principles of thermodynamics and electrochemistry are used to find output parameters such as cell efficiency, cell voltage and power output. 1D modeling can be used to model co- and counter-flow, variation of temperature and concentrations along the flow direction may be studied. There are several sections possible for a 2D cross-section, and the connection between interconnect and electrode is normally neglected in 2D modeling. 3D modeling is needed to acquire detailed knowledge of SOFC performance [42].

Most of the studies use only common SOFC material in their modeling, new studies are definitely needed to compare alternative materials, to assess the effect of material on efficiency, degradation, etc. Many thermal models consider the cell level only and assume the cell boundaries to be insulated. Stack or system level models should be developed further. Electrochemical modeling considering microstructure geometry and material properties is so far rare in the literature.

It is common to assume that the current density is uniform over the entire electrode, note that this is basically only valid as long as the gas concentration is uniform along the flow channel. The total pressure gradient inside the anode is normally assumed to be neglible. This is correct for a very short cell and when only hydrogen and carbon monoxide is used as fuel, because no net change in the number of moles occur in the gas phase [19].

**Table 4**
Comparison of SOFC models.

| | Pramuanjaroenkij et al. [26] | Hussain et al. [17] | Yuan and Sundén [15] | Yakabe et al. [24] | Haberman and Young [20] | Tseronis et al. [82] | Tseronis et al. [22] | Andersson [33] |
|---|---|---|---|---|---|---|---|---|
| *Dimensions* | | | | | | | | |
| 0D | | | | | | | | |
| 1D | | X | | | | X | | |
| 2D | X | | | | | X | X | X |
| 3D | | | X | X | X | | | |
| *Discretization method* | | | | | | | | |
| FDM | | | | | | | | |
| FVM | X | X | X | X | X | | X | |
| FEM | | | | | | X | | X |
| *Level of modeling* | | | | | | | | |
| Component | | X | X | X | | X | X | |
| Cell | X | | | X | | | | X |
| Stack | | | | | ½ | | | |
| System | | | | | | | | |
| *Comparison with exp. data* | | | | | | | | |
| Yes | | | | X | | | X | |
| No | X | X | X | | X | X | | X |
| *Governing equations* | | | | | | | | |
| Mass | X | X | X | X | X | X | X | X |
| Energy | X | | X | | X | | | X |
| Momentum | X | | X | X | X | X | | X |
| Ionic/ electronic | | X | X | | X | | | X |
| *Flow configuration* | | | | | | | | |
| Co | X | n/a | n/a | | | n/a | n/a | X |
| Counter | | n/a | n/a | X | | n/a | n/a | X |
| Cross | | n/a | n/a | | X | n/a | n/a | |
| *Material char. T dep.* | | | | | | | | |
| Yes | $\sigma$ | $\sigma$ | | | | | | $\sigma$ |
| No | | | X | X | X | X | X | |
| *Parameter study* | | | | | | | | |
| Yes | X | X | X | X | | X | X | X |
| No | | | | | X | | | |

*4.3.1. How far can SOFC modeling reach?*

There are still unresolved issues in fuel cell modeling. The exchange current density is used to calculate the activation polarization and it depends on the catalyst for the electrochemical reactions. One problem is that the data in literature is not identical or well explained. Further study of the mechanisms behind the activation polarization is important for the further development [78].

The macroscale modeling have gained a lot of success during the last years in understanding complex phenomena occurring during FC operation and it has been possible to improve the FC design. However the microstructure of the porous electrodes is normally not included in the model. Porosity and tortuosity are, for macroscale models, normally treated as fitting parameters. The difficulty is that these parameters are used to compensate for inaccurate modeling of several phenomena. It has also been shown that different porous microstructure can be characterized with the same porosity, but different hydraulic characteristics, i.e., phenomena at the microscale are not described well by macroscale parameters. One way to overcome these limitations is to apply LBM to simulate gas flow in porous media. It should be noted that LBMs do not require pressure–velocity decoupling or solution of a large system of algebraic equations [46]. Fuel cell modeling can be significantly improved if submodels being not too expensive (in computational time) are included in a general model [78].

A challenge for the future is to develop approaches for multiscale multi-physics modeling considering coupling of fluid flow, heat transfer, species transport, electrochemical kinetics and also reforming kinetics (when hydrocarbon fuels are used). It has been found that the reaction kinetics for the reforming reactions requires rigorous studies, several heterogeneous reaction mechanisms are developed. However, they did not match each other very well [78].

A grand challenge for future SOFC modeling development is the concept of an inverse coupled multi-physics modeling, where the nano-structured material design is calculated from the defined system requirements, instead of material and other engineering specifications. The activation- and diffusion related polarization losses depend strongly on the nano-structure of the cathode and anode materials, and are good examples for application of this potential approach [75].

## 5. Conclusions

The fuel cell is not a new invention, the principle dates back to 1838. However, the fuel cell technology is approaching the commercial phase, the potential for the future is enormous and fuel cells can be key components in a future sustainable energy system. To achieve this, the production cost must be decreased and the life time must be increased. One way to decrease the operating cost and also increase the life time is to increase the understanding of multiscale transport- and reaction mechanism within the cell. Fuel cell operation depends on complex interaction between multiphysics such as fluid flow, mass and heat transfer and (electro-) chemical reactions at various scales. Coupling of these multiscale phenomena, i.e., multiscale modeling is promising for future fuel cell research. Micro- and macroscale physical phenomena and chemical reactions could be solved together.

Future models need to go down in scale, to specify where the electrochemical and internal reforming reaction occurs, i.e., where

heat is released. Validation with experimental data is still too rare, and the quality of the models will be increased by doing this. Detailed analysis of mass transport phenomena with electrochemical processes, velocity, temperature distributions and the microstructure of component material properties need to be integrated for a performance analysis and efficiency optimization.

A challenge faced is to further develop multiscale models for fuel cell designs. They can provide a clear understanding of operating conditions, transport and reaction phenomena at the microscale connected to, e.g., conditions in the air and fuel channels at the macroscale. It is possible to couple different physical models, for example models at the microscale describing transport phenomena inside an anode with a macroscale model describing the entire fuel cell. Use of multiscale modeling in fuel cell research will lead to an increased power density and also to a decreased cost for development and production, and increased energy efficiency, etc.

## Acknowledgement

The Swedish Research Council (VR) and the European Research Council (ERC) support the current research.

## References

[1] Li P-W, Schaefer L, Chyu MK. Multiple transport processes in solid oxide fuel cells. In: Sundén B, Faghri M, editors. Transport phenomena in fuel cells. UK: WIT Press; 2005 [chapter 1].
[2] Yuan J, Faghri M, Sundén B. On heat and mass transfer phenomena in PEMFC and SOFC and modelling approaches. In: Sundén B, Faghri M, editors. Transport phenomena in fuel cells. UK: WIT Press; 2005 [chapter 4].
[3] Fuel cell handbook, 7th ed. Morgantown, Virginia (USA): EG&G Technical Services Inc., US Department of Energy; 2004.
[4] Kackac S, Pramuanjaroenkij A, Zhou X. A review of numerical modeling of solid oxide fuel cells. Int. J. Hydrogen Energy 2007;32:761–86.
[5] Zhu B. Next generation fuel cell R&D. Int. J. Energy Res. 2006;30:895–903.
[6] Ni M, Leung DYC, Leung MKH. Modeling of methane fed solid oxide fuel cells: comparison between proton conducting electrolyte and oxygen ion conducting electrolyte. J. Power Sources 2008;183:133–42.
[7] Saxe M. Bringing fuel cells to reality and reality to fuel cells, Doctoral thesis. Sweden: Department of Chemical Sciences and Engineering, KTH – Royal Institute of Technology; 2008.
[8] Kemm M. Dynamic solid oxide fuel cell modelling for non-steady state simulation of system applications. Doctoral thesis. Sweden: Department of Energy Sciences, Lund University; 2006.
[9] Zhu H, Kee R, Janardhanan V, Deutschmann O, Goodwin D. Modeling elementary heterogeneous chemistry and electrochemistry in solid-oxide fuel cells. J. Electrochem. Soc. 2005;152:A2427–40.
[10] Ni M, Leung MKH, C Leung DY. Ammonia-fed solid oxide fuel cells for power generation – a review. Int. J. Energy Res. 2009;33:943–59.
[11] Gooenough JB, Huang Y. Alternative anode materials for solid oxide fuel cells. J. Power Sources 2007;173:1–10.
[12] Ni M, Leung MKH, Leung DYC. Micro-scale modeling of solid oxide fuel cells with micro-structurally grades electrodes. J. Power Sources 2007;168:369–78.
[13] Calise F, Feruzzi G, Vanoli L. Parametric exergy analysis of a tubular solid oxide fuel cell (SOFC) stack through finite-volume model. Appl. Energy 2009;86:2401–10.
[14] Santin M, Traverso A, Magistri L. Liquid fuel utilization in SOFC hybrid systems. Appl. Energy 2009;86:2204–12.
[15] Yuan J, Sundén B. Analysis of chemically reacting transport phenomena in an anode duct of intermediate temperature SOFCs. J. Fuel Cell Sci. Technol. 2006;3:687–701.
[16] Hyun NJ, Hyup JD. A comprehensive micro-scale model for transport and reaction in intermediate temperature solid oxide fuel cells. Electrochim. Acta 2006;51:3446–60.
[17] Hussain MM, Li X, Dincer I. Mathematical modeling of transport phenomena in porous SOFC anodes. Int. J. Therm. Sci. 2007;46:48–86.
[18] Yuan J, Huang Y, Sundén B, Wang WG. Analysis of parameter effects on chemical coupled transport phenomena in SOFC anodes. Int. J. Heat Mass Transfer 2009;45:471–84.
[19] Suwanwarangkul R, Croiset E, Fowler MW, Douglas PL, Entchev E, Douglas MA, et al. Dusty-gas and Stefan–Maxwell models to predict the concentration overpotential of a SOFC anode. J. Power Sources 2003;122:9–18.
[20] Haberman BA, Young JB. Three-dimensional simulation of chemically reacting gas flows in the porous support structure of an integrated-planar solid oxide fuel cell. Int. J. Heat Mass Transfer 2004;47:3617–29.
[21] Ferguson JR, Fiard JM, Herbin R. Three-dimensional numerical simulation for various geometries of solid oxide fuel cells. J. Power Sources 1996;58:109–22.
[22] Tseronis K, Kookos I, Theodoropoulos K. Modelling mass transport in solid oxide fuel cell anodes: a case for a multidimensional dusty gas-based model. Chem. Eng. Sci. 2008;63:5626–38.
[23] Lehnert W, Meusinger J, Thom F. Modelling of gas transport phenomena in SOFC anodes. J. Power Sources 2000;87:57–63.
[24] Yakabe H, Hisinuma M, Uratani M, Matsuzaki Y, Yasuda I. Evaluation and modeling of performance of anode-supported solid oxide fuel cell. J. Power Sources 2000;86:423–31.
[25] Bove R, Ubertini S. Modeling solid oxide fuel cell operation: approaches, techniques and results. J. Power Sources 2006;159:543–59.
[26] Pramuanjaroenkij A, Kakac S, Zhou XY. Mathematical analysis of planar solid oxide fuel cells. Int. J. Hydrogen Energy 2008;33:2547–65.
[27] Janardhanan V, Deutschmann O. CFD analysis of a solid oxide fuel cell with internal reforming. J. Power Sources 2006;162:1192–202.
[28] Ivanov P. Thermodynamic modeling of the power plant based on the SOFC with internal steam reforming of methane. Electrochim. Acta 2007;52:3921–8.
[29] Lee WY, Wee D, Ghoniem AF. An improved one-dimensional membrane-electrolyte assembly model to predict the performance of solid oxide fuel cell including the limiting current density. J. Power Sources 2009;186:417–27.
[30] Chan SH, Khor KA, Xia ZT. A complete polarization model of a solid oxide fuel cell and its sensitivity to change of cell component thickness. J. Power Sources 2001;93:130–40.
[31] Ni M, Leung MKH, Leung DYC. Micro-scale modeling of a functionally graded Ni–YSZ anode. Chem. Eng. Technol. 2007;30:287–592.
[32] COMSOL Multiphysics 3.5 user guide. Stockholm, Sweden; 2008.
[33] Andersson M. Modeling and simulation for anode-supported SOFCs. Licentiate thesis. Department of Energy Sciences, Lund University; 2009.
[34] Bi W, Chen D, Lin Z. A key geometric parameter for the flow uniformity in planar solid oxide fuel cell stacks. Int. J. Hydrogen Energy 2009;34:3873–84.
[35] Le Bars M, Grae Worster M. Interfacial conditions between a pure fluid and a porous medium, implications for binary alloy solidification. J. Fluid Mech. 2006;550:149–73.
[36] Versteeg HK, Malalasekera W. An introduction to computational fluid dynamics. The finite volume method. UK: Pearson; 1995.
[37] Bessler WG, Gewies S, Vogler M. A new framework for physically based modeling of solid oxide fuel cells. Electrochim. Acta 2007;53:1782–800.
[38] Lister S, Djilali N. Two-phase transport in porous gas diffusion electrodes. In: Sundén B, Faghri M, editors. Transport phenomena in fuel cells. UK: WIT Press; 2005 [chapter 5].
[39] Boder M, Dittmeyer R. Catalytic modification of conventional SOFC anodes with a view to reducing their activity for direct internal reforming of natural as. J. Power Sources 2006;155:13–22.
[40] Damm DL, Fedorov AG. Local thermal non-equilibrium effects in porous electrodes of the hydrogen fueled SOFC. J. Power Sources 2006;159:1153–7.
[41] Chao CH, Hwang AJJ. Predictions of phase temperatures in a porous cathode of polymer electrolyte fuel cells using a two-equation model. J. Power Sources 2006;160:1122–30.
[42] Dincer I, Hamdullahpur F. A review on macro-level modeling of planar oxide fuel cells. Int. J. Energy Res. 2008;32:336–55.
[43] Haile SM. Fuel cell materials and components. Acta Mater. 2003;51:1981–2000.
[44] Vogler M, Bieberle-Hütter A, Gauckler L, Warnatz J, Bessler WG. Modelling study of surface reactions, diffusion, and spillover at a Ni/YSZ patterned anode. J. Electrochem. Soc. 2009;156:B663–72.
[45] Janardhanan VM, Heuveline V, Deutschmann O. Three-phase boundary length in solid-oxide fuel cells: a mathematical model. J. Power Sources 2008;178:368–72.
[46] Asinari P, Quaglia MC, von Sakovsky MR, Kasula BV. Direct numerical calculation of the kinematic tortuosity of reactive mixture flow in the anode layer of solid oxide fuel cells by Lattice Boltzmann Method. J. Power Sources 2007;170:359–75.
[47] Martinez AS, Brouwer J. Percolating modeling investigation of TPB formation in a solid oxide fuel cell electrode–electrolyte interface. Electochim. Acta 2008;53:3597–609.
[48] Janardhanan VM, Deutschmann O. Numerical study of mass and heat transport in solid-oxide fuel cells running on humidified methane. Chem. Eng. Sci. 2007;62:5473–86.
[49] Barzi YM, Ghassemi M, Hamedi MH, Afshari E. Numerical analysis of output characteristics of a tubular SOFC with different fuel compositions and mass flow rates. In: Eguchi K, Singhal SC, Yokokawa H, Mizusaki J, editors. Proceedings of solid oxide fuel cells 10 (SOFCX), ECS transactions, vol. 7; 2007. p. 1919–28.
[50] Clarke S, Dicks A, Pointon K, Smith T, Swann A. Catalytic aspects of the steam reforming of hydrocarbons in internal reforming fuel cells. Catal. Today 1997;38:411–23.
[51] Aguiar P, Adjiman CS, Brandon NP. Anode-supported intermediate-temperature direct internal reforming solid oxide fuel cell. II. Model-based dynamic performance and control. J. Power Sources 2005;147:136–47.
[52] Sanchez D, Chacartegui R, Munoz A, Sanchez T. On the effect of methane internal reforming modeling in solid oxide fuel cells. Int J. Hydrogen Energy 2008;33:1834–44.
[53] Klein J-M, Bultel Y, Georges S, Pons M. Modeling of a SOFC fuelled by methane: from direct internal reforming of gradual internal reforming. Chem. Eng. Sci. 2007;62:1636–49.

[54] Nagel F, Schildhauer T, Biollaz S, Stucki S. Charge, Mass and heat transfer interactions in solid oxide fuel cells operated with different fuel gases – a sensitivity analysis. J. Power Sources 2008;184:129–42.
[55] Wang L, Zhang H, Weng S. Modeling and simulation of solid oxide fuel cell based on the volume–resistance characteristic modeling technique. J. Power Sources 2009;177:579–89.
[56] Klein J-M, Bultel Y, Pons M, Ozil P. Current and voltage distributions in a tubular solid oxide fuel cell (SOFC). J. Appl. Electrochem. 2008;38:497–505.
[57] Aguiar P, Adjiman CS, Brandon NP. Brandon, anode-supported intermediate temperature direct internal reforming solid oxide fuel cell. I: model-based steady-state performance. J. Power Sources 2004;138:120–36.
[58] Hofmann P, Panopoulos KD, Fryda LE, Kakaras E. Comparison between two methane reforming models applied to a quasi-two-dimensional planar solid oxide fuel cell model. Energy 2008:1–7.
[59] King D, Strohm J, Wang X, Roh H-S, Wang C, Chin Y-H, et al. Effect on nickel microstructure on methane steam reforming activity of Ni–YSZ cermet anode catalyst. J. Catal. 2008;258:356–65.
[60] Sundén B, Yuan J. Development of multi-scale models for transport processes involving catalytic reactions in SOFCs. Int. J. Micro–nano Scale Transport 2010;1.
[61] Hecht E, Gupta G, Zhu H, Dean A, Kee R, Maier L, et al. Methane reforming kinetics within a Ni–YSZ SOFC anode support. Appl. Catal. A: General 2005;295:40–51.
[62] Molenda J, Swierczek K, Zajac W. Functional materials for IT-SOFC. J. Power Sources 2007;173:657–70.
[63] Janardhanan VM, Deutschmann O. CFD analysis of a solid oxide fuel cell with internal reforming: coupled interactions of transport, heterogeneous catalysis and electrochemical processes. J. Power Sources 2006;162:1192–202.
[64] Karakasidis T, Charitidis C. Multiscale modelling in nanomaterials science. Mater. Sci. Eng. 2007;C27:1082–9.
[65] Frayret C, Villesuzanne A, Pouchard M, Matar S. Density functional theory calculations on microscopic aspects of oxygen diffusion in ceria-based materials. Int. J. Quantum Chem. 2005;101:826–39.
[66] Cheng CH, Chang YW, Hong CW. Multiscale parametric studies on the transport phenomenon of a solid oxide fuel cell. J. Fuel Cell Sci. Technol. 2005;2:219–25.
[67] Modak AU, Lusk MT. Kinetic Monte Carlo simulation of a solid-oxide fuel cell. Solid State Ionics 2005;176:1281–91.
[68] Joshi AS, Grew KN, Peracchio AA, Chiu WKS. Lattice Boltzmann modeling of 2D gas transport in a solid oxide fuel cell anode. J. Power Sources 2007;164:631–8.
[69] Huang W, Huang X, Reifsnider K. Meso-scale multiphysics model of SOFC cathode processes. In: COMSOL users conference Boston; 2006.
[70] Pasaogullari U, Wang C-Y. Computational fluid dynamics modeling of solid oxide fuel cells. In: Singhal SC, Dokiya M, editors. Proceedings of SOFC-VIII; 2003. p. 1403–12.
[71] Autissier N, Larrain D, van Herle J, Favrat D. CFD simulation tool for solid oxide fuel cells. J. Power Sources 2004;131:131–9.
[72] Khaleel MA, Rector DR, Lin Z, Johnson K, Recknagle K. Multiscale electrochemistry modeling of solid oxide fuel cells. Int. J. Multiscale Comp. Eng. 2005;3:33–47.
[73] Dennis BH, Han Z, Jin W, Wang BP, Xu L, Aapro T, et al. Multi-physics simulation strategies with application to fuel cell modeling. In: 7th International conference on thermal, mechanical and multiphysics simulation and experiments in micro-electronics and micro-systems. EuroSimE; 2006.
[74] Asproulis N, Kalweit M, Drikakis D. Hybrid molecular-continuum methods for micro- and nanoscale liquid flows. In: 2nd Micro and nano flows conference West London, UK; 2009
[75] Reifsnider K, Huang X, Ju G, Solasi R. Multi-scale modeling approaches for functional nano-composite materials. J. Mater. Sci. 2006;41:6751–9.
[76] Bove R, Lunghi P, Sammes NM. SOFC mathematical model for systems simulation. Part one: from a micro-detailed to macro-black-box model. Int. J. Hydrogen Energy 2005;30:181–7.
[77] Haraldsson K, Wipke K. Evaluating PEM fuel cell system models. J. Power Sources 2004;126:55–97.
[78] Faghri A, Guo Z. Challenges and opportunities of thermal management issues related to fuel cell technology and modeling. Int. J. Heat Mass Transfer 2005;48:3891–920.
[79] Park J, Li X. Multi-phase micro-scale flow simulation in the electrodes of a PEM fuel cell by Lattice Boltzmann Method. J. Power Sources 2008;178:248–57.
[80] Nicotella C, Bertei A, Viviani M, Barbucci A. Morphology and electrochemical activity of SOFC composite cathodes: II. Mathematical modeling. J Appl. Electrochem. 2009;39:503–11.
[81] Peksen M, Peters R, Blum L, Stolten D. Numerical modeling and experimental validation of a planar type pre-reformer in SOFC technology. Int. J. Hydrogen Energy 2009;34:6425–36.
[82] Tseronis K, Kookos I, Theodoropoulos K. Modelling and design of the solid oxide fuel cell anode. In: COMSOL users conference Birmingham; 2006.
[83] Chan SH, Low CF, Ding OL. Energy and exergy analysis of simple solid-oxide fuel-cell power systems. J. Power Sources 2002;103:188–200.

# Paper II

This paper has been published in:

*Proceedings of the 7th International Fuel Cell Science, Engineering & Technology Conference, Newport Beach, California, USA, 2009,*
ASME FuelCell2009-85054.

© 2009 ASME.

**Proceedings of FuelCell2009**
**ASME 2009 Seventh International Fuel Cell Science, Engineering and Technology Conference**
**June 8-10, 2009 Newport Beach, California, USA**

# FuelCell2009-85054

## *LTNE APPROACH AND SIMULATION FOR ANODE-SUPPORTED SOFCS*

**Martin Andersson** **Jinliang Yuan** **Bengt Sundén**
**Department of Energy Sciences, Faculty of Engineering,**
**Lund University, Box 118, 221 00 Lund, Sweden**

**Wei Guo Wang**
**Ningbo Institute of Materials Technology and Engineering (NIMTE),**
**Chinese Academy of Science (CAS), 315040 Ningbo, People's Republic of China**

## ABSTRACT
Fuel cells are promising for future energy systems, since they are energy efficient and, when hydrogen is used as fuel, there are no emissions of greenhouse gases. Fuel cells have during recent years various improvements, however the technology is still in the early phases of development, this can be noted by the lack of dominant design both for singe fuel cells, stacks and for entire fuel cell systems. In this study a CFD approach (COMSOL Multiphysics) is employed to investigate the effect on temperature distribution from inlet temperature, oxygen surplus, ionic conductivity and current density for an anode-supported intermediate temperature solid oxide fuel cell (IT-SOFC). The developed model is based on the governing equations of heat-, mass- and momentum transport. A local temperature non equilibrium (LTNE) approach is introduced to calculate the temperature distribution in the gas- and solid phase separately.

The results show that the temperature increasing along the flow direction is controlled by the degree of surplus air. It is also found that the ohmic polarization in the electrolyte and the activation polarization in the anode and cathode have major influence on the performance. If a count flow approach is employed the inlet temperature for the fuel stream should be close to the outlet temperature for the air flow to avoid a too high temperature gradient.

*Keywords: SOFC, anode-supported, CFD, COMSOL Multiphysics, LTNE*

## INTRODUCTION AND PROBLEM STATEMENT
Fuel cells produce electricity and heat directly from chemical conversion of fuel and oxidant energies by electrochemical reactions [1-2]. The fuel cell is not a new invention, because the electrochemical process was discovered already in 1839. However the first real fuel cell system was not designed and built until the 1950s. The interest in fuel cells have been growing exponentially, concerning amount of scientific papers, after year 2000 [3]. Among the various types of fuel cells (FCs), the solid oxide fuel cell (SOFC) has attained significant interest due to its high efficiency and low emissions of pollutants to the environment. High temperature operation offers many advantages, such as high electrochemical reaction rate, flexibility of using various fuels and tolerance to impurities. SOFCs have in general either planar or tubular configurations [1-2, 4]. Fuel cell performance depends on thermal, electro-chemical, mechanical and chemical phenomena [5].

In an electrode supported SOFC either the anode or cathode is relatively thick and works as support material. This design makes it possible to have a very thin electrolyte, i.e. the ohmic losses decreases and the temperature can be lowered to 600-800 °C. Fuel cells working in this temperature range are classified as intermediate temperature (IT) [1, 2] if compared to conventional SOFCs that operate between 800 and 1000 °C [6]. A planar SOFC contains a dense ceramic electrolyte sandwiched between two porous electrodes. The electrolyte contains yttria-stabilized zirconia (YSZ), the cathode strontium doped lanthanium manganite (LSM) and the anode nickel/YSZ [1].

 Copyright © 2009 by ASME

Low temperature (LT)-SOFCs in the range of 300-600 °C is under development, the challenge is to increase the ionic conductivity in the electrolyte. Low temperatures make it possible to use cheaper materials throughout the fuel cell system, i.e., promotion of commercialization. An approach with material development in the nanoscale is expected to be very promising [7].

Fuel cell systems are still an immature technology in early phases of development, as can be noted due to lack of a dominant design, few commercial systems and a low market demand. The creation of strategic niche markets and search for early market niches are of a vital importance for the further development. It is expected that mass production will start when a dominant design is found and production cost will significantly decrease due to economy of scale [3].

Due to complex processes involved in fuel cells, it is not possible to solve the equations describing the physical phenomena analytically, a numerical approach, e.g. the Finite Element Method, needs to be applied to solve the equations in an approximate way [8].

A model that describes physical (mass- heat- and momentum) phenomena inside an anode-supported SOFC is developed, to deeply understand the effect of design and operating parameters. A two-dimensional numerical calculation procedure (CFD approach) is further applied. This study focuses on the effect of ionic electronic conductivity, inlet temperature, surplus of oxygen, current density and count flow. The considered cell includes interconnect, air- and fuel-channels, anode, cathode and electrolyte. Temperature dependent thermal-physical properties are taken into account as well. The temperature distribution in the solid phase and gas phase are calculated separately, based on the LTNE approach.

## MATHEMATICAL MODEL

A two-dimensional model for an anode-supported SOFC is developed and implemented in the commercial software COMSOL Multiphysics (version 3.5). Equations for momentum, mass and heat transport are solved simultaneously. The geometry is defined in table 1 and a sketch of the modeled cell can be seen in figure 1. Note the difference in scale between the cell length (x-direction, as in fig. 1) and various thicknesses (y- direction, as in fig. 1). It should be noted that the model in this study is 2D only, and the connection between the electrodes and interconnect can not be explicitly observed in this case.

Oxygen is reduced in the cathode (eqn. 1), and oxygen ions migrate through the electrolyte and reacts then with hydrogen in the anode (eqn. 2) [2, 9].

$$1/2\,O_2 + 2e^- \rightarrow O^{2-} \quad (1)$$

$$O^{2-} + H_2 \rightarrow H_2O + 2e^- \quad (2)$$

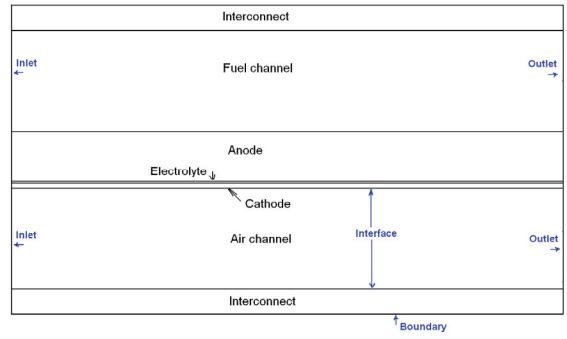


**Figure 1: Sketch of an anode-supported SOFC.**

**Table 1. Cell geometry [6].**

| | |
|---|---|
| Cell length | 0.4 m |
| Fuel channel height | 1 mm |
| Air channel height | 1 mm |
| Anode thickness | 500 μm |
| Cathode thickness | 50 μm |
| Electrolyte thickness | 20 μm |
| Interconnect thickness | 500 μm |

## Governing equations

### Momentum equation

The gases flow inside the fuel cell components, such as air- and fuel-channels and porous electrodes. A traditional modeling approach for such a system consists of solving the Darcy's equation in the porous medium and the Navier-Stokes equations in the channels separately. The problem with such an approach is to define interface conditions at the interface between the two domains. It is hard to define this tangential velocity component. To avoid this problem the Darcy-Brinkman equation is introduced and solved for the gas flow in the fuel- and air channels and in the porous media (electrodes) [10, 11].

The Darcy-Brinkman equation (eq. 3) is transformed into the standard Navier-Stokes equation when ($\kappa \rightarrow \infty$) and ($\varepsilon_p = 1$), and into the Darcy equation as $(Da \rightarrow 0)$, $Da$ is the Darcy number. The derivation of Navier-Stokes equation and Darcy equation from Darcy-Brinkman equation can be found in [10].

$$\left(\frac{\nu}{\kappa} + \rho \cdot \nabla \mathrm{u}\right)\mathrm{u} - \nabla\left[-p + \frac{1}{\varepsilon_p}\left\{\mathbf{T} - \left(\lambda - \kappa_{dv}\right)(\nabla \mathrm{u})\right\}\right] = \mathbf{F} \quad (3)$$


Copyright © 2009 by ASME

where **F** is the volume force vector, $\kappa$ is the permeability of the porous medium, $\varepsilon_p$ the porosity, $v$ the dynamic viscosity, u the velocity vector and **T** the viscous stress tensor $\left(\mathbf{T} = v\left(\nabla \mathrm{u} + (\nabla \mathrm{u})^T\right)\right)$. $\kappa_{dv}$ (deviation from thermodynamic equilibrium) is by default set to zero, which means that the fluid particles are in equilibrium with their surrounding. λ is the second viscosity and is, for gases, normally assumed as: $\lambda$=-2/3$v$ [12]. The equation for the continuity in the air- and fuel channels reads: $\nabla \mathrm{u} = 0$ [11]. The densities for the participating gases are calculated as [11]:

$$\rho_{mixture} = \frac{p \cdot \sum w_i M_i}{\mathrm{R}T} \tag{4}$$

The dynamic viscosity for each participating spices in the gas phase is calculated as [13]:

$$v_i = \sum_{k=1}^{7} \mathrm{b_k} \cdot \left(\frac{T}{1000}\right)^k \tag{5}$$

where $\mathrm{b_k}$ is the spices dependent parameter and "k" stands for the amount of spices dependent parameters in the viscosity equation. The dynamic viscosity for the gas mixtures is calculated as [13]:

$$v_{mixture} = \sum w_i v_i \tag{6}$$

## Mass transport equation

Maxwell-Stefan equation for mass diffusion and convection is used to describe the mass transport phenomena for the gases inside the fuel cell [11]. The Maxwell-Stefan equation is a simplified equation compared to "Dusty Gas Model", since the Knudsen diffusion (collisions between gas molecules and the porous material) is neglected. The reason for this treatment is to reduce the calculation cost and this model is already predefined in COMSOL Multiphysics. However adding the Knudsen diffusion term may increase the diffusion resistance. Maxwell-Stefan equation is solved for the fuel- and air channels and electrodes.

$$\nabla\left(-\rho w_i \sum D_{ij} \nabla x_j + \left(x_j - w_j\right)\frac{\nabla p}{p}\mathrm{u} - D_i^T \frac{\nabla T}{T}\right) + \rho \mathrm{u} \nabla w_j = R_i \tag{7}$$

$$x_j = \frac{w_j}{M_j} M \tag{8}$$

$$\sum_{i=1}^{n} w_i = 1 \tag{9}$$

where $w$ is the mass fraction, $x$ the mole fraction, n the number of species, $D_i^T$ the thermal diffusion coefficient and $D_{ij}$ the Maxwell-Stefan binary diffusion coefficient, $R_i$ the reaction rate, zero in this case since the electrochemical reactions is assumed to take place, and defined, at the interfaces between the electrolyte and electrodes. The electrochemical reactions occur in reality at an active reaction surface area, the tree phase boundary, where gas, ionic and electronic phases meet. The active reaction surface area will be considered in future research when the electrochemical reactions are defined as a source term in the mass transport governing equation instead of an interface condition, as done in this study. The diffusion coefficient in the porous electrodes is calculated as [14, 15]:

$$D_{ij,por} = D_{ij} \cdot \varepsilon_p / t \tag{10}$$

where $t$ is the tortuosity. $D_{ij}$ is calculated as [16]:

$$D_{ij} = \frac{2.66 \cdot 10^{-8} \cdot T^{3/2}}{p \cdot M_{ij}^{1/2} \cdot l_{ij}^2 \Omega_D} \tag{11}$$

$$\Omega_D = \frac{A}{\left(\frac{\mathrm{k'}\cdot T}{\mathrm{e_{ij}}}\right)^B} + \frac{C}{\exp\left(D \cdot \frac{\mathrm{k'}\cdot T}{\mathrm{e_{ij}}}\right)} + \frac{E}{\exp\left(F \cdot \frac{\mathrm{k'}\cdot T}{\mathrm{e_{ij}}}\right)} + \frac{G}{\exp\left(H \cdot \frac{\mathrm{k'}\cdot T}{\mathrm{e_{ij}}}\right)} \tag{12}$$

$$M_{ij} = \frac{2}{\frac{1}{M_i} + \frac{1}{M_j}} \tag{13}$$

$$l_{ij} = \frac{l_i + l_j}{2} \tag{14}$$

$$\mathrm{e_{ij}} = \sqrt{\mathrm{e_i} \cdot \mathrm{e_j}} \tag{15}$$

where $\Omega_D$ is the diffusion collision integral, $\mathrm{e_{ij}}$ is the average characteristic Lennard-Jones energy, $l_{ij}$ is the average characteristic length, $\mathrm{M_{ij}}$ is the average molecular weight, and k' is the Boltzmann's constant. A, B, C, D, E, F, G and H are constants, as shown in [16].

## Heat transfer equation

The temperature distribution is calculated separately for the gas phase (in air- and fuel-channels and electrodes) and for the solid phase (interconnect, electrodes and electrolyte). Heat is transferred between the phases at the channel walls and in the porous electrodes. The general heat conduction equation is used to calculate the temperature distribution for the solid materials, i.e., electrolyte, interconnect and electrodes [11]:

$$\nabla\left(-k_s \nabla T_s\right) = Q_s \tag{16}$$


Copyright © 2009 by ASME

where $k_s$ is the thermal conductivity of the solids, $T_s$ the temperature in the solid phase and $Q_s$ are the heat source (heat transfer between the solid- and gas-phase and heat generation due to ohmic polarization). Note that heat generated due to ohmic polarization is assumed to enter the solid phase (as a part of $Q_s$), heat generation due to electrochemical reactions, concentration- and activation polarization are simplified and defined as interface conditions, as for the mass transport the electrochemical reactions occur in reality at an active reaction surface area. The temperature distribution for the gas mixtures in the fuel- and air- channels and in the porous electrodes is calculated as [11]:

$$\nabla\left(-k_g \nabla T_g\right) = Q_g - \rho_g \cdot c_{p,g} \mathrm{u} \nabla T_g \tag{17}$$

where $c_p$ the heat capacity, $T_g$ the temperature in the gas phase and $Q_g$ the heat transfer between the gas- and solid-phase. Because the Reynolds number is very low, the heat transfer coefficient ($h_{s,g,por}$) in the porous electrodes can, be calculated as [17]:

$$h_{s,g,por} = \frac{2 \cdot k_g}{d_p} \tag{18}$$

where $d_p$ is the electrode particle diameter and $k_g$ the gas conductivity. The heat transfer between the gas phase and solid phase depends on the temperature difference and the particle surface area as [18]:

$$Q_g = h_v\left(T_g - T_s\right) = SA \cdot h_{s,g,por}\left(T_g - T_s\right) \tag{19}$$

where $h_v$ is the volume heat transfer coefficient and SA the surface area (760 000 $m^2/m^3$ for the cathode and 619 000 $m^2/m^3$ for the anode [19]). The temperature difference between the solid and gas phase has been found to be neglible (the average temperature difference is 0.0032 K for the cathode and $5.7 \cdot 10^{-5}$ K for the anode) for the situation considered in this study. This small temperature difference between the solid and gas phase in the porous electrodes is due to, the big surface area and very small particle diameter that is assumed for this study. As a comparison it can be mention that the temperature difference between the gas and solid phase where investigated in [17] and calculated to the order of $10^{-2}$ K, considering porous SOFC electrodes. The heat capacity for each gas specie is calculated as [13]:

$$c_{p,i}(T) = \sum_{k=1}^{7} \mathrm{a_k} \cdot \left(\frac{T}{1000}\right)^k \tag{20}$$

where $a_k$ is the species dependent parameter and "k" stands for the number of parameters in the heat capacity equation. The heat capacities for the gas mixtures can then be calculated when the individual species values are known [13]:

$$c_{p,mixture} = \sum w_i c_{p,i} \tag{21}$$

The gas thermal conductivity for each species in the gas phase is calculated as [13]:

$$k_{g,i}(T) = 0.01 \cdot \sum_{k=1}^{7} \mathrm{c_k} \cdot \left(\frac{T}{1000}\right)^k \tag{22}$$

where $c_k$ is the species dependent parameter and "k" stands for the number of parameters in the thermal conductivity equation. The conductivity for the gas mixtures can then be evaluated as [13]:

$$k_{g,mixture} = \sum w_i k_{g,i} \tag{23}$$

Ohmic polarization occurs due to resistance of the flow of ions in the electrolyte and electrical resistance in the electrodes. The electrodes and electrolyte are heated due to this effect [1,20]:

$$Q_{ohm} = \frac{i \cdot \eta_{ohm}}{\tau} \tag{24}$$

$$\eta_{ohm} = R_{ohm} \cdot i \tag{25}$$

$$R_{ohm} = \frac{\tau_a}{\sigma_a} + \frac{\tau_{el}}{\sigma_{el}} + \frac{\tau_c}{\sigma_c} \tag{26}$$

where $\tau$ is the component thickness and $R_{ohm}$ the electrolyte area-specific ohmic resistance. The electronic/ionic conductivities ($\sigma$), are calculated as [1, 21]:

$$\sigma_a = \frac{4.2 \cdot 10^7}{T} \cdot \exp\left(\frac{-1200}{T}\right) \tag{27}$$

$$\sigma_{el} = 33.4 \cdot 10^3 \cdot \exp\left(\frac{-10300}{T}\right) \tag{28}$$

$$\sigma_c = \frac{9.5 \cdot 10^7}{T} \cdot \exp\left(\frac{-1150}{T}\right) \tag{29}$$

## Boundary and interface conditions

### Momentum transport

The boundary conditions for the momentum transport equation are defined as a laminar flow profile for the inlet with an average air inflow velocity of 5.2 m/s (for an oxygen surplus factor of 4). The entrance length due to the build up of a fully developed velocity profile can be neglected since the channel


Copyright © 2009 by ASME

length is 400 times bigger than the height. The outlet is defined as [11]:

$$\nu\left(\nabla \mathrm{u} + (\nabla \mathrm{u})^T\right) \cdot \mathrm{n} = 0 \tag{30}$$

$$p = p_0 \tag{31}$$

where $p_0$ is a defined outlet pressure. The interfaces between the interconnects and gas channels have to be defined since the governing equation for momentum transport are not solved for the interconnects, the interfaces are defined as walls (u=0). Darcy-Brinkman equation makes it possible to define the interface between the air- and fuel-channels and the porous electrodes as continuous. The Darcy-Brinkman equation is not solved for the electrolyte and interface conditions need to be defined. Oxygen is consumed at the interface between the cathode and electrolyte, and the electrochemical reaction rate depends on the current density. As for the mass transport, the electrochemical reactions occur in reality at an active reaction surface area, but are in this paper simplified and assumed to occur at the interface between the electrodes and electrolyte. The gas velocity effect ($r$), calculated from the total mass flow given by the electrochemical reaction, on the momentum equation can be calculated as [11]:

$$r = -\frac{i \cdot M_{O_2}}{n_{e,c} \cdot \mathrm{F} \cdot \rho} \tag{32}$$

where $i$ is the current density and $n_{e,c}$ the number of electrons transfer per molecule of oxygen consumed (= 4). At the anode and electrolyte interface one molecule of water is produced for every molecule of hydrogen consumed, and the reaction effect is specified as [11]:

$$r = \frac{i \cdot \left(M_{H_2O} - M_{H_2}\right)}{n_{e,a} \cdot \mathrm{F} \cdot \rho} \tag{33}$$

where $n_{e,a}$ the number of electrons transfer per molecule of hydrogen consumed/water produced (= 2). The implementation of eq. 32 and 33 means that the cell overall mass balances show a very good result.

## Mass transport

The boundary conditions for the mass transport equation are defined as mass fraction for the gas channel inlet ($w_i$=$w_{i,0}$) and the boundaries. However the result can be presented as either mass or mole fraction. The convective flux for the gas channel outlet is defined as [11]:

$$\mathrm{n} \cdot \left( -\rho w_i \sum D_{ij} \left( \nabla x_j + \left(x_j - w_j\right) \frac{\nabla p}{p} \right) - D^T \frac{\nabla T}{T} \right) = 0 \tag{34}$$

The flows from the anode and the cathode to the electrolyte are defined as "Flux" [11]:

$$-\mathrm{n} \cdot \mathrm{N} = n_0 \tag{35}$$

$$\mathrm{N} = -\rho w_i \sum D_{ij} \left( \nabla x_j + \left(x_j - w_j\right) \frac{\nabla p}{p} \right) + D^T \frac{\nabla T}{T} + \rho w_i \mathrm{u} \tag{36}$$

where n stands for the normal vector to the boundary, and $n_0$ for the inward mass flux [11]:

$$n_0 = \frac{-i \cdot M_i}{n_e \mathrm{F}} \tag{37}$$

where $i$ is the current density and $n_e$ the number of electrons transferred per reaction, and F the Faraday constant. The interfaces between the interconnects and gas channels have to be defined since the governing equation for mass transport are not solved for the interconnects, they are defined as walls (n·N=0).

## Heat transfer

As described previously the temperature in the soild and gas phase is calculated separately, heat flows between the phases in the porous material and at the gas channels walls. The inlet temperature is defined by the operating conditions, for the gas flow channel inlet as ($T_g$=$T_0$). The outlet for the gas channels is defined as convective flux [11]:

$$-\mathrm{n} \cdot \left(-k \nabla T_g\right) = 0 \tag{38}$$

The boundaries at the top and bottom of the model are defined as symmetry, since it is assumed that the cell is surrounded by other cells with the same temperature distribution. The heat flux at the interface between the interconnects and gas channels as well as at the interface between the gas channels and electrodes is defined as [11]:

$$-\mathrm{n} \cdot \left(-k_s \nabla T_s\right) = q_s \tag{39}$$

$$q_s = h_{s,g,w} \cdot \left(T_{s,w} - T_{g,w}\right) \tag{40}$$

$$q_g = -q_s \tag{41}$$

where $T_s$ is the temperature in the solid phase, $T_g$ the temperature in the gas phase, $q_g$ is the heat flux from the gas phase, $q_s$ the heat flux to the solid phase and $h_{s,g,w}$ the heat transfer coefficient at the gas channel walls [4, 22]:


Copyright © 2009 by ASME

$$h_{s,g,w} = \frac{Nu \cdot k_g}{c_d} \tag{42}$$

where $Nu$ is Nusselt number, $k$ gas phase conductivity and $c_d$ the channel diameter. The value for Nusselt number (4.094) comes from [22] based on the fully developed flow for rectangular duct, assuming heat flux at two channel walls located opposite to each other, one between the interconnect and the gas channel and between the electrode and gas channel. Heat generated due to electrochemical reactions and due to polarization losses are, as previously described, defined at the electrodes/electrolyte interfaces:

$$-\mathrm{n} \cdot (-k \nabla T) = q_0 \tag{43}$$

$$q_0 = q_r + q_{losses} = -i \cdot \left( \frac{T \cdot \Delta S_r}{n_e \cdot \mathrm{F}} + \eta_{act,e} + \eta_{conc,e} \right) \tag{44}$$

where $q_o$ is the heat generated at the interface (specified as interface condition), $q_r$ the heat generated inside the cell due to change in enthalpy and $q_{losses}$ the heat generated due to potential losses inside the cell. It is assumed that this heat ($q_0$) is generated in the gas phase. The amount of heat due to electrochemical reactions can be calculated as [9,23]:

$$q_r = -T \cdot \Delta S_r \cdot \dot{n} = -\Delta S_r \frac{T \cdot i}{n_e \mathrm{F}} \tag{45}$$

$$\dot{n} = \frac{i}{n_e \mathrm{F}} \tag{46}$$

where $\dot{n}$ is the molar flux density [mol/(m$^2$s)] and $\Delta S_r$ is entropy change of reaction [-50.2 J/(K mol)], and calculated from data in [24]. The heat generation due to activation and concentration polarization can be calculated as [14, 20]:

$$q_{losses} = -i \cdot (\eta_{act,e} + \eta_{conc,e}) \tag{47}$$

The concentration polarizations due to concentration differences inside the cell are specified as [1]:

$$\eta_{conc,a} = \frac{\mathrm{R}T}{n_{e,a} \mathrm{F}} \ln \left( \frac{p_{H_2O,TPB} \cdot p_{H_2,b}}{p_{H_2,TPB} \cdot p_{H_2O,b}} \right) \tag{48}$$

$$\eta_{conc,c} = \frac{\mathrm{R}T}{n_{e,c} \mathrm{F}} \ln \left( \frac{p_{O_2,b}}{p_{O_2,TPB}} \right) \tag{49}$$

where $p_{i,TPB}$ stands for the partial pressure at three phase boundary (TPB) and $p_{i,b}$ the partial pressure at the interface between gas channel and electrode. Chemical reactions involve energy barriers (i.e., activation polarization) which must be overcome by the reacting species. The activation polarization can be considered as the extra potential needed to overcome the energy barrier of the rate-determining step to a value that the reaction proceeds at a desired rate. It is normally expressed by the Bultler-Volmer equation [14]:

$$i = i_0 \left\{ \exp\left( \beta \frac{n_e \mathrm{F} \eta_{act,e}}{\mathrm{R}T} \right) - \exp\left( -(1-\beta) \frac{n_e \mathrm{F} \eta_{act,e}}{\mathrm{R}T} \right) \right\} \tag{50}$$

where β is the transfer coefficient, and usually assumed to be 0.5. The Bultler-Volmer equation can then be expressed as [1, 14]:

$$i = 2 \cdot i_0 \cdot \sinh\left( \beta \frac{n_e \mathrm{F} \eta_{act,e}}{2\mathrm{R}T} \right) \tag{51}$$

$$\eta_{act,e} = \frac{2\mathrm{R}T}{n_e \mathrm{F}} \sinh^{-1}\left( \frac{i_e}{2 \cdot i_{0,e}} \right) \tag{52}$$

$$i_0 = \frac{RT}{n_e F} k''_e \cdot \exp\left( \frac{-E_e}{\mathrm{R}T} \right) \tag{53}$$

where $i_o$ is the exchange current density. The pre-exponential factor ($k''$) is 2.35 · $10^{11}$ $\Omega^{-1}$m$^{-2}$ for the cathode and 6.54 · $10^{11}$ $\Omega^{-1}$m$^{-2}$ for the anode respectively. The activation energy ($E$) is 137 kJ/mol for the cathode and 140 kJ/mol for the anode [1, 6].

## NUMERICAL METHODS

All the governing equations were numerically solved in COMSOL Multiphysics (version 3.5) using a stationary solver with a direct (UMFPACK) linear solver system. The residual convergence was limited to $10^{-6}$ for all variables. The grid independence was archived at 30 000 finite elements (figure 2), after which the change in maximum temperature was less than 0.1%, change in maximum velocity was less than 1%, oxygen consumption was less than 0.1% and the hydrogen consumption was less than 1% (compared with 53 000 finite elements).


Copyright © 2009 by ASME

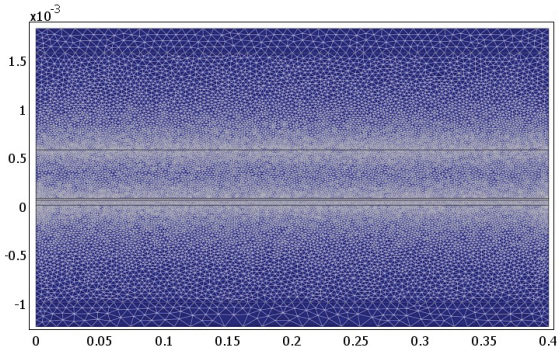


**Figure 2: Meshing of the considered geometry.**

## RESULTS AND DISCUSSION

Material characteristic data typical in literature are used in this study, as shown in table 2.

**Table 2. Material characteristic data**

| | | |
|---|---|---|
| $k_{s,a}$ | 11 W/m/K | [25] |
| $k_{s,c}$ | 6 W/m/K | [25] |
| $k_{s,el}$ | 2.7 W/m/K | [25] |
| $k_{s,int}$ | 20 W/m/K | [25] |
| $c_{p,a}$ | 450 J/kg/K | [26] |
| $c_{p,c}$ | 430 J/kg/K | [26] |
| $c_{p,el}$ | 470 J/kg/K | [26] |
| $c_{p,int}$ | 550 J/kg/K | [26] |
| $\rho_a$ | 3310 kg/m$^3$ | [26] |
| $\rho_c$ | 3030 kg/m$^3$ | [26] |
| $\rho_{el}$ | 5160 kg/m$^3$ | [26] |
| $\rho_{int}$ | 3030 kg/m$^3$ | [26] |
| $\kappa_e$ | $1.76 \cdot 10^{11}$ m$^2$ | [25] |
| $\varepsilon_e$ | 0.5 | [25] |
| $d_p$ | 1μm | [15] |
| $t$ | 5 | [15] |

A base condition is assumed that the cell average current density is 0.3 A/cm$^2$, surplus factor of oxygen is $S_{O2} = 4$, inlet temperature is 1000 K for both the air- and fuel-channels and the fuel consumption is $C_{fuel} = 80$ mole-%, and flow direction is left -> right. The above parameters are then varied one by one for parameter studies. The surplus of oxygen is specified as:

$$S_{O_2} = \frac{x_{O_2,0}}{x_{O_2,0} - x_{O_2,end}} - 1 \qquad (54)$$

where $x_{O2}$ is the molar fraction of oxygen. The consumption of fuel is specified as:

$$C_{fuel} = \frac{x_{H_2,0} - x_{H_2,end}}{x_{H_2,0}} \qquad (55)$$

The temperature increases along the x-direction (the main flow direction), as seen in fig. 3. The temperature difference in the y-direction inside the air channel occurs because the convective heat flux are bigger in the air channel (compared to the fuel channel) due to the relatively larger gas flow.

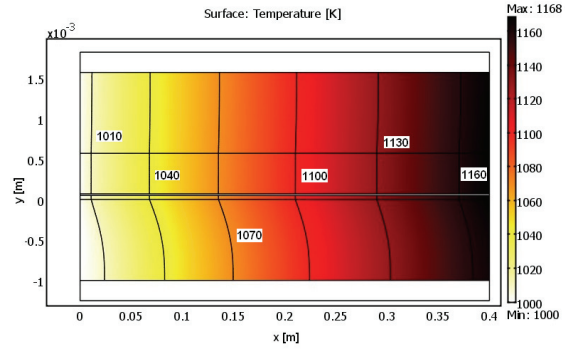


**Figure 3: Temperature for the gas phase.**

The mole fraction of oxygen (fig. 4) decreases along the flow direction in the air channel and the cathode. There is concentration difference in the y-direction as well, that drives the flow towards the cathode/electrolyte interface, however it is hard to see in the air channel as the cell length is 400 times bigger than the air channel height.

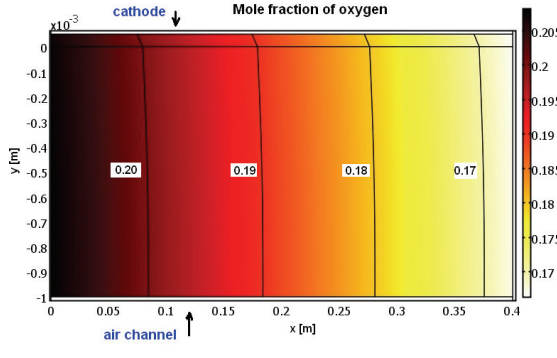


**Figure 4: Mole fraction of oxygen in the air channel and cathode**

The mole fraction of hydrogen decreases along the flow direction in the fuel channel, as shown in fig. 5. As for the mole fractions in the air channel, there is a concentration difference in the y-direction for hydrogen, which drives the


Copyright © 2009 by ASME

hydrogen molecules towards the anode/electrolyte interface, however this effect is very small (and impossible to see in the fuel channel), due to the fact that the cell length are is 400 times bigger than the fuel channel height.

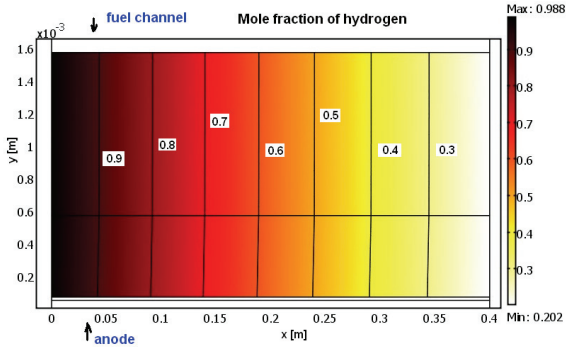


**Figure 5: Mole fraction of hydrogen in the fuel channel and anode.**

The polarization losses along the flow direction can be seen in fig. 6. It is found that the ohmic polarizations in the electrodes as well as the concentration polarizations are neglible compared to the activation polarizations and the ohmic polarization in the electrolyte, however a small effect from concentration polarization is seen in the anode close to the inlet. This effect is not expected as the highest fuel concentration can be found at the inlet, however the effect on the overall heat balance is found to be neglible. The activation- and ohmic polarizations decrease along the flow direction, as the temperature increase (see fig. 3). It is noted that the activation polarization is more temperature dependent than the ohmic polarization.

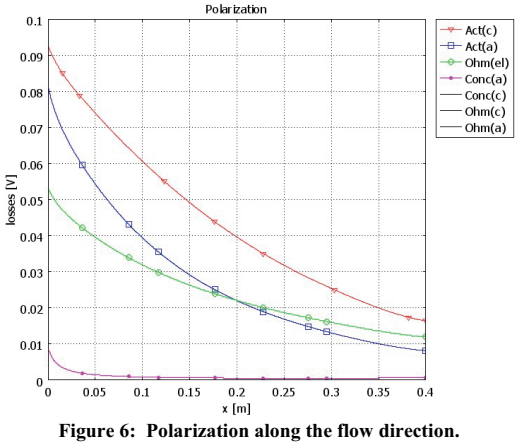


**Figure 6: Polarization along the flow direction.**

A parameter study is performed to investigate the effect of the oxygen surplus factor, the inlet temperature, the current density, the direction of flow and ionic conductivity. To be able to compare the different investigations with each other, the temperature in the electrolyte is plotted against the position in the flow direction, except for the case with count flow, where the temperatures inside the cell are plotted in two dimensions.

A big surplus flow of oxygen cools down the fuel cell, as can be seen in fig. 7. Change of the oxygen surplus factor is an easy way to control the temperature increase inside the cell, i.e. a higher surplus factor brings a reduced temperature increase along the flow direction. An increased surplus factor also gives a reduced concentration difference in the y-direction, i.e. reduced concentration polarization, however this effect is found to be neglible in this specific study. A higher surplus of oxygen also means that the energy needed in compressors (driving the air flow in the fuel cell system) will increase.

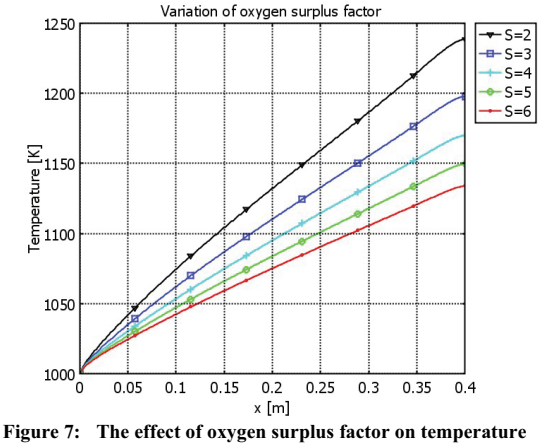


**Figure 7: The effect of oxygen surplus factor on temperature along the flow direction in the fuel cell.**

An increased inlet temperature gives a reduced temperature increase along the flow direction inside the fuel cell, as can be seen in fig. 8. This is due to the ohmic heating (ohmic polarization) and the activation polarization (inversed temperature dependent). The ohmic heating decreases with increased inlet temperature since the ionic conductivity in the electrolyte increases, also the electronic conductivity in the electrodes increases but this effect is found to be much smaller. Both the ionic conductivity and the exchange current density are material dependent, and it is possible to decrease the polarization losses with development of smart suitable materials.


Copyright © 2009 by ASME

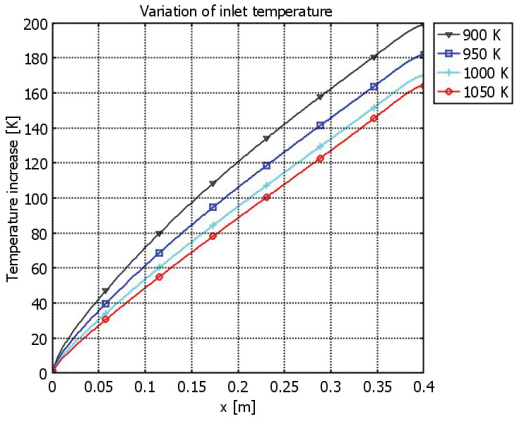


**Figure 8: The temperature increase along the flow direction for different inlet temperatures.**

The current density influence on the temperature distribution along the flow direction is shown in fig. 9. An increased current density means that the ohmic and activation polarization increase. A higher current density makes it possible to decrease the fuel cell stack size, however extra heat is produced, due to the increased polarization losses.

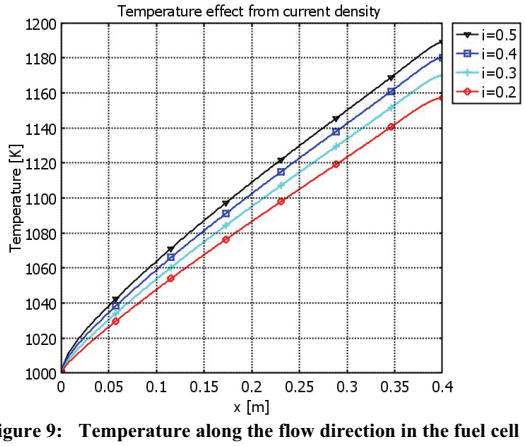


**Figure 9: Temperature along the flow direction in the fuel cell for different current densities.**

The effect of the ionic conductivity in the electrolyte and the electronic conductivity in the electrodes is investigated. A decreased ionic conductivity in the electrolyte make it harder for the oxygen ions to pass through the electrolyte and the ohmic polarization increases, i.e. the temperature within the cell increases, as seen in fig. 10. “50%” means that the ionic conductivity in the electrolyte is halved, and “200%” means that the ionic conductivity is doubled.

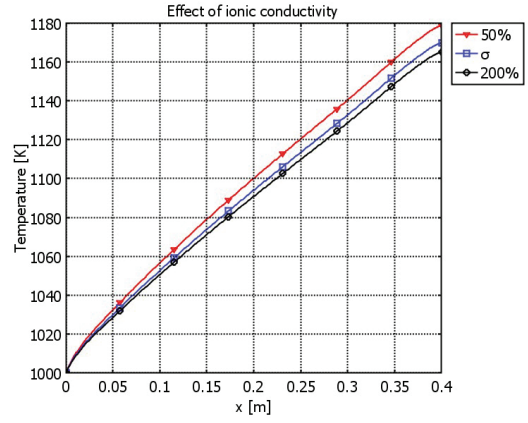


**Figure 10: Temperature distribution along the flow direction for different ionic/electronic conductivities.**

A simulation is also conducted to study the effect of count flow, i.e. the air enters into the fuel cell on one side (x = 0.4 m) and the fuel from the opposite side (x = 0), see figure 11. Both the air and fuel gas enter the cell at 1000 K. The fuel flow is cooled down by the air flow along the channel and the outlet temperature for the fuel gas stream is found to be close to the inlet temperature of the air flow. As the fuel gas stream enters into the cell it is quickly heated up to a temperature close to the outlet temperature of the air flow, and it is expected that this large temperature gradient will cause material problems. It is recommended for count flow to try to keep the inlet temperature of the fuel stream as close as possible to the outlet temperature of the air stream. Both the temperature gradient inside the cell and the maximum temperature are bigger for a count flow design, compared to the basic case:

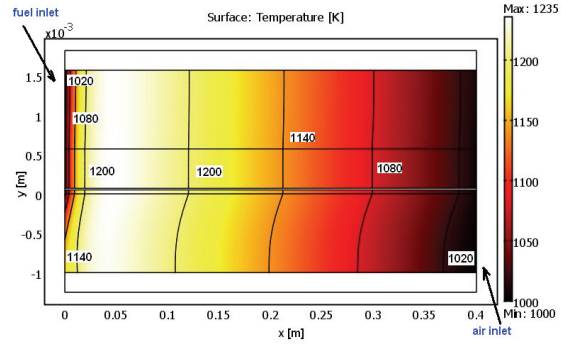


**Figure 11: The temperature along the x-axis in count flow**


Copyright © 2009 by ASME

## CONCLUSIONS

In this study, a CFD approach is developed and implemented to analyze physical phenomena that take place inside an anode-supported SOFC. Equations for heat-, mass- and momentum transport are solved simultaneously. A LTNE approach is applied to calculate the temperatures in the solid phase and gas phase separately. It is concluded that the temperature difference is neglible for the investigated conditions. It is found that activation polarization for both the anode and cathode as well as ohmic polarization in the electrolyte cause a significant effect on the temperature in intermediate temperature range. An increased inlet temperature decreases the polarization losses within the cell, however an increased operation temperature requires more expensive materials. An optimization should be done considering the current density and stack size (i.e., production cost). The ionic conductivity in the electrolyte can be increased with more advanced material or design. It is found that changing the oxygen surplus factor is an easy approach to control the temperature increase within the cell. It is revealed that it is important for the count flow design to keep the inlet temperature of the fuel stream close to the outlet temperature of the air stream to avoid too high temperature gradients close to the fuel flow inlet.

## NOMENCLATURE

| | |
|---|---|
| $\dot{n}$ | molar flux density, mol/(m$^2$s) |
| $C$ | consumption, dimensionless |
| $c_d$ | channel diameter, m |
| $c_p$ | specific heat capacity at constant pressure, J/kg/K |
| $Da$ | Darcy number, dimensionless |
| $D_{ij}$ | Maxwell-Stefan binary diffusion coefficient, m$^2$/s |
| $D_i^T$ | thermal diffusion coefficient, kg/(m·s) |
| $d_j$ | diffusional driving force, dimensionless |
| $d_p$ | electrode particle diameter, m |
| $E$ | activation energy, kJ/mol |
| e | characteristic Lennard-Jones energy, K |
| **F** | volume force vector, N/m$^3$ |
| F | Faraday constant, 96485 C/mol |
| $h_{s,g}$ | heat transfer coefficient, W/(m$^2$K) |
| $h_v$ | volume heat transfer coefficient, W/(m$^3$K) |
| $i$ | current density, A/cm$^2$ |
| $i_0$ | exchange current density, A/cm$^2$ |
| k' | Boltzmann's constant, J/K |
| $k$ | thermal conductivity, W/m/K |
| $k''$ | pre-exponential factor, 1/(Ωm$^2$) |
| $l_{ij}$ | characteristic length, Å |
| $M$ | molar mass of the mixture, kg/mol |
| $M_j$ | molar mass of species j, kg/mol |
| $n_0$ | inlet mass flux, kg/m$^2$/s |
| $n_e$ | number of electrons transferred per reaction |
| $Nu$ | Nusselt number, dimensionless |
| $p$ | pressure, Pa |
| $q$ | heat flux, W/m$^2$ |
| $Q$ | source term (heat), W/m$^3$ |
| $Q'$ | source term (mass), kg/(m$^3$s) |
| $r$ | velocity effect due to electrochemical reaction, m/s |
| $\bar{r}$ | average pore ratio, m |
| R | gas constant, 8.314 J/mol/K |
| $R_i$ | reaction rate, kg/m$^3$/s |
| $R_{ohm}$ | electrolyte area-specific ohmic resistance, Ω/m$^2$ |
| $S$ | surplus factor, dimensionless |
| $SA$ | surface area, m$^2$/m$^3$ |
| $\Delta S_r$ | entropy of reaction, J/K/mol |
| $T$ | temperature, K |
| **T** | viscous stress tensor, N/m |
| $t$ | tortuosity, dimensionless |
| u | velocity field, m/s |
| $v$ | dynamic viscosity, Pa·s |
| $w_i$ | mass fraction of species i, kg/kg |
| x, y | coordinate system, m |
| $x_j$ | molar fraction of species j, mol/mol |

**Greek symbols**

| | |
|---|---|
| $\varepsilon$ | porosity, dimensionless |
| $\eta$ | over potential, V |
| $\kappa$ | permeability, m$^2$ |
| $\kappa_{dv}$ | deviation from thermodynamic equilibrium, Pa·s |
| $\rho$ | density, kg/m$^3$ |
| $\sigma$ | ionic/electronic conductivity, Ω$^{-1}$m$^{-1}$ |
| $\tau$ | component thickness, m |
| $\Omega_D$ | diffusion collision integral, dimensionless |

**Subscripts**

| | |
|---|---|
| 0 | initial |
| a | anode |
| act | activation polarization |
| c | cathode |
| conc | concentration polarization |
| e | electrode, $e \in \{a, c\}$ |
| el | electrolyte |
| g | gas phase |
| $H_2$ | hydrogen |
| $H_2O$ | water |
| i | molecule i |
| int | interconnect |
| j | molecule j |
| K | Knudsen diffusion |
| losses | activation and concentration polarization |
| $O_2$ | oxygen |
| ohm | ohmic polarization |
| por | porous media |
| s | solid phase |
| TPB | three phase boundary |
| w | gas channel wall |


## ACKNOWLEDGMENTS

The Swedish Research Council (VR) and VR-Sida Swedish Research Links support the current research.


 Copyright © 2009 by ASME

## REFERENCES


[1] Patcharavorachot Y., Arpornwichanop A., Chuachuebsuk A., Electrochemical study of a planar solid oxide fuel cell: Role of support structures, *J. Power Sources*, **177**, pp. 254-261, 2008

[2] Andersson M., Yuan, J, Sundén B., Chemical Reacting Transport Phenomena and Multiscale Models for SOFCs, Proceedings of *Heat Transfer 2008,* WIT Press, UK, 2008

[3] Saxe M., Bringing fuel cells to reality and reality to fuel cells, Doctoral thesis, KTH- Royal Institute of Technology, 2008

[4] Yuan J., Yang G., Andersson M., Sundén B., CFD approach for chemical reaction coupled heat transfer in SOFC channels, Proceedings of *7th International Symposium on Heat Transfer (ISHT7),* Beijing, China, 2008

[5] Reifsnider K., Huang X., Ju G., Solasi R., Multi-scale Modeling Approaches for Functional Nano-composite Materials, *J. Mater. Sci.*, **41**, pp. 6751-6759, 2006

[6] Aguiar P., Adjiman C.S., Brandon N.P., Anode-supported intermediate temperature direct internal reforming solid oxide fuel cell. I: model-based steady-state performance, *J. Power Sources* **138**, pp.120-136, 2004

[7] Zhu B., Next generation fuel cell R&D, *Int. J. of Energy Res*., **30**, pp. 895-903, 2006

[8] Kemm M., Dynamic solid oxide fuel cell modelling for non-steady state simulation of system applications, Doctoral thesis, Lund University, 2006

[9] Bove R. Ubertini S., Modeling solid oxide fuel cell operation: Approaches, techniques and results, *J. Power Sources*, **159**, pp. 543-559, 2006

[10] Le Bars M., Grae Worster, M., Interfacial conditions between a pure fluid and a porous medium, implications for binary alloy solidification, *J. Fluid Mech.*, **550**, pp.149-173, 2006

[11] COMSOL Multiphysics 3.5 user guide, 2008

[12] Versteeg H.K., Malalasekera W., An introduction to computational fluid dynamics - The finite volume method, Pearson Education Limited, 1995

[13] Todd B., Young J.B., Thermodynamic and transport properties of gases for use in solid oxide fuel cell modeling, *J. Power Sources*, **110**, pp. 186-200, 2002

[14] Chan, S.H., Khor K.A., Xia Z.T., A complete polarization model of a solid oxide fuel cell and its sensitivity to change of cell component thickness, *J. Power Sources*, **93**, pp.130-140, 2001

[15] Nordelöf A., Salsing C., SOFC Modeling in FEMLAB, Chalmers University Sweden, Master thesis, 2003

[16] Reid R.C., Prausnitz J.M., Poling B.E., The properties of gases & liquids, fourth edition, R.R. Donnelley & Sons Company, 1986

[17] Damm D.L., Fedorov A.G., Local thermal non-equlibrium effects in porous electrodes of the hydrogen fueled SOFC, *J. Power Sources*, **159**, pp. 1153-1157, 2006

[18] Chao C.H., Hwang A.J.J., Predictions of phase temperatures in a porous cathode of polymer electrolyte fuel cells using a two-equation model, *J. Power Sources*, **160**, pp. 1122-1130, 2006

[19] Marrero-López D., Ruiz-Morales J.C. Peña-Martínez J., Canales-Vázquez J., Núñez P., Preparation of thin layer material with macroporous microstructure for SOFC applications, *J. Solid State Chemistry*, **181**, pp.685-692, 2008

[20] Chan S.H., Low C.F., Ding O.L., Energy and exergy analysis of simple solid-oxide fuel-cell power systems, *J. Power Sources*, **103**, pp. 188-200, 2002

[21] Ferguson J.R., Fiard J.M. Herbin R., Three dimensional numerical simulation for various geometries of solid oxide fuel cells, *J. Power Sources*, **58**, pp. 109-122, 1996

[22] Shah R.K., London A.L., Laminar flow forced convection in ducts. Academic Press , London, 1978

[23] Janardhanan V.M., Deutschmann O., Numerical study of mass and heat transport in solid-oxide fuel cells running on humidified methane, *Chem. Eng. Sci*., **62**, pp. 5473-5486, 2007

[24] Bessler W.G., Warnatz J., Goodwin D.G., The influence of equilibrium potential on the hydrogen oxidation kinetics of SOFC anodes, *Solid State Ionics*, **177**, pp. 3371-3383, 2007

[25] Kakac S., Pramuanjaroenkij A., Zhou X.Y., A review of numerical modeling of solid oxide fuel cells, *Int. J. Hydrogen Energy*, **32**, pp.761-786, 2006

[26] Janardhanan V.M., Deutschmann O., Numerical study of mass and heat transport in solid-oxide fuel cells running on humidified methane, *Chem. Eng. Sci.*, **62**, p. 5473-5486, 2007



Copyright © 2009 by ASME

# Paper III

This paper has been published in:

*ASME J. Fuel Cell Science and Technology,*
Vol. 8, 031013, 2011.

© 2011 ASME.

# Modeling Analysis of Different Renewable Fuels in an Anode Supported SOFC

**Martin Andersson**
e-mail: martin.andersson@energy.lth.se

**Hedvig Paradis**

**Jinliang Yuan**

**Bengt Sundén**

Department of Energy Sciences,
Faculty of Engineering,
Lund University,
Box 118,
221 00 Lund, Sweden

*It is expected that fuel cells will play a significant role in a future sustainable energy system due to their high energy efficiency and possibility to use as renewable fuels. Fuels, such as biogas, can be produced locally close to the customers. The improvement for fuel cells during the past years has been fast, but the technology is still in the early phases of development; however, the potential is enormous. A computational fluid dynamics (CFD) approach (COMSOL MULTIPHYSICS) is employed to investigate effects of different fuels such as biogas, prereformed methanol, ethanol, and natural gas. The effects of fuel inlet composition and temperature are studied in terms of temperature distribution, molar fraction distribution, and reforming reaction rates within a singe cell for an intermediate temperature solid oxide fuel cell. The developed model is based on the governing equations of heat, mass, and momentum transport, which are solved together with global reforming reaction kinetics. The result shows that the heat generation within the cell depends mainly on the initial fuel composition and the inlet temperature. This means that the choice of internal or external reforming has a significant effect on the operating performance. The anode structure and catalytic characteristic have a major impact on the reforming reaction rates and also on the cell performance. It is concluded that biogas, methanol, and ethanol are suitable fuels in a solid oxide fuel cell system, while more complex fuels need to be externally reformed.* [DOI: 10.1115/1.4002618]

*Keywords: SOFC, modeling, biogas, methanol, ethanol, natural gas, reforming, COMSOL MULTIPHYSICS*

## 1 Introduction and Problem Statement

Fuel cells (FCs) are promising due to its environmental advantages with higher efficiency and lower emissions of $SO_x$, $NO_x$, and $CO_2$ than conventional power generation [1]. The solid oxide fuel cell (SOFC) works at a high temperature such as 600–1000°C [2]. This allows SOFCs to operate with different types of fuels from both fossil and renewable sources. It opens up for an easier transition from conventional power generation with hydrocarbon based fuels to fuel cells with possibility for different fuels, especially SOFCs. Due to the increasing global awareness of how energy usage affects the environment, the interest of renewable energy has increased. SOFCs are generally more tolerant to contaminants than other fuel cells and the possibility to internally (as well as externally) reform the fuel makes them interesting for renewable energy resources [1]. Attractive fuels, which are considered in this study, are biogas, methanol, ethanol, and natural gas. The list of potential fuels for SOFC systems also includes gasoline, diesel, aviation fuel, ammonia, acetic acid, formic acid, butanol, butyric acid, and bottled gas. Coal and biomass can be used as raw fuels in a gasification process, which takes place before the fuel cell stack [3].

The aim of this paper is to study the possibility of using renewable fuels in SOFCs. The reforming reactions in SOFC systems can be conducted both externally and internally. The external reforming (ER), such as the prereformer in a SOFC system, means that the reformer is placed outside the cell, which is possible for all types of fuel cells. The internal reforming (IR) means that the reforming reactions occur within the cell. In the direct internal reforming (DIR) approach, the reforming processes occur together with the electrochemical reactions within the anode. In the indirect internal reforming (IIR) approach, the reforming reactions appear in a reformer (within the cell) in close contact with the anode where the exothermic electrochemical reactions take place. The IR reactions decrease the requirement for cell cooling (less surplus of air). Less steam is needed and finally, it offers advantages with respect to the capital cost. Up to half of the heat produced by the oxidation reaction could be "consumed" by the steam reforming (SR) process. This would improve the system electrical efficiency [4,5].

It is known that the use of heavy hydrocarbons ($C_4>$) can cause considerable coking and deactivation problems with SOFC anode catalysts. A prereformer can break down the hydrocarbons with longer coal chains to $C_1$ to $C_2$ molecules plus $H_2$ and CO [6]. An important part of the system design is the heat recovery, a big fraction of the heat generated in the cell can be used for the steam reforming reaction [7].

In this paper, a single intermediate temperature SOFC design, which uses externally reformed renewable fuels (prereformed methanol and ethanol and biogas) is studied. The renewable fuels are compared with natural gas due to the large quantity of information available in open literature. It would be interesting to apply DIR as well; however, more experimental studies need to be performed to achieve reliable kinetic data for Ni/YSZ reforming of methanol and ethanol. The approach with IIR is not yet very well developed but it can be an interesting design in the future.

**1.1 Electrochemical and Reforming Reactions.** The global reactions that take place within a SOFC using hydrogen, carbon monoxide, and methane as fuel can be described as: oxygen is reduced in the cathode (Eq. (1)). The oxygen ions are transported through the electrolyte, but the electrons are prevented to pass through the electrolyte. The electrochemical reactions (Eqs. (2) and (3)) take place in the anodic three-phase boundary (TPB). Methane needs to be reformed (Eq. (4)) before the electrochemi-

Contributed by the Advanced Energy Systems Division of ASME for publication in the JOURNAL OF FUEL CELL SCIENCE AND TECHNOLOGY. Manuscript received August 12, 2010; final manuscript received August 16, 2010; published online March 1, 2011. Editor: Nigel M. Sammes.



**Copyright © 2011 by ASME**

**Downloaded 02 Mar 2011 to 130.235.81.195. Redistribution subject to ASME license or copyright; see http://www.asme.org/terms/Terms_Use.cfm**

cal reactions. Carbon monoxide can be oxidized in the electrochemical reaction (Eq. (3)) but can also react with water (Eq. (5)). The reactions described here are the overall ones, more detailed reaction mechanisms can be found in Ref. [8]. Note that methane is not participating in the electrochemical reactions at the anodic TPB, it is catalytically converted within the anode into carbon monoxide and hydrogen, which are used as fuels in the electrochemical reactions [9],

$$O_2 + 4e^- \Leftrightarrow 2O^{2-} \tag{1}$$

$$H_2 + O^{2-} \Leftrightarrow H_2O + 2e^- \tag{2}$$

$$CO + O^{2-} \Leftrightarrow CO_2 + 2e^- \tag{3}$$

$$CH_4 + H_2O \Leftrightarrow 3H_2 + CO \tag{4}$$

$$CO + H_2O \Leftrightarrow H_2 + CO_2 \tag{5}$$

The net reaction of methanol, ethanol, and dimethyl ether (DME) to hydrogen and carbon monoxide are described in Eqs. (6)–(8), respectively. The produced carbon monoxide reacts then further with steam to hydrogen and carbon dioxide by the water-gas shift reaction, Eq. (5) [10],

$$CH_3OH \Leftrightarrow 2H_2 + CO \tag{6}$$

$$C_2H_5OH + H_2O \Leftrightarrow 4H_2 + 2CO \tag{7}$$

$$CH_3OCH_3 + H_2O \Leftrightarrow 4H_2 + 2CO \tag{8}$$

The steam reforming reaction rates for simple fuels is presented in Eqs. (4)–(8). Also more complex hydrocarbons (from renewable or fossil origin) can be used as raw energy within a fuel cell system for hydrogen production. External reforming is necessary due to relatively long carbon chains. The overall hydrocarbon reforming reaction can be written as [7]

$$C_nH_mO_z + yO_2 + 2\cdot(n - y - 0.5\cdot z)\cdot H_2O \Leftrightarrow nCO_2 + 2\cdot(n - y - 0.5\cdot z + 0.25\cdot m)\cdot H_2 \tag{9}$$

Equation (9) states the ideal reforming reaction where the only products are pure hydrogen and carbon dioxide. In reality within a fuel cell reformer, there are three ordinary reforming reactions: SR, partial oxidation (POX), and autothermal reforming (ATR). SR, Eq. (10), is effective for hydrogen production and largely exothermic. In POX, Eq. (11), the fuel is partially burned with a substoichiometric amount of air. An ATR system contains one reactor with SR and one with POX [7].

$$C_nH_mO_z + 2\cdot(n - z)\cdot H_2O \Leftrightarrow nCO + 2\cdot(n - z + 0.5\cdot m)\cdot H_2 \tag{10}$$

$$C_nH_mO_z + 0.5\cdot(n - z)\cdot O_2 \Leftrightarrow nCO + 0.5\cdot m\cdot H_2 \tag{11}$$

It should be noted that if sufficient amount of heat is available, SR gives most hydrogen per amount of raw fuel; however, the conversion of complex hydrocarbons may be more difficult, compared with POX [7].

**1.2 Renewable Fuels.** Using alternative fuels (compared with hydrogen) gives SOFCs a major advantage because pure hydrogen is highly flammable and volatile, which makes it problematic to handle. Also, hydrogen has low density, which makes storing costly. It should also be mentioned that pure hydrogen is expensive to obtain since it has to be extracted from another source, most commonly natural gas [11].

Like hydrogen, methanol and ethanol are useful energy carriers rather than primary fuels (natural gas, coal, etc.) through gasification or chemical synthesis reforming processes. The characteristics of these alcohol-based fuels are very similar to conventional liquid fuels (propane, butane, and diesel) and can be readily handled, stored, and transported [10]. The $CO_2$ emissions do not have to be an issue, when they are produced in a renewable manner, because it will lead to that the net effect on the emissions will be zero [12].

**Table 1 Enthalpy change of reforming reaction for different fuels suitable for SOFCs [10]**

| Fuel | $\Sigma\Delta h_r$ (kJ/mol) | $\Sigma\Delta h_r / n_{H_2}$ (kJ/mol per mole of $H_2$ generated) |
|---|---|---|
| Methane | −165 | −41.2 |
| Methanol | −49.4 | −16.5 |
| DME | −121 | −20.2 |
| Ethanol | −173 | −28.8 |

Methanol is interesting due to its ready availability, high specific energy, and easy storage and transportation. Ethanol is also a promising candidate since it is readily produced from renewable resources. When comparing these, ethanol has extra advantages in terms of power density, nontoxicity, transportation, and storage. However, because of incomplete oxidization, the ethanol processing reaction consists of a more complicated multistep reaction mechanism and involves a number of adsorbed intermediates and by-products. The chemical formula for biomass is generally written as $C_xH_yO_z$. The coefficients of $x$, $y$, and $z$ can be calculated for each biomass. Biomass can be converted into biogas, usually by anaerobic breakdown in the absence of oxygen. The biogas consists mainly of methane and carbon dioxide [7].

Steam reforming of various fuels available in SOFCs, such as methane (biogas and natural gas), methanol, DME, and ethanol, consumes heat. The enthalpy change of the reaction for the mentioned fuels can be seen in Table 1. Ethanol consumes the most heat per mole of fuel. However, when considering that reforming of the different fuels generate a different amount of hydrogen (to be used in the electrochemical reactions), the most heat per mole of hydrogen generated is required by the reforming of methane. Globally, all the heat needed for the reforming reactions is generated within the cell, thanks to the electrochemical reactions, and a higher efficiency can be achieved with the mentioned renewable fuels compared with pure hydrogen. It should be mentioned that the temperature can decrease close to the inlet if the steam reforming reaction rate is too high.

**1.3 Challenges With Renewable Fuels.** The direct use of hydrocarbon fuels can lead to the catalyst's rapid deactivation by carbon formation on a traditional SOFC anode and also sulfur poisoning [13]. A high inlet temperature along with internal reforming of a hydrocarbon can cause a high temperature gradient and tensions within the anode close to the fuel inlet due to the fast steam reforming reaction rate. This problem can be reduced if the fuel inlet temperature is lowered, part of the anode gas is recycled, anode reforming activity is reduced, or if (partial) prereforming is employed [5].

The probability for carbon depositions depends on the steam-to-carbon ratio and operating temperature. It has been well established that the key reactions occur over a surface layer of nickel particles. If a layer of carbon is allowed to build up and attach to a nickel crystallite rapid catalyst breakdown can occur due to the graphite formation. It should be noted that hydrocarbons with a longer carbon chain than methane have a higher propensity for carbon deposition [5,14]. It is concluded that methane and methanol with appropriate steam content can be directly fed to Ni/YSZ anode without the problem of carbon formation [6]. For fuels with a longer carbon chain, a prereformer (with a catalyst less sensitive to carbon formation than Ni/YSZ) should be included in the fuel cell system.

Sulfur needs to be removed before the fuel enters into the cell to avoid degradation within the cell. Various methods can be applied, such as high temperature desulfurization, where organic sul-



Downloaded 02 Mar 2011 to 130.235.81.195. Redistribution subject to ASME license or copyright; see http://www.asme.org/terms/Terms_Use.cfm

**Table 2 Cell geometry [2]**

| Cell component | Thickness |
|---|---|
| Cell length | 0.1 m |
| Fuel channel height | 1 mm |
| Air channel height | 1 mm |
| Anode thickness | 500 $\mu$m |
| Cathode thickness | 50 $\mu$m |
| Electrolyte thickness | 20 $\mu$m |
| Interconnect thickness | 500 $\mu$m |

fur compounds are reduced to hydrogen sulfite and the corresponding hydrocarbon, passing a cobalt or molybdenum catalyst supported on alumina. Adsorption methods can be applied for smaller SOFC systems [3].

For fuel cell systems, it is important to consider at what phase the fuel operates as the system can need extra equipments to handle the fuel storing and processing. The equipment besides the fuel cell generally takes up quite a lot of space and weight and for some fuels this becomes even more prominent when fuel storing space increases. Methane, DME, ammonia, and biogas are vapors at 1 bar and at 253–293 K. Methanol, ethanol, and diesel are liquids under these conditions. The vapors need to be pressurized to make the fuel storing in a commercial possible size with economically reasonable cost [15].

## 2 Mathematical Model

A two-dimensional model for an anode-supported SOFC is developed and implemented in the commercial software, COMSOL MULTIPHYSICS (version 3.5). Equations for momentum, mass, and heat transport are solved simultaneously. The geometry is defined in Table 2, and a sketch of the investigated cell can be seen in Fig. 1. Note the difference in scale between the cell length ($x$-direction, as in Fig. 1) and various component thicknesses ($y$-direction, as in Fig. 1). It should be mentioned that the model in this study is 2D only, and the connection between the electrodes and interconnect cannot be explicitly observed in this case.

**2.1 Momentum Transport.** The gases flow inside the fuel cell components, such as in the air and fuel channels, and in the porous electrodes. The Darcy–Brinkman equation is introduced and solved for the gas flow in the fuel and air channels and in the porous materials simultaneously [16,17]. The Darcy–Brinkman equation (Eq. (12)) is transformed into the standard Navier–Stokes equation when ($\kappa \to \infty$) and ($\varepsilon_p = 1$) and into the Darcy equation as (Da $\to 0$). Da is the Darcy number. The derivation of the Navier–Stokes and Darcy equations from the Darcy–Brinkman equation can be found in Ref. [16],

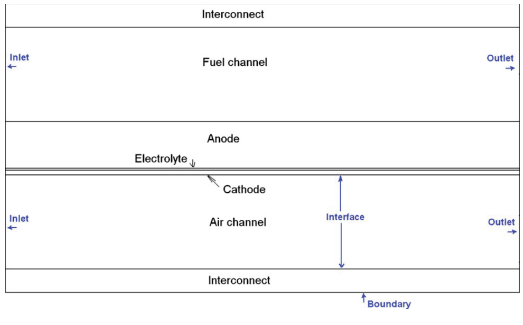


**Fig. 1 Sketch of an anode-supported SOFC, not to scale**

$$\left(\frac{\mu}{\kappa} + \rho \cdot \nabla \mathrm{u}\right)\mathrm{u} - \nabla\left[-p + \frac{1}{\varepsilon_p}\{\mathbf{T} - (\lambda)(\nabla \mathrm{u})\}\right] = \mathbf{F} \tag{12}$$

where $\mathbf{F}$ is the volume force vector, $\kappa$ is the permeability of the porous medium, $\varepsilon_p$ is the porosity, $\mu$ is the dynamic viscosity, u is the velocity vector, and $\mathbf{T}$ is the viscous stress tensor ($\mathbf{T} = v(\nabla \mathrm{u} + (\nabla \mathrm{u})^T)$). $\lambda$ is the second viscosity and for gases; it is normally assumed as $\lambda = -2\mu/3$ [18]. The densities and viscosities for the participating gases are dependent on local concentration and temperature, as described in Refs. [2,11]. The gas inlet velocities are defined as a laminar flow profile. The outlet is defined as pressure (=1 atm).

**2.2 Mass Transport.** The Maxwell–Stefan equation for mass diffusion and convection is used to describe the mass transport phenomena for the gases inside the fuel cell [17]. The Maxwell–Stefan equation is solved for the fuel and air channels and the electrodes,

$$\nabla\left(-\rho \cdot w_i \sum^{n} \bar{D}_{ij} \cdot \nabla x_j (x_j - w_j)\frac{\nabla p}{p} \cdot \mathrm{u} - D_i^T \cdot \frac{\nabla T}{T}\right) + \rho \cdot \mathrm{u} \cdot \nabla w_j = S_i \tag{13}$$

where $w$ is the mass fraction, $x$ is the molar fraction, $n$ is the number of species, $D_i^T$ is the thermal diffusion coefficient, and $D_{ij}$ is the Maxwell–Stefan binary diffusion coefficient. $S_i$, source term by chemical reactions, is only defined for the internal reforming reactions because the electrochemical reactions are assumed to take place at the interfaces between the electrolyte and electrodes. The diffusion coefficient is dependent on temperature, as described in Refs. [2,11]. On the air side, nitrogen and oxygen are involved, and only one Maxwell–Stefan diffusion coefficient needs to be calculated. On the fuel side, methane, water, hydrogen, carbon monoxide, and carbon dioxide are present, and ten pairs of Maxwell–Stefan diffusion coefficient need to be calculated. The boundary conditions for the mass transport equation are defined as mass fraction for the gas channel inlets; the outlets are defined as convective flux [2].

**2.3 Heat Transport.** The temperature distribution is calculated separately for the gas phase (in air and fuel channels and electrodes) and for the solid phase (interconnects, electrodes, and electrolyte). Heat is transferred between the phases at the channel walls and in the porous electrodes. The general heat conduction equation is used to calculate the temperature distribution for the solid materials, i.e., electrolyte, interconnect, and electrodes [17],

$$\nabla(-k_s \cdot \nabla T_s) = Q_s \tag{14}$$

where $k_s$ is the thermal conductivity of the solids, $T_s$ is the solid temperature, and $Q_s$ is the heat source (heat transfer between the solid and gas phases and heat generation due to Ohmic polarization). Note that heat generated due to Ohmic polarization is assumed to enter the solid phase (as a part of $Q_s$), heat generation due to electrochemical reactions, concentration and activation polarization are simplified and defined as interface conditions, such as for the mass transport. The temperature distribution for the gas mixtures in the fuel and air channels and in the porous electrodes is calculated as [17]

$$\nabla(-k_g \cdot \nabla T_g) = Q_g - \rho_g \cdot c_{p,g} \cdot \mathrm{u} \cdot \nabla T_g \tag{15}$$

in which $c_{p,g}$ is the gas phase heat capacity, $T_g$ is the temperature in the gas phase, and $Q_g$ is the heat transfer between the gas and solid phases. Because the Reynolds number is small, the heat transfer coefficient ($h_{s,g,\mathrm{por}}$) in the porous electrodes (spherical particles are assumed) can be calculated as [19]



Downloaded 02 Mar 2011 to 130.235.81.195. Redistribution subject to ASME license or copyright; see http://www.asme.org/terms/Terms_Use.cfm

$$h_{s,g,\mathrm{por}} = \frac{2 \cdot k_g}{d_p} \tag{16}$$

where $d_p$ is the electrode particle diameter and $k_g$ is the gas conductivity. The heat transfer between the gas and solid phase depends on the temperature difference and the particle area to volume ratio as [20]

$$Q_g = h_v \cdot (T_g - T_s) = AV \cdot h_{s,g,\mathrm{por}} \cdot (T_g - T_s) \tag{17}$$

in which $h_v$ is the volume heat transfer coefficient and $AV$ is the area to volume ratio, which is used for heat transfer between the solid and gas phase. Note that the surface to volume ratio for heat transfer is higher than that for chemical reactions because not all the available surface is covered with active nickel catalyst. The heat transfer area to volume ratio equals to the material specific available area (area per weight) times the density. The heat capacity and the thermal conductivity in the gas phase depend on the temperature and the concentration, as described in Refs. [2,11]. The heating due to Ohmic polarization is described in Sec. 2.4.

The inlet gas temperature is defined by the operating temperature (1000 K), and the outlet one is defined as a convective flux. The boundaries at the top and at the bottom of the cell are defined by symmetries because it is assumed that the cell is surrounded by other cells with the same temperature distribution. The heat flux between the electrodes/interconnect and gas channels are specified at two channel walls, located opposite to each other, with a constant Nusselt number (4.094) from Ref. [21], based on the fully developed flow for a rectangular duct (aspect ratio is 1 for both channels). The cell is also heated due to change in entropy in the electrochemical reactions and concentration and activation polarizations, as described in Sec. 2.4.

**2.4 Electrochemical Reactions.** Two approaches for defining the electrochemical reactions can be found in literature, either as source terms in the governing equations [22,23] or as interface conditions defined at the electrode/electrolyte interfaces [24,25]. The later approach is employed in this study because the thickness of the active layer is sufficiently thin, compared with the thickness of the electrode [24,25]. The charge transfer equations are not solved in this study; however, the temperature effects from Ohmic, concentration, and activation polarization losses are included in the equations for heat transport.

Both hydrogen and carbon monoxide can participate in electrochemical reactions with oxygen ions (Eqs. (2) and (3)). The electrochemical oxidation of hydrogen is several times higher than that of carbon monoxide while the water-gas shift reaction is relatively fast [23]. The contribution of oxidation of carbon monoxide has been neglected in this study. The cell average current density in this study is specified as 0.3 $\mathrm{A/cm^2}$.

Ohmic polarization occurs due to resistance of the flow of ions in the electrolyte and electrical resistance in the electrodes. The electrodes and electrolyte are heated due to this effect [26,27],

$$Q_{\mathrm{ohm}} = \frac{i \cdot \eta_{\mathrm{ohm}}}{\tau} \tag{18}$$

$$\eta_{\mathrm{ohm}} = R_{\mathrm{ohm}} \cdot i \tag{19}$$

$$R_{\mathrm{ohm}} = \frac{\tau_a}{\sigma_a} + \frac{\tau_{\mathrm{el}}}{\sigma_{\mathrm{el}}} + \frac{\tau_c}{\sigma_c} \tag{20}$$

where $\tau$ is the component thickness and $R_{\mathrm{ohm}}$ is the electrolyte area-specific Ohmic resistance. The electronic/ionic conductivities ($\sigma$) are calculated as described in Ref. [26].

Heat generated due to electrochemical reactions and due to polarization losses are, as previously described, defined at the electrodes/electrolyte interfaces,

$$-n \cdot (-k \nabla T) - = q_0 \tag{21}$$

$$q_0 = q_r + q_{\mathrm{losses}} = -i \cdot \left( \frac{T \cdot \Delta S_r}{n_e \cdot F} + \eta_{\mathrm{act},e} + \eta_{\mathrm{conc},e} \right) \tag{22}$$

where $q_0$ is the heat generated at the interface (specified as interface condition), $q_r$ is the heat generated inside the cell due to change in enthalpy, and $q_{\mathrm{losses}}$ is the heat generated due to potential losses inside the cell. The amount of heat generated due to electrochemical reactions can be calculated as [28]

$$q_r = -T \cdot \Delta S_r \cdot \dot{n} = -\Delta S_r \frac{T \cdot i}{n_e F} \tag{23}$$

$$\dot{n} = \frac{i}{n_e F} \tag{24}$$

where $\dot{n}$ is the molar flux density ($\mathrm{mol/(m^2\ s)}$) and $\Delta S_r$ is entropy change of reaction (−50.2 J/(K mol)), calculated from data in Ref. [29]. The heat generation due to activation and concentration polarizations can be calculated as [27,30]

$$q_{\mathrm{losses}} = -i \cdot (\eta_{\mathrm{act},e} + \eta_{\mathrm{conc},e}) \tag{25}$$

The concentration polarizations due to concentration differences inside the cell are specified as [26]

$$\eta_{\mathrm{conc},a} = \frac{RT}{n_{e,a} F} \ln\left( \frac{p_{\mathrm{H_2O,TPB}} \cdot p_{\mathrm{H_2},b}}{p_{\mathrm{H_2,TPB}} \cdot p_{\mathrm{H_2O},b}} \right) \tag{26}$$

$$\eta_{\mathrm{conc},c} = \frac{RT}{n_{e,c} F} \ln\left( \frac{p_{\mathrm{O_2},b}}{p_{\mathrm{O_2,TPB}}} \right) \tag{27}$$

where $p_{i,\mathrm{TPB}}$ stands for the partial pressure at the boundary TPB and $p_{i,b}$ is the partial pressure at the interface between gas channel and electrode. Chemical reactions involve energy barriers (i.e., activation polarization), which must be overcome by the reacting species. The activation polarization can be considered as the extra potential needed to overcome the energy barrier of the rate-determining step to a value that the reaction proceeds at a desired rate [30],

$$\eta_{\mathrm{act},e} = \frac{2RT}{n_e F} \sinh^{-1}\left( \frac{i_e}{2 \cdot i_{0,e}} \right) \tag{28}$$

$$i_{0,e} = \frac{RT}{n_e F} k''_e \exp\left( \frac{-E_e}{RT} \right) \tag{29}$$

where $i_{0,e}$ is the exchange current density. The pre-exponential factor ($k''$) is $2.35 \times 10^{11}\ \Omega^{-1}\ \mathrm{m^{-2}}$ for the cathode and $6.54 \times 10^{11}\ \Omega^{-1}\ \mathrm{m^{-2}}$ for the anode, respectively. The activation energy ($E$) is 137 kJ/mol for the cathode and 140 kJ/mol for the anode [26].

**2.5 Internal Reforming Reactions.** Sufficient activity for the reforming reactions is provided inside the SOFC anode [31]. Reaction kinetics from Ref. [32] for the steam reforming (an expression dependent on the active area to volume ratio) and from Ref. [33] for the water-gas shift reactions are used to calculate the reaction rates in this work. Other global kinetic models can be found in Refs. [34,35]. The catalytic steam reforming reaction occurs at the surface of the nickel catalyst and is specified as [32,36]

$$r_r = AV \cdot \left( 943 \exp\left( \frac{-225 \times 10^3}{R \cdot T} \right) \cdot p_{\mathrm{CH_4}} p_{\mathrm{H_2O}} - 7.74 \times 10^{-9} \exp\left( \frac{-1937}{R \cdot T} \right) \cdot p_{\mathrm{CO}} p_{\mathrm{H_2}}^3 \right) \tag{30}$$

where $p_i$ is the partial pressure of gas species $i$, $T$ is the temperature, $r$ is the reaction rate, and $AV$ is the active area to volume ratio. Equation (30) originates from experiments performed at the Research Center Jülish, and the anode material consists of Ni-



Downloaded 02 Mar 2011 to 130.235.81.195. Redistribution subject to ASME license or copyright; see http://www.asme.org/terms/Terms_Use.cfm

8YSZ substrate with a standard composition of $C_nH_mO_z$ Ni [36].

The range for the $AV$ (related to catalytic kinetic reactions) varies in literature between $1\times10^5$ $m^2/m^3$ [37] and $2.2\times10^6$ $m^2/m^3$ [32] for SOFC anodes. The measured specific surface area ($m^2/g$) for Ni/YSZ material developed for SOFC anodes (with a pore size of 225 nm) is $70\times10^6$ $m^2/m^3$ [38]. Note that not all the surfaces are available for catalytic reactions due to the distribution of catalyst, nonavailable pores, and mass transfer limitations among others. An $AV$ of $2.2\times10^6$ $m^2/m^3$, corresponding to 3.1% of the total Ni/YSZ specific area to volume ratio, is used in this work. The trend for the development during the past years is in the direction of employing smaller particles to get larger $AV$.

The reaction rate (Eq. (30)) is of the Arrhenius type. It consists of three parts, partial pressures, pre-exponential factor, and activation energy. The pre-exponential factor describes the amount of collisions between the molecules within the reaction and the exponential expression with the activation energy describes the probability for the reaction to occur. The pre-exponential factors depend strongly on the properties of the anode material and the temperature. The activation energy is based on the catalytic characteristics, such as chemical composition. The large difference between the activation energies in open literature [11,32,34–36,39] makes it probable that more parameters have significant influences on the reaction rate. To truly enhance the understanding of these phenomena, microscale modeling is needed.

Different approaches for defining the water-gas shift reaction can be found in literature: (1) global reaction mechanism that considers reaction in the anode only [9,23,33], (2) global reaction mechanism that considers reaction in the anode and in the fuel channel [32,40], and (3) a more advanced reaction mechanism that includes catalytic surface reaction kinetics for integrated steam reforming, water-gas shift reaction, and the Boudouard mechanism [8,41]. Based on the global scheme for the anode, the expression for the catalyzed water-gas shift reaction in Ref. [33] has been selected in this study:

$$r_s = k_{sf} \cdot \left( p_{H_2O} p_{CO} - \frac{p_{H_2} p_{CO_2}}{K_{ps}} \right) \tag{31}$$

The rate constant ($k_{sf}$) and the equilibrium constant ($K_{ps}$) are temperature dependent expressions calculated from experimental data, as described in Ref. [33].

The source terms $S_i$ (implemented in the Maxwell Stefan equation for mass transport), due to the catalytical reforming reactions, are defined as [23]

$$S_{H_2} = (3r_r + r_s) \cdot M_{H_2} \tag{32}$$

$$S_{CH_4} = -r_r \cdot M_{CH_4} \tag{33}$$

$$S_{H_2O} = (-r_r - r_s) \cdot M_{H_2O} \tag{34}$$

$$S_{CO} = (r_r - r_s) \cdot M_{CO} \tag{35}$$

where $M_i$ is the molecular weight and $S_i$ is the source term of species $i$. The last species ($CO_2$) can be obtained because the sum of the mass fractions equals unity. The heat generation/consumption due to the reforming reactions is specified in [11]

$$Q_s = \sum_i r_i \cdot \Delta h_i \tag{36}$$

where $\Delta h_i$ is the enthalpy change due to the reactions and $Q_s$ is the heat generation in the solid phase.

**2.6 Cell Operating Conditions.** The investigation performed in this study concerns biogas, prereformed methanol, ethanol, and natural gas. The inlet molar fractions are specified in Table 3. The molar fractions based on initial steam-to-fuel ratios (SFs) of 3 and 5 (for methanol and ethanol) are calculated from the experiments performed in Ref. [6]. After the prereforming of ethanol, the fuel mixture contains some ethylene and etan. To simplify the calculation and due to the lack of kinetic information in considering reforming of ethylene and etan on Ni/YSZ catalyst, these concentrations are assumed to be methane. For the case of biogas, a small fraction of hydrogen is added to enable electrochemical reactions close to the inlet as well, and steam is added to avoid carbon deposition and to be used in the reforming reactions. The fuel composition for 30% prereformed natural gas is defined by the International Energy Agency (IEA) and is frequently used in literature. The flow rates for the different cases are calculated to keep the fuel utilization being 80%. The flow rate of air is kept constant for all cases and the oxygen utilization is set to be 20%.

**Table 3 Inlet molar fractions**

| | $H_2$ | CO | $CO_2$ | $CH_4$ | $H_2O$ |
|---|---|---|---|---|---|
| Methanol, SF=3 | 0.270 | 0.115 | 0.051 | 0.017 | 0.547 |
| Methanol, SF=5 | 0.247 | 0.072 | 0.042 | 0.011 | 0.628 |
| Ethanol, SF=3 | 0.359 | 0.114 | 0.030 | 0.112 | 0.385 |
| Ethanol, SF=5 | 0.312 | 0.081 | 0.036 | 0.080 | 0.491 |
| Biogas steam mixture | 0.03 | 0 | 0.27 | 0.36 | 0.34 |
| 30% prereformed natural gas [11] | 0.263 | 0.0294 | 0.0436 | 0.171 | 0.493 |

## 3 Results and Discussion

The predicted temperature distribution for the case with prereformed methanol with initial SFs of 3 and 5 can be seen in Figs. 2 and 3, respectively. Increased SF means a slightly decreased temperature rise (5 K difference in the maximum temperature between these two cases) due to a higher flow rate in the flow channel (to keep the fuel utilization to 80%). It should be mentioned that the flow rate in the air channel is significantly higher than in the fuel channel. The temperature difference in the $y$-direction (Fig. 4) in the air channels occurs because the convective heat flux are bigger in the air channel (compared with the fuel channel) due to the relatively larger air flow rate.

The temperature distribution for biogas is shown in Fig. 5, that for prereformed ethanol (SF=3) is shown in Fig. 6, and that for 30% prereformed natural gas is shown in Fig. 7. The case with biogas and natural gas contains more methane compared with that of prereformed ethanol and methanol. A higher fraction of methane means a decreased total temperature rise due to the heat consumption in the steam reforming reaction.

The developed model is also used to simulate cases with an even higher concentration of methane and also a higher inlet temperature (compared with the cases in Table 3). The limitation to be

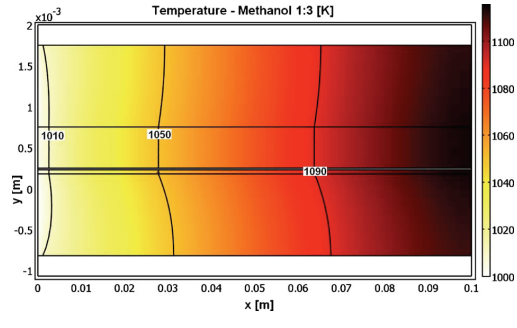


**Fig. 2 Gas phase temperature distribution for prereformed methanol (SF=3)**



Downloaded 02 Mar 2011 to 130.235.81.195. Redistribution subject to ASME license or copyright; see http://www.asme.org/terms/Terms_Use.cfm

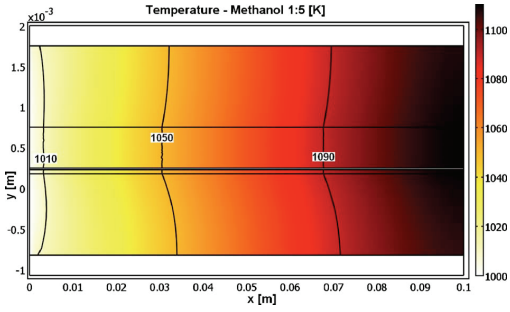


**Fig. 3 Gas phase temperature distribution for prereformed methanol (SF=5)**

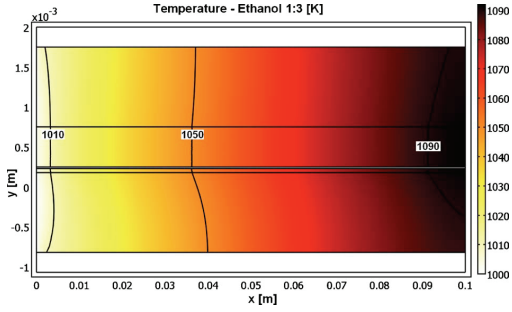


**Fig. 6 Gas phase temperature distribution for prereformed ethanol (SF=3)**

considered is that the probability of carbon deposition increases when the SC is too low. The potential trouble with a high temperature gradient close to the fuel inlet can be managed with lowering the inlet temperature or diluting the fuel since a higher temperature or a less diluted fuel gives a higher steam reforming reaction rate and also a higher temperature gradient. This is not a problem, for the cases specified in Table 3, since a relatively low inlet temperature (1000 K) as well as prereformed fuel mixtures is used. The activation energy in the methane steam reforming reaction is high for this case; i.e., the probability for reaction is very low. A catalytic composition with decreased activation energy will cause a steeper temperature gradient. When the inlet temperature is increased, a high temperature gradient close to the inlet can occur, as observed in Fig. 8, where the inlet gas temperature for the case with biogas is increased with 100 K. Note that the heat generated by the electrochemical reactions and polarization losses is still higher than the heat consumed by the reforming reactions when the complete cell is studied.

The predicted molar fractions in the fuel channel for the participating gas species along the flow direction for the case with prereformed methanol (SF=3) are shown in Fig. 9, and those for the case with biogas are shown in Fig. 10. Hydrogen is consumed and water is generated (due to the electrochemical reactions) along the flow direction for all the investigated situations. There is a consumption of water as carbon monoxide and methane are reformed. Depending on the inlet fraction, a decrease in the molar fraction of water can be observed close to the inlet, e.g., for the

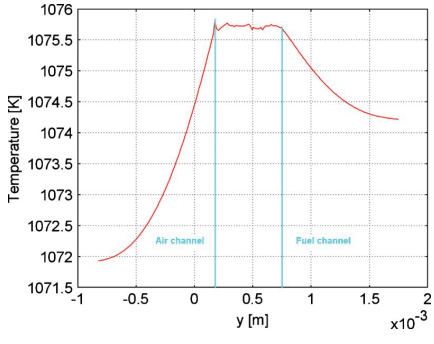


**Fig. 4 Gas phase temperature distribution for prereformed methanol (SF=3) in the middle of the cell (at $x$=0.05 m)**

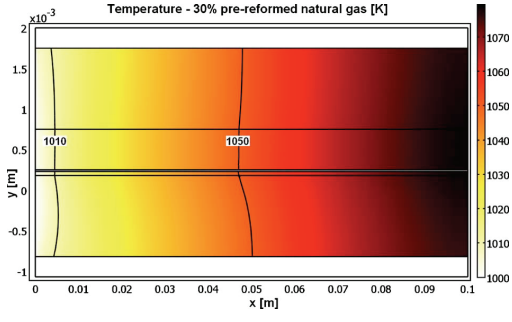


**Fig. 7 Gas phase temperature distribution for 30% prereformed natural gas**

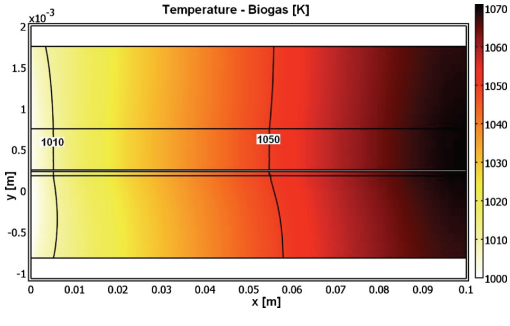


**Fig. 5 Gas phase temperature distribution for biogas-steam mixture**

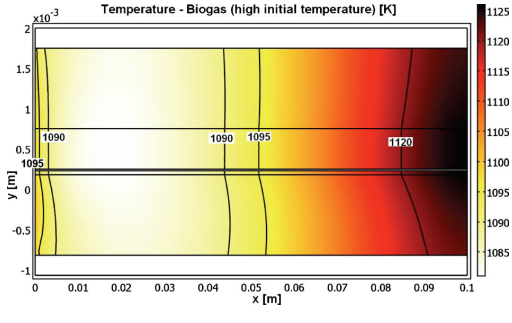


**Fig. 8 Gas phase temperature distribution for biogas-steam mixture with an increased inlet temperature**



Downloaded 02 Mar 2011 to 130.235.81.195. Redistribution subject to ASME license or copyright; see http://www.asme.org/terms/Terms_Use.cfm

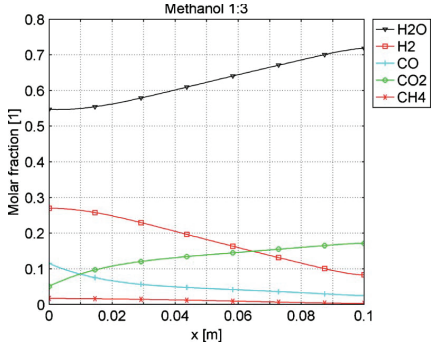


**Fig. 9 Molar fraction of the gas species in the fuel channel along the flow direction for prereformed methanol (SF=3)**

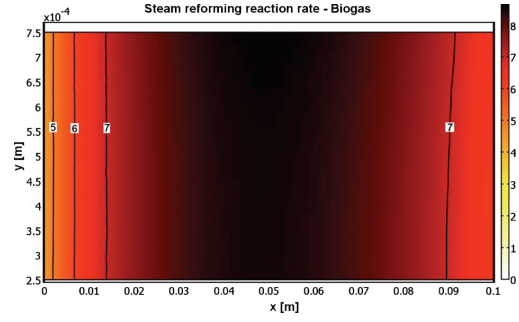


**Fig. 11 Reaction rate (in mol/(m$^3$ s)) for the steam reforming reaction within the anode for the case with biogas-steam mixture**

cases with prereformed methanol. The molar fraction of carbon monoxide depends on the water-gas shift reaction. The case with biogas contains initially very little hydrogen. The generation of more hydrogen depends on the steam reforming reaction, which depends on the active area to volume ratio, temperature, and gas species concentrations. Note that the total amount of molecules (within the fuel cell) increases as the steam reforming reaction proceeds to the right.

For the situations with high inlet concentrations of methane (for example, the case with biogas, shown in Fig. 11), the steam reforming reaction rate (within the anode) is high as long as high concentration of methane is available. The lower rate close to the inlet is due to a lower temperature. The reaction rate expression has, as previously mentioned, high activation energy. This is the reason for the relatively low reaction rate, which enables the methane steam reforming reaction rate to be similar within the entire length of the anode. It should be mentioned that the backward reaction rate is negligible, compared with the forward reaction rate for the situations applied in this study. The reaction rate increases as the temperature and concentration of steam increase and decreases as the concentration of methane decreases. Note that there is a difference in scale between the *x*- and *y*-directions. The steam reforming reaction rate in the anode for the case with prereformed methanol (SF=3) is shown in Fig. 12. It contains initially very little methane. This gives a low initial steam reforming reaction rate, which increases as the carbon monoxide and the hydrogen are consumed, as well as the temperature is increased. It is possible to change the reaction rate, either by changing the particle size of active catalyst or the porous structure, i.e., active catalytic area.

As shown in Fig. 13, high reaction rates for the water-gas shift reaction are obtained when the inlet concentrations are far from equilibrium conditions in terms of temperature and concentrations, for example, for methanol with the SF of 3. The reaction rate for the water-gas shift reaction in the anode for the case with biogas is shown in Fig. 14. The reaction proceeds initially to the left due to a low concentration of carbon monoxide and a high concentration of carbon dioxide. As hydrogen is consumed and water generated by the electrochemical reaction within the anode, this reaction proceeds to the right. The water-gas shift reaction is

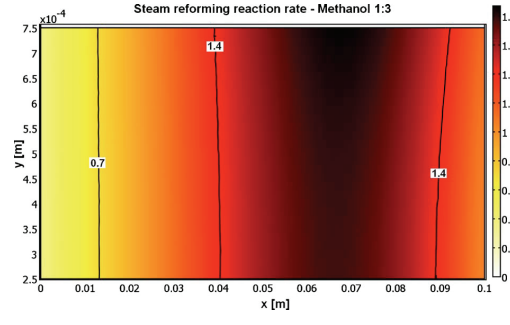


**Fig. 12 Reaction rate (in mol/(m$^3$ s)) for the steam reforming reaction within the anode for prereformed methanol (SF=3)**

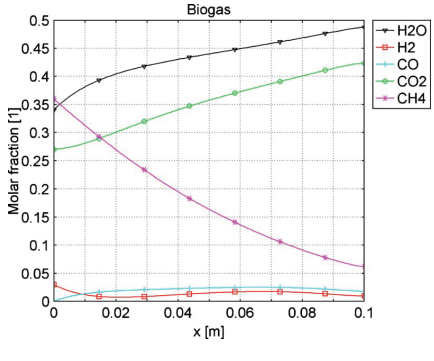


**Fig. 10 Molar fraction of the gas species in the fuel channel along the flow direction for biogas-steam mixture**

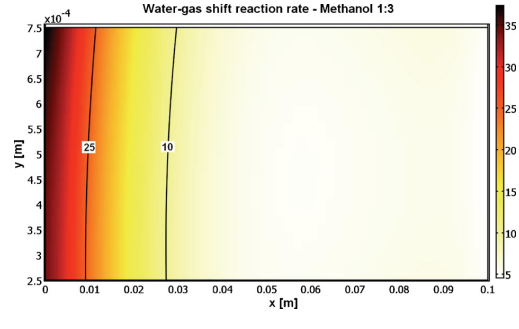


**Fig. 13 Reaction rate (in mol/(m$^3$ s)) for the water-gas shift reaction within the anode for prereformed methanol (SF=3)**



**Downloaded 02 Mar 2011 to 130.235.81.195. Redistribution subject to ASME license or copyright; see http://www.asme.org/terms/Terms_Use.cfm**

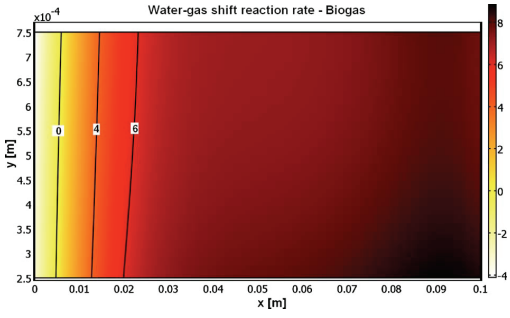


**Fig. 14 Reaction rate (in mol/(m$^3$ s)) for the water-gas shift reforming reaction within the anode for biogas-steam mixture**

coupled to the steam reforming reaction, due to the production of carbon monoxide and hydrogen, and consumption of water.

No validation with experimental data has been conducted. However, some comparison with literature has been done. The result in this study follows the same trend concerning temperature and concentration distributions along the flow direction as in Refs. [32,40,41].

## 4 Conclusions

A CFD approach is developed and implemented to analyze physical phenomena, which take place inside a single anode-supported SOFC. Equations for mass, heat, and momentum transport are solved simultaneously. The temperature distributions in the gas and solid phases are calculated separately according to the local temperature nonequilibrium approach. The operating parameters are kept constant, while the inlet fuel compositions are varied to illustrate biogas, prereformed methanol, ethanol, and natural gas.

The heat, which is generated due to the electrochemical reactions, can be used for internal steam reforming reaction within the anode and/or outside the cell for external reforming and preheating of the fuel and air. It is concluded that a fuel containing a high percentage of methane and also a high inlet temperature gives a steep temperature gradient close to the fuel inlet (i.e., the case with biogas and an increased inlet temperature). The case with prereformed methanol contains only a small amount of methane, which makes the total heat generation higher, compared with the other investigated cases. It is found that for the steam reforming reaction, the backward reaction rate is negligible, compared with the forward one, for the conditions within a SOFC. The probability for methane steam reforming reaction is low due to the high activation energy. To increase the reaction rate significantly, a new catalytic composition should be introduced. The low reforming reaction rate has advantages in terms of a low temperature gradient, i.e., decreased risk of mechanical failure.

It is concluded that biogas, methanol, and ethanol are suitable alternative fuels for a SOFC system. The reforming of ethanol is more complex and gives more by-products compared with the reforming of methanol and methane. Utilization of a fuel with an even longer coal chain makes the reforming more complex and the possibility of internal reforming (within the anode) disappear. Addition of more steam to fuel decreases the risk of carbon deposition at the anode catalytic active area.

Further development of SOFCs can enhance the transition from fossil fuels to renewable fuels. The choice of the fuel for a commercial fuel cell system will depend on the available fuel infrastructure, complexity of system, environmental requirements to be considered, and price for the different fuels.

## Acknowledgment

The Swedish Research Council (VR) and the European Research Council (ERC) support the current research.

## Nomenclature

$AV$ = (active) area to volume ratio, m$^2$/m$^3$
$c_p$ = specific heat capacity at constant pressure, J/kg K
Da = Darcy number, dimensionless
$D_{ij}$ = Maxwell–Stefan binary diffusion coefficient, m$^2$/s
$D_i^T$ = thermal diffusion coefficient, kg/(m s)
$d_p$ = electrode particle diameter, m
$E$ = activation energy, kJ/mol
$\mathbf{F}$ = volume force vector, N/m$^3$
$F$ = Faraday constant, 96,485 C/mol
$h$ = enthalpy, J/mol
$h_{s,g}$ = heat transfer coefficient, W/(m$^2$ K)
$h_v$ = volume heat transfer coefficient, W/(m$^3$ K)
$i$ = current density, A/cm$^2$
$i_0$ = exchange current density, A/cm$^2$
$k$ = thermal conductivity, W/m/K
$k''$ = pre-exponential factor, 1/($\Omega$ m$^2$)
$M_j$ = molar mass of species $j$, kg/mol
$n_e$ = number of electrons transferred per reaction
$p_i$ = pressure of species $i$, Pa
$q$ = heat flux, W/m$^2$
$Q$ = source term (heat), W/m$^3$
$R$ = gas constant, 8.314 J/mol K
$r$ = reaction rate, mol/(m$^2$ s), mol/(m$^3$ s)
$R_{\text{ohm}}$ = electrolyte area-specific Ohmic resistance, $\Omega$/m$^2$
$S_i$ = source term (mass), kg/(m$^3$ s)
$\mathbf{T}$ = viscous stress tensor, N/m
$T$ = temperature, K
u = velocity field, m/s
$v$ = dynamic viscosity, Pa s
$w_i$ = mass fraction of species $i$, kg/kg
$x, y$ = coordinate system, m
$x_j$ = molar fraction of species $j$, mol/mol
$\Delta S_r$ = entropy of reaction, J/K mol

### Greek Symbols

$\varepsilon_p$ = porosity, dimensionless
$\eta$ = over potential, V
$\kappa$ = permeability, m$^2$
$\lambda$ = second viscosity, Pa s
$\mu$ = dynamic viscosity, Pa s
$\rho$ = density, kg/m$^3$
$\sigma$ = ionic/electronic conductivity, $\Omega^{-1}$ m$^{-1}$
$\tau$ = component thickness, m

### Subscripts

0 = initial
$a$ = anode
act = activation polarization
$c$ = cathode
conc = concentration polarization
$e$ = electrode, $e \in \{a, c\}$
el = electrolyte
$g$ = gas phase
$i$ = molecule i
$j$ = molecule j
losses = activation and concentration polarization
ohm = Ohmic polarization
por = porous media
$r$ = steam reforming reaction



**Downloaded 02 Mar 2011 to 130.235.81.195. Redistribution subject to ASME license or copyright; see http://www.asme.org/terms/Terms_Use.cfm**

$s$ = solid phase, water-gas shift reaction

**Chemical**

$C_2H_5OH$ = ethanol
$CH_3OCH_3$ = dimethyl ether (DME)
$CH_3OH$ = methanol
$CH_4$ = methane
$C_nH_mO_z$ = hydrocarbon with a carbon chain of $n$ atoms
$CO$ = carbon monoxide
$CO_2$ = carbon dioxide
$e^-$ = electron
$H_2$ = hydrogen
$H_2O$ = water
Ni = nickel
$O_2$ = oxygen
YSZ = yttria-stabilized zirconia

## References


[1] Staniforth, J., and Ormerod, M., 2002, "Implications for Using Biogas as a Fuel Source for Solid Oxide Fuel Cells: Internal Dry Reforming in a Small Tubular Solid Oxide Fuel Cell," Catal. Lett., **81**, pp. 19–23.

[2] Andersson, M., Yuan, J., Sundén, B., and Wang, W. G., 2009, "LTNE Approach and Simulation for Anode-Supported SOFCs," *Proceedings of the Seventh International Fuel Cell Science, Engineering and Technology Conference*, Newport Beach, CA.

[3] Ormerod, R. M., 2004, "Fuels and Fuel Processing in Solid Oxide Fuel Cells," *Solid Oxide Fuel Cells*, S. C. Singhal and K. Kendall, eds., Springer-Verlag, Berlin, pp. 333–362.

[4] Dokmaingam, P., Assabumrungrat, S., Soottitantawat, A., and Laosiripojana, N., 2010, "Modelling of Tubular-Designed Solid Oxide Fuel Cell With Indirect Internal Reforming Operation Fed by Different Primary Fuels," J. Power Sources, **195**, pp. 69–78.

[5] Andersson, M., Paradis, H., Yuan, J., and Sundén, B., 2010, "Catalyst Materials and Catalytic Steam Reforming Reactions in SOFC Anodes," *Proceedings of the International Green Energy Conference*, Waterloo, ON, Canada.

[6] Laosiripojana, N., and Assabumrungrat, S., 2007, "Catalytic Steam Reforming of Methane, Methanol and Ethanol Over Ni/YSZ: The Possible Use of These Fuels in Internal Reforming SOFC," J. Power Sources, **163**, pp. 943–951.

[7] Xuan, J., Leung, M. K. H., Leung, D. Y. C., and Ni, M., 2009, "A Review of Biomass-Derived Fuel Processors for Fuel Cell Systems," Renewable Sustainable Energy Rev., **13**, pp. 1301–1313.

[8] Janardhanan, V., and Deutschmann, O., 2006, "CFD Analysis of a Solid Oxide Fuel Cell With Internal Reforming," J. Power Sources, **162**, pp. 1192–1202.

[9] Ni, M., Leung, M. K. H., and Leung, D. Y. C., 2007, "Micro-Scale Modeling of Solid Oxide Fuel Cells With Micro-Structurally Grades Electrodes," J. Power Sources, **168**, pp. 369–378.

[10] Cocco, D., and Tola, V., 2009, "Use of Alternative Hydrogen Energy Carriers in SOFC-MGT Hybrid Power Plants," Energy Convers. Manage., **50**, pp. 1040–1048.

[11] Andersson, M., 2009, "SOFC Modeling Considering Mass and Heat Transfer, Fluid Flow With Internal Reforming Reactions," Licentiate thesis, Department of Energy Sciences, Lund University, Sweden.

[12] Mignard, D., and Pritchard, C., 2008, "On the Use of Electrolytic Hydrogen From Variable Renewable Energies for the Enhanced Conversion of Biomass to Fuels," Chem. Eng. Res. Des., **86**, pp. 473–487.

[13] Cimenti, M., and Hill, J. M., 2009, "Thermodynamic Analysis of Solid Oxide Fuel Cells Operated With Methanol and Ethanol Under Direct Utilization, Steam Reforming, Dry Reforming or Partial Oxidation Conditions," J. Power Sources, **186**, pp. 377–384.

[14] Clarke, S., Dicks, A., Pointon, K., Smith, T., and Swann, A., 1997, "Catalytic Aspects of the Steam Reforming of Hydrocarbons in Internal Reforming Fuel Cells," Catal. Today, **38**, pp. 411–423.

[15] Paradis, H., Andersson, M., Yuan, J., and Sundén, B., 2010, "Review of Different Renewable Fuels for Potential Utilization in SOFCs," *Proceedings of the International Green Energy Conference*, Waterloo, ON, Canada.

[16] Le Bars, M., and Worster, M. G., 2006, "Interfacial Conditions Between a Pure Fluid and a Porous Medium, Implications for Binary Alloy Solidification," J. Fluid Mech., **550**, pp. 149–173.

[17] COMSOL, 2008, COMSOL MULTIPHYSICS 3.5 User Guide, Stockholm, Sweden.

[18] Versteeg, H. K., and Malalasekera, W., 1995, *An Introduction to Computational Fluid Dynamics, The Finite Volume Method*, Pearson, UK.

[19] Damm, D. L., and Fedorov, A. G., 2006, "Local Thermal Non-Equlibrium Effects in Porous Electrodes of the Hydrogen Fueled SOFC," J. Power Sources, **159**, pp. 1153–1157.

[20] Chao, C. H., and Hwang, A. J. J., 2006, "Predictions of Phase Temperatures in a Porous Cathode of Polymer Electrolyte Fuel Cells Using a Two-Equation Model," J. Power Sources, **160**, pp. 1122–1130.

[21] Shah, R. K., and London, A. L., 1978, *Laminar Flow Forced Convection in Ducts*, Academic, London, UK.

[22] Hussain, M. M., Li, X., and Dincer, I., 2007, "Mathematical Modeling of Transport Phenomena in Porous SOFC Anodes," Int. J. Therm. Sci., **46**, pp. 48–56.

[23] Yuan, J., Huang, Y., Sundén, B., and Wang, W. G., 2009, "Analysis of Parameter Effects on Chemical Coupled Transport Phenomena in SOFC Anodes," Heat Mass Transfer, **45**, pp. 471–484.

[24] Suwanwarangkul, R., Croiset, E., Fowler, M. W., Douglas, P. L., Entchev, E., and Douglas, M. A., 2003, "Dusty-Gas and Stefan-Maxwell Models to Predict the Concentration Overpotential of a SOFC Anode," J. Power Sources, **122**, pp. 9–18.

[25] Tseronis, K., Kookos, I. K., and Theodoropoulos, C., 2006, "Modeling Mass Transport in Solid Oxide Fuel Cell Anodes: A Case for a Multidimensional Dusty Gas-Based Model," Chem. Eng. Sci., **63**, pp. 5626–5638.

[26] Patcharavorachot, Y., Arpornwichanop, A., and Chuachuebsuk, A., 2008, "Electrochemical Study of a Planar Solid Oxide Fuel Cell: Role of Support Structures," J. Power Sources, **177**, pp. 254–261.

[27] Chan, S. H., Low, C. F., and Ding, O. L., 2002, "Energy and Exergy Analysis of Simple Solid-Oxide Fuel-Cell Power Systems," J. Power Sources, **103**, pp. 188–200.

[28] Bove, R., and Ubertini, S., 2006, "Modeling Solid Oxide Fuel Cell Operation: Approaches, Techniques and Results," J. Power Sources, **159**, pp. 543–559.

[29] Bessler, W. G., Warnatz, J., and Goodwin, D. G., 2007, "The Influence of Equilibrium Potential on the Hydrogen Oxidation Kinetics of SOFC Anodes," Solid State Ionics, **177**, pp. 3371–3383.

[30] Chan, S. H., Khor, K. A., and Xia, Z. T., 2001, "A Complete Polarization Model of a Solid Oxide Fuel Cell and Its Sensitivity to Change of Cell Component Thickness," J. Power Sources, **93**, pp. 130–140.

[31] Ferguson, J. R., Fiard, J. M., and Herbin, R., 1996, "Three-Dimensional Numerical Simulation for Various Geometries of Solid Oxide Fuel Cells," J. Power Sources, **58**, pp. 109–122.

[32] Klein, J.-M., Bultel, Y., Georges, S., and Pons, M., 2007, "Modeling of a SOFC Fuelled by Methane: From Direct Internal Reforming to Gradual Internal Reforming," Chem. Eng. Sci., **62**, pp. 1636–1649.

[33] Haberman, B. A., and Young, J. B., 2004, "Three-Dimensional Simulation of Chemically Reacting Gas Flows in the Porous Support Structure of an Integrated-Planar Solid Oxide Fuel Cell," Int. J. Heat Mass Transfer, **47**, pp. 3617–3629.

[34] Nagel, F., Schildhauer, T., Biollaz, S., and Stucki, S., 2008, "Charge, Mass and Heat Transfer Interactions in Solid Oxide Fuel Cells Operated With Different Fuel Gases—A Sensitivity Analysis," J. Power Sources, **184**, pp. 129–142.

[35] Sanchez, D., Chacartegui, R., Munoz, A., and Sanchez, T., 2008, "On the Effect of Methane Internal Reforming in Solid Oxide Fuel Cells," Int. J. Hydrogen Energy, **33**, pp. 1834–1844.

[36] Drescher, I., Lehnert, W., and Meusinger, J., 1998, "Structural Properties of SOFC Anodes and Reactivity," Electrochim. Acta, **43**(19–20), pp. 3059–3068.

[37] Danilov, V., and Tade, M., 2009, "A CFD-Based Model of a Planar SOFC for Anode Flow Field Design," Int. J. Hydrogen Energy, **34**, pp. 8998–9006.

[38] Marrero-López, D., Ruiz-Morales, J. C., Peña-Martínez, J., Canales-Vázquez, J., and Núñez, P., 2008, "Preparation of Thin Layer Material With Macroporous Microstructure for SOFC Applications," J. Solid State Chem., **181**, pp. 685–692.

[39] Paradis, H., Andersson, M., Yuan, J., and Sundén, B., 2010, "CFD Modeling Considering Different Kinetic Models for Internal Reforming Reactions in an Anode-Supported SOFC," *Proceedings of the Eighth International Fuel Cell Science, Engineering and Technology Conference*, Brooklyn, NY.

[40] Aguiar, P., Adjiman, C. S., and Brandon, N. P., 2004, "Anode-Supported Intermediate Temperature Direct Internal Reforming Solid Oxide Fuel Cell. I: Model-Based Steady-State Performance," J. Power Sources, **138**, pp. 120–136.

[41] Hofmann, P., Panopoulos, K. D., Fryda, L. E., and Kakaras, E., 2009, "Comparison Between Two Methane Reforming Models Applied to a Quasi-Two-Dimensional Planar Solid Oxide Fuel Cell Model," Energy, **34**, pp. 2151–2157.




**Downloaded 02 Mar 2011 to 130.235.81.195. Redistribution subject to ASME license or copyright; see http://www.asme.org/terms/Terms_Use.cfm**

# Paper IV

This paper has been published in:

*ASME J. Fuel Cell Science and Technology,*
Vol. 8, 031014, 2011.

© 2011 ASME.

# CFD Modeling: Different Kinetic Approaches for Internal Reforming Reactions in an Anode-Supported SOFC

**Hedvig Paradis**[1]
e-mail: hedvig.paradis@energy.lth.se

**Martin Andersson**

**Jinliang Yuan**

**Bengt Sundén**

Department of Energy Sciences,
Faculty of Engineering,
Lund University,
P.O. Box 118,
221 00 Lund, Sweden

*Fuel cells are electrochemical devices that convert chemical energy into electricity. Solid oxide fuel cells (SOFCs) are a particularly interesting type because they can reform hydrocarbon fuels directly within the cell, which is possible, thanks to their high operating temperature. The purpose of this study is to develop an anode-supported SOFC theoretical model to enhance the understanding of the internal reforming reactions and their effects on the transport processes. A computational fluid dynamics approach, based on the finite element method, is implemented to unravel the interaction among internal reforming reactions, momentum, and heat and mass transport. The three different steam reforming reaction rates applied were developed and correlated with experimental studies found in the literature. An equilibrium rate equation is implemented for the water-gas shift reaction. The result showed that the reaction rates are very fast and differ quite a lot in size. The pre-exponential values, in relation to the partial pressures, and the activation energy affected the reaction rate. It was shown that the anode structure and catalytic composition have a major impact on the reforming reaction rate and cell performance. The large difference between the different activation energies and pre-exponential values found in the literature reveals that several parameters probably have a significant influence on the reaction rate. As the experiments with the same chemical compositions can be conducted on a cell or only on a reformer, it is important to reflect over the effect this has on the kinetic model. To fully understand the effect of the parameters connected to the internal reforming reaction, microscale modeling is needed.* [DOI: 10.1115/1.4002906]

*Keywords: SOFC, modeling, internal reforming reactions, anode-supported, transport processes*

## 1 Introduction

Fuel cells are energy conversion devices that produce electricity and heat directly from a hydrogen-based fuel through electrochemical reactions when the device is fed with an oxidant. SOFC is a high temperature cell that operates at 600–1000°C [1]. If the electrolyte is kept thin, it is possible to reduce the temperature to a moderate level (600–800°C [1]) and still maintain the environment for the internal reforming reaction. A single SOFC consists of an air channel and a fuel channel, two porous electrodes that are separated by an electrolyte. The fuel electrode is the anode and the oxidant electrode is the cathode. The electrolyte works as a passage for the ions and blockage for the electrons. The oxygen ions react with hydrogen and carbon monoxide in the fuel mixture at the anode/electrolyte interface and produce water and carbon dioxide while releasing electrons that flow via external circuits to the cathode/electrolyte. Unlike the porous electrode, the electrolyte should not be permeable for gas. The anode is usually nickel/zirconia cermet, which provides high electrochemical performance and good chemical stability, and the cathode is usually a perovskite material.

The aim of this study is to find out of how the internal reforming reactions of methane affect the physical processes. Because SOFCs operate at high temperature, they supply a sufficiently good condition to internally reform the hydrocarbon-based fuel within the cells. For this reason, it is possible to work with a broader variety of fuels, e.g., methane, propane, or ethanol, besides hydrogen [2]. The following global reactions are considered in this model,

$$O_2 + 4e^- \Leftrightarrow 2O^{2-} \tag{1}$$

$$H_2 + O^{2-} \Leftrightarrow H_2O + 2e^- \tag{2}$$

$$CO + O^{2-} \Leftrightarrow CO_2 + 2e^- \tag{3}$$

$$CH_4 + H_2O \Leftrightarrow 3H_2 + CO \tag{4}$$

$$CO + H_2O \Leftrightarrow H_2 + CO_2 \tag{5}$$

Equation (1) is the reduction of oxygen in the cathode. Equations (2) and (3) are the electrochemical reactions at the anodic three-phase boundary (TPB). TPB is the region where the electrolyte and electrode meet. Equation (4) is the steam reforming of methane (usually called catalytic steam reforming reaction), which needs to be carried out before the electrochemical reactions. Carbon monoxide can be oxidized as in Eq. (3) or react with water as in Eq. (5). Equation (5) is often called the water-gas shift reforming reaction.

## 2 Mathematical Model

A computational fluid dynamics (CFD) approach is applied to solve the equations for momentum and heat and mass transport simultaneously. A two-dimensional model is adopted for the anode-supported SOFC and implemented in COMSOL MULTIPHYS-

[1]Corresponding author.

Contributed by the Advanced Energy Systems Division of ASME for publication in the JOURNAL OF FUEL CELL SCIENCE AND TECHNOLOGY. Manuscript received August 17, 2010; final manuscript received September 21, 2010; published online March 1, 2011. Editor: Nigel M. Sammes.



**Copyright © 2011 by ASME**

**Downloaded 02 Mar 2011 to 130.235.81.195. Redistribution subject to ASME license or copyright; see http://www.asme.org/terms/Terms_Use.cfm**

**Table 1 Cell dimensions [1]**

| Part of the cell | Size (mm) |
|---|---|
| Cell length | 100 |
| Air channel height | 1 |
| Fuel channel height | 1 |
| Electrolyte height | 0.02 |
| Cathode height | 0.05 |
| Anode height | 0.5 |
| Interconnect height | 0.5 |

ics. The geometry is defined in Table 1 and a sketch of the model is shown in Fig. 1.

**2.1 Mass Transport.** To represent the mass transport for the gases within the cell, the Maxwell–Stefan equation for mass diffusion and convection is used. The Maxwell–Stefan equation is a simplified equation of the Dusty gas model. For flows with low velocity in the porous medium, it is often assumed that the transport process is dominated by diffusion [3]. The Knudsen term is used when the pores are small compared with the free mean path of the gas [1,4]. The Knudsen diffusion is neglected in study to save computational cost. The Maxwell–Stefan equation is defined for the domain including the electrodes and the fuel and air channels, as follows [1]:

$$\nabla\left(-\rho\cdot w_i\sum D_{ij}\cdot\nabla x_j+(x_j-w_j)\cdot\frac{\nabla p}{p}\cdot u-D_i^T\cdot\frac{\nabla T}{T}\right)+\rho\cdot u\cdot\nabla w_j=S_i \tag{6}$$

where $w$ is the mass fraction, $D_{ij}$ is the Maxwell–Stefan binary diffusion coefficient, $x$ is the mole fraction, $D_i^T$ is the thermal diffusion coefficient, and $S_i$ is the source term. $S_i$ is zero for the electrochemical reactions because they are assumed, in this study, to take place at the interfaces between the electrolyte and electrodes. This is possible because the active layer is considered to be very thin compared with the thick electrode [5]. They are therefore defined as an interface condition instead. The diffusion coefficient in the porous electrodes is $D_{ij,\mathrm{por}}$, calculated as [1]

$$D_{ij,\mathrm{por}}=D_{ij}\cdot\frac{\varepsilon_p}{t} \tag{7}$$

where $\varepsilon_p$ is the porosity and $t$ is the tortuosity.

The mass or molar fractions for the air and fuel channel inlets are defined and the outlet conditions are defined as the convective flux.

**2.2 Heat Transport.** The heat transfer within the cell consists of convection between the solid surface and the gas flow, conduction in the solid and the porous parts, and heat generation/consumption occurs due to the electrochemical reactions at the TPB as well as the internal reforming reactions. Thermal radiation is not included in this study as the cell is considered to be in the middle of the stack surrounded by cells with the same boundary condition for the temperature (symmetry). If thermal radiation between the walls and gas mixtures is considered, it could have some influence on the results. The prediction of the temperature distribution can either be conducted by a local thermal equilibrium (LTE) or a local thermal nonequilibrium (LTNE) approach. For this study, the LTNE approach is used due to low Reynolds number and large differences in thermal conductivities between the gas and solid phases. The temperature distribution is calculated separately for the gas and solid phases. The general heat conduction equation is used to calculate the temperature distribution for the solid medium in the porous electrodes [1],

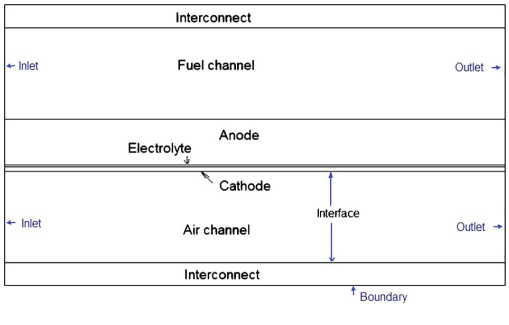


**Fig. 1 Schematic figure of a unit cell in an anode-supported SOFC model, not to scale**

$$\nabla(-k_s\cdot\nabla T_s)=Q_s \tag{8}$$

where $k_s$ is thermal conductivity for the solid media, $T_s$ is the temperature in the solid phase, and $Q_s$ is the heat source (heat transfer between the gas and solid phases, the heat generation due to the Ohmic polarization and due to the internal reforming reactions). The temperature for the gas phase in the fuel gas and air channels and the porous electrodes are calculated as

$$\nabla(-k_g\cdot\nabla T_g)=Q_g-\rho_g\cdot c_{p,g}\cdot u\cdot\nabla T_g \tag{9}$$

where $T_g$ is the gas temperature, $c_{p,g}$ is the heat capacity, $k_g$ is the gas conductivity, and $Q_g$ is the heat transfer between the gas and solid phases. Because the Reynolds number is low, the heat transfer coefficient $h_{s,g,\mathrm{por}}$ (when spherical particles are assumed in the porous electrodes) can be calculated as [1]

$$h_{s,g,\mathrm{por}}=\frac{2\cdot k_g}{d_p} \tag{10}$$

where $d_p$ is the electrode particle diameter. The heat transfer between the gas and solid phases is defined as

$$Q_g=-Q_s=h_v\cdot(T_g-T_s)=AV\cdot h_{s,g,\mathrm{por}}\cdot(T_g-T_s) \tag{11}$$

where $h_v$ is the volume heat transfer coefficient and $AV$ the active surface area to volume ratio.

The boundaries at the top and the bottom of the cell model are defined by symmetries since the cell is considered to be surrounded by other similar cells with the same temperature distribution. The temperatures at the air and fuel channel inlets are defined as constant and at the outlets the boundaries are defined as the convective flux.

**2.3 Momentum Transport.** The approach to momentum equation is selected to separately solve the Darcy's equation for the porous electrodes and the Navier–Stokes equations for the channels. The Darcy–Brinkman equation is then used to solve the gas flow in the gas phase [1],

$$\left(\frac{\mu}{\kappa}+\rho\cdot\nabla u\right)\cdot u-\nabla\left[-p+\frac{1}{\varepsilon_p}\cdot\{\boldsymbol{T}-(\lambda-\kappa_{\mathrm{dv}})\cdot(\nabla u)\}\right]=\boldsymbol{F} \tag{12}$$

where $\mu$ is the dynamic viscosity, $\kappa$ is the permeability of the porous medium, $\varepsilon_p$ is the porosity, $\boldsymbol{T}$ is the viscous stress tensor, and $\boldsymbol{F}$ is the volume force vector. $\lambda$ is the second viscosity and for gases it is normally set to $\lambda=-2/3\cdot\mu$ [1]. $\kappa_{\mathrm{dv}}$ is the deviation from the thermodynamic equilibrium and is by default set to zero. The Darcy–Brinkman equation is converted into the Darcy equation when the Darcy number $\mathrm{Da}\to 0$ in the porous layers and into the Navier–Stokes equation when $\kappa\to\infty$ and $\varepsilon_p=1$ in the fuel and air channels.

The velocity profile is defined at the air and fuel channel inlets as the laminar flow and the pressure at the outlets.



Downloaded 02 Mar 2011 to 130.235.81.195. Redistribution subject to ASME license or copyright; see http://www.asme.org/terms/Terms_Use.cfm

**2.4 Electrochemical Reactions.** The electrochemical reactions occur at the TPB. Ions migrate in the ionic phase and conduction of the electrons occurs in the electronic phase. The electrolyte functions on one hand to transport the oxygen ions to the anode and, on the other hand, to block the electrons crossing from the anode to the cathode. The flow of electronic charges through the external circuit balances the flow of ionic charges through the electrolyte. This transport is described in terms of the ion transport from the conservation of charge [1],

$$\nabla \cdot i = 0 = \nabla \cdot i_{\mathrm{io}} + \nabla \cdot i_{\mathrm{el}} \tag{13}$$

$$-i_{\mathrm{io}} = \nabla \cdot i_{\mathrm{el}} \tag{14}$$

$$i_{\mathrm{io}} = -\sigma_{\mathrm{io}}^{\mathrm{eff}} \cdot \nabla \phi_{\mathrm{io}} \tag{15}$$

where $i_{\mathrm{io}}$ and $i_{\mathrm{el}}$ are charge fluxes for ions and electrons, respectively, and $\phi_{\mathrm{io}}$ is the ionic potential in the electrolyte. The Nernst potential is calculated as the sum of the potential differences across the anode and the cathode as [1]

$$E = \Delta\phi_a + \Delta\phi_c \tag{16}$$

where $E$ is the reversible electrochemical cell voltage and $\phi$ is the charge potential. At the interface between the electrode and electrolyte, the Butler–Volmer equation is used to calculate the volumetric current density [1],

$$i = i_0 \left\{ \exp\left( \beta \cdot \frac{n_e \cdot F \cdot \eta_{\mathrm{act},e}}{R \cdot T} \right) - \exp\left( -(1-\beta) \cdot \frac{n_e \cdot F \cdot \eta_{\mathrm{act},e}}{R \cdot T} \right) \right\} \tag{17}$$

where $i_0$ is the exchange current density, $F$ is the Faraday constant, $\beta$ is the transfer coefficient, $n_e$ is the number of electrons transferred per reaction, $\eta_{\mathrm{act},e}$ is the electrode activation polarization overpotential, and finally $R$ is the ideal gas constant. If the transfer coefficient $\beta$ is assumed to be 0.5, the Butler–Volmer equation is reduced to

$$i = 2 \cdot i_0 \cdot \sinh\left( \frac{n_e \cdot F \cdot \eta_{\mathrm{act},e}}{2 \cdot R \cdot T} \right) \tag{18}$$

$$\eta_{\mathrm{act},e} = \frac{2 \cdot R \cdot T}{n_e \cdot F} \sinh^{1}\left( \frac{i_e}{2 \cdot i_{0,e}} \right) \tag{19}$$

$$i_0 = \frac{R \cdot T}{n_e \cdot F} \cdot k_e'' \cdot \exp\left( \frac{-E_e}{R \cdot T} \right) \tag{20}$$

where $k''$ is the pre-exponential factor and $E$ is the activation energy. The gas species distributions are implemented by source terms due to the electrochemical reaction as [1,6]

$$r_{\mathrm{H_2}} = \frac{-i}{2 \cdot F} \tag{21}$$

$$r_{\mathrm{H_2O}} = \frac{i}{2 \cdot F} \tag{22}$$

$$r_{\mathrm{O_2}} = \frac{-i}{4 \cdot F} \tag{23}$$

where $i$ is the current density and $F$ is the Faraday constant.

**2.5 Internal Reforming Reactions.** The internal reforming reaction rates are taken into account by the source terms in the Maxwell–Stefan equation. The mass source terms due to the reforming reactions are expressed as

$$S_{\mathrm{H_2}} = (3r_r + r_s) \cdot M_{\mathrm{H_2}} \tag{24}$$

$$S_{\mathrm{CH_4}} = -r_r \cdot M_{\mathrm{CH_4}} \tag{25}$$

$$S_{\mathrm{H_2O}} = (-r_r - r_s) \cdot M_{\mathrm{H_2O}} \tag{26}$$

$$S_{\mathrm{CO}} = (r_r - r_s) \cdot M_{\mathrm{CO}} \tag{27}$$

The equation for $CO_2$ can be solved separately because the sum of the mass fractions is equal to unity. The reaction rate $r_r$ is for the catalytic steam reforming reaction and $r_s$ is for the water-gas shift reaction.

The reaction rates for the methane steam reforming reaction are evaluated by kinetic models and for the water-gas shift reaction an equilibrium approach is applied. The three reaction kinetic approaches applied are from Refs. [7–11]. It is worth noting that both Achenbach and Riensche's [8,9] kinetics (Eq. (28)) together with Leinfelder's [10] (Eq. (29)) kinetics are an Arrhenius kinetics reaction rate type, while Drescher's kinetics [11] (Eq. (30)) is a Langmuir–Hinshelwood type. They are selected on the basis of the different order of the partial pressure and the broad range of the activation energy. The kinetics differences depend on how the experimental configuration is set up, and the material decomposition and operating conditions are selected. Equation (28) is found by the combination of both the study of Achenbach and Riensche [8] and the study of Achenbach [9], where it could be found that the reaction order of the partial pressure of methane is unity and the partial pressure of water has no catalytic effect on the reaction, which leads to the simplified equation [8,9]. Note that Leinfelder [10] found a positive reaction order of water and Achenbach and Riensche [8,9] found a reaction order of zero.

The reaction rates from these three different experimental studies are shown below,

$$r_{r,\mathrm{AchRie}} = 4274 \cdot p_{\mathrm{CH_4}} \cdot \exp\left( \frac{-82{,}000}{R \cdot T_s} \right) \cdot AV \tag{28}$$

$$r_{r,\mathrm{Lei}} = 30.8 \times 10^{10} \cdot p_{\mathrm{CH_4}} \cdot p_{\mathrm{H_2O}} \cdot \exp\left( \frac{-205{,}000}{R \cdot T_s} \right) \cdot AV \tag{29}$$

$$r_{r,\mathrm{Dre}} = \frac{288.52 \cdot p_{\mathrm{CH_4}} \cdot p_{\mathrm{H_2O}} \cdot \exp\left( \frac{-11{,}000}{R \cdot T_s} \right)}{1 + 16.0 \cdot p_{\mathrm{CH_4}} + 0.143 \cdot p_{\mathrm{H_2O}} \cdot \exp\left( \frac{39{,}000}{R \cdot T_s} \right)} \cdot AV \tag{30}$$

where $p$ is the partial pressure and $T_s$ is the solid phase temperature. $AV$ is the active surface area to volume ratio. The units for all the steam reforming reaction rates are mol/s $m^3$.

The reaction rates above are described from the global kinetic point of view, which only depends on a few parameters. As it appears not to be sufficient to only describe the reaction rates with a few empirical parameters, it is necessary to develop a suitable micromodel for the SOFC. However, the global kinetic models may still predict valuable behaviors.

The reaction rate equations (Eqs. (28) and (29)) are of the Arrhenius type. The rate equation consists of three parts, partial pressures, pre-exponential factor, and activation energy. These parameters differ quite a lot in the literature among different research works. The pre-exponential factor describes the number of collisions between the molecules within the reaction. The exponential expression with activation energy describes the probability for the reaction to occur. As the activation energy increases, the catalytic reaction becomes less probable. The activation energy is based on the catalytic characteristics, such as chemical composition. Even though the activation energy may be high, which lead to a decrease in the reaction rate, the overall reaction rate however can still be fast due to the pre-exponential value. The pre-exponential factors depend strongly on both the temperature and properties of the anode material. It is possible to change the reaction rate, either by changing the particle size of the active catalysts or the porous structure, i.e., the active catalytic area. The large



**Downloaded 02 Mar 2011 to 130.235.81.195. Redistribution subject to ASME license or copyright; see http://www.asme.org/terms/Terms_Use.cfm**

difference between the activation energies found in the literature [1,7–12] suggests that more parameters have significant influence on the reaction rate.

According to Nagel et al. [7], a small steam-to-carbon (SC) ratio yields positive reaction orders and a high SC ratio yields negative reaction orders. For this study, the steam to carbon ratio is around 2, which agrees with the three kinetic models. Achenbach and Riensche [8,9] applied a 14 mm thick nickel cermet semidisk consisting of 20 wt % Ni and 80 wt % $ZrO_2$ (stabilized). The active surface area was $3.86\times10^{-4}$ $m^2$. The temperature was varied from 700°C to 940°C and the system pressure from 1.1 bar to 2.8 bar. Leinfelder [10] applied a 50 $\mu$m thick anode built up by two layers with 64 wt % Ni and 36 wt % YSZ and 89 wt % Ni and 11 wt % YSZ, respectively. The active surface area for the anode was $2.5\times10^{-3}$ $m^2$. The test was conducted for temperatures of 840–920°C and at a pressure of 1 bar. Drescher [11] applied an anode consisting of 50 wt % Ni and 8 mol % YSZ. Achenbach and Riensche's model is based on a work on a reformer, while the other two, Leinfelder's and Drescher's, are based on a unit cell.

In this study, the temperature is varied from 727°C to 827°C (1000–1100 K) since this is the range within which the experiments were carried out. The active surface area to volume ratio is varied between $10\times10^4$ $m^2/m^3$ and $5\times10^5$ $m^2/m^3$. The active surface area to volume ratio has been adopted according to a common used value in the literature [6,12–16]. Several authors have applied an active surface area to volume ratio of $5\times10^5$ for modeling work. Janardhanan and Deutschmann [6] applied a slightly smaller surface area to volume ratio of 102,500 $m^2/m^3$, whereas Klein et al. [12] applied a much larger value of $2.2\times10^6$ $m^2/m^3$. Note that only a small part of the whole active surface acts as a locus for the chemical reactions. The trend for the development during the past years is in the direction of employing smaller particles to get a larger $AV$.

The water-gas shift reaction is considered to be very quick and to remain in equilibrium by several authors in the literature [5,12,17]. The equilibrium approach in the fuel channel and the anode can be defined as

$$r_s = k_s \cdot p_{CO} \cdot \left(1 - \frac{p_{CO_2} \cdot p_{H_2}}{K_{e,s} \cdot p_{CO} \cdot P_{H_2O}}\right) \tag{31}$$

$$K_{e,s} = \exp\left(\frac{4276}{T} - 3.961\right) \tag{32}$$

where $k_s$ is the reaction rate constant and $K_{e,s}$ is the equilibrium constant for the water-gas shift reaction. The value for $k_s$ is calculated according to Haberman and Young [18]. The unit for the water-gas shift reaction rate is mol/s $m^3$. The heat generation and heat consumption are defined as source terms in the governing equations. The heat generation in the fuel channel enters in the gas phase. The heat generation and the heat consumption are assumed to occur on the solid surface. The heat generation and heat consumption due to the reforming reactions are implemented in Eq. (8) and defined as

$$Q_{int,ref} = \sum_i r_i \cdot \Delta h_{reac,i} \tag{33}$$

where $\Delta h_{reac}$ is the enthalpy change due to the reactions and $Q_{int,ref}$ is the heat generation.

## 3 Results and Discussion

**3.1 Base Conditions.** According to the standards by the International Energy Agency (IEA) [1], the inlet temperature was specified to be 1000 K (727°C) both for the air and fuel channels. The fuel composition for 30% pre-reformed natural gas is defined by IEA and is frequently used in the literature. The catalytic active surface area to volume ratio $10\times10^5$ $m^2/m^3$ is a reappearing value found in the literature. The average cell current density is specified to be 0.3 $A/cm^2$. The 30% pre-reformed natural gas is supplied by external reformers, and the inlet conditions are specified in Table 2. The material characteristics are specified in Table 3. The model has been checked for all cases to fulfill the requirement of grid independency.

**Table 2 Inlet mole fraction for the fuel gas species [1]**

| Fuel gas species | Inlet mole fraction |
|---|---|
| $H_2$ | 0.2626 |
| $CH_4$ | 0.171 |
| CO | 0.0294 |
| $H_2O$ | 0.4934 |
| $CO_2$ | 0.0436 |

The flow direction is set to be from left to right for air and fuel channels as well as the anode and the cathode. It should be explicitly mentioned that the length of the cell is 100 times longer than the height of the air or the fuel channel.

The predicted gas phase temperature in the cell is plotted in Figs. 2–4 for Achenbach and Riensche's, Leinfelder's, and Drescher's kinetics, respectively. There is a decrease in temperature after a short distance from the inlet for both the fuel and air channels. In the fuel channels, it is due to the steam reforming reaction, which consumes the heat when the methane is reformed to hydrogen and carbon monoxide. The temperature on the air side is lower due to a higher air flow rate. The decrease in temperature close to the inlet is 50 K for both Achenbach abd Riensche's and Leinfelder's kinetics. The area of the temperature drop is larger for Achenbach and Riensche's kinetics than those from both Leinfelder's and Drescher's kinetics. But the recovery to a higher temperature occurs faster for both Leinfelder's and Drescher's kinetics than for Achenbach and Riensche's kinetics, the latter of which is affected by the fast conversion of methane to hydrogen and carbon monoxide. The temperature distribution for Drescher's ki-

**Table 3 Material characteristics data [1,4,6]**

| | |
|---|---|
| Anode thermal conductivity, $k_{s,a}$ | 11 W/m K |
| Cathode thermal conductivity, $k_{s,c}$ | 6 W/m K |
| Electrolyte thermal conductivity, $k_{s,el}$ | 2.7 W/m K |
| Interconnect thermal conductivity, $k_{s,int}$ | 20 W/m K |
| Anode heat capacity, $c_{p,a}$ | 450 J/kg K |
| Cathode heat capacity, $c_{p,c}$ | 430 J/kg K |
| Electrolyte heat capacity, $c_{p,el}$ | 470 J/kg K |
| Interconnect heat capacity, $c_{p,int}$ | 550 J/kg K |

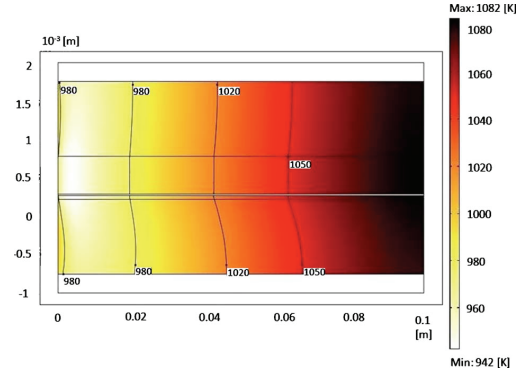


**Fig. 2 Temperature distribution (K) for Achenbach and Riensche's kinetics**



Downloaded 02 Mar 2011 to 130.235.81.195. Redistribution subject to ASME license or copyright; see http://www.asme.org/terms/Terms_Use.cfm

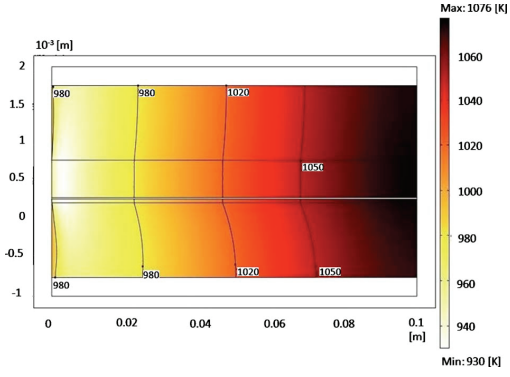


**Fig. 3 Temperature distribution (K) for Leinfelder's kinetics**

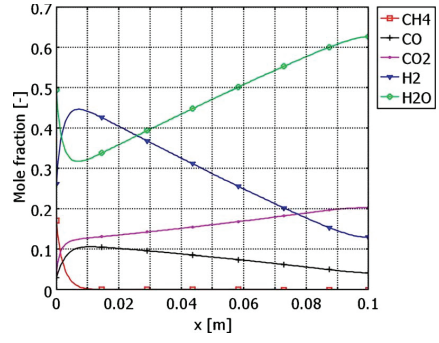


**Fig. 5 Mole fraction of the gas species in the fuel channel along the flow direction for Leinfelder's kinetics**

netics does not drop initially as much as the other two. A higher maximum temperature is also obtained for Drescher's kinetics. Note that the labels of the temperature range are different for each case. But the plotted temperature lines in the figures are the same for every condition and kinetics, i.e., 980 K, 1020 K, and 1050 K. The maximum and minimum temperatures are printed for each case as well.

The effect on mole fraction distribution for the different gas species is similar for both Achenbach and Riensche's and Leinfelder's kinetics and, therefore, only the mole fraction distribution for Leinfelder's kinetics is presented in Fig. 5. Methane reacts with steam at the surface of the Ni-catalyst in the anode, which leads to the production of carbon monoxide and hydrogen. The hydrogen is consumed at the TPB for the electrochemical reactions. As shown in Fig. 6, Drescher's kinetics obtained the maximum mole fraction of hydrogen faster and a higher maximum mole fraction than Achenbach and Riensche's and Leinfelder's kinetics. The initial consumption of water and the initial generation of hydrogen for Drescher's kinetics result in larger gradients of the mole fractions. All three kinetics are fast although Drescher's kinetics, expressed by a Langmuir–Hinshelwood type, differs slightly more from the others. It deserves to be pointed out that Drescher's kinetics includes both positive and negative orders of the partial pressure of methane and water, as well as two different activation energies for the denominator and the numerator, which can have some effect on the results.

The reaction rates for both the steam reforming reaction and the water-gas shift reaction are plotted in Figs. 7–9 for Achenbach and Riensche's, Leinfelder's, and Drescher's kinetics, respectively. It should be clearly noted that the reaction rates are only plotted for the entrance region, through 0.01 m. For Achenbach and Riensche's kinetics, the distribution of the steam reforming reaction rate is plotted in detail in Fig. 10. Close to the inlet where the concentration of methane is high, the reaction rate for the steam reforming reaction is high. All of the anode depth is used for the reaction. As shown in the figures, the reaction rate for the steam reforming and the water-gas shift is much faster for Drescher's kinetics than for both Achenbach and Riensche's and Leinfelder's kinetics. Yet, Leinfelder's kinetics is faster than Achenbach and

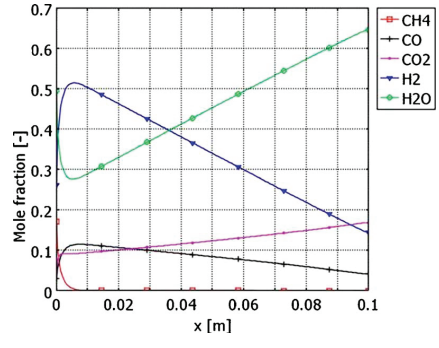


**Fig. 6 Mole fraction of the gas species in the fuel channel along the flow direction for Drescher's kinetics**

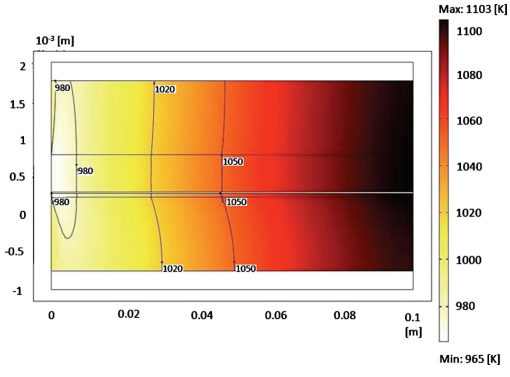


**Fig. 4 Temperature distribution (K) for Drescher's kinetics**

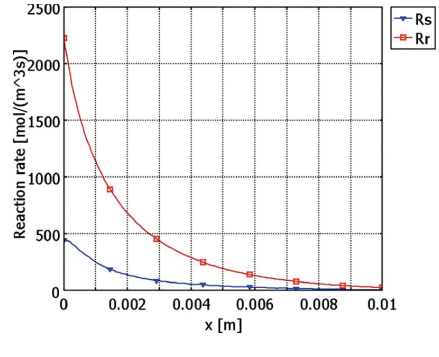


**Fig. 7 Reforming reaction rate (mol/m³ s) for the entrance region (until 0.01 m) along the flow direction for Achenbach and Riensche's kinetics**



Downloaded 02 Mar 2011 to 130.235.81.195. Redistribution subject to ASME license or copyright; see http://www.asme.org/terms/Terms_Use.cfm

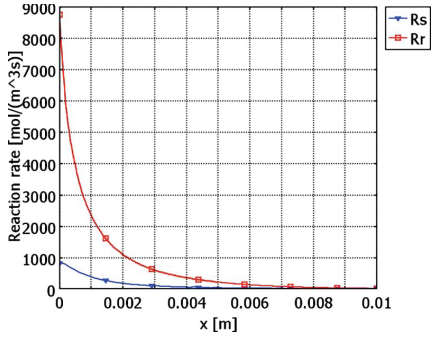


**Fig. 8 Reforming reaction rate (mol/m$^3$ s) for the entrance region (until 0.01 m) along the flow direction for Leinfelder's kinetics**

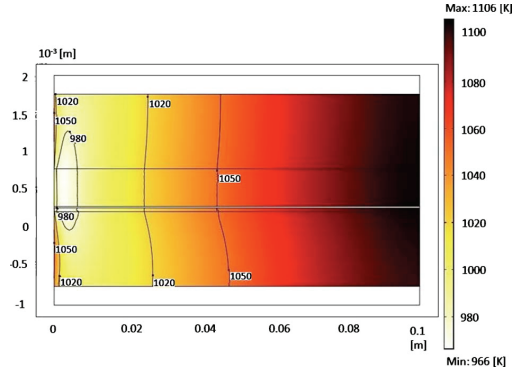


**Fig. 11 Temperature distribution (K) for Leinfelder's kinetics (T=1100 K)**

Riensche's. Close to the inlet in the anode where carbon monoxide generation is high, the reaction rate for the water-gas shift reaction is at the highest. The high generation of carbon monoxide is due to the steam reforming reaction. Furthermore, more hydrogen is produced when steam is generated due to the fact that the water-gas shift equation is in equilibrium through the process. As hydrogen is consumed, steam is generated thanks to the electrochemical reaction at the TPB. The reaction rate for the water-gas shift reaction reaches a higher value due to the faster reaction rate for the steam reforming reaction for Drescher's and Leinfelder's kinetics compared with Achenbach and Riensche's kinetics. The comparison between the different kinetic models need to be evaluated on a more detailed level as it cannot be correctly explained by just a few empirical parameters, such as the activation energy and the pre-exponential value. To fully understand the effect and dependency of the parameters, micromodeling is needed. What can be concluded from this study is that the configuration and geometrical properties of the anode and the chemical composition and catalytic characteristics are important. To draw confirmatory conclusions from the modeling work, it is be important to reveal the difference of the kinetic models from the experimental work carried out on SOFC and a reformer based on the same properties.

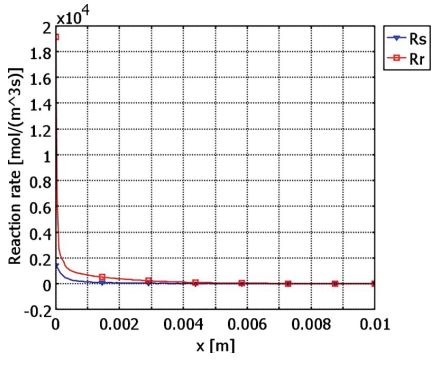


**Fig. 9 Reforming reaction rate (mol/m$^3$ s) for the entrance region (until 0.01 m) along the flow direction for Drescher's kinetics**

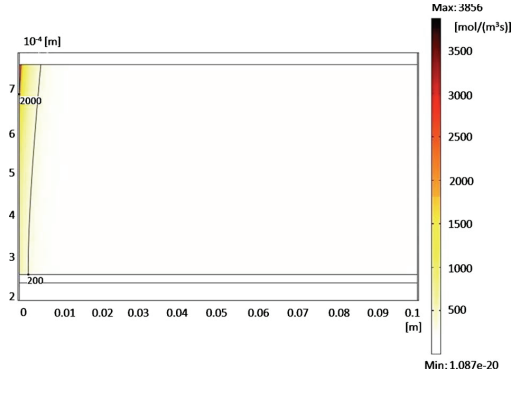


**Fig. 10 Distribution of the steam reforming reaction rate in the anode for Achenbach and Riensche's kinetics**

**3.2 Temperature Effects.** A parameter study was carried out for Leinfelder's kinetics because it is found, based on the above discussion, that the reaction rates for Leinfelder's kinetics are not as fast as Drescher's, but they are slightly faster than Achenbach and Riensche's. The inlet temperature was increased 50 K for Leinfelder's kinetics. The other parameters were kept the same as in the base case. The temperature distribution for both cases results in a similar way but obviously resulted in a higher temperature range, as shown in Fig. 11. The mole fraction distribution for the fuel gas species has the same range and trend as the base case. The reaction rates are slightly faster for a higher inlet temperature, but this is not shown here because of the similarity to the base case. In Fig. 12, the reaction rates are presented for Leinfelder's kinetics with an increased inlet temperature. Again, the reaction rates are only plotted for the entrance region, through 0.01 m. Due to the increased inlet temperature, the maximum reaction rates are almost doubled compared with the base case at the inlet.

**3.3 Active Surface Area to Volume Ratio Effects.** A parameter study was also conducted for the active surface area to volume ratio from $10\times10^4$ m$^2$/m$^3$ to $5\times10^5$ m$^2$/m$^3$, which is a frequently used interval in the literature. All the other parameters were kept the same as the base case. The temperature profile is distributed in a similar overall trend as for the base case by comparing Figs. 3 and 13. The temperature was distributed in the same range for the two larger active surface area to volume ratios but the initial drop for the larger is greater than for a smaller one; however, compared with the base case, the minimum temperature differs by 20 K. Each mole fraction profile is distributed in a similar way as the specific base case for that mole fraction. The mole fractions reach approximately the same maximum value for the different active surface area to volume ratios but occur at



Downloaded 02 Mar 2011 to 130.235.81.195. Redistribution subject to ASME license or copyright; see http://www.asme.org/terms/Terms_Use.cfm

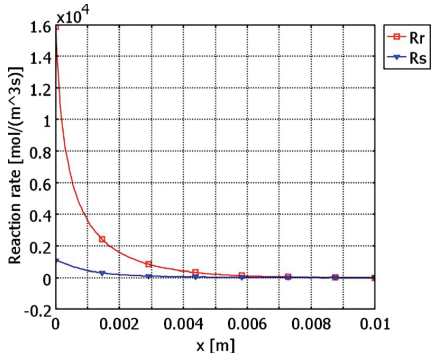


**Fig. 12 Reforming reaction rate (mol/m$^3$ s) for the entrance region (until 0.01 m) along the flow direction for Leinfelder's kinetics (T=1100 K)**

different distances from the inlet. A higher ratio results in the maximum of all the mole fraction species to occur closer to the inlet. In Fig. 14, the reaction rates for Leinfelder's kinetics with an increased active surface area to volume are presented. Again, the reaction rates are only plotted for the entrance region through 0.01

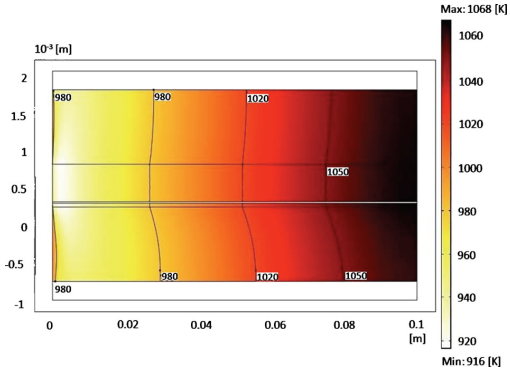


**Fig. 13 Temperature distribution (K) for Leinfelder's kinetics (AV=5 E5)**

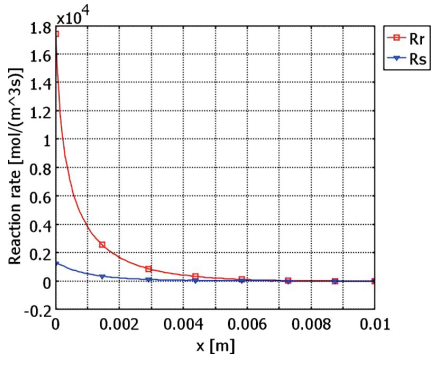


**Fig. 14 Reforming reaction rate (mol/m$^3$ s) for the entrance region (until 0.01 m) along the flow direction for Leinfelder's kinetics (AV=5 E5)**

m. The characteristics are distributed in a similar way for the reaction rates as for the base case, but the maximum value is more or less doubled for an increased active surface area to volume ratio. The reaction rates show the same trend when the inlet temperature is increased and similarly when the active surface area to volume ratio is increased. Similar maximum rates are obtained as the base case when an increased inlet temperature or an increased active surface area to volume ratio is used.

## 4 Conclusions

In this study, a finite-element-based model for an anode-supported SOFC has been developed to better understand the internal reforming reactions of methane and the effects on the transport processes. The model has implemented COMSOL MULTIPHYSICS for the analysis of three different kinetic models. The equations for momentum and heat and mass transport are solved simultaneously. The three different reaction rates by experimental work found in the literature were examined. An equilibrium equation was employed for the water-gas shift reforming reaction rate. Parameter studies were also conducted for the inlet temperature and the active surface area to volume ratio.

The steam reforming reaction rates in this study are shown to be very fast. They differ slightly across the three models, which seems to be an effect of great differences of the pre-exponential value and the activation energy. Both these two parameters, pre-exponential value and activation energy, are connected to the partial pressure of methane and water. The model seems to be sensitive to the variation in the steam reforming reaction rate. Both the inlet temperature and the active surface area to volume ratio showed an effect on the reaction rates in terms of the maximum value. The temperature distributions were in the same range when the active surface area to volume ratio was increased. But with increased active surface area to volume ratio, the initial drop became much larger as the steam reforming reaction rate was subsequently increased. The reason why the different kinetics differs so much is that they are sensitive to how the experiment is designed.

The large difference between the different activation energies and pre-exponential values found in the literature shows that a larger number of parameters will have significant influence on the reaction rate, and to understand this relationship between the parameters, microscale modeling should be developed.

## Acknowledgment

The financial support from the European Research Council (ERC) and the Swedish Research Council (VR) is gratefully acknowledged.

## Nomenclature

$AV$ = active surface area to volume ratio, m$^2$/m$^3$
$c_p$ = specific heat capacity at constant pressure, J/kg K
$D_{ij}$ = Maxwell–Stefan binary diffusion coefficient, m$^2$/s
$D_i^T$ = thermal diffusion coefficient, kg/m s
$\mathbf{F}$ = volume force vector, N/m$^3$
$h$ = enthalpy, J/mol
$h_{s,g}$ = heat transfer coefficient, W/m$^2$ K
$h_v$ = volume heat transfer coefficient, W/m$^3$ K
$i$ = current density, A/cm$^2$
$i_0$ = exchange current density, A/cm$^2$
$k$ = thermal conductivity, W/m K
k′ = Boltzmann's constant, J/K
$k''$ = pre-exponential factor, 1/Ω m$^2$
$M_j$ = molar weight of species j, kg/mol
$n_0$ = inlet mass flux, kg/m$^2$ s
$n_e$ = number of electrons transferred per reaction
$p$ = pressure, Pa



Downloaded 02 Mar 2011 to 130.235.81.195. Redistribution subject to ASME license or copyright; see http://www.asme.org/terms/Terms_Use.cfm

$Q$ = source term (heat), $W/m^3$
$R$ = gas constant, 8.314 J/mol K
$r$ = reaction rate, $mol/m^2$ s, $mol/m^3$ s
$S_i$ = source term (mass), $kg/m^3$ s
$\mathbf{T}$ = viscous stress tensor, N/m
$T$ = temperature, K
$u$ = velocity field, m/s
$v$ = dynamic viscosity, Pa s
$w_i$ = mass fraction of species $i$, kg/kg
$x_j$ = molar fraction of species $j$, mol/mol

**Greek Symbols**

$\varepsilon_p$ = porosity, dimensionless
$\eta$ = overpotential, V
$\kappa$ = permeability, $m^2$
$\lambda$ = second viscosity, Pa s
$\mu$ = dynamic viscosity, Pa s
$\rho$ = density, $kg/m^3$
$\sigma$ = ionic/electronic conductivity, $\Omega^{-1}$ $m^{-1}$

**Subscripts**

0 = initial
act = activation polarization
$e$ = electrode, $e \in \{a,c\}$
el = electrolyte
$g$ = gas phase
$i$ = molecule $i$
$j$ = molecule $j$
$p$ = porous media
por = porous media
$r$ = steam reforming reaction
$s$ = solid phase, water-gas shift reaction

**Chemical**

$CH_4$ = methane
CO = carbon monoxide
$CO_2$ = carbon dioxide
$H_2$ = hydrogen
$H_2O$ = water
$O_2$ = oxygen
Ni = nickel
YSZ = yttria-stabilized zirconia

## References


[1] Andersson, M., Yuan, J., and Sundén, B., 2010, "Review on Modeling Development for Multiscale Chemical Reactions Coupled Transport Phenomena in Solid Oxide Fuel Cells," Appl. Energy, **87**, pp. 1461–1476.

[2] Yuan, J., Huang, Y., Sundén, B., and Wang, W. G., 2009, "Analysis of Parameter Effects on Chemical Coupled Transport Phenomena in SOFC Anodes," Heat Mass Transfer, **45**, pp. 471–484.

[3] Yang, Y., Du, X., Yang, L., Huang, Y., and Xian, H., 2009, "Investigation of Methane Steam Reforming in Planar Porous Support of Solid Oxide Fuel Cell," Appl. Therm. Eng., **29**, pp. 1106–1113.

[4] Kakaç, S., Pramuanjaroenkij, A., and Zhou, X. Y., 2007, "A Review of Numerical Modeling of Solid Oxide Fuel Cells," Int. J. Hydrogen Energy, **32**, pp. 761–786.

[5] Lehnert, W., Meusinger, J., and Thom, F., 2000, "Modelling of Gas Transport Phenomena in SOFC Anodes," J. Power Sources, **87**, pp. 57–63.

[6] Janardhanan, V., and Deutschmann, O., 2006, "CFD Analysis of a Solid Oxide Fuel Cell With Internal Reforming," J. Power Sources, **162**, pp. 1192–1202.

[7] Nagel, F. P., Schildhauer, T. J., Biollaz, S. M. A., and Stucki, S., 2008, "Charge, Mass and Heat Transfer Interactions in Solid Oxide Fuel Cells Operated With Different Fuel Gases—A Sensitivity Analysis," J. Power Sources, **184**, pp. 129–142.

[8] Achenbach, E., and Riensche, E., 1994, "Methane/Steam Reforming Kinetics for Solid Oxide Fuel Cells," J. Power Sources, **52**, pp. 283–288.

[9] Achenbach, E., 1994, "Three-Dimensional and Time-Dependent Simulation of a Planar Solid Oxide Fuel Cell Stack," J. Power Sources, **49**, pp. 333–348.

[10] Leinfelder, R., 2004, "Reaktionskinetische Untersuchungen zur Methan-Dampf-Reformierung und Shift-Reaktion an Anoden Oxidkeramischer Brennstoffzellen," Ph.D. thesis, Universität Erlangen-Nürnberg, Erlangen-Nürnberg, Germany.

[11] Drescher, I., 1999, "Kinetik der Methan-Dampf-Refomierung," Ph.D. thesis, Institut für Werkstoffe und Verfahren der Energietechnik, Forschungszentrums Jülich, Jülich, Germany.

[12] Klein, J.-M., Bultel, Y., Georges, S., and Pons, M., 2007, "Modeling of a SOFC Fuelled by Methane: From Direct Reforming to Gradual Internal Reforming," Chem. Eng. Sci., **62**, pp. 1636–1649.

[13] Hussain, M. M., Li, X., and Dincer, I., 2007, "Mathematical Modeling of Transport Phenomena in Porous SOFC Anodes," Int. J. Therm. Sci., **46**, pp. 48–56.

[14] Danilov, V. A., and Tade, M. O., 2009, "A CFD-Based Model of a Planar SOFC Anode Flow Field Design," Int. J. Hydrogen Energy, **34**, pp. 8998–9006.

[15] Costamagna, P., Costa, P., and Antonucci, V., 1998, "Micro-Modelling of Solid Oxide Fuel Cell Electrodes," Electrochim. Acta, **43**, pp. 375–394.

[16] Hecht, E., Gupta, G., Zhu, H., Dean, A., Kee, R., Maier, L., and Deutschmann, O., 2005, "Methane Reforming Kinetics Within a Ni-YSZ SOFC Anode Support," Appl. Catal., A, **295**, pp. 40–51.

[17] Aguiar, P., Adjiman, C. S., and Brandon, N. P., 2004, "Anode-Supported Intermediate Temperature Direct Internal Reforming Solid Oxide Fuel Cell I: Model-Based Steady-State Performance," J. Power Sources, **132**, pp. 113–126.

[18] Haberman, B. A., and Young, J. B., 2004, "Three-Dimensional Simulation of Chemically Reacting Gas Integrated-Planar Solid Oxide Fuel Cell," Int. J. Heat Mass Transfer, **47**, pp. 3617–3629.





**Downloaded 02 Mar 2011 to 130.235.81.195. Redistribution subject to ASME license or copyright; see http://www.asme.org/terms/Terms_Use.cfm**

# Paper V

This paper has been published in:

*Proceeding of the 219th ECS Meeting in Montreal - Twelfth International Symposium (SOFC-XII), ECS Transactions, Canada,*
Vol. **35**, pp. 1799-1809, 2011.

© 2011 ECS.

# Analysis of Microscopic Anode Structure Effects on an Anode-Supported SOFC Including Knudsen Diffusion

M. Andersson [a], X. Lu [b], J. Yuan [a], B. Sundén [a]

[a] Department of Energy Sciences, Lund University, SE-221 00 Lund, Sweden
[b] Marine Engineering College, Dalian Maritime University, Dalian 116026, China

In this study a two dimensional CFD (COMSOL Multiphysics) is employed to study the effect of anode microscopic structures on the transport phenomena and reactions for an anode-supported solid oxide fuel cell (SOFC). FCs can be considered as energy devices, involving multiple processes, such as (electro-) chemical reactions, heat exchange, gas- and ionic transport. All these complex processes are strongly integrated, needing modeling as an important tool to understand the couplings between mass-, heat-, momentum transport and chemical reactions. For the porous material, the Knudsen diffusion is taken into account in this study. The chemical- and electrochemical reaction rates depend on temperature, material structure, catalytic activity, degradation and partial pressure among others. It is found that the anode thickness and also the anode pore size need to be optimized to achieve high cell efficiency, when the Knudsen diffusion effects are included.

## Introduction and Problem Statement

Fuel cells (FCs) produce electricity and heat directly from chemical conversion of fuel and oxidant energies by electrochemical reactions (1). The fuel cell is not a new invention, because the electrochemical process was discovered already in 1839. However the first real fuel cell system was not designed and built until the 1950s. The interest in fuel cells have been growing exponentially, concerning the number of scientific papers published after year 2000 (2). Among the various types of FCs, the solid oxide fuel cell (SOFC) has attained significant interests due to its high efficiency and low emissions of pollutants to the environment. High temperature operation offers many advantages, such as high electrochemical reaction rate, flexibility of using various fuels and tolerance to impurities. SOFC has in general either planar or tubular configurations (1-2), and its performance depends on thermal, (electro-) chemical and mechanical phenomena (3).

In an electrode-supported SOFC either the anode or cathode is relatively thick and works as support material. This design makes it possible to have a very thin electrolyte, i.e., the ion transfer losses decreases and the temperature can be lowered to 600-800 °C. Fuel cells working in this temperature range are classified as intermediate temperature (IT) (1) if compared to conventional (electrolyte-supported) SOFCs that operate between 800 and 1000 °C (4).

The global reactions that take place within a SOFC using a mixture of hydrogen, carbon monoxide and methane as fuel and oxygen in air as reductance can be described

as: oxygen is reduced in the cathode, Eq. 1. The oxygen ions are transported through the electrolyte, but the electrons are prevented to pass through the electrolyte. The electrochemical reactions, Eqs. 2-3, take place in the anodic three-phase boundary (TPB). Methane needs to be reformed, Eq. 4, before the electrochemical reactions. Carbon monoxide can be oxidized in the electrochemical reaction, Eq. 3, but can also react with water (Eq. 5) (5). The reactions described here are the overall ones, more detailed reaction mechanisms can be found in (6). Note that methane is not participating in the electrochemical reactions at the anodic TPB, it is catalytically converted within the anode, into carbon monoxide and hydrogen, which are used as fuel in the electrochemical reactions (5).

$$O_2 + 4e^- \Leftrightarrow 2O^{2-} \quad [1]$$

$$H_2 + O^{2-} \Leftrightarrow H_2O + 2e^- \quad [2]$$

$$CO + O^{2-} \Leftrightarrow CO_2 + 2e^- \quad [3]$$

$$CH_4 + H_2O \Leftrightarrow 3H_2 + CO \quad [4]$$

$$CO + H_2O \Leftrightarrow H_2 + CO_2 \quad [5]$$

## Mathematical Model

A two-dimensional model for an anode-supported SOFC is developed and implemented in the commercial software, COMSOL Multiphysics (version 3.5). Equations for momentum-, mass- and heat transport are solved together with rate equations for internal reforming reactions. The geometry is defined in Table I and a sketch of the modeled cell can be seen in Fig 1. Note the difference in scale between the cell length (x-direction, as in Fig. 1) and various component thicknesses (y- direction, as in Fig. 1). It should be mentioned that the model in this study is 2D only, and the connection between the electrodes and interconnect can not be explicitly observed in this case.

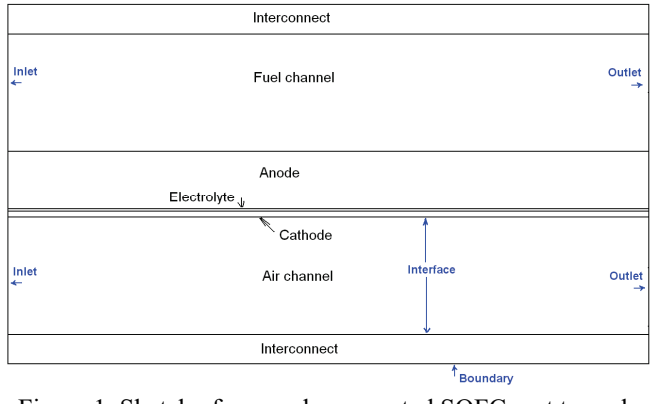


Figure 1. Sketch of an anode-supported SOFC, not to scale.

**TABLE I. Cell geometry (7-8)**

| Cell Component | Thickness |
|---|---|
| Cell length | 0.1 m |
| Fuel channel height | 1 mm |
| Air channel height | 1 mm |
| Anode thickness | 500 μm |
| Cathode thickness | 50 μm |
| Electrolyte thickness | 20 μm |
| Interconnect thickness | 500 μm |

Momentum transport

The gases flow inside the fuel cell components, such as in the air and fuel channels, and in the porous electrodes. The Darcy-Brinkman equation is introduced and solved for the gas flow in the fuel and air channels, and in the porous materials simultaneously (9-10). The Darcy-Brinkman equation (Eq. 6) is transformed into the standard Navier-Stokes equation when $\kappa \to \infty$ and $\varepsilon_p = 1$, and into the Darcy equation as $Da \to 0$. $Da$ is the Darcy number. The derivation of Navier-Stokes equation and Darcy equation from Darcy-Brinkman equation can be found in (9).

$$\left(\frac{\mu}{\kappa} + \rho \cdot \nabla \mathbf{u}\right)\mathbf{u} - \nabla\left[-p + \frac{1}{\varepsilon_p}\{\mathbf{T} - (\lambda - \kappa_{dv})(\nabla \mathbf{u})\}\right] = \mathbf{F} \qquad [6]$$

where $\mathbf{F}$ is the volume force vector, $\kappa$ is the permeability of the porous medium, $\varepsilon_p$ the porosity, $\mu$ the dynamic viscosity, u the velocity vector and $\mathbf{T}$ the viscous stress tensor $\left(\mathbf{T} = \nu\left(\nabla \mathbf{u} + (\nabla \mathbf{u})^T\right)\right)$. $\lambda$ is the second viscosity, and for gases it is normally assumed as: $\lambda = -2\mu/3$ (11). The densities and viscosities for the participating gases are dependent on local concentration and temperature, as described in (7-8). The gas inlet velocities are defined as a laminar flow profile. The outlets are defined as pressure (= 1 atm).

Mass transport

In the porous material, there are two kinds of mass diffusion mechanisms, i.e., molecular and Knudsen diffusions. The molecular diffusion is significant in the case of large pores, whose size is much bigger than the mean free path of the diffusion gas molecules (12-13). In this case, the intermolecular collisions will be dominated. For a multi-component gas mixture system, the diffusion coefficients are calculated by the expressions in (7-8).

Knudsen diffusion is important when the mean free path is much bigger than the pore size, and molecules collide with the solid walls more often than with other molecules**.** At the SOFC operating temperature of around 1000 K, the mean free path of these gas components is about 0.2-0.5 μm. In this study, the radius of pores is assumed as 0.34 μm, which is of the same order as the mean free path. In other words the Knudsen diffusion should be included in the SOFC models. The Knudsen diffusion coefficient of the component $i$ with the component $j$ in a gas mixture, $D_{k,ij}$, can be calculated based on the free molecule flow theory (14):

$$D_{k,ij} = \frac{2}{3} r_e \sqrt{\frac{8RT}{\pi(\frac{M_i + M_j}{2})^2}} \quad [7]$$

where $r_e$ is the effective radius of the pore, $R$ the universal gas constant. In the porous media, there is an increased diffusion length due to the tortuous paths of real pores, and the coefficients are usually corrected with porosity $\varepsilon$ and tortuosity $\tau$ (13,14):

$$D_{eff,ij} = \frac{\varepsilon}{\tau} \cdot D = \frac{\varepsilon}{\tau} \cdot \left( \frac{D_{i,j} \cdot D_{k,ij}}{D_{i,j} + D_{k,ij}} \right) \quad [8]$$

Equation 9 is used to describe the mass transport phenomena for each gas component inside the cell (10) and solved for the fuel and air channels and the electrodes.

$$\nabla \left( -\rho \cdot w_i \sum^{n} \overline{D}_{eff,ij} \cdot \nabla x_j \left( x_j - w_j \right) \frac{\nabla p}{p} \cdot \mathrm{u} - D_i^T \cdot \frac{\nabla T}{T} \right) + \rho \cdot \mathrm{u} \cdot \nabla w_j = S_i \quad [9]$$

where $w$ is the mass fraction, $x$ the molar fraction, $n$ the number of species and $D_i^T$ the thermal diffusion coefficient. $S_i$, the source term by the chemical reactions, is only defined for the internal reforming reactions, because the electrochemical reactions are assumed to take place at the interfaces between the electrolyte and the electrodes. The ordinary diffusion coefficients are also dependent on the local temperature, as described in (7-8).

On the air side nitrogen and oxygen are involved and only one Maxwell-Stefan diffusion coefficient needs to be calculated. On the fuel side methane, water, hydrogen, carbon monoxide and carbon dioxide are present and 10 pairs of the Maxwell-Stefan diffusion coefficients need to be calculated and implemented in the model. The boundary conditions for the mass transport equation are defined as mass fraction for the gas channel inlets, the outlets are defined as convective flux.

Heat transport

The temperature distribution is calculated separately for the gas phase (in the air and fuel channels and the electrodes) and for the solid phase (the interconnects, the electrodes and the electrolyte). Heat is transferred between the phases at the channel walls and in the porous electrodes. The governing equations for the transport of heat are defined and explained in (7-8). The inlet gas temperature is defined by the operating temperature (1000 K) and the outlet one is defined as a convective flux. The boundaries at the top and the bottom of the cell are defined as symmetries, because it is assumed that the cell is surrounded by other ones with the same temperature distribution.

Electrochemical reactions

Two approaches for defining the electrochemical reactions can be found in the literature, either as source terms in the governing equations (14-15) or as interface conditions defined at the electrode/electrolyte interfaces (16-17). The later approach is

employed in this study, because the thickness of the active layer is sufficiently thin, compared to the thickness of the electrode (16-17). The charge transfer equations are not solved in this study, however effects of the ohmic-, the concentration- and the activation polarization losses are included in the governing equations for heat transport by interface or source terms. The equations for polarization losses and exchange current density are described in (7-8).

Both hydrogen and carbon monoxide can participate in electrochemical reactions with oxygen ions (Eqs. 2-3). The electrochemical oxidation of hydrogen is several times higher than that of carbon monoxide, while the water-gas shift reaction is relatively fast (14). The contribution of oxidation of carbon monoxide has been neglected in this study. The cell average current density is specified to 0.3 A/cm$^2$ in this study.

Internal reforming reactions

Sufficient activity for the reforming reactions is provided inside the SOFC anode (18). Reaction kinetics from (19) for the steam reforming (an expression dependent on the active area to volume ratio) and from (20) for the water-gas shift reactions are used to calculate the reaction rates in this work. Other global kinetic models can be found in (21-22). The catalytic steam reforming reaction occurs at the surfaces of the nickel catalysts and is specified as (19,23):

$$r_r = AV \cdot \left( 943 \cdot \exp\left( \frac{-225 \cdot 10^3}{R \cdot T} \right) \cdot p_{CH_4} p_{H_2O} - 7.74 \cdot 10^{-9} \cdot \exp\left( \frac{-1937}{R \cdot T} \right) \cdot p_{CO} p_{H_2}^3 \right) \qquad [10]$$

where $p_i$ is the partial pressure of gas species $i$, $T$ the temperature, $r$ the reaction rate and $AV$ the active surface area to volume ratio. Equation 10 origins from the experiments performed at Research Centre Jülish, and the anode material consists of Ni−8YSZ substrate with a standard composition of 50 wt% Ni (23).

The range for the AV (related to catalytic kinetic reactions) varies in the literature between $1 \cdot 10^5$ m$^2$/m$^3$ (24) and $2.2 \cdot 10^6$ m$^2$/m$^3$ (19) for SOFC anodes. The measured specific surface area (m$^2$/g) for Ni/YSZ material developed for SOFC anodes is $70 \cdot 10^6$ m$^2$/m$^3$ (25). Note that not all the surfaces are available for catalytic reactions, due to the distribution of catalyst, non available pores and mass transfer limitations among others. An AV of $2.2 \cdot 10^6$ m$^2$/m$^3$, corresponding to 3.1 percent of the total Ni/YSZ specific area to volume ratio, is used in this work. The trend for the development during the last years is in the direction of employing smaller pores to get a larger AV.

The reaction rate, eq. 10, is of the Arrhenius type. It consists of three parts, partial pressures, pre-exponential factor and activation energy. The pre-exponential factor describes the amount of collisions between the molecules within the reaction and the exponential expression with the activation energy describes the probability for the reaction to occur. The pre-exponential factors depend strongly on the properties of the anode material and the temperature. The activation energy is based on the catalytic characteristics, such as chemical composition. The large difference between the activation energies in the open literature (19, 21-23) makes it probable that more parameters have significant influences on the reaction rate. To truly enhance the understanding of these

phenomena microscale modeling involving microscopic feature of the porous structures is needed.

Different approaches for defining the water-gas shift reaction can be found in literature: **1.** Global reaction mechanism that considers reaction in the anode only (5,14,20). **2.** Global reaction mechanism that considers reaction in the anode and in the fuel channel (4,19). **3.** A more advanced reaction mechanism that includes catalytic surface reaction kinetics for integrated steam reforming, water-gas shift reaction and the Boudouard mechanism can be found in, e.g., (4,6). Based on the global scheme for the anode, the expression for the catalyzed water-gas shift reaction in (20) has been selected in this study:

$$r_s = k_{sf} \cdot \left( p_{H_2O} p_{CO} - \frac{p_{H_2} p_{CO_2}}{K_{ps}} \right) \qquad [11]$$

The rate constant ($k_{sf}$) and the equilibrium constant ($K_{ps}$) are temperature dependent expressions calculated from experimental data, as described in (20).

The source terms $S_i$ (implemented in the Maxwell-Stefan equations for the gas species), due to the catalytical reforming reactions and the heat generation/consumption due to the reforming reactions is specified in (7-8).

## Results and Discussion

The fuel gas inlet conditions are specified as $x_{H2} : x_{CH4} : x_{CO} : x_{H2O} : x_{CO2} = 0.2626 : 0.171 : 0.0294 : 0.4934 : 0.0436$ (defined by IEA as 30% pre-reformed natural gas) (7-8), and the gas inlet temperature is specified as 1000 K. An average cell current density is 0.3 A/cm$^2$, an oxygen consumption is 20 % (mole), fuel consumption 80 % (mole), and flow direction from left -> right for both the anode and the fuel channels are defined. Typical SOFC material characteristic data used in this work are found in (7-8). The pore radius is for the standard case defined as 0.34 μm and the ratio of the anode thickness to the anode height to 33%.

Parameter studies are also performed for the anode pore size and the anode thickness ratios. The anode thickness ratio is defined as:

$$th_{anode}(\%) = \frac{d_{anode}}{d_{anode} + d_{fuelchannel}} \qquad [12]$$

The anode thickness ratio is 33% for the standard case, and 25% and 40% for the parameter studies. Note that the fuel channel height is kept constant for all the investigated cases.

As predicted, the temperature increases along the x-direction (the main flow direction), as seen in Fig. 2a. The heat generation is due to the electrochemical reactions and related over-potential losses. The methane steam reforming (MSR) consumes heat, up to half of the heat generated. The temperature difference in the y-direction inside the air channel

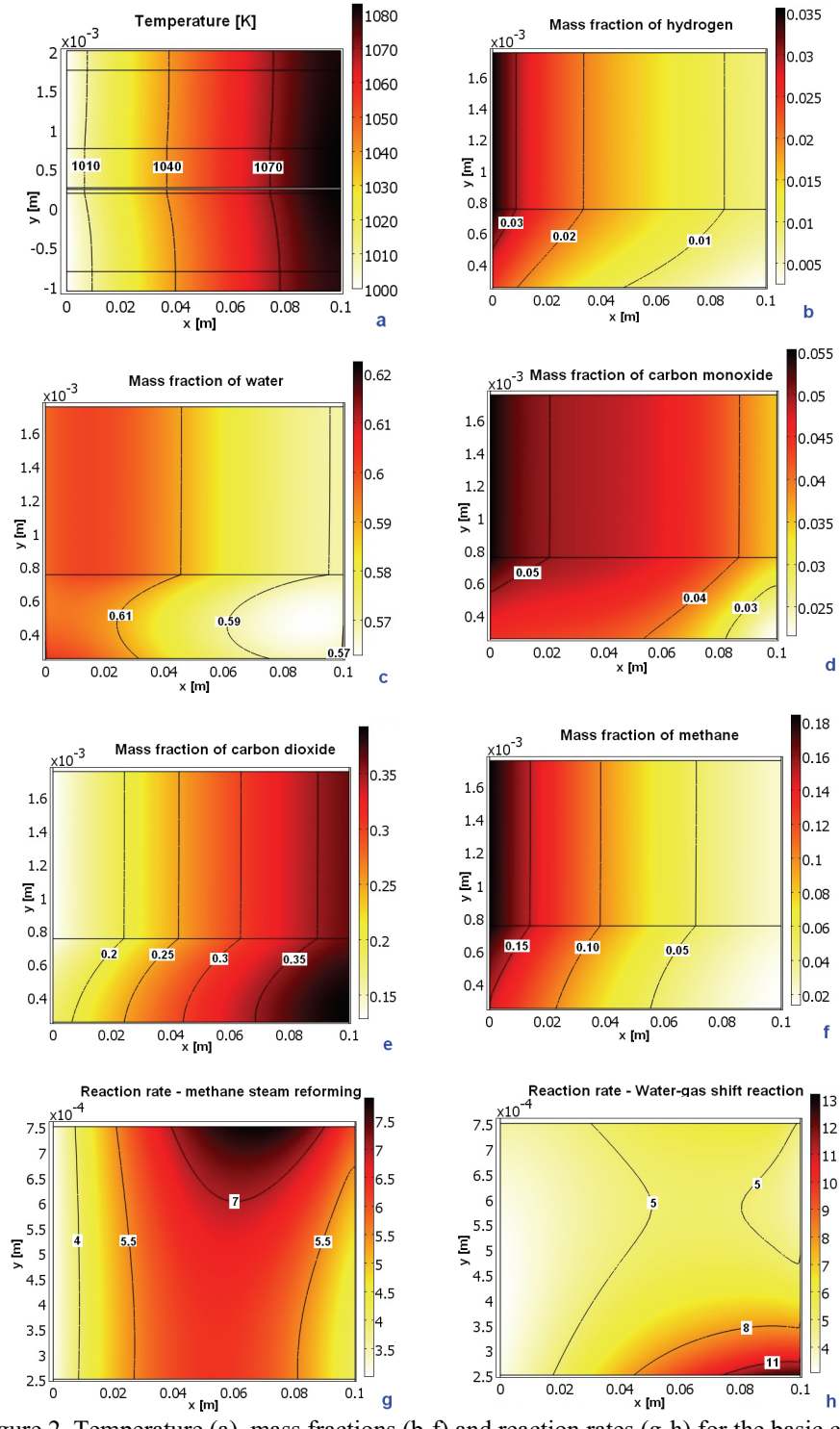


Figure 2. Temperature (a), mass fractions (b-f) and reaction rates (g-h) for the basic case.

occurs because the convective heat flux are bigger in the air channel (compared to the fuel channel) due to the relatively larger air flow rate. No significant difference for the temperature distribution can be seen when this model is compared to our previous developed model (7) with neglected Knudsen diffusion. Note the different scale in the x and y direction. For temperature distribution and mass fraction distributions the fuel channel (top) and anode (bottom) are presented, while for the reaction rate only the anode is shown.

The mass fraction of hydrogen (Fig. 2b) decreases due to the electrochemical reactions at the anode/electrolyte interface and increases due to the reforming reactions. The effect of Knudsen diffusion is significant. Large concentration gradients can be observed through the cell (y-direction) and the amount of hydrogen available for electrochemical reactions, at the TPB, is reduced, compared to our model with neglected Knudsen diffusion (7). Water (Fig. 2c) is generated due to the electrochemical reactions and consumed in the reforming reactions. The concentration of water reaches to its lowest value in the middle of the anode (y-direction). This effect can not be observed in our previously developed model, with neglected Knudsen diffusion (7). Carbon monoxide (Fig. 2d) is generated in the MSR and consumed in the water-gas shift reaction (WGSR). The concentration gradient through the anode is, due to the Knudsen diffusion effect, large and the smallest concentration is found at the TPB. Carbon dioxide (Fig. 2e) is generated in the WGSR and transported through the anode and out of the cell with the exhaust flow stream. A distinct concentration gradient can be seen through the anode (y-direction), due to the Knudsen diffusion effect. The highest concentration is found close to the gas outlet at the TPB. Methane (Fig. 2f) is consumed in the MSR. Also for methane a clear concentration gradient is seen through the anode, due to the Knudsen diffusion effect. The lowest concentration is found at the TPB close to the gas outlet.

The MSR (Fig. 1g) reaction rate depends on the available active area, temperature, and concentration of methane and water within the anode. It increases as the temperature increases along the flow direction and decreases as the amount of methane is reduced. In our previously developed model (7), with no Knudsen diffusion effect, only very small differences in reaction rate through the anode can be observed, however in this model the reaction rate is higher close to the fuel channel and lower closer to the TPB. The WGSR reaction rate (Fig. 2h) reaches its highest value close to the anode/electrolyte interface. As hydrogen is consumed and steam generated due to electrochemical reaction the water-gas shift reaction proceeds to the right and more hydrogen is generated. Our model (7), where Knudsen diffusion is neglected, predicted large concentration gradients within the anode (x-direction) close to the inlet. This effect does not appear in this model, due to larger diffusion resistance. It should be mentioned that the forward and backward reaction rates are in the same magnitude for the WGSR, to be compared to the MSR, where the backward reaction is neglible.

The anode pore size is varied to investigate the effects on transport processes, in terms of the hydrogen mass fraction distribution (Fig. 3a-b). These plots should be compared to Fig. 1b, where the mass fraction distribution for the standard case ($r$=0.34μm) is shown. An increased pore size means decreased mass transfer resistance but also a decreased surface area. Decreased mass transfer resistance gives a less steep concentration change in the y-direction in the anode. A decreased surface area results in a decreased MSR, i.e., the hydrogen concentration in the exhaust gas decreases.

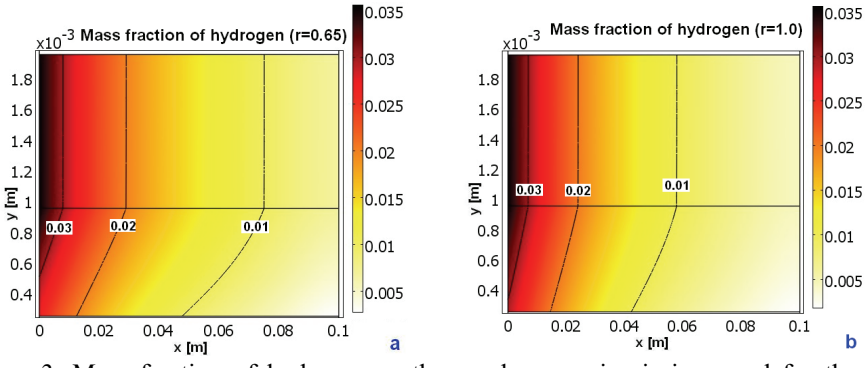


Figure 3. Mass fraction of hydrogen as the anode pore size is increased for the fuel channel (up) and anode.

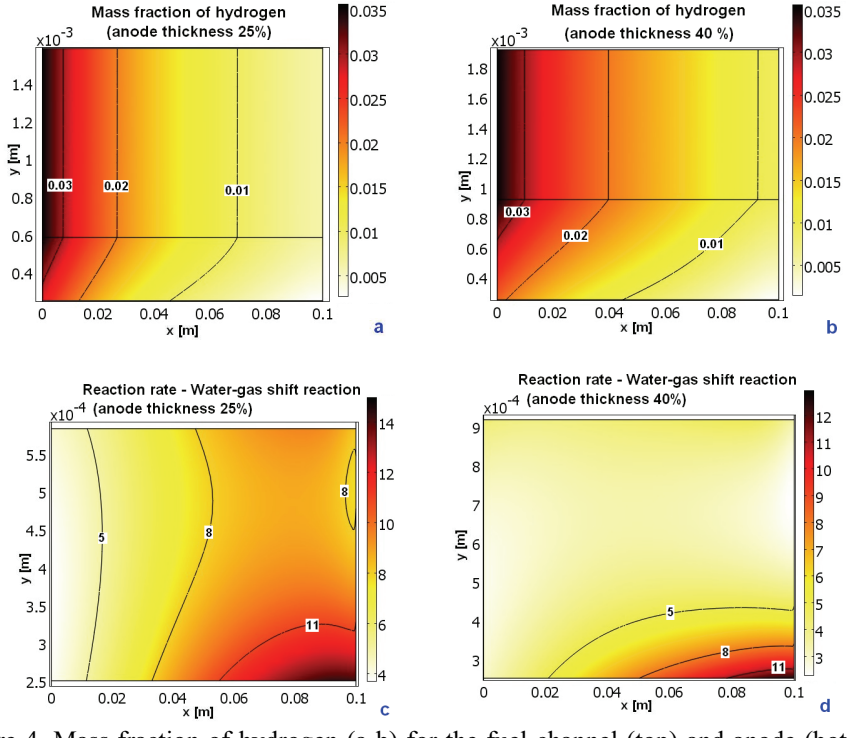


Figure 4. Mass fraction of hydrogen (a-b) for the fuel channel (top) and anode (bottom) and water-gas shift reaction rate (c-d) within the anode, affected by anode thickness.

The anode thickness is varied to investigate the consequences on the hydrogen mass fraction distribution (Fig. 4 a-b) and also WGSR reaction rate (Fig. 4 c-d). Comparisons are made to Fig. 1 b and h, respectively, where the standard case is revealed. A thicker anode (40%) gives higher mass fraction of hydrogen at the fuel channel/anode interface, but the large diffusion resistance (due to the longer diffusion length within the anode)

gives a low value at the anode/electrolyte interface and also a large concentration change in the y-direction. A thinner anode (25%) makes the smaller diffusion resistance between the fuel channel and anode/electrolyte interface, however the active surface area available for MSR is also reduced. Only a portion of the anode is used for the most WGSR in the case of a thicker anode, compared to the case with a thinner anode, where the reaction is distributed over a major part of the anode, as shown in Figs. 4a and 4c.

## Conclusion

A CFD approach is developed and implemented to analyze physical and chemical phenomena, which take place inside a single anode-supported SOFC by including Knudsen diffusion effects. Equations for mass-, heat- and momentum transport are coupled to the internal reforming reactions. The heat, which is generated due to the electrochemical reactions, is used for internal steam reforming reaction within the anode and/or outside the cell for external reforming and pre-heating of the fuel and air.

From the above analysis, there is an obvious change of concentration distributions in the anode, it means that there are extra resistances in the porous material because the size of pores is at the same order of the magnitude as the mean free path, i.e., the Knudsen diffusion plays an important role. Taking Knudsen diffusion into account is reasonable and necessary.

It is concluded that the pore size and the anode thickness need to be optimized to achieve good performance and a high efficiency particularly when the Knudsen diffusion is included. Thinner anodes reduces the diffusion length and resistance, however the active surface area for methane steam reforming is simultaneously reduced. Smaller anode pore size increases the active surface area, however the diffusion resistance through the anode is increased. It should be mentioned that the operating temperature may be optimized to compensate these effects of various changes from cell design and configuration parameters.

## Acknowledgments

The financial support from the Swedish Research Council (VR) and the European Research Council (ERC) is gratefully acknowledged.

## References

1. Y. Patcharavorachot, A. Arpornwichanop, A. Chuachuebsuk, *J. Power Sources*, **177**, 254-261 (2008).
2. M. Saxe, Doctoral thesis, KTH, Sweden (2008).
3. K. Reifsnider, X. Huang, G. Ju, R. Solasi, *J. Mater. Sci.*, **41**, 6751-6759 (2006).
4. P. Aguiar, C.S. Adjiman and N.P. Brandon, *J. Power Sources,* **138**, 120-136 (2004).
5. M. Ni, M.K.H. Leung, D.Y.C., *J. Power Sources*, **168,** 369-378 (2007).
6. V. Janardhanan, O. Deutschmann, *J. Power Sources*, **162**, 1192-1202 (2006).
7. M. Andersson, SOFC Modeling Considering Mass and Heat Transfer, Fluid Flow with Internal Reforming Reactions, Licentiate Thesis, Department of Energy Sciences, Lund University, Sweden, (2009).

8. M. Andersson, H. Paradis, J. Yuan, B. Sundén, *J. Fuel Cells* (2010, in press).
9. M. Le Bars, M.G. Worster, 2006, *J. Fluid Mech.*, **550**, 149-173 (2006).
10. COMSOL Multiphysics 3.5 user guide, Stockholm, Sweden (2008).
11. H.K. Versteeg, W. Malalasekera, An Introduction to Computational Fluid Dynamics, The Finite Volume Method, Pearson, UK (1995).
12. S. Yixiang, C. Ningsheng, C. Li, *J. Power Sources,* **164**, 639-648 (2007).
13. D. Y. Murzin, T. Salmi, Catalytic Kinetics, Elsevier Science (2005).
14. J. Yuan, Y. Huang, B. Sundén, W. Wang, *Heat Mass Transfer,* **45**, 471-484 (2009).
15. M. Hussein, X. Li, I. Dincer, *Int. J. Thermal Sciences*, **46**, 48-86 (2007).
16. R. Suwanwarangkul, E. Croiset, M.W. Fowler, P.L. Douglas, E. Entchev, M.A. Douglas, *J. Power Sources*, **122**, 9-18 (2003).
17. K. Tseronis, I.K. Kookos, C. Theodoropoulos, *Chem. Eng. Sci.*, **63**, 5626-5638 (2006).
18. J.R. Ferguson, J.M. Fiard, R. Herbin, *J. Power Sources,* **58**, 109-122 (1996).
19. J.-M. Klein, Y. Bultel, S. Georges, M. Pons, *Chem. Eng. Sci.*, **62**, 1636-1649 (2007).
20. B.A. Haberman, J.B. Young, *Int. J. Heat and Mass Transfer*, **47**, 3617-3629 (2004).
21. F. Nagel, T. Schildhauer, S. Biollaz, S. Stucki, *J. Power Sources*, **184**, 129-142 (2008).
22. D. Sanchez, R. Chacartegui, A. Munoz, T. Sanchez, *Int. J. Hydrogen Energy*, **33**, 1834-1844 (2008).
23. I. Drescher, W. Lehnert, J. Meusinger, *Electrochimica Acta,* **43**, 3059-3068 (1998).
24. V. Danilov, M. Tade, *Int. J. Hydrogen Energy*, **34**, 8998-9006 (2009).
25. D. Marrero-López, J.C. Ruiz-Morales, J. Peña-Martínez, J. Canales-Vázquez, P. Núñez, *J. Solid State Chemistry*, **181**, 685-692 (2008).

# Paper VI

This paper has been accepted for publication in (available online):

*Int. J. Energy Research,*
DOI: 10.1002/er.1875.

© 2011 John Wiley & Sons, Ltd.

INTERNATIONAL JOURNAL OF ENERGY RESEARCH
*Int. J. Energy Res.* (2011)
Published online in Wiley Online Library (wileyonlinelibrary.com). DOI: 10.1002/er.1875

# Review of catalyst materials and catalytic steam reforming reactions in SOFC anodes

Martin Andersson*,†, Hedvig Paradis, Jinliang Yuan and Bengt Sundén

Department of Energy Sciences, Faculty of Engineering, Lund University, Box 118, 221 00 Lund, Sweden

## SUMMARY

It is expected that fuel cells will play a significant role in the future sustainable energy system, because of their high energy efficiency and possibility to use renewable fuels. Fuels, such as biogas, can be produced locally close to the customers. The improvement for FCs during the last years has been fast, but the technology is still in the early phases of development, in terms of cost, stability and market sharing.

The reforming reaction of hydrocarbons (e.g., methane) is significant for an effective solid oxide fuel cell operation. This reaction could either be described by global kinetics or by elementary surface reaction kinetics. When a global approach is applied, the reaction rates depend on temperature, partial pressures, activation energy and the pre-exponential factor. Note that the last two mentioned parameters are normally calculated from experimental data. Different detailed reaction mechanisms (considering elementary surface kinetics) are developed, but there is a disagreement considering the involved reaction pathways, rate-limiting steps and intermediate species. It is found that detailed kinetics of the reforming reaction is important for design and development of new effective catalytic materials. A thermodynamic analysis tells that nickel and ruthenium are suitable catalytic materials for the methane reforming reactions. Copyright © 2011 John Wiley & Sons, Ltd.

**KEY WORDS**

SOFC; internal reforming; catalytic activity; reaction pathway; catalyst

**Correspondence**

*Martin Andersson, Department of Energy Sciences, Faculty of Engineering, Lund University, Box 118, 221 00 Lund, Sweden.
†E-mail: Martin.Andersson@energy.lth.se

Received 27 September 2010; Revised 27 January 2011; Accepted 24 March 2011

## 1. INTRODUCTION

Fuel cells (FCs) directly convert the free energy of a chemical reactant to electrical power and heat. This is different from a conventional thermal power engine, where the fuel is oxidized in a combustion process combined with a conversion process (thermal–mechanical–electrical energy), which takes place after the combustion. FCs do not store energy as batteries do [1]. The FC is not a new invention, since the electrochemical process was discovered already in 1838–1839 [2]. Among various types of FCs, the solid oxide fuel cell (SOFC) has attained significant interests due to its high efficiency and low emissions of pollutants to the environment. High temperature (HT) operation offers SOFC many advantages, such as high electrochemical reaction rate, flexibility of using various fuels and toleration of impurities [3].

The SOFC electrolyte is non-porous ceramic, normally $Y_2O_3$ stabilized $ZrO_2$ (YSZ). At an operating temperature between 600 and 1000°C, the ceramic electrolyte becomes non-conductive for electrons, but conductive to oxygen ions. Cathodes are mostly made from electronically conducting oxides or mixed electronically conducting and ion-conduction ceramics. The anode consists normally of nickel/yttria stabilized zirconia (Ni/YSZ) cermet. This composition enables internal reforming (IR) reactions of methane, due to the catalyst material characteristics. SOFCs can be designed with planar, tubular or monolithic structures. The planar configuration is normally more compact, compared to the tubular one, i.e. a higher specific power per volume is achieved. The tubular and planar SOFCs can be either electrolyte-, anode-, cathode- or metal supported. An electrolyte-supported SOFC has thin anode and cathode ($\sim 50\,\mu m$), and the thickness of the electrolyte is more than 100 μm. This design works preferably at temperatures around 1000°C. In an electrode-supported SOFC, either the anode or the cathode is thick enough to serve as the supporting substrate for cell fabrication, normally between 0.3 and 1.5 mm. The electrolyte is in this configuration very

Copyright © 2011 John Wiley & Sons, Ltd.

thin, and the operating temperature can be reduced to an intermediate temperature (IT), i.e. 600–800°C [4].

SOFCs can work with a variety of fuels, e.g. hydrogen, carbon monoxide, methane and combinations of these [5,6]. Oxygen is reduced in the cathode (Equation (1)). The oxygen ions are transported through the electrolyte, but the electrons are prevented to pass through the electrolyte. The electrochemical reactions (Equations (2) and (3)) take place at the anodic three-phase boundary (TPB). Methane needs to be reformed (Equation (4)) before the electrochemical reactions [7]. Carbon monoxide can be oxidized in the electrochemical reaction (Equation (3)), but can also react with water (Equation (5)). The reactions described here are the overall reactions, more detailed reaction mechanisms are discussed in Section 4.

$$O_2 + 4e^- \Leftrightarrow 2O^{2-} \quad (1)$$

$$H_2 + O^{2-} \Leftrightarrow H_2O + 2e^- \quad (2)$$

$$CO + O^{2-} \Leftrightarrow CO_2 + 2e^- \quad (3)$$

$$CH_4 + H_2O \Leftrightarrow 3H_2 + CO \quad (4)$$

$$CO + H_2O \Leftrightarrow H_2 + CO_2 \quad (5)$$

The aim of this work is to review the state-of-the-art for catalyst materials and models of the methane reforming reactions that occur within a SOFC. The global kinetic schemes as well as the elementary surface reaction kinetics are studied. Metals suitable for the catalysts of the methane steam-reforming reactions are compared. Different reaction mechanisms, including comparison of surface coverages, are outlined and discussed.

## 2. INTERNAL REFORMING REACTIONS

The reforming reactions (Equations (4) and (5)) in SOFC systems can be conducted both externally and internally. The external reforming, such as the pre-reformer in a SOFC system, indicates that the reformer is placed outside the cell, which is possible for all types of FCs. The IR refers to that the reforming reactions occur within the cell. A pre-reformer needs extra steam, since it cannot directly use the steam generated in the electrochemical reactions. The IR can be direct or indirect. In the direct internal reforming (DIR) approach, the reforming processes occur together with the electrochemical reactions within the anode. In the indirect internal reforming (IIR) approach, the reforming reactions appear in a reformer (within the cell) in close contact with the anode where the exothermic electrochemical reactions take place. The IR reactions decrease the requirement for cell cooling (less surplus of air). Less steam is needed and finally it offers advantages with respect to the capital cost. Up to half of the heat produced by the electrochemical reactions could be 'consumed' by the steam reforming process (Equation (4)). This would improve the system electrical efficiency [8,9].

The probability for carbon depositions depends on the steam-to-carbon ratio and on the catalytic composition [10,11]. It has been well established that the key reactions occur over a surface layer of nickel particles. If a layer of carbon is allowed to build up and attach to a nickel crystallite rapid catalyst breakdown can occur, due to the coke formation. It should be noted that hydrocarbons with a longer carbon chain than methane have a higher propensity for the carbon deposition [10]. The risk of carbon deposition can be decreased if the pre-reforming is carried out before the cell, or the anode structure or configuration is modified:

- Complete or partial replacement of doped zirconia with doped ceria or ceria-zirconia possessing a higher lattice oxygen reactivity/mobility. This can be combined with complete or partial replacement of Ni with an electron conductor that does not catalyze carbon formation, such as Cu [11,12]. Anodes based on Cu-Co have been found to reduce the risk for carbon formation [11].
- Replacement of doped zirconia by complex perovskites with their doping by metals active in the steam reforming reaction [12].
- Complete or partial replacement of Ni by precious metals in cermets with complex perovskites or doped zirconia as oxide phases [12].

It should be noted that cells with Cu-$CeO_2$-YSZ anodes demonstrate comparable performance when operating on CO or syngas as on $H_2$, for Ni-YSZ the performance is significantly lower when operating on CO or syngas. It has also been shown that adding Co to Cu-$CeO_2$-YSZ improves the performance [13]. When steam is used as oxidant, i.e. for methane steam reforming and for water–gas shift reaction, the reaction rates for ceria-supported metals can be scientifically higher than that for ceria or the transition metal alone, due to interactions between the support and the transition metal [14].

In a conventional HT SOFC the endothermic steam reforming reaction is very fast. This can result in a sharp temperature drop at the inlet of the stack. This temperature gradient results in thermal tensions, which in the worst case causes mechanical failure of the cells [8]. The problem of the tensions and the big temperature gradient close to the inlet region could be solved with different approaches:

- Lowering the operating temperature to an intermediate range to reduce the steam reforming reaction rates (Equation (4)) [15].

- Recycling a part of the anode exhaust gas to obtain a dilution of the fuel [8].
- The anode material can be designed with the aim of a decreased steam reforming activity. Until now these new SOFC materials, such as perovskite oxides or cermets containing iron or copper, have too low electrical conductivity or electrocatalytic activity to meet real world requirements [8].

## 3. GLOBAL REACTION KINETICS

Several kinetic expressions considering the steam reforming reaction have been developed and published in the literature. The reaction order varies significantly between the schemes, in terms of orders of methane and water ($m$ and $n$ in Equation (6)), see [1] for typical values. The reaction order of methane ($m$) varies between 0.85 and 1.4. For water, both negative and positive values for reaction order ($n$) exist. However, it has been shown that all these findings could be correct for the chosen operating conditions of the experiments. A small steam-to-carbon (SC) ratio gives positive reaction order of water. SC in the order of 2 yields the reaction orders of water close to zero, and high SC gives negative values [16]. Experimental work has shown that it is possible to change the steam reforming reaction orders by modifying the anode, for example, $m$ increased from 0.85 to 1.4 and $n$ decreased from $-0.35$ to $-0.8$ when other compounds are added to the Ni-YSZ anode [15]. As revealed in [1], comparison with experimental data is rare, but it is worthwhile to note that the reaction orders ($m$ and $n$) usually originate from fitting experimental data to a kinetic expression.

$$r_{\mathrm{r,Arr}} = k \cdot p_{\mathrm{CH_4}}^{m} \cdot p_{\mathrm{H_2O}}^{n} \cdot \exp\left(\frac{-E_{\mathrm{a}}}{R \cdot T}\right) \qquad (6)$$

where $r_{\mathrm{r}}$ is the reaction rate of the steam reforming reaction (Equation (4)), $p$ the partial pressure, $R$ the ideal gas constant and $T$ the temperature. The unit for the reaction rate is dependent on the pre-exponential factor. Normally, the unit for the methane steam reforming reaction rate is in $\mathrm{mol\,s^{-1}\,m^{-2}}$, and can then be converted to $\mathrm{mol\,s^{-1}\,m^{-3}}$ after multiplying it with the ratio between the active surface area to the volume ($AV$, in $\mathrm{m^2\,m^{-3}}$). The range for the AV (related to catalytic kinetic reactions) varies in the literature between $1 \times 10^5\,\mathrm{m^2\,m^{-3}}$ [17] and $2.2 \times 10^6\,\mathrm{m^2\,m^{-3}}$ [18] for SOFC anodes. For example, the measured ratio for Ni/YSZ material developed for SOFC anodes (with a pore size of 225 nm) is $70 \times 10^6\,\mathrm{m^2\,m^{-3}}$ [19]. Note that not all the surfaces are available for the catalytic reactions, due to the distribution of the catalysts, non-available pores and mass transfer limitations among others. An AV of $2.2 \times 10^6\,\mathrm{m^2\,m^{-3}}$ corresponds to 3.1% of the total Ni/YSZ surface area in this specific case. The kinetic expression for the methane steam reforming in Equation (6) is of Arrhenius type, and can be compared to an expression of the Langmuir–Hinshelwood type, as shown in Equation (7) [20]:

$$r_{\mathrm{r,Lang.}} = k \cdot \frac{p_{\mathrm{CH_4}} \cdot p_{\mathrm{H_2O}} \cdot K_{\mathrm{CH_4}} \cdot K_{\mathrm{H_2O}}}{(1 + p_{\mathrm{CH_4}} \cdot K_{\mathrm{CH_4}} + p_{\mathrm{H_2O}} \cdot K_{\mathrm{H_2O}})^2} \qquad (7)$$

The kinetic expressions, in Equations (6) and (7), can be compared to the equilibrium approach in Equation (8) [16]:

$$r_{\mathrm{r,eq}} = k \cdot p_{\mathrm{CH_4}} \cdot p_{\mathrm{H_2O}} \cdot \left(1 - \frac{p_{\mathrm{CO}} \cdot p_{\mathrm{H_2}}^3}{K_{\mathrm{e,STR}} \cdot p_{\mathrm{CH_4}} \cdot p_{\mathrm{H_2O}}}\right) \qquad (8)$$

where $K_{\mathrm{e}}$ is the equilibrium constant. The reaction orders in Equation (8) are the same as the molar proportions for the respective gas species in the global chemical reaction (1 for both methane and water for the forward reaction, and 3 for hydrogen and 1 for carbon monoxide for the backward reaction).

Different approaches for defining the water–gas shift reaction (Equation (5)) can be found in the literature:

- Global catalytic reaction mechanism that considers reaction in the anode only [21,22].
- Global catalytic reaction mechanism that considers reaction in the anode and gas reaction in the fuel channel [15,18].
- A more advanced reaction mechanism that includes the catalytic surface reaction kinetics for the steam reforming, the water–gas shift and the Boudouard reactions can be found in [23,24], among others.

It is frequently stated in the literature [15,18] that the water–gas shift reaction should be considered to be in (or very close to) the equilibrium state. The equilibrium can be assumed since this reaction is very fast under the conditions found within a SOFC. When the equilibrium is assumed, the reaction can be expressed with an equilibrium-limited shift reaction rate expression, the first order in carbon monoxide as in [25]:

$$r_{\mathrm{s}} = k_{\mathrm{s}} \cdot p_{\mathrm{CO}} \cdot \left(1 - \frac{p_{\mathrm{CO_2}} \cdot p_{\mathrm{H_2}}}{K_{\mathrm{e,s}} \cdot p_{\mathrm{CO}} \cdot p_{\mathrm{H_2O}}}\right) \qquad (9)$$

where $r_{\mathrm{s}}$ is the reaction speed of the water–gas shift reaction, $k_{\mathrm{s}}$ the pre-exponential factor, $p_i$ partial pressure for the respective species and $K_{\mathrm{e,s}}$ the temperature-dependent equilibrium constant.

## 4. ELEMENTARY SURFACE REACTIONS KINETICS

Elementary-kinetic electrochemical reactions in the SOFC electrodes are strongly connected to the heterogeneous catalysis and the surface chemistry. Note that information considering the surface coverages of intermediate species are not available when

the global approach is applied. Both for the anode and cathode there is a disagreement considering the involved reaction pathways, rate-limiting steps and intermediate species [26,27]. Elementary-kinetic models are normally limited to only the electroactive region, and couplings to transport models are still rare. The surface coverage can be calculated with, for example, a mean-field approach, where it is assumed that the surface state can be described with average quantities, such as surface coverage, thermodynamic and kinetic adsorbate properties. The surface state species composition (segregation phenomena and impurities) and the detailed surface structure (steps, edges and terraces), evaluated at atomic scales, are then not further resolved, when using the mean-field approach. The concentration of the different surface-phase species is then normalized to the total concentration of available surface sites, yielding a dimensionless coverage. The surface phase is coupled to the gas-phase species via desorption and adsorption reactions, and to bulk-phase species via surface/bulk exchange reactions. The surface-phase species are also participating in these reactions among themselves [26].

A thermodynamic analysis can be performed to observed trends of reforming reactivity of different metals. Jones *et al.* [28] investigated suitable catalysts for the methane steam reforming reaction. Au, Ag, Cu, Pt, Pd, Ni, Co, Ru and W are included in the concerned analysis. All these metals are counted as transition elements in the periodic table (previously named d-block). Potential metals are excluded stepwise [28]:

- An overall energy diagram tells that the noble metals (Au, Ag and Cu) are unsuitable for the steam reforming reaction, since the first six steps of the reactions, all the way from $CH_4(g)+H_2O(g)$ to $C^*+O^*$, are significantly uphill energetically.
- It is also concluded that W binds $C^*$ and $O^*$ very strongly, and the further reaction is unlikely to appear.
- In terms of the free energy profiles of the reaction, Pt and Pd are found to be unfavorable for the adsorption and desorption of water molecules.
- A possibility of poisoning effects appears, for example, for Co, where $O^*$ and $OH^*$ are adsorbed more strongly, compared to the other investigated metals.

This simple investigation revealed that Ni and Ru might be suitable for the catalytic methane steam reforming reaction [28]. SOFCs contain in general a porous Ni/YSZ structure in the anodes, which enables the electrochemical reactions at the TPB [1]. It can be concluded that Ni is a good candidate as the catalytic material in the SOFC anodes, due to its low cost and possibility for both the electrochemical reactions and also the steam reforming reactions.

### 4.1. Different pathways for the catalytic methane steam reforming reaction

Knowledge of the catalytic reaction mechanism considering the steam reforming reaction of hydrocarbons is counted as a key importance for designing an anode material with a high efficiency and a long life length [29]. The $CO^*$ formation as well as the $CH_4(g)$ adsorption have been suggested as the rate limiting steps. According to Jones *et al.* [28] the rate limiting step changes from $CO^*$ formation to $CH_4(g)$ adsorption as the temperature is increased.

The conception with the rate limiting steps describes the phenomena occurring at the microscopic scale, to be compared to the equilibrium constants at the macroscopic scale. Le Chatelier's principle tells that the equilibrium constant for the steam reforming reaction increases as the temperature is increased, since this reaction is endothermic. An increased equilibrium constant indicates that the equilibrium proceeds further to the right (Equation (4)). The water–gas shift reaction is exothermic and its equilibrium constant decreases as the temperature is increased. An increased pressure causes the equilibrium shifting to the side with fewer moles of the gases, i.e. the equilibrium constant is decreased for the steam reforming reaction. For the water–gas shift reaction, the pressure has no effect on the equilibrium constant, since the right and left side contains the same amount of moles. Note that the steam reforming reaction does normally not reach equilibrium conditions within a SOFC, compared to the water–gas shift reaction that is normally assumed (within the open literature) to be in the equilibrium.

A multi-step heterogeneous reaction mechanism (HCR) for Ni/YSZ catalysts has been developed by Hecht *et al.* in [30]. This mechanism consists of 21 reversible reactions, 6 gas-phase species and 12 surface adsorbed species. The mechanism is elementary in nature and covers the global aspects of the steam reforming, the water–gas shift, the Bouduard reactions and also the surface-carbon coverage. A simplified sketch of this reaction mechanism can be seen in Figure 1. Most of the expressions are expressed in the Arrhenius rate form and depends on the surface coverages. This model is validated by the experimental results. The experiments (using a porous Ni-YSZ anode) were designed to measure the extent of reformation processes under the conditions well away from equilibrium conditions. Pure steam reforming and pure dry reforming with carbon dioxide as well as a combination of these were included in the validation. Note that this mechanism is not validated on the conditions where coking and bulk-phase Ni oxidation occur [30].

The HCR developed by Hecht *et al.* in [30] was extended by Janardhanan and Deutschmann in [23] to describe a larger temperature range between 220 and 1700°C (compared to a constant temperature of

800°C). However, the same chemical reaction schemes were applied.

Hofmann *et al.* [24] compared the HCR from Janardhanan and Deutschmann in [23] with a simplified approach, where the methane steam reforming is described by a global kinetic approach and the water–gas shift reaction is in the equilibrium. The HCR model can be used to calculate the catalytic surface coverages. It is concluded that the HCR predicts a less steep methane consumption along the flow channel. A slower methane conversion indicates less hydrogen available throughout the cell. Also, the temperature distribution is significantly affected by the steam reforming reaction, with a flatter temperature gradient by the HCR model compared to that by a global approach.

Blaylock *et al.* [31] investigated different reaction pathways and kinetics of the methane steam reforming reaction over the Ni(111) surfaces, in order to develop a comprehensive *ab initio* microkinetic model. The Ni(111) surface is sometimes also referred as Ni terrace, known to be catalytically active, and it is the most stable facet on Ni crystallites. The reaction scheme consists of seven gas-phase species, 18 surface adsorbed species and 36 reversible reactions. A simplified sketch of this reaction scheme can be found in Figure 2. Besides the Ni terrace also the step sites catalyze the methane steam reforming reaction, i.e. a model that considers only the Ni terrace underestimates the reaction rate.

The reaction mechanism, from Hecht *et al.* in [30] and the one from Blaylock *et al.* in [31] (Figure 2) differs concerning the amount of intermediate adsorbed surface species included. The later approach with a larger amount of adsorbed surface species contains obviously a lager amount of reaction steps (Figure 1). It should be noted that more intermediate gas-phase species are also included in [31], i.e. $CH_2O$ and $CH_3OH$ (not shown in Figure 2).

Density functional theory (DFT) calculations are performed to investigate the thermo-chemistry of the methane steam reforming. It is found that cleaving of a C–H bond is in general predicted to have a smaller barrier than cleavage of a O–H bond, on the Ni(111) surface. The oxygen addition as well as the hydroxyl addition reactions are predicted to have higher barriers, compared to the dehydrogenation reactions. It is concluded that it is easier to remove an atom of hydrogen, compared to the one of oxygen, from carbon, i.e. the probability that $CH_xOH$ will form $CH_{(x-1)}OH$ is higher than for $CH_xO$. The reactions occurring from the adsorption of $CH_4(g)$ until the formation of $CH^*$ occur relatively smoothly [31]. Vang *et al.* [32] pointed out that the bond breaking selectivity on the different catalytic sites determines the selectivity that can be observed on the macroscopic scale. It is found that C–C bond breaking can be prevented by blocking the step sites, instead the breaking of C–H bonds will be more significant.

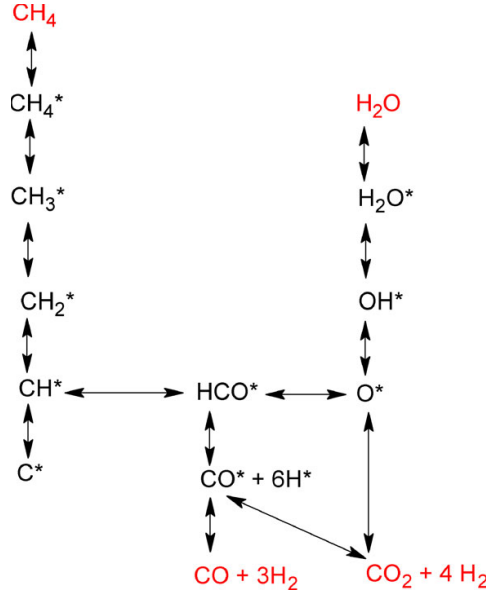


**Figure 1.** Simplified sketch of the catalytic reforming reaction mechanism proposed by Hecht *et al.* [30] and Janardhanan and Deutschmann [23] among others. Note that the generation and consumption of H*, O* and OH* in each reaction step is not explicitly shown in the figure.

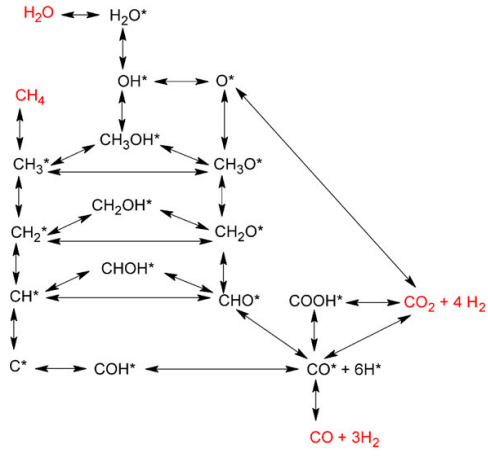


**Figure 2.** Simplified sketch of the catalytic reforming reaction mechanism proposed by Blaylock *et al.* [31]. Note that the generation and consumption of H*, O* and OH* in each reaction step are not explicitly shown in the figure.

**Table I.** Surface coverages when methane steam reforming reaction is applied in SOFCs.

| | Blaylock *et al.* [31] | Janardhanan and Deutschmann [23]* | Hecht *et al.* [30]† | Hofmann *et al.* [24]‡ | Li *et al.* [33]§ | Li *et al.* [33]¶ |
|---|---|---|---|---|---|---|
| Ni | 0.77 | 0.58–0.66 | 0.60–0.70 | 0.76–0.77 | 0.4–0.6 | 0.57–0.73 |
| H* | 0.15 | 0.10–0.15 | 0.05–0.12 | 0.05–0.07 | 0.13–0.18 | 0.12–0.22 |
| CO* | 0.077 | 0.19–0.25 | 0.10–0.30 | 0.05–0.11 | 0.18–0.50 | 0.12–0.18 |
| O* | $3.5 \times 10^{-4}$ | n/a | 0.00–0.15 | 0.07–0.11 | 0.00–0.02 | 0.01–0.02 |

*Janardhanan and Deutschmann [23] vary the current density to investigate the effect on surface coverage. The values presented in this table correspond to a current density between 10 000 and 22 000 A $m^{-2}$ with an inlet molar fractions of $H_2O$ being 0.40 and of $CH_4$ 0.60.
†Hecht *et al.* [30] present the surface coverage as a function of location within the anode.
‡Hofmann *et al.* [24] vary inlet conditions, according to findings in literature.
§Li *et al.* [33] keep the inlet temperature at 800°C, for a different current density (between 0 and 10 000 A $m^{-2}$).
¶Li *et al.* [33] vary the inlet temperature (between 750 and 950°C), while keeping the current density to 10 000 A $m^{-2}$.

As predicted in [31] 87% of the total reaction flux is involved in the reaction of CH* with one oxygen containing species. CHO* is formed from CH* and O*, and decomposed later to form CO* and H*. This single reaction path corresponds to approximately 56% of the total reaction flux. The formation of CHOH* from OH* and CH*, with a subsequent reaction to COH*, is the second-most-active pathway and corresponds to 31% of the total reaction flux. The reaction of $CH_2^*$ with either OH* or O* involves 12% of the total flux.

It can be seen in Table I that three surface-phase species, H*, CO* and O*, make up most of the predicted surface coverages, as revealed in the open literature. It should be noted that empty Ni surfaces account for more than half of the available surface sites. It is also found that the surface coverage depends on the current density, gas-phase species concentration, temperature and the location within the anode. Blaylock *et al.* [31] included additional surface species, as follows in the order of decreasing surface coverages: $H_2O^*$, $CO_2^*$, $CH^*$, $OH^*$, $CH_2^*$, $C^*$, $COH^*$, $CH_3^*$, $CHO^*$, $CH_3OH^*$, $CH_3O^*$, $COOH^*$, $CHOH^*$, $CH_2O^*$, $CH_2OH^*$.

A higher fraction of $H_2O$ in the fuel mixture gives a higher coverage of H*, but a lower of CO*. As the current density increases, the surface fraction of empty Ni sites increases, but the coverages of H* and CO* decrease [23]. The coverage of O* reaches its highest values close to the TPB, but for H* the opposite trend appears, as hydrogen is consumed at the TPB. The CO* coverage has its maximum value in the middle (considering the thickness) of the anode and the fraction of empty Ni surface sites reaches its minimum value in the same area [30]. An increased temperature increases the fraction of empty Ni sites and decreases the surface coverages of CO*, H* and O* [33].

The steam reforming reaction has at least two kinds of active catalytic sites on Ni, the very active one

associated with the step and defect sites on the surface and the less active one associated with the close-packed facets. It is found that there are at least two different reaction channels for the steam reforming of methane on Ni, the one associated with steps with a low activation barrier and the one with the terraces with a higher activation barrier. It is concluded that there are many more active terrace sites compared to the active step sites. The coke formation occurs at the step sites. It is possible to add different additives that block different step sites and certainly decreases the probability for the coke formation. An optimized catalyst will have just enough additives that the coke formation is effectively blocked, while the fast channel reaction can still proceed [34].

Metal particles grown at HT on coke or oxide substrate have polyhedral shapes exhibiting (111), (100) and (110) facets. Ni(111) is frequently included in the kinetic and thermodynamic studies, but Ni(100) and Ni(110) are less studied. Wang *et al.* [35] used a DFT approach to investigate and clarify the thermodynamics of $CH_4$ dissociation on Ni-based catalysts:

Ni(111) has four possible surface sites: the top site (tp), the bridge site (br), the hexagonal-closed-packed site (hcp) and the face-centered cubic site (fcc). Stable structures are found for $CH_3^*$(tp-a1, tp-a2, hcp-c and fcc-d), $CH_2^*$(tp–a, hcp-c and fcc-d), $CH^*$ (hcp-c and fcc-d), $C^*$ (hcp-c and fcc-d) and $H^*$ (tp-a, hcp-c and fcc-d). On the basis of the binding energy it is found that $CH_x$ and H prefer to chemisorb on the hcp and fcc [35].

Ni(100) has three possible surface sites: the tp, the br and the hollow site (hl). Stable structures are found for $CH_3^*$(tp-e1, tp-e2, br-f1 and br-f2), $CH_2^*$(tp–e1, tp-e2, br-f and hl-g), $CH^*$ (hl-g), $C^*$ (hl-g) and $H^*$ (tp-e, br-f and hl-g). On the basis of the binding energy it is concluded that $CH_3$ prefers to chemisorb on the br, while $CH_2$, CH, C and H prefer to chemisorb on the hl. It is further concluded that Ni(100) has a high reactivity, but a low stability as the catalyst for $CH_4$ steam reforming reaction [35].

Ni(110) has six possible surface sites: the top-up site (tu), the short bridge site (sb), the top-down site (td), the long-bridge site (lb), the hollow site formed by two top-layers Ni and one sub-layer Ni (u2dl) and the hollow site formed by one top-layer Ni and two sub-layers Ni (uld2). Stable structures are found for $CH_3^*$(tu-h1, tu-h2, sb-i1 and sb-i2), $CH_2^*$(tu–h, sb-I and td-j), $CH^*$ (sp-I, usdl-l, lb-k and td-j), $C^*$ (tu-h, sb-i, lb-k, td-j) and $H^*$ (tu-h, sb-I, u2dl-l and lb-k). On the basis of the binding energy it is found that $CH_3$ and $CH_2$ prefer to chemisorb on the sb, while CH, C and H prefer to chemisorb on the lb, td and u2dl, respectively [35].

## 4.2. Microkinetic models

A great deal of information is available for Ni as the reforming catalyst, because it has been commonly used for catalysis in the chemical industry. For SOFC anodes, the ceramic oxygen-ion conductor YSZ itself also has catalytic activity for the partial oxidation. Most reaction rates are represented in an Arrhenius-type equation or as a sticking coefficient. A kinetic model can be constructed by combining thermochemical values for each species with calculated activation energies and transition-state properties. The forward rate coefficients are described either as a surface reaction rate coefficient or an adsorption reaction. The original kinetic data were often taken from a variety of different catalysis studies, which makes the mechanism not thermodynamically consistent. Therefore, some of the original kinetic parameters are often modified to ensure the overall consistency concerning the enthalpy and the entropy. This approach permits the computation of the reverse reaction rate coefficients, which in turn is dependent on the forward reaction rate coefficients [30]. Since this mechanism is based on the elementary steps, it, therefore, represents all the global processes in the anode.

For the surface reactions and the desorption reactions, often the Arrhenius form is applied for the reaction rate constants, at least for small or moderate variations of the temperature for the reactions [36]. The Arrhenius form is introduced in Equation (6) for the global reaction kinetics and can be compared to the following equations. The reaction rate constant of a generalized modification of an Arrhenius-type equation including the surface-phase species coverages can be expressed as [23]:

$$k_i = A_i \cdot T^{n_i} \cdot \exp\left(\frac{-E_i}{R \cdot T}\right) \prod_{k=1}^{K_g+K_s} \theta_k^{\mu_{ki}} \cdot \exp\left(\frac{-\varepsilon_{ki} \cdot \theta_k}{R \cdot T}\right) \tag{10}$$

where $A_i$ is the pre-exponential factor, $T$ the reaction temperature, $n_i$ the temperature exponent fraction, $R$ the gas constant and $E_i$ the activation energy for the reaction $i$. To describe the coverage dependency, $\mu_{ki}$ and $\varepsilon_{ki}$ (coverage dependent activation energy) are introduced for the parameters for species $k$ and reaction $i$.

The species molar production rate depends on the surface-phase species concentration which is sometimes expressed as the coverage $\theta_k$. The coverage is the fraction of the surface sites covered by the adsorbed species $k$ to the total active sites on the catalyst surface. The relation between the surface coverage or the surface concentration is expressed as [37]:

$$\theta_k = \frac{c_k \cdot \sigma_k}{\Gamma_{\text{tot}}} \tag{11}$$

where $\theta_k$ is the surface coverage, $\sigma_k$ the co-ordination number (number of the sites required for a species of adsorption), $c_k$ the concentration and $\Gamma_{\text{tot}}$ the total surface site density.

The reaction rate constant for the surface reaction can also be written as [31]:

$$k_i = \left(\frac{k_b \cdot T}{h}\right) \cdot \left(\frac{Q^{TS} \cdot (Q'_{slab})^{R_{tot}-1}}{\prod_{r=1}^{R_{tot}} Q_r}\right) \cdot v \frac{N_{sites}^{0\ R_{tot}-1}}{C_T^{R_{ads}-1}} \cdot \exp\left(\frac{-E_b}{R \cdot T}\right) \quad (12)$$

where $k_b$ is the Boltzmann constant, $h$ the Plank constant, $Q$ the total partition function, $R_{tot}$ the total number of the reactants participating in the reaction, $R_{ads}$ the total number of adsorbate reactants and $N_{sites}$ the standard-state number of the binding sites per adsorbate.

Non-activated adsorption is calculated using the kinetic theory of the gases assuming the sticking coefficient to be equal to the fraction of vacant sites. The forward reaction rate constant can be presented for the non-activated adsorption as [31]:

$$k_i = \sqrt{\frac{k_b \cdot T}{2 \cdot \pi \cdot M}} \quad (13)$$

where $M$ is the molecular mass of the gas-phase species and $k_j$ the reaction rate constant.

Hecht *et al.* [30], Janharhanen and Deutschmann [23] and Hofmann *et al.* [24] were, for the adsorption reactions, applying an approach with a sticking coefficient instead of the approach in Equation (10). The forward reaction rate constants including the sticking coefficient for the non-activated adsorption reaction can be expressed as [24]:

$$k_i = \frac{\gamma_j}{(\Gamma_{tot})^m} \cdot \sqrt{\frac{R \cdot T}{2 \cdot \pi \cdot M}} \quad (14)$$

where $\gamma_j$ is the sticking coefficient.

For the activated adsorption and for the surface reactions, the transition-state theory can be applied to obtain the reaction rate coefficients for the forward reaction. The forward reaction rate constant for the activated molecular adsorption is written as [31]:

$$k_i = \left(\frac{k_b \cdot T}{h}\right) \cdot \left(\frac{Q^{TS}}{Q_{gas} \cdot Q_{slab}}\right) \cdot \left(\frac{R \cdot T}{p_0}\right) \cdot \Gamma_{tot} \cdot \exp\left(\frac{-E_b}{R \cdot T}\right) \quad (15)$$

where $E_b$ is the classical electronic energy barrier of adsorption and $p_0$ the standard pressure.

The construction of a kinetic model for the relationship between the standard free energy change of an elementary reaction step and the equilibrium constant needs to be formed. When the equilibrium constant and the forward reaction rate constant are known, the reverse reaction rate constant can be expressed as [38]:

$$k_{-1,i} = \frac{k_i}{K_{e,i}} \quad (16)$$

where $K_{e,j}$ is the equilibrium constant. The equilibrium constant of a reaction can be defined as [36]:

$$K_{e,j} = \exp\left(-\frac{\Delta G_i}{R \cdot T}\right) = \exp\left(-\frac{\Delta H_i - T \cdot \Delta S_i}{R \cdot T}\right) \quad (17)$$

where $\Delta G$ is a change in Gibbs energy due to the chemical reaction, $\Delta H$ the enthalpy change and $\Delta S$ the entropy change of the reaction. It should be noted that the principle of reversibility should be used with some caution. The mechanism for the reaction can be reversible for a given set of concentrations, temperature and pressure, but may not be valid for different sets of reaction conditions. The reaction may proceed through the same steps in the forward and the backward reactions but the rate of the individual steps may differ by several orders of magnitude [36].

## 5. CONCLUSIONS

Understanding of the methane steam reforming reactions and catalyst materials structure is expected to be of significant importance for the further SOFC development. The reforming reaction rates are either described by a global kinetics approach or by a more detailed approach applying elementary surface reaction kinetics. It is concluded that the reaction order varies significantly in the global models. The reaction order for water can be negative or positive. It is found that the water–gas shift reaction is usually assumed to be in equilibrium. Different mechanisms considering elementary surface kinetics have been developed. However, there is a disagreement considering the involved reaction pathways, the intermediate species and rate-limiting steps. The CO* formation as well as the methane adsorption have been suggested as the rate limiting steps. It should be noted that empty nickel occupies normally more than half of the available surfaces, as identified in the open literature. Three surface species (H*, CO* and O*) are the dominant components in terms of the surface coverage. The nickel particle surfaces contain variable structures for the catalytic reactions. Typically, only parts of them are chemically available. This might be the reason why lower reaction rates were predicted by the detailed models, compared to those by the global models.

## NOMENCLATURE

| | |
|---|---|
| $c_k$ | = concentration (mol m$^{-2}$) |
| $E$ | = activation energy (kJ mol$^{-1}$) |
| $E_b$ | = classical electronic energy barrier of adsorption (J mol$^{-1}$) |
| $\Delta G$ | = Gibbs energy (J mol$^{-1}$) |
| $h$ | = Plank constant (J s) |
| $\Delta H$ | = enthalpy change of reaction (J mol$^{-1}$) |
| $k$ | = reaction rate constant (mol m$^{-3}$ Pa$^{-2}$ s$^{-1}$) |

$k_b$ = Boltzmann constant ($1.38 \times 10^{-23}$ J K$^{-1}$)
$K_e$ = equilibrium constant, unit depends on the actual reaction
$M$ = molecular mass (kg mol$^{-1}$)
$N_{sites}$ = standard-state number of binding sites per adsorbate.
$p$ = pressure (Pa, bar)
$Q$ = total partition function
$r$ = chemical reaction rate (mol m$^{-3}$ s$^{-1}$, mol m$^{-2}$ s$^{-1}$)
$R$ = gas constant (8.314 J mol$^{-1}$ K$^{-1}$)
$R_{ads}$ = total number of adsorbate reactants
$R_{tot}$ = total number of reactants participating in the reaction
$SA$ = surface area ratio (m$^2$ m$^{-3}$)
$\Delta S$ = entropy change of reaction (J mol$^{-1}$ K$^{-1}$)
$T$ = temperature (K)

*Greek symbols*

$\sigma_k$ = co-ordination number (mol m$^{-2}$)
$\theta_k$ = surface coverage (−)
$\gamma_j$ = sticking coefficient (−)
$\Gamma_{tot}$ = surface site density (mol m$^{-2}$)

*Abbreviations*

DFT = density functional theory
DIR = direct internal reforming
ER = external reforming
FC = fuel cell
g = gas phase
HCR = heterogeneous reaction mechanism
HT = high temperature
IIR = indirect internal reforming
IR = internal reforming
IT = intermediate temperature
LT = low temperature
PEMFC = proton exchange membrane fuel cell
SC = steam-to-carbon ratio
SOFC = solid oxide fuel cell
TPB = three-phase boundary
YSZ = yttria-stabilized zirconia

*Chemical*

* = surface species connected to the catalytic (Ni) active area
Ag = silver
Au = gold
$CeO_2$ = ceria
$CH_4$ = methane
CO = carbon monoxide
Co = cobalt
$CO_2$ = carbon dioxide
Cu = copper
$H_2$ = hydrogen
$H_2O$ = water
Ni = nickel
$O_2$ = oxygen
Pd = palladium
Pt = platinum
Ru = ruthenium
W = tungsten

*Facets on Ni*

br = bridge site, on Ni(111) and Ni(100)
fcc = face-centered cubic site, on Ni(111)
hcp = hexagonal-closed-packed site, on Ni(111)
hl = hollow site, on Ni(111)
lb = long-bridge site, on Ni(110)
sb = short bridge site, on Ni(110)
td = top-down site, on Ni(110)
tp = top site, on Ni(111) and Ni(100)
tu = top-up site, on Ni(110)
u2dl = hollow site formed by two top-layers Ni and one sub-layer Ni, on Ni(110)
uld2 = hollow site formed by one lop-layer Ni and two sub-layers Ni, on Ni(110)

## ACKNOWLEDGEMENTS

The financial support from the Swedish Research Council (VR, 621-2010-4581) and the European Research Council (ERC, 226238-MMFCs) is gratefully acknowledged.

## REFERENCES

1. Andersson M, Yuan J, Sundén B. Review on modeling development for multiscale chemical reactions coupled transport phenomena in solid oxide fuel cells. *Applied Energy* 2010; **87**:1461–1476. DOI: 10.1016/j.apenergy.2009.11.013.
2. Saxe M. Bringing fuel cells to reality and reality to fuel cells, *Doctoral Thesis*, Department of Chemical Sciences and Engineering, KTH-Royal Institute of Technology, Sweden, 2008.
3. Kemm M. Dynamic solid oxide fuel cell modelling for non-steady state simulation of system applications, *Doctoral Thesis*, Department of Energy Sciences, Lund University, Sweden, 2006.
4. Kakac S, Pramuanjaroenkij A, Zhou X. A review of numerical modeling of solid oxide fuel cells. *International Journal of Hydrogen Energy* 2007; **32**: 761–786.
5. Zhu H, Kee R, Janardhanan V, Deutschmann O, Goodwin D. Modeling elementary heterogeneous chemistry and electrochemistry in solid-oxide fuel cells. *Journal of Electrochemical Society* 2005; **152**: A2427–A2440.

6. Ni M, Leung MKH, Leung DYC. Ammonia-fed solid oxide fuel cells for power generation—a review. *International Journal of Energy Research* 2009; **33**:943–959.
7. Gooenough JB, Huang Y. Alternative anode materials for solid oxide fuel cells. *Journal of Power Sources* 2007; **173**:1–10.
8. Boder M, Dittmeyer R. Catalytic modification of conventional SOFC anodes with a view to reducing their activity for direct internal reforming of natural gas. *Journal of Power Sources* 2006; **155**:13–22.
9. Dokmaingam P, Assabumrungrat S, Soottitantawat A, Laosiripojana N. Modelling of tubular-designed solid oxide fuel cell with indirect internal reforming operation fed by different primary fuels. *Journal of Power Sources* 2010; **195**:69–78.
10. Clarke S, Dicks A, Pointon K, Smith T, Swann A. Catalytic aspects of the steam reforming of hydrocarbons in internal reforming fuel cells. *Catalysis Today* 1997; **38**:411–423.
11. Gross MD, Vohs JM, Gorte RJ. A study of thermal stability and methane tolerance of Cu-based SOFC anodes with electrodeposited Co. *Electrochimica Acta* 2007; **52**:1951–1957.
12. Sadykov VA, Mezentseva NV, Bunina RV, Alikina GM, Lukashevich AI, Kharlamova TS, Rogov VA, Zaikovskii VI, Ishchenko AV, Krieger TA, Bobrenok OF, Smirnova A, Irvine J, Vasylyev OD. Effect of complex oxide promoters and Pd on activity and stability of Ni/YSZ (ScSZ) cermets as anode materials for IT SOFC. *Catalysis Today* 2008; **131**:226–237.
13. Costa-Nunes O, Gorte RJ, Vohs JM. Comparison of the performance of Cu-CeO2-YSZ and Ni-YSZ composite SOFC anodes with H2, CO, and syngas. *Journal of Power Sources* 2005; **141**:241–249.
14. Gorte RJ. Ceria in catalysis: from automotive applications to the water-gas shift reaction. *AIChE Journal* 2010; **56**:1126–1135.
15. Aguiar P, Adjiman CS, Brandon NP. Anode-supported intermediate-temperature direct internal reforming solid oxide fuel Cell II. Model-based dynamic performance and control. *Journal of Power Sources* 2005; **147**:136–147.
16. Nagel F, Schildhauer T, Biollaz S, Stucki S. Charge, mass and heat transfer interactions in solid oxide fuel cells operated with different fuel gases—a sensitivity analysis. *Journal of Power Sources* 2008; **184**:129–142.
17. Danilov VA, Tade MO. A CFD-based model of a planar SOFC for anode flow field design. *International Journal of Hydrogen Energy* 2009; **34**: 8998–9006.
18. Klein J-M, Bultel Y, Georges S, Pons M. Modeling of a SOFC fuelled by methane: from direct internal reforming of gradual internal reforming. *Chemical Engineering Science* 2007; **62**:1636–1649.
19. Marrero-López D, Ruiz-Morales JC, Peña-Martínez J, Canales-Vázquez J, Núñez P. Preparation of thin layer material with macroporous microstructure for SOFC applications. *Journal of Solid State Chemistry* 2008; **181**:685–692.
20. Drescher I, Kinetik der Methane-Dampf-Reformierung (in German), kinetics of the methane steam reforming (title translated to English), *Doctoral Thesis*, Research Institute Jülich, Germany, 1999.
21. Yuan J, Huang Y, Sundén B, Wang WG. Analysis of parameter effects on chemical reaction coupled transport phenomena in SOFC anodes. *Heat and Mass Transfer* 2009; **45**:471–484.
22. Haberman BA, Young JB. Three-dimensional simulation of chemically reacting gas flows in the porous support structure of an integrated-planar solid oxide fuel cell. *International Journal of Heat and Mass Transfer* 2004; **47**:3617–3629.
23. Janardhanan VM, Deutschmann O. CFD analysis of a solid oxide fuel cell with internal reforming: coupled interactions of transport, heterogeneous catalysis and electrochemical processes. *Journal of Power Sources* 2006; **162**:1192–1202.
24. Hofmann P, Panopoulos KD, Fryda LE, Kakaras E. Comparison between two methane reforming models applied to a quasi-two-dimensional planar solid oxide fuel cell model. *Energy* 2008; **34**:2151–2157.
25. Wang L, Zhang H, Weng S. Modeling and simulation of solid oxide fuel cell based on the volume–resistance characteristic modeling technique. *Journal of Power Sources* 2008; **177**:579–589.
26. Bessler WG, Gewies S, Vogler M. A new framework for physically based modeling of solid oxide fuel cells. *Electrochimica Acta* 2007; **53**: 1782–1800.
27. King D, Strohm J, Wang X, Roh H-S, Wang C, Chin Y-H, Wang Y, Lin Y, Rozmiarek R, Singh P. Effect on nickel microstructure on methane steam reforming activity of Ni-YSZ cermet anode catalyst. *Journal of Catalysis* 2008; **258**:356–365.
28. Jones G, Jakobsen JG, Shim SS, Kleis J, Andersson MP, Rossmeisl J, Abild-Pedersen F, Bligaard T, Helveg S, Hinnemann B, Rostrup-Nielsen JR, Chorkendorff I, Sehested J, Jens K, Norskov JK. First principles calculations and experimental insight into methane steam reforming over transition metal catalysts. *Journal of Catalysis* 2008; **259**:147–160.

29. Molenda J, Swierczek K, Zajac W. Functional materials for IT-SOFC. *Journal of Power Sources* 2007; **173**:657–670.
30. Hecht E, Gupta G, Zhu H, Dean A, Kee R, Maier L, Deutschmann O. Methane reforming kinetics within a Ni-YSZ SOFC anode support. *Applied Catalysis A*: *General* 2005; **295**:40–51.
31. Blaylock D, Ogura WT, Green WH, Beran GJO. Computational investigation of thermochemistry and kinetics of steam methane reforming on Ni(111) under realistic conditions. *Journal of Physical Chemistry C* 2009; **113**:4898–4908.
32. Vang RT, Honkala K, Dahl S, Vestergaard EK, Schnadt J, Lægsgaard E, Clausen BS, Nørskov JK, Besenbacher F. Controlling the catalytic bond-breaking selectivity of Ni surfaces by step blocking. *Nature Materials* 2005; **4**:160–162.
33. Li C, Shi Y, Cai N. Elementary reaction kinetic model of an anode-supported solid oxide fuel cell fueled with syngas. *Journal of Power Sources* 2010; **195**:2266–2282.
34. Bengaard HS, Norskov JK, Sehested J, Clausen BS, Nielsen LP, Molenbroek AM, Rostrup-Nielsen JR. Steam reforming and graphite formation on Ni catalysts. *Journal of Catalysis* 2002; **209**:365–384.
35. Wang S-G, Cao D-B, Li Y-W, Wang J, Jiao H. $CH_4$ dissociation on Ni surfaces: density functional theory study. *Surface Science* 2006; **600**:3226–3234.
36. Stolze P. Microkinetic simulation of catalytic reactions. *Progress in Surface Science* 2000; **65**:65–150.
37. Janardhanan VM, Heuveline V, Deutschmann O. Performance analysis of a SOFC under direct internal reforming conditions. *Journal of Power Sources* 2007; **172**:296–307.
38. Yang Y, Du X, Yang L, Huang Y, Xian H. Investigation of methane steam reforming in planar porous support of solid oxide fuel cell. *Applied Thermal Engineering* 2009; **29**:1106–1113.

# Paper VII

This paper has been published in:

*Proceedings of the ASME 9th International Fuel Cell Science, Engineering & Technology Conference, Washington, DC, USA,*
ASME ESFuelCell2011-54006, 2011.

© 2011 ASME.

**Proceedings of the ASME 2011 Ninth International Fuel Cell Science, Engineering and Technology Conference**
**FuelCell2011**
**August 7-10, 2011, Washington, DC, USA**

# ESFuelCell2011-54006

# MODELING VALIDATION AND SIMULATION OF AN ANODE SUPPORTED SOFC INCLUDING MASS AND HEAT TRANSPORT, FLUID FLOW AND CHEMICAL REACTIONS

**Martin Andersson** **Jinliang Yuan** **Bengt Sundén**
Department of Energy Sciences, Faculty of Engineering,
Lund University, Box 118, 221 00 Lund, Sweden

**Ting Shuai Li** **Wei Guo Wang**
Division of Fuel Cell and Energy Technology, Ningbo Insitute of Material Technology & Engineering,
Chinese Academy of Sciences, 519 Zhuangshi Road, Ningbo, 315201, China

## ABSTRACT

Fuel cells are electrochemical devices that directly transform chemical energy into electricity, which are promising for future energy systems, since they are energy efficient and, when hydrogen is used as fuel, there are no direct emissions of greenhouse gases. The cell performance depends strongly on the material characteristics, the operating conditions and the chemical reactions that occur inside the cell. The chemical- and electrochemical reaction rates depend on temperature, material structure, catalytic activity, degradation and the partial pressures for the different species components. There is a lack of information, within the open literature, concerning the fundamentals behind these reactions. Experimental as well as modeling studies are needed to reduce this gap.

In this study experimental data collected from an intermediate temperature standard SOFC with $H_2/H_2O$ in the fuel stream are used to validate a previously developed computational fluid dynamics model based on the finite element method. The developed model is based on the governing equations of heat and mass transport and fluid flow, which are solved together with kinetic expressions for internal reforming reactions of hydrocarbon fuels and electrochemistry. This model is further updated to describe the experimental environment concerning cell design. Discussion on available active area for electrochemical reactions and average ionic transport distance from the anodic- to the cathodic three-phase boundary (TPB) are presented. The fuel inlet mole fractions are changed for the validated model to simulate a $H_2/H_2O$ mixture and 30 % pre-reformed natural gas.

*Keywords:* *SOFC, Modeling, Validation, Active Area, Ionic Transport Distance, COMSOL Multiphysics*

## INTRODUCTION AND PROBLEM STATEMENT

Fuel cells (FCs) are promising due to advantages of higher efficiency and lower emissions of $SO_X$, $NO_X$ and $CO_2$ than conventional power generation [1]. The solid oxide fuel cell (SOFC) is a high temperature fuel cell, which operates at 600-1000 ºC [2]. This temperature allows SOFCs to operate with different types of fuels from both fossil and renewable sources. It opens a way for an easier transition from conventional power generation with hydrocarbon based fuels to fuel cells with possibility for different fuels, especially SOFCs. Due to the increasing global awareness of that energy usage affects the environments, the interest of renewable energy has increased. SOFCs are generally more tolerant to contaminants than other fuel cells and the possibility to internally (as well as externally) reform the fuel make them interesting for renewable energy resources [1].

Numerical results of SOFC models are only approximations of real conditions and the validation is an important and necessary step in the development of reliable and accurate computational models. A range of validity can be established between the developed model and experimental

 Copyright © 2011 by ASME

data. When poor agreement is found between experiments and computations, the task is to understand where the errors come from, the modeling or the experimental work, for the objective to make better models or perform better experiments. It should be noted that CFD (computational fluid dynamics) models makes it possible to reduce the amount of experimental tests needed for cell development, only a limited amount of tests is required to validate the accuracy of the model. This means that the development cost can be decreased [3].

The aim of this paper is to validate a previously developed model, for an intermediate temperature anode-supported SOFC, with the scale of single unit-cell [2,5]. A NIMTE (Ningbo Insitute of Material Technology & Engineering) standard cell is used, as described in the next section.

The global reactions that take place within a SOFC, using hydrogen as fuel, can be described as: oxygen is reduced at the cathodic three-phase boundary (TPB), eqn. (1). The oxygen ions are transported through the electrolyte, but the electrons are prevented to passing through the electrolyte. The electrochemical reactions between hydrogen and oxygen ions, eqn. (2), take place in the anodic TPB [6-7].

$$\frac{1}{2}O_2 + 2e^- \Leftrightarrow O^{2-} \quad (1)$$

$$H_2 + O^{2-} \Leftrightarrow H_2O + 2e^- \quad (2)$$

When a fuel containing methane or carbon monoxide, i.e., the main components of natural gas is supplied, the reforming takes place within the anode. Methane is reformed with steam (eqn. (MSR, 3)). Carbon monoxide can be oxidized in the electrochemical reaction, and also react with water (eqn. (WGSR, 4)) [6]. The reactions described here are the overall ones, more detailed reaction mechanisms can be found in [7].

$$CH_4 + H_2O \Leftrightarrow 3H_2 + CO \quad \text{(MSR, 3)}$$

$$CO + H_2O \Leftrightarrow H_2 + CO_2 \quad \text{(WGSR, 4)}$$

## EXPERIMENTAL STUDY ON THE NIMTE STANDARD CELL

Experiments were carried out for a typical intermediate temperature anode-supported SOFC manufactured by Division of Fuel Cell and Energy Technology at NIMTE, and a SEM image is shown in Figure 1. The cell consists of a 400 μm thick Ni (40%) / YSZ (60%) anode substrate and an active anodic layer of 15 μm, where the electrochemical reactions occur. The electrolyte is a 10 μm thick layer of YSZ. The cathode consists of a 20 μm thick active layer of LSM/YSZ and a buffer layer of 50 μm LSM. Note that the anode active- and support layers have the same material composition, and the interface may not be very distinct. The major function of the anodic active layer is for the electrochemical reactions at TPBs, while the support layer should enable internal reforming reactions. It is a fact that a fine porous microstructure with a high surface area may lead to a decreased mechanical strength. The anode is often used as the mechanical support for the cell, i.e., this can be problematic. Since the active region in the anode where the electrochemical reactions take place does not extend too long from the anode–electrolyte interface, a graded porosity can be used to maximize the amount of TPB in the active region. The high mechanical strength is maintained for the rest of the anode which is used primarily as the cell support and for internal reforming reactions, when hydrocarbons are supplied as fuel [8].

The anodic porosity measured is 28 %. The fuel- and air flows are arranged as counter-flows. For the testing, a fuel flow rate of 800 sccm and an air flow rate of 2000 sccm are used. The single cell sample has dimensions of 5*5.8 $cm^2$, with an active area of 4*4 $cm^2$. An alumina testing house is used, where the cell temperature is kept constant during the tests, i.e., 750 °C for this case. Voltage probes are placed on the surface of the anode- and cathode support. The measurement data from the cell testing are presented and compared with our model predictions in the validation section.

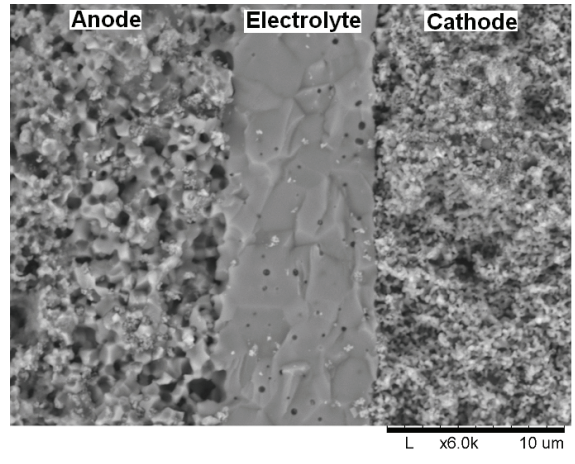


**Figure 1: A SEM image of a tested SOFC cross section, with (from left to right) anode active layer, electrolyte and cathode active layer.**

## MATHEMATICAL MODEL

A two-dimensional (2D) model for an anode-supported SOFC is developed and implemented in the commercial software, COMSOL Multiphysics (version 3.5a). Equations for momentum-, mass- and heat transport are solved simultaneously. As our model is defined in 2D only, i.e., the calculation is for a domain at the mid-plane of a unit cell. In reality the current density will be higher in the middle of the electrodes. The model is in this paper validated against a 1D


Copyright © 2011 by ASME

(flow direction) current density, i.e., the y-direction is neglected. The geometry is defined in Table 1 and a sketch of the investigated cell can be seen in Figure 2. The thickness of the electrodes, electrolyte and interconnect are updated (compared to our previous model [2,4-5]) to describe a standard intermediate temperature SOFC developed at NIMTE. Note that Figure 2 is not to scale.

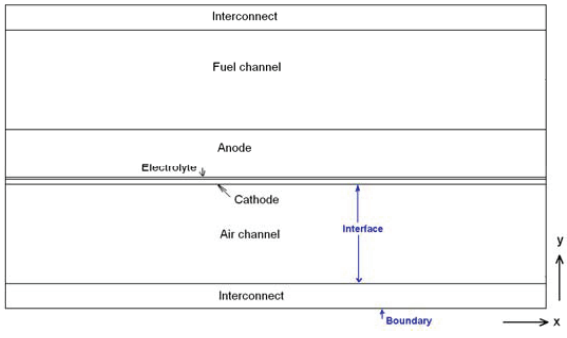


**Figure 2: Sketch of an anode-supported SOFC, not to scale.**

**Table 1: Cell geometry**

| Cell Component | Thickness (τ) |
|---|---|
| Cell length | 0.04 / 0.1 m [1] |
| Fuel channel height | 1 mm |
| Air channel height | 1 mm |
| Anode thickness | 415 μm [2] |
| Cathode thickness | 70 μm [3] |
| Electrolyte thickness | 10 μm |
| Interconnect thickness | 300 μm |

## Momentum transport

The gases flow inside the fuel cell components, such as in the air and fuel channels, and in the porous electrodes. The Darcy-Brinkman equation is introduced and solved for the gas flow in the fuel and air channels, and in the porous materials simultaneously [9-10]. The Darcy-Brinkman equation (eqn.(5)) is transformed into the standard Navier-Stokes equation when ($\kappa \to \infty$) and ($\varepsilon_p = 1$), and into the Darcy equation as ($Da \to 0$). $Da$ is the Darcy number. The derivation of Navier-Stokes equation and Darcy equation from Darcy-Brinkman equation can be found in [9].

$$\left(\frac{\mu}{\kappa}+\rho\cdot\nabla\mathrm{u}\right)\mathrm{u}-\nabla\left[-p+\frac{1}{\varepsilon_p}\left\{\mathbf{T}-\left(\frac{-2}{3}\cdot\mu\right)(\nabla\mathrm{u})\right\}\right]=\mathbf{F} \qquad (5)$$

where $\mathbf{F}$ is the volume force vector, $\kappa$ is the permeability of the porous medium, $\varepsilon_p$ the porosity, $\mu$ the dynamic viscosity, u the velocity vector and $\mathbf{T}$ the viscous stress tensor $\left(\mathbf{T}=\mu\left(\nabla\mathrm{u}+(\nabla\mathrm{u})^T\right)\right)$. The density and viscosity for the participating gas mixtures are dependent on local mole fraction and temperature, as described in [2,5]. The gas inlet velocities are defined as a laminar flow profile. The average velocities for the validation are based on the measured flow rates by taking into account the fuel- and oxygen utilization, respectively. The outlets are defined as pressure (1 atm).

## Mass transport

In the porous material, there are two kinds of mass diffusion mechanisms; molecular and Knudsen diffusions. The molecular diffusion (collisions between gas molecules) is significant in the case of large pores, whose size is much bigger than the mean free path of the diffusion gas molecules [11-12]. For a multi-component gas mixture system, the diffusion coefficients are calculated by the expressions in [13], based on bi-component coefficients of the gases. Knudsen diffusion is important when the mean free path is in the same order or bigger than the pore size, and molecules collide with the solid walls more often than with other molecules**.** At the SOFC operating temperature of around 1000 K, the mean free path of these gas components is about 0.2-0.5 μm. In this study, the radius of pores is assumed as 0.34 μm, which is of the same order as the mean free path. In other words the Knudsen diffusion should be included in the SOFC models. The Knudsen diffusion coefficient of the component $i$ with the component $j$ in a gas mixture, $D_{k,ij}$, is calculated based on the free molecule flow theory, as described in [14]:

$$D_{k,ij}=\frac{2}{3}\cdot r_e\cdot\sqrt{\frac{8\cdot\mathrm{R}\cdot T}{\pi\cdot M_{ij}}} \qquad (6)$$

where $r_e$ is the effective radius of the pores, R the universal gas constant. In the porous media, there is an increased diffusion length due to the tortuous paths of connected real pores, and the coefficients are usually corrected by porosity $\varepsilon$ and tortuosity $\tau$ [12,14]:

$$D_{eff,ij}=\frac{\varepsilon}{\tau}\cdot\left(\frac{D_{i,j}\cdot D_{k,ij}}{D_{i,j}+D_{k,ij}}\right) \qquad (7)$$

Equation (8) is used to describe the mass transport phenomena for each gas component inside the cell [10] and solved for the fuel- and air channels and the electrodes.

$$\nabla\left(-\rho\cdot w_i\sum_{n}^{n}D_{eff,ij}\cdot\nabla x_j+\left(x_j-w_j\right)\frac{\nabla p}{p}\cdot\mathrm{u}-D_i^T\cdot\frac{\nabla T}{T}\right)+\rho\cdot\mathrm{u}\cdot\nabla w_j=S_i \qquad (8)$$

where $w$ is the mass fraction, $x$ the molar fraction, $n$ the number of species and $D_i^T$ the thermal diffusion coefficient. $S_i$, the

[1] The cell length in the experimental cell used for validation is 4 cm. In the final model the cell length equals 10 cm.

[2] The anode consists of a 400 μm thick support layer and a 15 μm functional layer.

[3] The cathode comprises of a 50 μm thick support layer and a 20 μm functional layer.


Copyright © 2011 by ASME

source term by the chemical reactions, is defined for the internal reforming reactions.

Two approaches for defining the electrochemical reactions can be found in the literature, either as source terms in the governing equations [14-15] or as interface conditions defined at the electrode/electrolyte interfaces [16-17]. The later concept is employed in this study, because the thickness of the active layer is relatively thin [16-17]. This limitation will be released later in our future studies. The boundary conditions for the mass transport equation are defined as mass fractions for the gas channel inlets and the outlets are defined as convective flux.

### Heat transport

The temperature distribution is calculated separately for the gas phase (in air and fuel channels and electrodes) and for the solid phase (interconnects, electrodes and electrolyte). Heat is transferred between the phases at the channel walls and in the porous electrodes. The general heat conduction equation is used to calculate the temperature distribution for the solid materials, i.e., electrolyte, interconnect and electrodes [10]:

$$\nabla\left(-k_s \cdot \nabla T_s\right) = Q_s \tag{9}$$

where $k_s$ is the thermal conductivity of the solids, $T_s$ the solid temperature and $Q_s$ the heat source (heat transfer between the solid and gas phases, and heat generation due to ohmic polarization). Heat generation due to electrochemical reactions, mole fraction and activation polarization are simplified and defined as interface conditions, such as for the mass transport.

The temperature distribution for the gas mixtures in the fuel and air channels and in the porous electrodes is calculated as [10]:

$$\nabla\left(-k_g \cdot \nabla T_g\right) = Q_g - \rho_g \cdot c_{p,g} \cdot \mathrm{u} \cdot \nabla T_g \tag{10}$$

in which $c_{p,g}$ is the gas phase specific heat (dependent on temperature and mole fraction, as described in [5]), $T_g$ the temperature in the gas phase, and $Q_g$ the heat transfer between the gas and solid phases and the heat consumption due to internal reforming reactions.

The heat transfer between the gas- and solid phase, in the electrodes, depends on the temperature difference and the particle surface area ratio as [18]:

$$Q_g = h_v \cdot \left(T_g - T_s\right) = AV \cdot h_{s,g,por} \cdot \left(T_g - T_s\right) \tag{11}$$

in which $h_v$ is the volume heat transfer coefficient and $AV$ the surface area ratio, which is used for heat transfer between the solid- and gas phase. The heat transfer coefficient ($h_{s,g,por}$) is calculated as described in [19]. Note that the surface area for heat transfer is higher than that for chemical reactions, because not all the available surface is covered with active nickel catalyst. The specific heat and the thermal conductivity of the gas phase depend on the local temperature and the mole fraction, as described in [2,5].

The inlet gas temperature is defined by the operating temperature and the outlet is defined as a convective flux. The boundaries at the top and the bottom of the cell are defined by symmetries, since it is assumed that the cell is surrounded by other cells with the same temperature distribution. The heat flux between the electrodes/interconnect and gas channels are specified at two channel walls, located opposite to each other, with a constant Nusselt number (4.094) from [20], based on the fully developed flow for a square duct (aspect ratio is 1 for both channels).

### Electrochemical reactions

The charge transfer equations are not solved in this study, however the effects from ohmic-, concentration- and activation polarization losses are included in the equations for heat transport. The electromotive force (reversible open-circuit voltage, $E^{OCV}$) is determined by the difference in the thermodynamic potentials of the electrode reactions [21-23]. When a hydrogen-steam mixture is used as fuel, it can be calculated by the Nernst equation [23]:

$$E^{OCV} = E^0 - \frac{\mathrm{R} \cdot T}{2 \cdot \mathrm{F}} \cdot \ln\left(\frac{p_{H_2O}}{p_{H_2}\sqrt{p_{O_2}}}\right) \tag{12}$$

$$E^0 = 1.253 - 2.4516 \cdot 10^{-4} \cdot T \tag{13}$$

where $E^0$ is the temperature dependent open circuit voltage at standard pressure and $p_i$ the partial pressure, at the TPB, in atm.

It should be noted that eqns. (12)-(13) are only valid for pure hydrogen-steam mixtures. The electromotive force for only carbon monoxide or methane as fuel is presented in eqns. (14)-(15), respectively. $E^0$ for carbon monoxide decreases with increased temperature, but it is not temperature dependent for methane, due to a constant molar number of products and reactants [21-22]. In this study only eqns. (12)-(13) are used to calculate the electromotive force, i.e., it is assumed that methane and carbon monoxide reacts with steam and only $H_2$ participates in the electrochemical reactions. For this case of the mixture of $H_2$, $CH_4$ and CO presented the Nernst equation may not be applicable. Our aim is to release this limitation in future studies.

$$E_{CO}^{OCV} = E_{CO}^0 - \frac{\mathrm{R} \cdot T}{2 \cdot \mathrm{F}} \cdot \ln\left(\frac{p_{CO_2}}{p_{CO}\sqrt{p_{O_2}}}\right) \tag{14}$$

$$E_{CH_4}^{OCV} = E_{CH_4}^0 - \frac{\mathrm{R} \cdot T}{8 \cdot \mathrm{F}} \cdot \ln\left(\frac{p_{CO_2} \cdot {p_{H_2O}}^2}{p_{CH_4} \cdot {p_{O_2}}^2}\right) \tag{15}$$


Copyright © 2011 by ASME

Due to internal resistance and overpotential losses the actual voltage ($E$) becomes less than the open-circuit voltage. $E$ can be expressed as [23]:

$$E = E^{OCV} - \eta_{act} - \eta_{ohm} - \eta_{conc} \tag{16}$$

where $\eta$ are the respectively polarization losses.

Ohmic polarization occurs due to resistance of the flow of ions in the electrolyte and electrical resistance in the electrodes. The electrodes and electrolyte are heated due to this effect [23-24]:

$$Q_{ohm} = \frac{i \cdot \eta_{ohm}}{\tau} \tag{17}$$

$$\eta_{ohm} = \left( \frac{\tau_a}{\sigma_a} + \frac{\tau_{el}}{\sigma_{el}} + \frac{\tau_c}{\sigma_c} \right) \cdot i \tag{18}$$

where $\tau$ is the component thickness. The electronic/ionic conductivities ($\sigma$) are calculated as described in [23].

Heat generation due to the electrochemical reactions and concentration- and activation polarization losses are defined at the electrodes/electrolyte interfaces:

$$-\mathrm{n} \cdot \left(-k \nabla T\right)_{-} = q_0 \tag{19}$$

$$q_0 = q_r + q_{losses} = -i \cdot \left( \frac{T \cdot \Delta S_r}{n_e \cdot \mathrm{F}} + \eta_{act,e} + \eta_{conc,e} \right) \tag{20}$$

where $q_o$ is the total heat generation, $q_r$ the heat generated inside the cell due to change in enthalpy and $q_{losses}$ the heat generated due to concentration- and activation polarization losses inside the cell. The amount of heat generated due to electrochemical reactions can be calculated as [25]:

$$q_r = -T \cdot \Delta S_r \cdot \dot{n} = -\Delta S_r \frac{T \cdot i}{n_e \mathrm{F}} \tag{21}$$

$$\dot{n} = \frac{i}{n_e \mathrm{F}} \tag{22}$$

where $\dot{n}$ is the molar flux density [mol/(m$^2$s)] and $\Delta S_r$ entropy change of the reaction (-50.2 J/(K mol)), calculated from data in [26]. The concentration polarizations are specified as [23]:

$$\eta_{conc,a} = \frac{\mathrm{R}T}{n_{e,a} \mathrm{F}} \ln \left( \frac{p_{H_2O,TPB} \cdot p_{H_2,b}}{p_{H_2,TPB} \cdot p_{H_2O,b}} \right) \tag{23}$$

$$\eta_{conc,c} = \frac{\mathrm{R}T}{n_{e,c} \mathrm{F}} \ln \left( \frac{p_{O_2,b}}{p_{O_2,TPB}} \right) \tag{24}$$

where $p_{i,TPB}$ stands for the partial pressure at three phase boundary (TPB) and $p_{i,b}$ the partial pressure at the interface between gas channel and electrode. The chemical reactions involve energy barriers (i.e., activation polarization) which must be overcome by the reacting species.

The activation polarization can be considered as the extra potential needed to overcome the energy barrier of the rate-determining step to a value that the reaction proceeds at a desired rate [27]:

$$\eta_{act,e} = \frac{2\mathrm{R}T}{n_e \mathrm{F}} \sinh^{-1} \left( \frac{i_e}{2 \cdot i_{0,e}} \right) \tag{25}$$

$$i_{0,e} = \frac{\mathrm{R}T}{n_e F} k''_e \cdot \exp \left( \frac{-E_e}{\mathrm{R}T} \right) \tag{26}$$

where $i_{0,e}$ is the exchange current density. The pre-exponential factor ($k''$) is $2.35 \cdot 10^{11}$ $\Omega^{-1}$m$^{-2}$ for the cathode and $6.54 \cdot 10^{11}$ $\Omega^{-1}$m$^{-2}$ for the anode, respectively. The activation energy ($E$) is 137 kJ/mol for the cathode and 140 kJ/mol for the anode [23].

### Internal reforming reactions

Sufficient activity for the reforming reactions is provided inside the SOFC anode [28]. Reaction kinetics from [29] for the steam reforming, eqn. (MSR, 3), (an expression dependent on the active area to volume ratio) and from [30] for the water-gas shift, eqn. (WGSR, 4), reactions are used to calculate the reaction rates in this work. Other global kinetic models can be found in [31-32]. The catalytic methane steam reforming reaction occurs at the surfaces of the nickel catalysts and is specified as [29,33]:

$$r_r = AV \cdot \begin{pmatrix} 943 \cdot \exp\left( \frac{-225 \cdot 10^3}{R \cdot T} \right) \cdot p_{CH_4} p_{H_2O} \\ -7.74 \cdot 10^{-9} \cdot \exp\left( \frac{-1937}{R \cdot T} \right) \cdot p_{CO} p_{H_2}^3 \end{pmatrix} \tag{27}$$

where $p_i$ is the partial pressure of gas species $i$, $T$ the temperature, $r$ the reaction rate and $AV$ the active surface area to volume ratio. Equation (27) origins from the experiments performed at Research Centre Jülish, and the anode material consists of Ni−8YSZ substrate [33].

The range for the AV (related to catalytic kinetic reactions) varies in the literature between $1 \cdot 10^5$ m$^2$/m$^3$ [34] and $2.2 \cdot 10^6$ m$^2$/m$^3$ [29] for SOFC anodes. The measured specific surface area for Ni/YSZ material developed for SOFC anodes is $70 \cdot 10^6$ m$^2$/m$^3$ in [35]. Note that not all the surfaces are available for the catalytic reactions, due to the distribution of catalyst, unavailable pores and mass transfer limitations among others. An AV of $2.2 \cdot 10^6$ m$^2$/m$^3$, corresponding to 3.1 percent of the total Ni/YSZ specific area to volume ratio, is used in this work.


Copyright © 2011 by ASME

The trend for the FC development in recent years has been in the direction of employing smaller pores to get a larger AV.

Based on the global scheme for the anode, the expression for the catalyzed water-gas shift reforming reaction eqn. (WGSR, 4) in [30] has been selected in this study:

$$r_s = k_{sf} \cdot \left( p_{H_2O} p_{CO} - \frac{p_{H_2} p_{CO_2}}{K_{ps}} \right) \quad (28)$$

The rate constant ($k_{sf}$) and the equilibrium constant ($K_{ps}$) are temperature dependent expressions calculated from the experimental data, as described in [30].

The source terms $S_i$ (implemented in the Maxwell-Stefan equations for the gas species, eqn. (8)), due to the catalytical reforming reactions and the heat generation/consumption due to the reforming reactions, is specified in [4-5].

## VALIDATION

The electrochemical reactions, within the anode as well as within the cathode, occur at the TPBs, i.e., the sites which is connected to the ionic-, electronic- as well as gas phase. The reaction rate decreases drastically as the distance from the electrolyte/electrode interphase increases [16-17]. Two approaches are available to describe the electrochemical reactions in a CFD model, either as a source term (volume), or as an interphase condition (cross-sectional area, x- and z directions). When the concept with the source term is applied, the active thickness of the anode (h) and the active area for electrochemical reactions per volume (AV) need to be defined, as can be seen in Figure 3. For the concept with the interface condition, as applied in this study, the factor "f" is introduced. It is calculated by validating a theoretical model with the experiments. It can be described as the active area available for electrochemical reactions divided by the x-z cross sectional area. To compare the two concepts, f = AV • h.

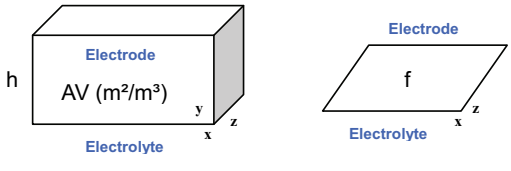


**Figure 3: Sketch over the concepts (source term, to the left, and interface condition, to the right) to define active area for the electrochemical reactions**

The test results from the NIMTE standard cell experiments are presented in Figure 4. The cell testing is conducted at 750 °C. It is assumed that the temperature is constant within the cell, since the cell is placed in a heated oven. In Figure 4, the geometric dimensions and the active area available for electrochemical reactions (Figure 3) are updated, in which f is 0.60. The agreement is not very good at high currents, where the model predicts higher currents compared to the experiments. It would be possible to validate the model to a constant voltage, and an accurate agreement with the experiments would be reached, however the purpose of this validation is to develop a model valid for a range of cell voltages.

The agreement between the modeling and experimental results is improved, when the ohmic losses are increased (by a factor of two) to consider that the electrochemical reactions take place in a region away from the electrode/electrolyte interface, i.e., to consider the distance that the oxygen ions need to be transported, from the air side to the fuel side of the cell. This transport distance factor is ignored in our previous model since the charge transport equations are not included. The agreement between the experiments and the model is improved, as seen in Figure 4 and f is 0.88. Note that the agreement is good when the voltage varies between 0.6 and 1.0 V.

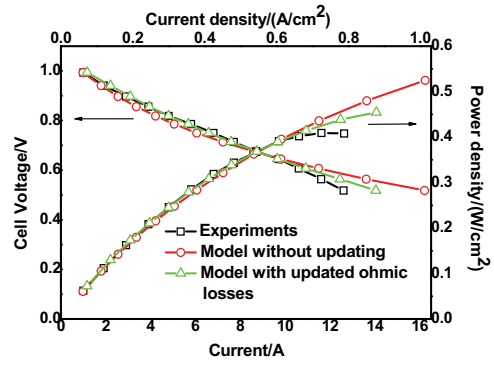


**Figure 4: Comparison between the measured and predicted performance of single SOFC cell.**

## SIMULATION RESULTS FROM VALIDATED MODEL

As a first step simulation results with a hydrogen-steam mixture ($x_{H2}$ : $x_{H2O}$ = 0.90 : 0.10) are presented, i.e., at the conditions similar to the experiments. A base condition is assumed that the cell voltage is 0.7 V, the oxygen utilization 18 % and the fuel utilization 70 %. Co-flow is applied in this model. The inlet temperature for the air and fuel flows are adjusted to make sure that the cell average temperature is 750 °C, the one used in the experimental work and for the validation.

The anode current density along the flow direction is presented in Figure 5. The current density increases along the main flow direction as the temperature rises and this increase eases as the mole fraction of hydrogen within the anode decreases.


Copyright © 2011 by ASME

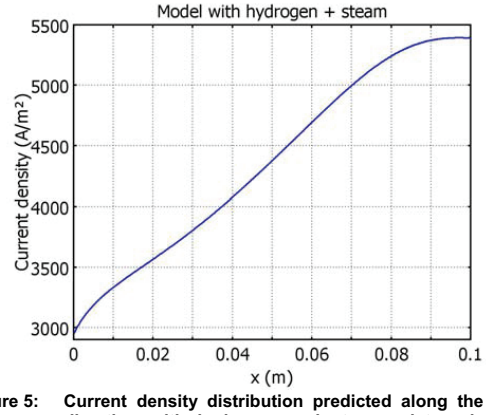


**Figure 5: Current density distribution predicted along the flow direction with hydrogen and steam mixture in fuel stream.**

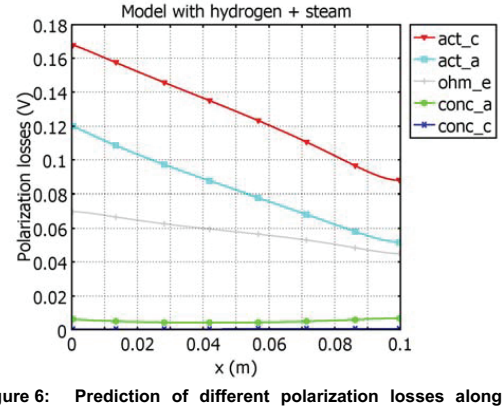


**Figure 6: Prediction of different polarization losses along the flow direction with hydrogen and steam mixture in fuel stream.**

A future step could adjust the active area, porosity and/or particle size along the flow direction to adequate the current density. The polarization losses within the cell are presented in Figure 6. The activation polarization loss corresponds to a majority of the losses and is larger in the cathode compared to the anode and it decreases as the temperature increases. Also the ohmic losses within the electrolyte decreases along the flow direction as the temperature increases. The polarization loss due to concentration differences across the anode is small for these conditions at the inlet and of the fuel composition.

The fuel inlet conditions are further modified as 30% pre-reformed natural gas, as defined by IEA and frequently found in the open literature, i.e, $x_{H2} : x_{CH4} : x_{CO} : x_{H2O} : x_{CO2} = 0.2626 : 0.171 : 0.0294 : 0.4934 : 0.0436$ [31]. The voltage, oxygen and fuel utilization and average temperature are the same as the case above.

The anode current density along the flow direction (Figure 7) increases initially as the temperature increases. It decreases as the mole fraction of hydrogen decreases. Note that the current density is significantly lower for this case with 30 % pre-reformed natural gas, compared to the case with a hydrogen-steam mixture (Figure 5).

The polarization losses are presented in Figure 8. It should be noted that the reversible open-circuit voltage is lower for the case with pre-reformed natural gas, since the mole fraction of hydrogen is lower and the mole fraction of steam is higher, compared to the hydrogen-steam mixture (Figure 6). This gives a lower total amount of polarization losses, since the cell voltage is defined to the same constant value (0.7 V). The same trend for the polarization losses are found, except for the anode concentration polarization, a lower mole fraction of hydrogen give higher losses, due to the fact that hydrogen is consumed in the electrochemical reactions.

The molar fraction of hydrogen (Figure 9) decreases due to the electrochemical reactions at the anode/electrolyte interface and increases due to the reforming reactions (MSR+WGSR) within the anode. The effect of Knudsen diffusion (collisions between gas molecules and the porous walls) is significant. Large mole fraction gradients can be observed through the cell (y-direction). Water (Figure 10) is generated due to the electrochemical reactions and consumed in the reforming reactions (MSR+WGSR). The mole fraction of water reaches its highest value at the anode/electrolyte interface and increases along the flow direction. Carbon monoxide (Figure 11) is generated in the eqn. (MSR, 3) and consumed in the water-gas shift reaction (WGSR). The mole fraction gradient through the anode (y-direction) is large and the smallest mole fraction is found at the TPB and decreasing along the flow direction. Carbon dioxide (Figure 12) is generated in the WGSR and transported through the anode and out of the cell with the exhaust flow stream. A distinct mole fraction gradient can be seen through the anode (y-direction). The highest mole fraction is found close to the gas outlet at the TPB.

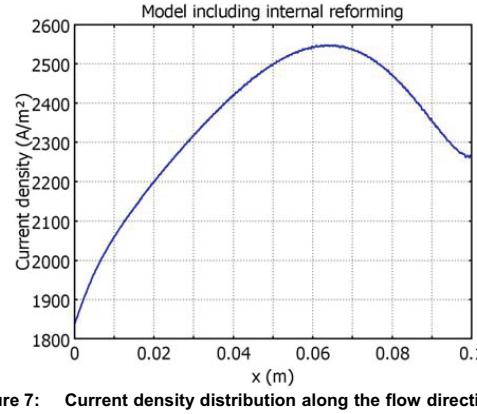


**Figure 7: Current density distribution along the flow direction for the model with natural gas in the fuel stream.**


Copyright © 2011 by ASME

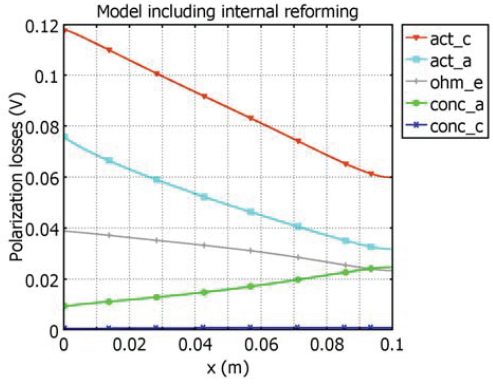


**Figure 8: Different polarization losses along the flow direction for the model with natural gas in the fuel stream.**

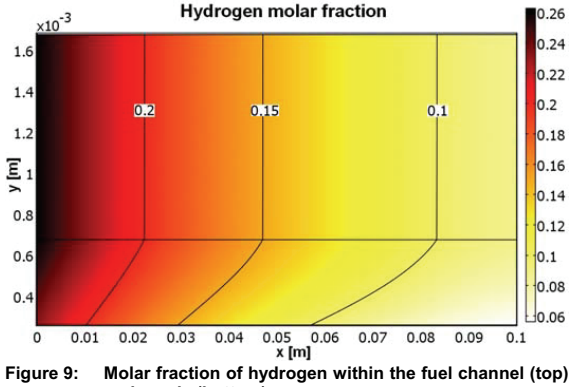


**Figure 9: Molar fraction of hydrogen within the fuel channel (top) and anode (bottom).**

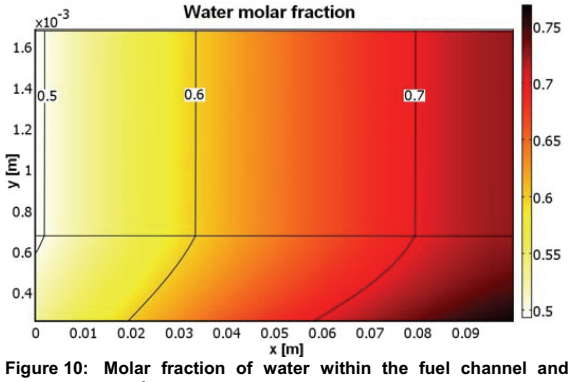


**Figure 10: Molar fraction of water within the fuel channel and anode.**

Methane (Figure 13) is consumed in the eqn. (MSR, 3). Also for methane a clear mole fraction gradient can be observed

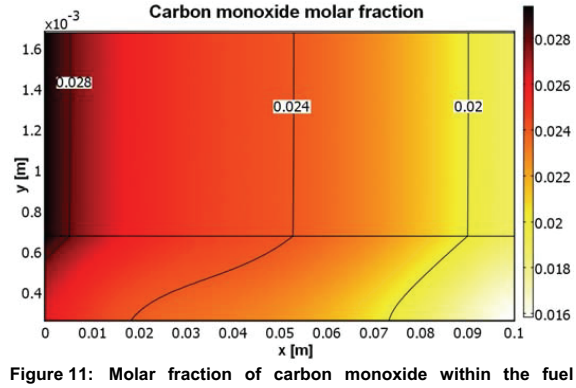


**Figure 11: Molar fraction of carbon monoxide within the fuel channel and anode.**

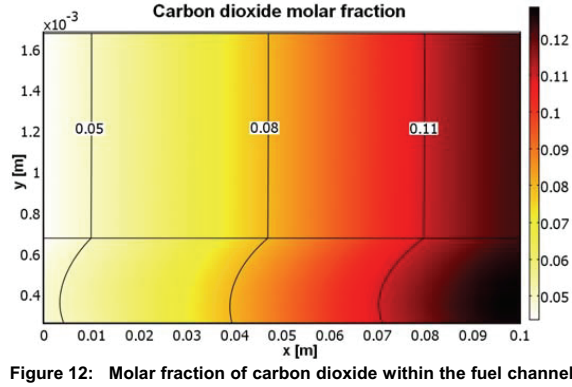


**Figure 12: Molar fraction of carbon dioxide within the fuel channel and anode.**

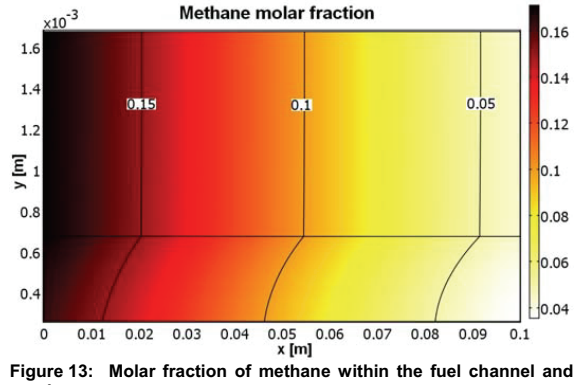


**Figure 13: Molar fraction of methane within the fuel channel and anode.**


Copyright © 2011 by ASME

through the anode, and the lowest mole fraction is at the TPB close to the gas outlet.

## CONCLUSIONS

In this study a SOFC CFD model (single cell anode-supported SOFC) is validated to experiments performed at NIMTE, Ningbo, China. The model contains equations for mass-, heat- and momentum transport, and chemical reactions covering internal reforming reactions and electrochemistry. The temperature distribution in the gas- and solid phase are calculated separately, according to the LTNE approach. An ionic transport distance factor to consider the distance that the oxygen ions need to be transported, from the air side to the fuel side of the cell, as well as a factor covering the active area available for electrochemical reactions divided with the x-z-cross sectional area is discussed.

The validated model is further applied to calculate the current density, molar fraction distributions as well as the different polarization losses for a case with a hydrogen-steam mixture, which is compared to a case with 30 % pre-reformed natural gas. It is concluded that the activation loss is the major of the polarization losses. The reversible open-circuit voltage is lower when pre-reformed natural gas is used as fuel, compared to the hydrogen-steam mixture.

Further development of SOFCs can enhance the transition from fossil fuels to renewable fuels. The choice of fuel for a commercial fuel cell system will depend on the available fuel infrastructure, complexity of system that is acceptable, environmental requirements to be considered and price for the different fuels etcetera.

## NOMENCLATURE

| | |
|---|---|
| $AV$ | active surface area to volume ratio, $m^2/m^3$ |
| $c_p$ | specific heat at constant pressure, J/kg/K |
| $Da$ | Darcy number, - |
| $D_{ij}$ | Maxwell-Stefan binary diffusion coefficient, $m^2/s$ |
| $D_{k,ij}$ | Knudsen diffusion coefficient, $m^2/s$ |
| $D_i^T$ | thermal diffusion coefficient, kg/(m·s) |
| $E$ | activation energy, kJ/mol, |
| $E^0$ | open circuit voltage at standard pressure, V |
| $E^{OCV}$ | reversible open circuit voltage, V |
| **F** | volume force vector, $N/m^3$ |
| F | Faraday constant, 96485 C/mol |
| $h_{s,g}$ | heat transfer coefficient, $W/(m^2K)$ |
| $h_v$ | volume heat transfer coefficient, $W/(m^3K)$ |
| $i$ | current density, $A/cm^2$ |
| $i_0$ | exchange current density, $A/cm^2$ |
| $k$ | thermal conductivity, W/m/K, reaction rate constant |
| $k''$ | pre-exponential factor, $1/(\Omega m^2)$ |
| $K$ | equilibrium constant |
| $M_j$ | molar mass of species j, kg/mol |
| $n_e$ | number of electrons transferred per reaction |
| $p$ | pressure, Pa, atm |
| $q$ | heat flux, $W/m^2$ |
| $Q$ | source term (heat), $W/m^3$ |
| R | gas constant, 8.314 J/mol/K |
| $r$ | reaction rate, $mol/(m^3s)$ |
| $S_i$ | source term (mass), $kg/(m^3s)$ |
| **T** | viscous stress tensor, $N/m^2$ |
| $T$ | temperature, K |
| u | velocity field, m/s |
| $w_i$ | mass fraction of species i, kg/kg |
| x, y, z | coordinate system, m |
| $x_j$ | molar fraction of species j, mol/mol |

### Greek symbols

| | |
|---|---|
| $\Delta S_r$ | entropy of reaction, J/K/mol |
| $\varepsilon_p$ | porosity, dimensionless |
| $\eta$ | over potential, V |
| $\kappa$ | permeability, $m^2$ |
| $\mu$ | dynamic viscosity, Pa s |
| $\rho$ | density, $kg/m^3$ |
| $\sigma$ | ionic/electronic conductivity, $\Omega^{-1}m^{-1}$ |
| $\tau$ | component thickness, m |

### Subscripts

| | |
|---|---|
| 0 | initial |
| a | anode |
| act | activation |
| b | electrode/gas channel interface |
| c | cathode |
| conc | concentration |
| e | electrode, $e \in \{a, c\}$ |
| eff | effective |
| el | electrolyte |
| g | gas phase |
| i | molecule i |
| j | molecule j |
| ohm | ohmic |
| por | porous media |
| s | solid phase |

### Abbreviations

| | |
|---|---|
| 2D | two-dimensional |
| FC | fuel cell |
| IEA | International Energy Agency |
| IT | intermediate temperature |
| MSR | methane steam reforming reaction |
| sccm | standard cubic centimeters per minute |
| SOFC | solid oxide fuel cell |
| TPB | three-phase boundary |
| WGSR | water-gas shift reforming reaction |

### Chemical

| | |
|---|---|
| $CH_4$ | methane |
| CO | carbon monoxide |
| $CO_2$ | carbon dioxide |


Copyright © 2011 by ASME

| | |
|---|---|
| $e^-$ | electron |
| $H_2$ | hydrogen |
| $H_2O$ | water |
| LSM | lanthanum strontium manganite |
| Ni | nickel |
| $O^{2-}$ | oxygen ion |
| $O_2$ | oxygen (gas phase molecule) |
| YSZ | yttria-stabilized zirconia |

## ACKNOWLEDGMENTS

The financial support from the Swedish Research Council (VR-621-2010-4581), the European Research Council (ERC-226238-MMFCs) and Swedish Research Links (348-2008-5999) is gratefully acknowledged. The Chinese Academy of Engineering (CAE) and the Royal Swedish Academy of Engineering Sciences (IVA) have supported the first author for a three month research visit to NIMTE, Chinese Academy of Sciences (CAS) in Ningbo, China.

## REFERENCES

[1] Staniforth J., Ormerod M., Implications for Using Biogas as a Fuel Source for Solid Oxide Fuel Cells: Internal Dry Reforming in a Small Tubular Solid Oxide Fuel Cell, *Catalysis Letter*, **81,** pp. 19-23, 2002.

[2] Andersson M., Yuan J., Sundén B., Wang W.G., LTNE Approach and Simulation for Anode-Supported SOFCs, ASME FuelCell2009-85054, Proceedings of 7th *International Fuel Cell Science, Engineering & Technology Conference*, Newport Beach, California, USA, 2009.

[3] Peksen M., Peters R., Blum L., Stolten D., Numerical Modelling and Experimental Validation of a Planar Type Pre-Reformer in SOFC Technology, *Int. J. Hyrogen Energy*, **34**, pp. 6425-6436, 2009.

[4] Andersson M., Paradis H., Yuan J., Sundén B., Modeling Analysis of Different Renewable Fuels in an Anode supported SOFC, *J. Fuel Cells*, **8**, 031013, 2011.

[5] Andersson M., 2009, SOFC Modeling Considering Mass and Heat Transfer, Fluid Flow with Internal Reforming Reactions, Licentiate Thesis, Department of Energy Sciences, Lund University, Sweden, ISSN 0282-1990.

[6] Ni M., Leung M.K.H., Leung D.Y.C., Micro-Scale Modeling of Solid Oxide Fuel Cells with Micro-structurally Grades Electrodes, *J. Power Sources*, **168**, pp. 369-378, 2007.

[7] Janardhanan V., Deutschmann O., CFD Analysis of a Solid Oxide Fuel Cell with Internal Reforming, *J. Power Sources,* **162**, pp. 1192-1202, 2006.

[8] Gorte R.J., Vohs J.M., Nanostructured Anodes for Solid Oxide Fuel Cells, *Current Opinion in Colloid & Interface Science,* **14,** pp. 236–244, 2009.

[9] Le Bars M., Worster M.G., Interfacial Conditions Between a Pure Fluid and a Porous Medium, Implications for Binary Alloy Solidification, *J. Fluid Mech.*, **550**, pp. 149-173, 2006.

[10] COMSOL Multiphysics 3.5 user guide, Stockholm, Sweden, 2008.

[11] Shi Y., Cai N., Li C., Numerical Modeling of an Anode-Supported SOFC Button Cell Considering Anodic Surface Diffusion, *J. Power Sources,* **164**, 639-648, 2007.

[12] Murzin D.Y., Salmi T., Catalytic Kinetics, Elsevier Science, 2005.

[13] Reid R.C., Prausnitz J.M., Poling B.E., The Properties of Gases & Liquids (fourth edition), McGraw-Hill Book Company, New York, USA, 1987.

[14] Yuan J., Huang Y., Sundén B., Wang W.G., Analysis of Parameter Effects on Chemical Coupled Transport Phenomena in SOFC Anodes, *Heat Mass Transfer*, **45**, pp. 471-484, 2009.

[15] Hussein M., Li X., Dincer I., Mathematical Modeling of Transport Phenomena in Porous SOFC Anodes, *Int. J. Thermal Sciences*, **46**, pp. 48-86, 2007.

[16] Suwanwarangkul R., Croiset E., Fowler M.W., Douglas P.L., Entchev E., Douglas M.A., Dusty-gas and Stefan-Maxwell Models to Predict the Concentration Overpotential of a SOFC Anode,, *J. Power Sources*, **122**, pp. 9-18, 2003.

[17] Tseronis K., Kookos I.K., Theodoropoulos C., Modeling Mass Transport in Solid Oxide Fuel Cell Anodes: A Case for a Multidimensional Dusty Gas-Based Model, *Chem. Eng. Sci.*, **63**, pp. 5626-5638, 2006.

[18] Chao C.H., Hwang A.J.J., Predictions of Phase Temperatures in a Porous Cathode of Polymer Electrolyte Fuel Cells using a Two-Equation Model,, *J. Power Sources*, **160**, pp. 1122-1130, 2006.

[19] Damm D.L., Fedorov A.G., Local Thermal Non-Equlibrium Effects in Porous Electrodes of the Hydrogen Fueled SOFC, *J. Power Sources*, **159**, pp. 1153-1157, 2006.

[20] Shah R.K., London A.L., Laminar Flow Forced Convection in Ducts. Academic Press, London, UK, 1978.

[21] Fuel Cell Handbook ($7^{th}$ edition), U.S. DoE, Morgantown, West Virginia, 2004.

[22] Winkler W., Nehter P., Thermodynamics of Fuel Cells, Fuel Cells and Hydrogen Energy, pp. 15-50, 2008.

[23] Patcharavorachot Y., Arpornwichanop A., Chuachuebsuk A., Electrochemical Study of a Planar Solid Oxide Fuel Cell: Role of Support Structures, *J. Power Sources*, **177**, pp. 254-261, 2008.

[24] Chan S.H., Low C.F., Ding O.L., Energy and Exergy Analysis of Simple Solid-Oxide Fuel-Cell Power Systems, *J. Power Sources*, **103**, pp. 188-200, 2002.

[25] Bove R. Ubertini S., Modeling Solid Oxide Fuel Cell Operation: Approaches, Techniques and Results, *J. Power Sources*, **159**, pp. 543-559, 2006.

[26] Bessler W.G., Warnatz J., Goodwin D.G., The Influence of Equilibrium Potential on the Hydrogen Oxidation Kinetics of SOFC Anodes, *Solid State Ionics*, **177**, pp. 3371-3383, 2007.

[27] Chan S.H., Khor K.A., Xia Z.T., A Complete Polarization Model of a Solid Oxide Fuel Cell and its Sensitivity to Change of Cell Component Thickness, *J. Power Sources*, **93**, pp.130-140, 2001.

 Copyright © 2011 by ASME

[28] Ferguson J.R., Fiard J.M., Herbin R., 1996, Three-dimensional Numerical Simulation for Various Geometries of Solid Oxide Fuel Cells, *J. Power Sources*, **58**, pp. 109-122.

[29] Klein J.-M., Bultel Y., Georges S., Pons M., 2007, Modeling of a SOFC Fuelled by Methane: From Direct Internal Reforming to Gradual Internal Reforming, *Chem. Eng. Sci.*, **62**, pp. 1636-1649.

[30] Haberman B.A., Young J.B., 2004, Three-Dimensional Simulation of Chemically Reacting Gas Flows in the Porous Support Structure of an Integrated-Plannar Solid Oxide Fuel Cell, *Int. J. Heat and Mass Transfer*, **47**, pp. 3617-3629.

[31] Nagel F., Schildhauer T., Biollaz S., Stucki S., 2008, Charge, Mass and Heat Transfer Interactions in Solid Oxide Fuel Cells Operated with Different Fuel Gases – A Sensitivity Analysis, *J. Power Sources,* **184**, pp. 129-142.

[32] Sanchez D., Chacartegui R.,Munoz A., Sanchez T., 2008, On the Effect of Methane Internal Reforming in Solid Oxide Fuel Cells, *Int. J. Hydrogen Energy*, **33**, pp. 1834-1844.

[33] Drescher I., Lehnert W., Meusinger J., 1998, Structural Properties of SOFC Anodes and Reactivity, *Electrochimica Acta*, **43**(19-20), pp 3059-3068.

[34] Danilov V., Tade M., 2009, A CFD-Based Model of a Planar SOFC for Anode Flow Field Design, *Int. J. Hydrogen Energy*, **34**, pp. 8998-9006.

[35] Marrero-López D., Ruiz-Morales J.C. Peña-Martínez J., Canales-Vázquez J., Núñez P., 2008, Preparation of Thin Layer Material with Macroporous Microstructure for SOFC Applications, *J. Solid State Chemistry*, **181**, pp. 685-692.


Copyright © 2011 by ASME

# Paper VIII

This paper has been accepted for publication in:

*Int. J. Heat and Mass Transfer*
DOI: 10.1016/j.ijheatmasstransfer.2011.10.032.

© 2011 Elsevier.

International Journal of Heat and Mass Transfer xxx (2011) xxx–xxx

Contents lists available at SciVerse ScienceDirect

International Journal of Heat and Mass Transfer

journal homepage: www.elsevier.com/locate/ijhmt

# SOFC modeling considering electrochemical reactions at the active three phase boundaries

Martin Andersson *, Jinliang Yuan, Bengt Sundén

*Department of Energy Sciences, Lund University, P.O. Box 118, SE-221 00 Lund, Sweden*

ARTICLE INFO

*Article history:*
Received 22 July 2011
Received in revised form 12 October 2011
Available online xxxx

*Keywords:*
SOFC
CFD modeling
Charge transport
Electrochemical reactions
TPB

ABSTRACT

It is expected that fuel cells will play a significant role in a future sustainable energy system, due to their high energy efficiency and the possibility to use renewable fuels. A fully coupled CFD model (COMSOL Multiphysics) is developed to describe an intermediate temperature SOFC single cell, including governing equations for heat, mass, momentum and charge transport as well as kinetics considering the internal reforming and the electrochemical reactions. The influences of the ion and electron transport resistance within the electrodes, as well as the impact of the operating temperature and the cooling effect by the surplus of air flow, are investigated. As revealed for the standard case in this study, 90% of the electrochemical reactions occur within 2.4 μm in the cathode and 6.2 μm in the anode away from the electrode/electrolyte interface. In spite of the thin electrochemical active zone, the difference to earlier models with the reactions defined at the electrode–electrolyte interfaces is significant. It is also found that 60% of the polarizations occur in the anode, 10% in the electrolyte and 30% in the cathode. It is predicted that the cell current density increases if the ionic transfer tortuosity in the electrodes is decreased, the air flow rate is decreased or the cell operating temperature is increased.

© 2011 Elsevier Ltd. All rights reserved.

## 1. Introduction

Fuel cells (FCs) are promising due to the advantages of higher efficiency and lower emissions of $SO_X$, $NO_X$ and $CO_2$, compared to conventional power generation devices. Solid oxide fuel cells (SOFCs) are generally more tolerant to contaminants than other fuel cells and the possibility to internally (as well as externally) reform the hydrocarbon fuels make them interesting for renewable energy resources [1]. Validated models are necessary to understand various transport processes and reactions for improving the cell performance. However, a validity range should be evaluated between the developed models and experimental data. It should be noted that CFD (computational fluid dynamics) models make it possible to reduce the amount of experimental tests needed for cell development, and only a limited amount of tests is then required to validate the accuracy of the models [2,3], as revealed in recent reviews on solid oxide fuel cell modeling and development by Wang et al. [4], Kakac et al. [5] and Andersson et al. [6].

The focus and the selected scale (system, stack, cell, component or functional materials) differ significantly between different models, as described in the open literature. For example, two approaches for defining the electrochemical reactions can be found in the literature, either as source terms in the governing equations [7] or as interface conditions defined at the electrode/electrolyte interfaces [8,9]. When the interface condition approach is applied the ionic resistance in the electrodes is neglected and the electrochemical reactions reduce to the interface conditions in the governing equations for heat, mass and momentum transport.

Shi and Xue [10] developed a 2D CFD model, including phenomena of heat, mass, ion, and electron transport as well as electrochemical reactions. Heterogeneous electrode properties were also taken into account by linear functionally graded porosity and various nonlinear distributions according to their cell design. Also Ni et al. [11] studied heterogeneous electrodes, but at the microscale level, and their model predicts the overpotential losses by capturing the coupled mass transfer and the electrochemical reactions. A 2D isothermal mechanistic model for a SOFC button cell was developed by Shi et al. [12], including polarization effects, molecular and Knudsen diffusion, gas transport, ionic and electronic conduction, surface diffusion of intermediate species and electrochemical reactions. Kanno et al. [13] and Iwai et al. [14] introduced a concept of different tortuosity factors for the transport of ions, electrons and gas-phase molecules, i.e., the real (average) transport distance for the ions and the electrons within the electrodes was evaluated and applied in the simulation. The tortuosity factors can be calculated, for example, by the lattice Boltzmann method.

An early polarization model, involving the Butler–Volmer equation, was developed by Chan et al. [15] in 2001 to lift the

* Corresponding author. Tel.: +46 46 222 49 08; fax: +46 46 222 47 17.
*E-mail addresses:* martin.andersson@energy.lth.se (M. Andersson), jinliang.yuan@energy.lth.se (J. Yuan), bengt.sunden@energy.lth.se (B. Sundén).

0017-9310/$ - see front matter © 2011 Elsevier Ltd. All rights reserved.
doi:10.1016/j.ijheatmasstransfer.2011.10.032

Please cite this article in press as: M. Andersson et al., SOFC modeling considering electrochemical reactions at the active three phase boundaries, Int. J. Heat Mass Transfer (2011), doi:10.1016/j.ijheatmasstransfer.2011.10.032

**Nomenclature**

| | |
|---|---|
| $A_{i,e}$ | pre-exponential factor, $1/(\Omega\,m^2)$ |
| $AV$ | active area to volume ratio, $m^2/m^3$ |
| $c_p$ | specific heat at constant pressure, J/(kg·K) |
| $D$ | diffusion coefficient, $m^2/s$ |
| $D_i^T$ | thermal diffusion coefficient, kg/(m s) |
| $E$ | actual voltage, V |
| $E_a$ | activation energy, J/mol |
| $E^0$ | ideal voltage before partial pressure consideration, V |
| $E_{eq}$ | equilibrium voltage, V |
| $E^{OCV}$ | ideal voltage after partial pressure consideration, V |
| $\mathbf{F}$ | volume force vector, $N/m^3$ |
| $F$ | Faraday constant, 96485 C/mol |
| $\Delta H$ | enthalpy change of reaction, J/mol |
| $i$ | current density, $A/m^2$ |
| $i_0$ | exchange current density, $A/m^2$ |
| $k$ | thermal conductivity, W/(m K) |
| $l_{ij}$ | characteristic length, Å |
| $M_j$ | molecular weight of species $j$, kg/mol, g/mol |
| $n_e$ | number of electrons transferred per reaction, – |
| $p$ | pressure, Pa or bar |
| $Q_h$ | source term (heat), $W/m^3$ |
| $r$ | reaction rate, $mol/(m^3\,s)$ |
| $r_e$ | pore radius, m |
| $R$ | gas constant, 8.314 J/(mol K) |
| $S_i$ | source term (mass), $kg/(m^3\,s)$ |
| $\Delta S$ | entropy change of reaction, J/(K mol) |
| $T$ | temperature, K |
| $\vec{u}$ | velocity vector, m/s |
| $V$ | volume fraction, – |
| $w_i$ | mass fraction of species $i$, kg/kg |
| x, y | coordinate system, m |
| $x_j$ | mole fraction of species $j$, mol/mol |

*Greek symbols*

| | |
|---|---|
| $\beta$ | transfer coefficient, – |
| $\varepsilon$ | porosity, – |
| $\eta$ | over potential (or polarization), V |
| $\phi$ | potential, V |
| $\kappa$ | permeability, $m^2$ |
| $\mu$ | dynamic viscosity, Pa s |
| $\rho$ | density, $kg/m^3$ |
| $\sigma$ | ionic/electronic conductivity, $\Omega^{-1}\,m^{-1}$ |
| $\tau$ | tortuosity, – |
| $\Psi$ | viscous stress tensor, $N/m^2$ |
| $\Omega_D$ | diffusion collision integral, – |

*Subscripts*

| | |
|---|---|
| $a$ | anode |
| $act$ | activation |
| $c$ | cathode |
| $conc$ | concentration |
| $e$ | electrode, e ∈ {a,c}, electrochemical |
| $el$ | electrolyte |
| $eff$ | effective (average) |
| $g$ | gas-phase |
| $i$ | (gas-phase) molecule $i$ |
| $j$ | (gas-phase) molecule $j$ |
| $K$ | Knudsen diffusion |
| $l$ | electrolyte material |
| $ohm$ | ohmic |
| $ref$ | (internal) reforming reactions |
| $s$ | solid-phase, electrode material |

*Abbreviations*

| | |
|---|---|
| CFD | computational fluid dynamics |
| FC | fuel cell |
| IEA | International Energy Agency |
| LTE | local temperature equilibrium |
| LTNE | local temperature non equilibrium |
| NIMTE | Ningbo Institute of Material Technology & Engineering |
| sccm | standard cubic centimeters per minute |
| SOFC | solid oxide fuel cell |
| TPB | three-phase boundary |

*Chemical*

| | |
|---|---|
| $CH_4$ | methane |
| CO | carbon monoxide |
| $CO_2$ | carbon dioxide |
| $e^-$ | elektron |
| $H_2$ | hydrogen |
| $H_2O$ | water |
| LSM | strontium doped lanthanum manganite |
| Ni | nickel |
| $N_2$ | nitrogen |
| $O_2$ | oxygen |
| YSZ | yttria-stabilized zirconia |

limitations of the Tafel equation. Patcharavorachot et al. [16] developed a pure electrochemical reaction model, i.e., neglecting the mass and the heat transport, the fluid flow and the internal reforming reactions. Bessler et al. [17] studied electrochemistry of SOFC anodes, focusing on the nickel/yttria-stabilized zirconia (Ni/YSZ) materials, and the electrochemical reactions were described in multi-steps in the Arrhenius form. The Butler–Volmer equations are often used to describe the overpotential/current density relationship, however, a more detailed approach was developed by Bessler et al. [18] to include an elementary-kinetic multistep description of electrochemistry with coupled surface chemistry, charge-transfer reactions, physical representation of the electric potential steps and other transport phenomena. On the other hand, in the above mentioned models, only pure hydrogen is considered for the electrochemical reactions at the fuel side, i.e., it is assumed that carbon monoxide and methane are fully reformed to hydrogen before the electrochemical reactions occur. This limitation was released by Hajimolana et al. [19].

SOFCs enable internal reforming of hydrocarbons with relatively short carbon chains. A review on the reaction kinetics was given by Mogensen et al. in [20] and it is concluded that there are large differences in the published kinetic expressions for the steam reforming reactions. Vakouftsi et al. [21] developed a 3D CFD model for a planar SOFC, including mass transport, electrochemical reactions and global scale kinetic expressions for the methane steam reforming reaction (MSR) and the water–gas shift reaction (WGSR) in the Arrhenius form. Nagel et al. [22] studied the relations between mass, heat and charge transport within SOFCs, using a finite volume method, considering different fuel gas compositions. A dynamic SOFC model, including mass and energy balances, electrochemical reactions and internal reforming reaction kinetics, was developed by Aguiar et al. [23] to study load step-changes. A heterogeneous chemistry multistep mechanism

Please cite this article in press as: M. Andersson et al., SOFC modeling considering electrochemical reactions at the active three phase boundaries, Int. J. Heat Mass Transfer (2011), doi:10.1016/j.ijheatmasstransfer.2011.10.032

for the steam reforming reaction of methane and carbon monoxide in the SOFC anode was presented by Janardhanan and Deutschmann in [24], including 21 reversible reaction steps for 6 gas-phase species and 12 surface-adsorbed species.

The aim of this work is to investigate the influence of the ion and electron transport resistance within the anode and cathode by solving a fully coupled CFD model including the governing equations for heat, mass, momentum, ion and electron transport occurring in an intermediate temperature SOFC single cell. The advances compared to our previous work [3,6,8] include the addition of the governing equations for the ion transport (in YSZ) and the electron transport (in Ni or LSM), i.e., the current density distributions are calculated from local conditions (2D) throughout the cell, instead of just defining an average value (0D) [3,25] or with a 1D approach at the electrode-electrolyte interface [7]. Further advances are made for the electrochemical reactions, which are defined as source terms instead of interface conditions (as in [3,7,25]) concerning mass, heat, momentum, ion and electron governing transport equations. The uniqueness of this paper by the macroscale approach, is the implementation of the tortuosity factors and the material specific volume fractions for the ion and electron transport within the electrodes, combined with a complete set of simultaneously solved governing equations with the global internal reforming reaction kinetics. Other operating parameters are kept constant, while the inlet temperature, the air flow rate or the ionic tortuosity are varied for conducting a parameter study.

## 2. Mathematical model and major assumptions

A 2D CFD model for an anode-supported SOFC is developed and implemented in the commercial software, COMSOL Multiphysics (version 4.1). The equations for momentum, mass, ion, electron and heat transport are solved simultaneously. The geometry, based on a standard cell (Fig. 1) by Ningbo Institute of Material Technology and Engineering (NIMTE), China, is defined in Table 1, and a sketch of the investigated cell can be seen in Fig. 2. Note that Fig. 2 is not to scale.

The NIMTE standard cell consists of a 400 μm thick Ni (40%)/YSZ (60%) anode substrate and additionally an active anodic layer of 15 μm, where the electrochemical reactions occur. The electrolyte is a 10 μm thick layer of YSZ. The cathode consists of a 20 μm thick active layer of LSM/YSZ and a buffer layer of 50 μm LSM. Note that the anode active- and support layers have the same material composition, and the interface may not be very distinct, compared to the cathode, where the active and support layers have different compositions. It is a fact that a fine porous microstructure with a high surface area may lead to a decreased mechanical strength. Because the TPB does not extend too far from the anode–electrolyte interface, a graded porosity can be used to maximize the length of the TPBs in the active region. The high mechanical strength is maintained for the rest of the anode which is used primarily as the cell support and for the internal reforming reactions, when hydrocarbons are supplied as the fuels.

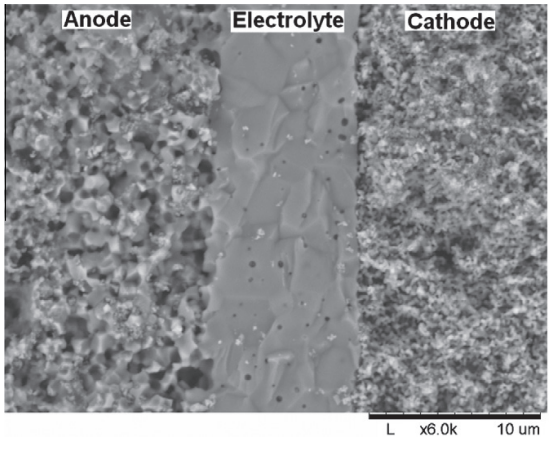


**Fig. 1.** A SEM image of a tested SOFC cross-section, with (from left to right) anode active layer, electrolyte and cathode active layer.

**Table 1**
Cell geometry.

| Cell component | Thickness |
|---|---|
| Cell length | 0.1 m |
| Fuel channel height | 1 mm |
| Air channel height | 1 mm |
| Anode thickness | 415 μm |
| Cathode thickness | 70 μm |
| Electrolyte thickness | 10 μm |
| Interconnect thickness | 300 μm |

### 2.1. Heat transport

A local temperature equilibrium (LTE) approach is applied, i.e., the temperature is assumed to be locally the same for the gas- and solid-phases (within the electrodes). Previously a local temperature non-equilibrium (LTNE) approach have been applied [3]. However, the temperature difference between the solid- and gas-phases within the electrodes is found to be negligible. The governing equation for the temperature distribution is in this work defined as:

$$\rho_g \cdot c_{p,g} \cdot \vec{u} \cdot \nabla T = \nabla \bullet (k_{eff} \nabla T) + Q_h \tag{1}$$

where $Q_h$ is the heat generation/consumption (source term defined in Eqs. (8)–(11)), $T$ the temperature, $k_{eff}$ the effective thermal conductivity, $c_p$ the gas-phase specific heat, $\rho_g$ the gas-phase density and $\vec{u}$ the velocity vector. The overall governing equation for the heat transport, Eq. (1), reduces to pure heat conduction in the electrolyte and the interconnector. The effective value of the thermal conductivity in the porous electrodes can be specified as [7]:

$$k_{eff} = \varepsilon \cdot k_g + (1 - \varepsilon) \cdot k_s \tag{2}$$

where $\varepsilon$ is the porosity, *eff* means effective, *s* solid and *g* gas-phase. The conductivity, the specific heat and the density for the solid materials in the different subdomains are outlined in Table 2.

The specific heat for each gas species and the gas mixture is calculated as [26]:

$$c_{p,i} = \sum_{k=1}^{7} a_k \cdot \left(\frac{T}{1000}\right)^k \tag{3}$$

$$c_{p,g} = \sum_i x_i \cdot c_{p,i} \tag{4}$$

where $a_k$ is the species dependent parameter (extracted from [26]) and "$k$" stands for the number of parameters involved in the specific heat calculation. The thermal conductivity for each species of the gas-phase, as well as for the gas mixture, is defined as [26]:

$$k_i = 0.01 \cdot \sum_{k=1}^{7} c_k \cdot \left(\frac{T}{1000}\right)^k \tag{5}$$

$$k_g = \sum_i x_i \cdot k_i \tag{6}$$

where $c_k$ is the species dependent parameter (extracted from [26]) and "$k$" stands for the number of parameters in the thermal conductivity evaluation.

Please cite this article in press as: M. Andersson et al., SOFC modeling considering electrochemical reactions at the active three phase boundaries, Int. J. Heat Mass Transfer (2011), doi:10.1016/j.ijheatmasstransfer.2011.10.032

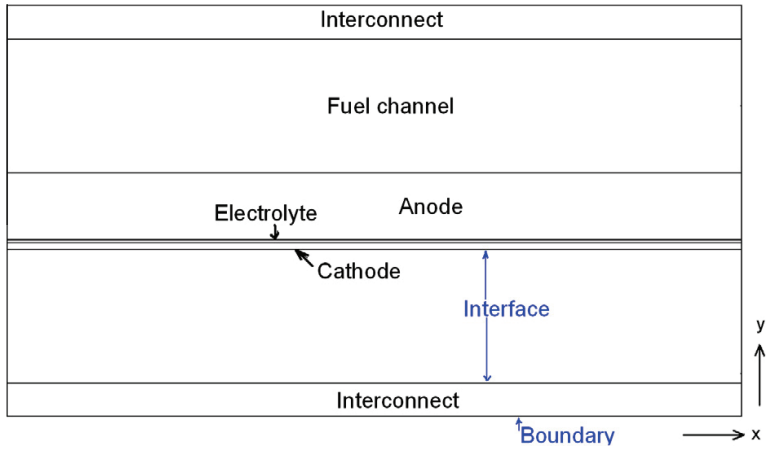


**Fig. 2.** Sketch of an anode-supported SOFC (not to scale).

**Table 2**
Material parameters.

| | Thermal conductivity [5] (W/m/K) | Specific heat [24] (J/kg/K) | Density [24] (kg/m$^3$) |
|---|---|---|---|
| Anode (Ni/YSZ) | 11 | 450 | 3310 |
| Cathode (LSM/YSZ) | 6 | 430 | 3030 |
| Electrolyte (YSZ) | 2.7 | 470 | 5160 |
| Interconnect (stainless steel) | 20 | 550 | 3030 |

The heat consumption/generation due to the internal reforming reactions in the anode is implemented by:

$$Q_{h,ref} = r_{ref} \cdot \Delta H_{ref} \tag{7}$$

where $r_{ref}$ is the reaction rate (in mol/m$^3$ s) and $\Delta H_{ref}$ the enthalpy change of the reforming reactions. The reaction rate will be introduced in Section 2.6. The heat generation due to the activation and the concentration polarizations is defined as [19,25]:

$$Q_{h,act+conc} = -(\eta_{act,e} + \eta_{conc,e}) \cdot i \cdot AV_e \tag{8}$$

where $i$ is the ion current density, $\eta_{act}$ the activation polarization (defined in Section 2.4), $\eta_{conc}$ the concentration polarization (defined in Section 2.4), $AV_e$ the electrochemical active area to volume ratio. The $AV_e$ is for the anode and the cathode are calculated by comparing the model versus experimental data as described in Section 3. The heat generation due to the ohmic polarization is calculated as [19,25]:

$$Q_{h,ohm} = \frac{i_s^2}{\sigma_s} + \frac{i_l^2}{\sigma_l} \tag{9}$$

where $\sigma$ is the conductivity, $i$ the current density, $l$ the index for the electrolyte material (YSZ) and $s$ for the electrode materials (Ni or LSM). This is an extension and improvement compared to our previous models [3,8,25], where the ion transport in the YSZ within the anode and the cathode is neglected. The expressions for ionic and electronic conductivity are introduced in Section 2.4.

The amount of the heat generated (within the cathode side)/consumed (within the anode side) due to the change of entropy in the electrochemical reactions is defined as [25]:

$$Q_{h,e} = -\Delta S_e \frac{T \cdot i \cdot AV_e}{n_e \cdot F} \tag{10}$$

where $F$ is the Faraday constant, $n_e$ the number of electrons transferred per reaction and $\Delta S_e$ the entropy change of the electrochemical reactions, calculated from the data in [27] for the anode and the cathode TPBs, respectively. The inlet gas temperature is defined by the operating temperature (1010 K) and the outlet is defined as a convective flux. The boundaries at the top and the bottom of the cell are defined as symmetry conditions, because it is assumed that the cell is surrounded by other ones with the identical temperature distribution.

### 2.2. Mass transport

In the porous material, there are two kinds of mass diffusion mechanisms: molecular and Knudsen diffusions. The molecular diffusion (collisions between gas molecules) is significant in the case of large pores, whose size is much bigger than the mean free path of the diffusion gas molecules [12,28]. The Knudsen diffusion is important when the mean free path is of the same order or bigger than the pore size, and the molecules collide with the solid walls more often than with other molecules. At the SOFC operating temperature, the mean free path of these gas components is about 0.2–0.5 μm. In this study, the radius of pores is assumed as 0.34 μm, which is of the same order as the mean free path, i.e., the Knudsen diffusion should be included in the SOFC models. The Knudsen diffusion coefficient of the gas component $i$ with the component $j$ in a gas mixture, $D_{K,ij}$, is calculated based on the free molecule flow theory [7]:

$$D_{K,ij} = \frac{2}{3} \cdot r_e \cdot \sqrt{\frac{8 \cdot R \cdot T}{\pi \cdot M_{ij}}} \tag{11}$$

$$M_{ij} = \frac{2}{\frac{1}{M_i} + \frac{1}{M_j}} \tag{12}$$

where $r_e$ is the effective radius of the pores and $R$ the universal gas constant.

The ordinary diffusion coefficients ($D_{ij}$), for a multi-component gas mixture system, are calculated as [29]:

$$D_{ij} = \frac{2.66 \cdot 10^{-8} \cdot T^{3/2}}{p \cdot M_{ij}^{1/2} \cdot l_{ij}^2 \cdot \Omega_D} \tag{13}$$

where $l_{ij}$ is the characteristic length and $\Omega_D$ the diffusion collision integral, as defined in [29]. In the porous media, there is a reduced void volume and an increased diffusion length based on the local

Please cite this article in press as: M. Andersson et al., SOFC modeling considering electrochemical reactions at the active three phase boundaries, Int. J. Heat Mass Transfer (2011), doi:10.1016/j.ijheatmasstransfer.2011.10.032

microstructures, and the coefficients are usually corrected by porosity and tortuosity, respectively [7,28]:

$$D_{eff,ij} = \frac{\varepsilon}{\tau} \cdot r_e \cdot \left( \frac{D_{ij} \cdot D_{K,ij}}{D_{ij} + D_{K,ij}} \right) \tag{14}$$

Eq. (15) is used to describe the mass transport phenomena for each gas component inside the cell and solved for the fuel- and air channels and the electrodes.

$$-\nabla\left(\rho \cdot w_i \sum^{n} D_{eff,ij} \cdot \nabla x_j\right) + \left((x_j - w_j)\frac{\nabla p}{p} \cdot (\nabla \bullet \vec{u})\right) - \nabla\left(D_i^T \cdot \frac{\nabla T}{T}\right) + \rho \cdot \vec{u} \cdot \nabla w_j = S_i \tag{15}$$

where $w$ is the mass fraction, $x$ the mole fraction, $n$ the number of species and $D_i^T$ the thermal diffusion coefficient. $S_i$, the source term by the chemical reactions, is defined for the internal reforming (within the anode) and the electrochemical reactions (within the anode and cathode). The fuel inlet conditions (mole fractions) are defined as 30% pre-reformed natural gas, as defined by International Energy Agency (IEA): $x_{H2}$:$x_{CH4}$:$x_{CO}$:$x_{H2O}$:$x_{CO2}$ = 0.2626:0.171:0.0294:0.4934:0.0436 [22]. The air inlet is defined as air, including oxygen and nitrogen. The fuel and gas channel outlets are defined as convective fluxes.

### 2.3. Momentum transport

The Darcy–Brinkman equation, Eq. (16), is introduced and solved for the gas flow in the fuel and air channels, and in the porous materials simultaneously [3]:

$$\left(\frac{\mu}{\kappa} + \rho \cdot \nabla \bullet \vec{u}\right) \cdot \vec{u} - \nabla\left[-p + \frac{1}{\varepsilon}\left\{\Psi - \left(\frac{-2}{3} \cdot \mu\right)(\nabla \bullet \vec{u})\right\}\right] = \mathbf{F} \tag{16}$$

where $\mathbf{F}$ is the volume force vector, $\kappa$ the permeability of the porous medium ($1.76 \cdot 10^{-11}$ m$^2$ [5]), $\varepsilon_p$ the porosity, $\mu$ the dynamic viscosity and $\psi$ the viscous stress tensor. The densities for the participating gases are calculated, according to the ideal gas law [30]:

$$\rho_g = \frac{p \cdot \sum x_i \cdot M_i}{R \cdot T} \tag{17}$$

The dynamic viscosity for each participating species in the gas-phase, as well as for the gas mixture, is evaluated as [26]:

$$\mu_i = \sum_{k=1}^{7} b_k \cdot \left(\frac{T}{1000}\right)^k \tag{18}$$

$$\mu_g = \sum_i x_i \cdot \mu_i \tag{19}$$

where $b_k$ is the species dependent parameter and "$k$" stands for the number of species dependent parameters in the viscosity equation.

The gas inlets velocities are defined as a laminar flow profile, and the average values are based on the fuel- and oxygen utilization, i.e., 70% and 18%, respectively, for the standard case in this study. At the outlets the pressure (1 atm) is fixed.

### 2.4. Ion and electron transport

The potential difference between the anode and the cathode current collectors corresponds to the total cell voltage. The governing equations for the ion and electron transport are implemented as:

$$i_l = -\sigma_l \nabla \phi_l \tag{20}$$

$$i_s = -\sigma_s \nabla \phi_s \tag{21}$$

where $\phi$ is the potential. The potential at the anode current collector is set to zero and the potential at the cathode current collector is set as the cell operating voltage (0.7 V in this study). All other boundaries and interfaces are electrically insulated. The electronic conductivities in the anode ($\sigma_{s,a}$) and the cathode ($\sigma_{s,c}$), and the ionic conductivity in the electrolyte material ($\sigma_{l,el}$) are calculated as [19,31]:

$$\sigma_{s,c} = \frac{4.2 \cdot 10^7}{T} \cdot \exp\left(\frac{-1200}{T}\right) \tag{22}$$

$$\sigma_{l,el} = 33.4 \cdot 10^3 \cdot \exp\left(\frac{-10300}{T}\right) \tag{23}$$

$$\sigma_{s,a} = \frac{9.5 \cdot 10^7}{T} \cdot \exp\left(\frac{-1150}{T}\right) \tag{24}$$

The actual lengths that the ions and electrons are transported in the electrodes increase due to the real/functional material compositions and their micro structures. This is accounted for by using the structure-dependent tortuosity factors and the volume fractions. The effective ionic- and electronic conductivity in the electrodes are defined as [13]:

$$\sigma_{l,e,\mathrm{YSZ}} = \sigma_{l,e} \cdot \frac{V_{\mathrm{YSZ},e}}{\tau_{\mathrm{YSZ},e}} \tag{25}$$

$$\sigma_{s,a,\mathrm{Ni}} = \sigma_{s,a} \cdot \frac{V_{\mathrm{Ni},a}}{\tau_{\mathrm{Ni},a}} \tag{26}$$

$$\sigma_{s,c,\mathrm{LSM}} = \sigma_{s,c} \cdot \frac{V_{\mathrm{LSM},c}}{\tau_{\mathrm{LSM},c}} \tag{27}$$

where $\tau$ is the tortuosity factor and $V$ the volume fraction for the specific materials. Note that the ionic conductivity in the electrodes was not included in our previous work [3,6,8,25]. To the authors knowledge this is the first cell scale SOFC model, which considers the microstructure effects by including the tortuosity factors and material volume fractions for the ion and electron transport within the anode and the cathode. As found later in this work, the influence is significant on both the ion transport from the electrolyte to the active TPB areas and the ohmic polarization. Kanno et al. calculated (by LBM) the tortuosity factors and the values between 7 and 17 are found for Ni and between 6 and 14 for YSZ, respectively [13]. Iwai et al. evaluated the tortuosity factors statistically with the random walk process of nonsorbing particles as well as with the LBM method, and values between 6.91 and 29.46 were found for Ni and between 9.84 and 27.89 for YSZ, respectively, depending slightly on the evaluation methods, but mostly on the direction ($x$, $y$ and $z$) [14]. Vivet et al. [32] calculated the tortuosity in the range of 3.04 and 6.24 for Ni, and between 1.79 and 2.10 for YSZ, respectively. For this work the dimensionless parameters for the electrode structure stated in Table 3 are employed. It is worthwhile to note that there is an negligible transport of oxygen ions in Ni material and of electrons in YSZ material [32], and therefore it is not considered in this study.

The activation polarizations ($\eta_{act}$) are defined as [30]:

$$\eta_{act,a} = \phi_s - \phi_l - E_{eq,a} \tag{28}$$

$$\eta_{act,c} = \phi_s - \phi_l - E_{eq,c} \tag{29}$$

where the index $a$ stands for the anode, $c$ for the cathode, and $E_{eq}$ is the equilibrium voltage.

The electromotive force (ideal voltage after partial pressure consideration, $E^{OCV}$) is determined by the difference in thermodynamic

**Table 3**
Charge transport properties for the porous electrodes.

| | $V_{\mathrm{YSZ}}$ | $V_{\mathrm{Ni}}$ or $V_{\mathrm{LSM}}$ | $\varepsilon_e$ | $\tau_s$ | $\tau_l$ |
|---|---|---|---|---|---|
| Anode | 0.42 | 0.28 | 0.30 | 10 | 10 |
| Cathode | 0.42 | 0.28 | 0.30 | 10 | 10 |

Please cite this article in press as: M. Andersson et al., SOFC modeling considering electrochemical reactions at the active three phase boundaries, Int. J. Heat Mass Transfer (2011), doi:10.1016/j.ijheatmasstransfer.2011.10.032

potentials of the electrode reactions [16,33]. Due to the internal resistance and the polarizations, the actual voltage ($E$) becomes less than the ideal voltage, and is expressed as [16]:

$$E = E^{OCV} - \eta_{act} - \eta_{ohm} - \eta_{conc} \tag{30}$$

The concentration polarizations ($\eta_{conc}$) are calculated by [3,34]:

$$\eta_{conc,a} = \frac{R \cdot T}{n_{e,a} \cdot F} \cdot \ln\left(\frac{p_{H_2O,TPB} \cdot p_{H_2,b}}{p_{H_2,TPB} \cdot p_{H_2O,b}}\right) \tag{31}$$

$$\eta_{conc,c} = \frac{R \cdot T}{n_{e,c} \cdot F} \cdot \ln\left(\frac{p_{O_2,b}}{p_{O_2,TPB}}\right) \tag{32}$$

where the index TPB stands for the three phase boundary (TPB) and $b$ for the boundary between the gas channel and the electrode.

When a hydrogen–steam mixture is used as fuel, the electromotive force can be calculated by the standard Nernst equation [16]:

$$E^{OCV}_{H_2/O_2} = E^0_{H_2/O_2} - \frac{R \cdot T}{2 \cdot F} \cdot \ln\left(\frac{p_{H_2O}}{p_{H_2}\sqrt{p_{O_2}}}\right) \tag{33}$$

$$E^0_{H_2/O_2} = 1.253 - 2.4516 \cdot 10^{-4} \cdot T \tag{34}$$

where $E^0$ is the ideal voltage before partial pressure consideration and $p_i$ the partial pressure, at the TPB, in atm. It should be noted that Eqs. (33) and (34) are only valid for pure hydrogen–steam mixtures. The electromotive force for only carbon monoxide or methane as fuel is presented in Eqs. (35) and (36), respectively. $E^0$ for carbon monoxide decreases with increased temperature, but it is not temperature dependent for methane, due to a constant molar number of the products and the reactants [33,35]. In this study only Eqs. (33) and (34) are used to calculate the electromotive force, i.e., it is assumed that methane and carbon monoxide fully react with steam and only $H_2$ participates in the electrochemical reactions. For the case of pre-reformed natural gas ($H_2/H_2O/CH_4/CO/CO_2$) present, the Nernst equation may not be the most applicable expression. Our aim is to release this limitation in our future studies

$$E^{OCV}_{CO/O_2} = E^0_{CO/O_2} - \frac{R \cdot T}{2 \cdot F} \cdot \ln\left(\frac{p_{CO_2}}{p_{CO}\sqrt{p_{O_2}}}\right) \tag{35}$$

$$E^{OCV}_{CH_4/O_2} = E^0_{CH_4/O_2} - \frac{R \cdot T}{8 \cdot F} \cdot \ln\left(\frac{p_{CO_2} \cdot p^2_{H_2O}}{p_{CH_4} \cdot p^2_{O_2}}\right) \tag{36}$$

### 2.5. Electrochemical reactions

The cathodic electrochemical reactions within an SOFC can be described globally as: oxygen is reduced at the cathodic TPB, Eq. (37). The oxygen ions are transported through the YSZ (in the electrodes and electrolyte), and the electrons are prevented to pass through the electrolyte. The anodic electrochemical reactions between hydrogen and oxygen ions, Eq. (38), take place at the anodic TPB [11,24]

$$\frac{1}{2}O_2 + 2e^- \Longleftrightarrow O^{2-} \tag{37}$$

$$H_2 + O^{2-} \Longleftrightarrow H_2O + 2e^- \tag{38}$$

The current density (per unit volume) in the anode as well as in the cathode is calculated, by the Butler–Volmer equation [15]:

$$i_e = AV_e \cdot i_{0,e}\left\{\exp\left(\beta \cdot \frac{n_e \cdot F \cdot \eta_{act,e}}{R \cdot T}\right) - \exp\left(-(1-\beta)\frac{n_e \cdot F \cdot \eta_{act,e}}{R \cdot T}\right)\right\} \tag{39}$$

where $\beta$ is the transfer coefficient, usually assumed to be 0.5. The Butler–Volmer equation can then be expressed as [15]:

$$i_e = AV_e \cdot 2 \cdot i_{0,e} \cdot \sinh\left(\frac{n_e \cdot F \cdot \eta_{act,e}}{2 \cdot R \cdot T}\right) \tag{40}$$

where $i_{0,e}$ is the exchange current density. The exchange current density is calculated by [16,23]:

$$i_{0,e} = \frac{R \cdot T}{n_e \cdot F} A_{i,e} \cdot \exp\left(\frac{-E_{a,e}}{R \cdot T}\right) \tag{41}$$

where the pre-exponential factor ($A_{i,e}$) is $2.35 \cdot 10^{11}\ \Omega^{-1}\ m^{-2}$ for the cathode and $6.54 \cdot 10^{11}\ \Omega^{-1}\ m^{-2}$ for the anode, respectively. An activation energy ($E_{a,e}$) of 137 kJ/mol for the cathode and 140 kJ/mol for the anode are used by Patcharavorachot et al. [16] and Aguiar et al. [23], while the values between 110 and 140 kJ/mol for the anode and 130 and 190 kJ/mol for the cathode appear in various work available in the open literature [5,36–40].

The influence of different polarizations/potentials varies depending on cell structure/design and operating conditions. The different potentials vary along the flow direction and they are affected by, for example, the local temperature as well as the local hydrogen and oxygen concentrations. It is concluded in Sohn et al. [41] that for an intermediate temperature SOFC with a co-flow configuration, the activation polarization is dominant in the cathode near the fuel and air inlets, and in the anode near the outlets. Also the counter-flow configuration was investigated and the variation in the cathodic activation overpotential is smaller, compared to the co-flow configuration. For both the co-flow and the counter-flow configurations the activation polarization in the cathode is dominating at lower current densities and the activation polarization in the anode at higher ones. The dominance of the anode activation at high current densities is explained by the depletion of hydrogen according to a high fuel utilization [41]. The influence from the ionic polarization depends mostly on the ionic transfer conductivity within the electrolyte and the electrolyte thickness, where a decreased thickness means a decreased ohmic polarization. When the concentration of fuel or oxidant reaches zero at the TPB, the concentration overpotentials increase and the voltage reaches zero [23]. Bessler et al. [18] studied an electrode-supported SOFC and found that the polarizations within the cathode are small compared to the one within the anode or electrolyte. Xiao et al. [42] investigated an anode supported SOFC with a Ni/YSZ anode and a LSM cathode and concluded that the cathodic polarization decreases with increasing temperature, but the anodic polarization increases with increasing temperature, partly due to an increase in the resistivity of the Ni/YSZ cermet connected to the drop in metallic conductivity as the temperature increases.

### 2.6. Internal reforming reactions

When a fuel containing methane and carbon monoxide is supplied, the reforming reactions take place within the anode. Methane reacts with steam in the MSR (Eq. (42)). Carbon monoxide can be oxidized in the electrochemical reaction, but mainly reacts further with water in the WGSR (Eq. (43)) [11]. The reaction kinetics from Klein et al. [43] for the MSR (an Arrhenius form expression dependent on the active area to volume ratio) and from Haberman and Young [44] for the WGSR are used to calculate the reaction rates in this work. The range for the $AV_{MSR}$ (related to catalytic kinetic reactions) varies in the literature between $1 \cdot 10^5\ m^2/m^3$ [45] and $2.2 \cdot 10^6\ m^2/m^3$ [43] for SOFC anodes. The $AV_{MSR}$ can be compared to the total measured surface area to volume ratio ($AV_{tot}$), that reaches $1 \cdot 10^8\ m^2/m^3$ for Ni/YSZ material developed for SOFC anodes (with a nickel content of 50%, surface area of 27 $m^2/g$ and a power density of 3.75 $g/cm^3$ [46]), while the surface area in Mamak et al. [47] reaches 162–112 $m^2/g$ for the materials containing 13-40 mole-% Ni or NiO. Note that not all the surfaces are available for the

Please cite this article in press as: M. Andersson et al., SOFC modeling considering electrochemical reactions at the active three phase boundaries, Int. J. Heat Mass Transfer (2011), doi:10.1016/j.ijheatmasstransfer.2011.10.032

catalytic reactions, due to the distribution of catalyst, dead pores and mass transfer limitations among others. An $AV_{MSR}$ of $7{\cdot}10^6$ $m^2/m^3$ is applied in this work, which corresponds to 7 percent of the total Ni/YSZ surface area to volume ratio, when compared to the $AV_{tot}$ in Aruna et al. [46]. The relatively high $AV_{MSR}$ compensates partly for a high activation energy in the Klein kinetics

$$CH_4 + H_2O \Longleftrightarrow 3H_2 + CO \quad (MSR) \tag{42}$$

$$CO + H_2O \Longleftrightarrow H_2 + CO_2 \quad (WGSR) \tag{43}$$

## 3. Solution methods and model validation

All the equations, defined in Section 2 above, are numerically solved in COMSOL Multiphysics (version 4.1:0.185) using a stationary segregated solver with a direct (MUMPS) linear solver system. The governing equations are segregated in 5 different groups: 1. velocity field, pressure distribution and pressure corrections, 2. temperature distribution, 3. ion and electron distribution, 4. mass fraction distribution on the air side ($O_2/N_2$) and 5. mass fraction distribution on the fuel side ($H_2/H_2O/CH_4/CO/CO_2$). The segregated solver solves for 2,290,000 degrees of freedom and the tolerance is defined to 0.001 for each segregated group. Grid independence was achieved at 716,000 elements, after which the change in the maximum temperature is less than 0.08%, in the maximum air velocity less than 0.36%, in the minimum oxygen mole fraction less than 0.25%, in the minimum hydrogen mole fraction less than 0.35%, in the methane conversion less than 0.22% and in the maximum current density at the inlet less than 0.07% (compared with the predictions by 1,180,000 elements). It should be noted that the mesh is finest close to the electrode-electrolyte interface and coarsest for the air- and fuel channels and for the interconnects. The reason for such a mesh arrangement is mainly due to the charge transport and the electrochemical reactions (affecting the governing transport equations for ion, electron, mass, heat and momentum) appearing only in the regions close to the electrode-electrolyte interface.

Numerical results of any SOFC models are only approximations of real conditions and the validation is an important and necessary step in the development of reliable and accurate computational models. A range of validity should be evaluated and can be established by comparing the developed model with experimental data. It should be noted that CFD models make it possible to reduce the amount of experimental tests needed for cell development. Our model relies on the experimental data from a standard cell developed at Ningbo Institute of Material Technology & Engineering (NIMTE) in China. The air- and fuel flow rates and operating temperature are implemented in the model directly for the validation, and the $AV_e$ for the anode and the cathode is calculated/validated from the voltage/current density measurements. For the experiments a fuel flow rate of 800 sccm (standard cubic centimeters per minute) and an air flow rate of 2000 sccm are used. The single cell sample has dimensions of $5 \cdot 5.8\ cm^2$, with an active area of $4 \cdot 4\ cm^2$. An alumina testing house is used, where the cell temperature is kept constant during the tests, i.e., 750 °C for this case. Voltage probes are placed on the surface of the anode- and cathode support. The NIMTE standard cell design/structure is defined in Section 2 above. Note that the validation performed covers overall phenomena occurring at the macroscale only. An extended validation including transport and reaction phenomena occurring in the microscale is also interesting for future studies.

## 4. Results and discussion

The predicted temperature increases along the *x*-direction (the main flow direction), as seen in Fig. 3. Heat is generated due to the change of entropy by the electrochemical reactions in the cathode, as well as the activation-, ohmic- and concentration polarizations within the anode, electrolyte and cathode, and the WGSR in the anode. On the other hand heat is consumed in the anode, due to change of entropy by the electrochemical reactions and the MSR. The predicted temperature difference in the *y*-direction inside the air channel occurs because the convective heat flux is bigger compared to the fuel channel due to the relatively larger mass flow rate.

The ion current density along the *y*-direction (i.e., the cross-section normal to the flow direction) is shown in Fig. 4 at the inlet and the outlet. For the standard case the current density distribution shows a similar behavior at the inlet and outlet, because the decrease of ideal voltage due to the temperature increase and the consumption of fuel and oxygen is compensated by an increase of the current density due to an increased cell temperature. It can be seen that the current density gradients are steeper on the cathode side, than on the anode side. In this model the volume fractions of the solid materials and pores as well as the tortuosities are accounted for, as defined in Eqs. (30)–(32), to better describe realistic transport distances for the ions and the electrons within the anode and the cathode. This means an increased ion/electron resistance, compared to the simplified models. In this study the electrochemical reactions are implemented as source terms in the governing equations for heat, mass, momentum, ion and electron transport. The electrochemical reactions occur within a few micro meters close to the electrode-electrolyte interface, as shown in Fig. 4. It is found that the electrochemical reaction zone is only 2.4 μm deep in the active region from the interface in the cathode, and 6.2 μm in the anode. This zone is defined as where the ion current density is higher than 300 $A/m^2$, i.e., around 10% of the maximum value at the inlet for the standard case. The depth of the electrochemically active reaction zones is quite small compared to the designed active layers with a finer structure and a higher surface area than the ones in the buffer layers. As mentioned above, for the NIMTE standard cell, the thickness of the active layers is 20 μm and 15 μm for the cathode and the anode, respectively.

The potential distribution is shown in Fig. 5 for the positions close to the inlets and the outlets. The ideal voltage decreases along the flow direction due to both the temperature increase and the consumption of fuel and oxygen. It can be revealed from Fig. 5 that around 60% of the polarizations occur in the anode, 10% in the electrolyte and 30% in the cathode, i.e., any efforts to improve the fuel cell performance should be focused on decreasing the anode activation polarization, or improving the volumetric current density on the anode side. These findings are different compared to our previous predictions [3,6,8], where the electrochemical reactions are defined at the electrode-electrolyte interfaces only and the cathodic activation polarization dominates over the anodic one. This difference might be particular due to a larger active TPB $AV_e$ applied on the cathodic side ($2.6 \cdot 10^6\ m^2/m^3$) compared to the anode side ($1.3 \cdot 10^5\ m^2/m^3$). This makes the electrochemical reaction zone thinner within the cathode. As a result the current density per active TPB area is lower at the cathode–electrolyte interface (1400 $A/m^2$ as a maximum value), compared to the anode–electrolyte interface (9400 $A/m^2$). This gives lower polarizations on the cathode side, but the current density per unity volume is higher on the cathode side ($3.6 \cdot 10^9\ A/m^3$ as a maximum value at the cathode-electrolyte interface), compared to the anode side ($1.5 \cdot 10^9\ A/m^3$).

The activation polarizations along the flow direction (*x*-direction) within the anode and the cathode for the standard case are shown in Fig. 6. There can be compared with the ones predicted by our previous model [8] in Fig. 7, where the electrochemical reactions as well as the activation and concentration polarization

Please cite this article in press as: M. Andersson et al., SOFC modeling considering electrochemical reactions at the active three phase boundaries, Int. J. Heat Mass Transfer (2011), doi:10.1016/j.ijheatmasstransfer.2011.10.032

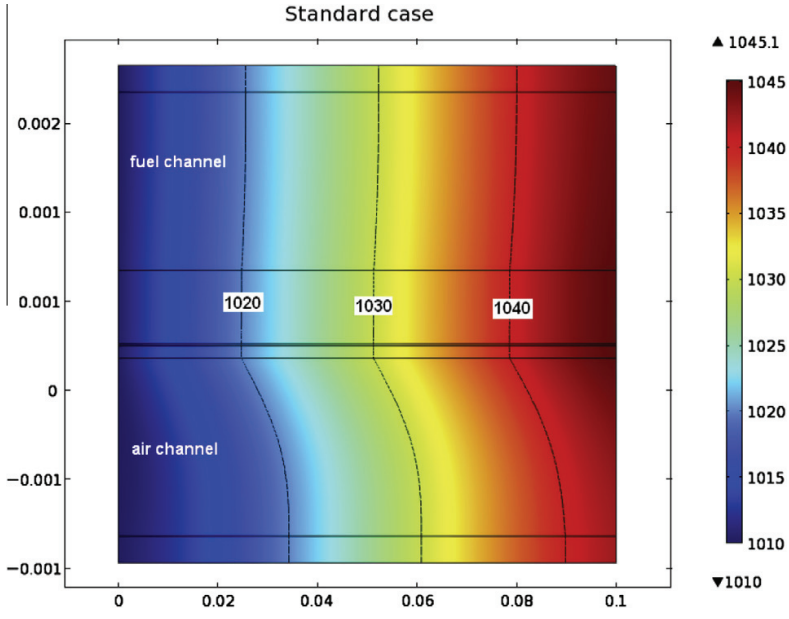


**Fig. 3.** Temperature distribution (K) along the main flow direction of a singe cell.

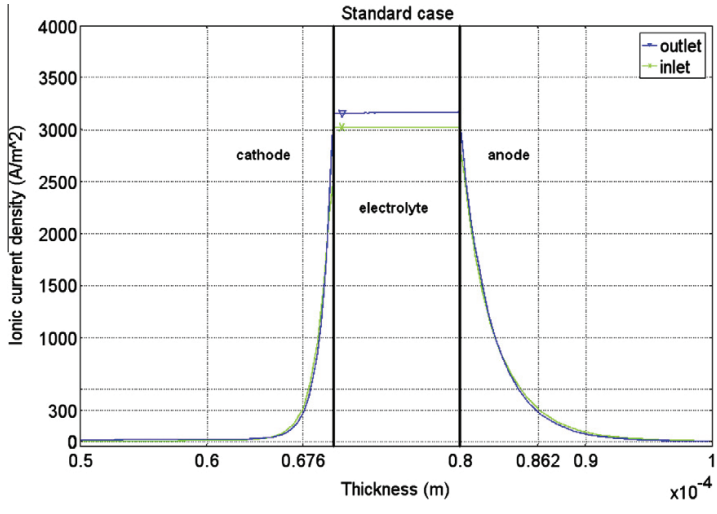


**Fig. 4.** Profile of ion current density (A/m$^2$). Note that for the anode and cathode, only the parts (20 μm) closest to the electrolyte interface are highlighted in the figure, and the "zero" is assigned at the air channel-cathode interface.

are defined as interface conditions at the electrode-electrolyte interfaces. For both models, the cell voltage is defined to 0.7 V and a similar trend is found, i.e., the total polarization decreases along the flow direction (as the temperature increases) and the activation polarizations dominate, compared to the ohmic and the concentration polarizations. However, in this study, the activation polarization on the anode side is bigger than that on the cathode side, partially due to the different $AV_e$ implemented, as discussed in the previous paragraph. This effect was not included when the electrochemical reactions were defined at the electrode-electrolyte interface in our earlier models [3,6,8]. The activation polarization distributions represent the biggest difference between the models. It should be noted that in the current model, the current density per active area and the activation polarization is highest at the electrode-electrolyte interface and decreases rapidly within the electrodes as the distance to the interface increases. On the other hand, the ohmic polarization for the ion transfer for the, within the electrodes, at positions far from the interface increases. The couplings between the different polarizations are defined in Eqs. (28) and (29). The variation in the ionic polarization through the electrolytes ($y$-direction in the model) was neglected in the previous models. This comparison

Please cite this article in press as: M. Andersson et al., SOFC modeling considering electrochemical reactions at the active three phase boundaries, Int. J. Heat Mass Transfer (2011), doi:10.1016/j.ijheatmasstransfer.2011.10.032

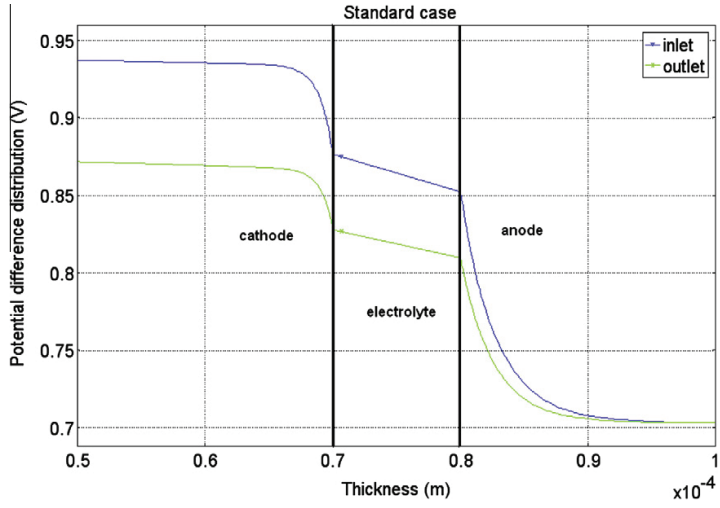


**Fig. 5.** Potential difference distribution. Note that for the anode and cathode, only the parts (20 μm) closest to the electrolyte interface are shown in the figure, and the "zero" is defined at the air channel-cathode interface.

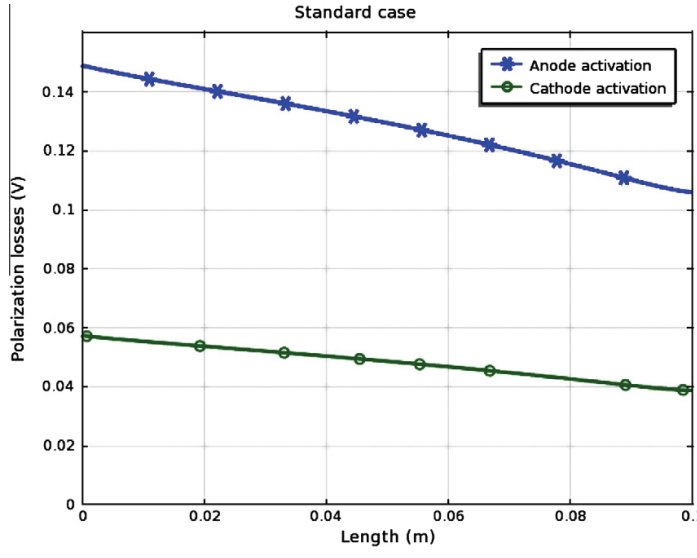


**Fig. 6.** Activation polarization along the flow direction in the anode and cathode predicted by the current model.

clearly shows that the impact of modeling the detailed charge transfer reactions and polarizations is significant, despite that a few micrometer thin reaction zone appeared in both anode and the cathode.

The mole fraction distributions along the main flow direction for hydrogen, water, methane, carbon monoxide and carbon dioxide at the fuel channel-anode interface are shown in Fig. 8, and the ones at the cross-section normal to the flow direction at the outlet are presented in Fig. 9. The mole fraction of hydrogen decreases along the flow direction (Fig. 8) due to the electrochemical reactions close to the anode-electrolyte interface and increases due to the reforming reactions (MSR + WGSR) within the anode. It should be noted that the WGSR is at equilibrium and is pushed towards the left direction as the electrochemical reactions proceed along the flow direction. Large hydrogen mole fraction gradients can be observed through the anode (Fig. 9). Water is generated due to the electrochemical reactions and is consumed in the reforming reactions (MSR + WGSR). The mole fraction distribution for water has a large gradient through the anode, because the water molecules need to be transported back through the porous media from the active electrochemical reaction zone to the locations for the reforming reactions and to the fuel channel (to be transported out of the cell). Carbon monoxide is generated in the MSR and consumed in the WGSR, and its mole fraction gradient through the anode (Fig. 9) is small and the lowest mole fraction is found at the TPB in the electrochemically active region. The carbon monoxide mole fraction along the flow direction increases initially (Fig. 8). Carbon dioxide is generated in the WGSR and transported

Please cite this article in press as: M. Andersson et al., SOFC modeling considering electrochemical reactions at the active three phase boundaries, Int. J. Heat Mass Transfer (2011), doi:10.1016/j.ijheatmasstransfer.2011.10.032

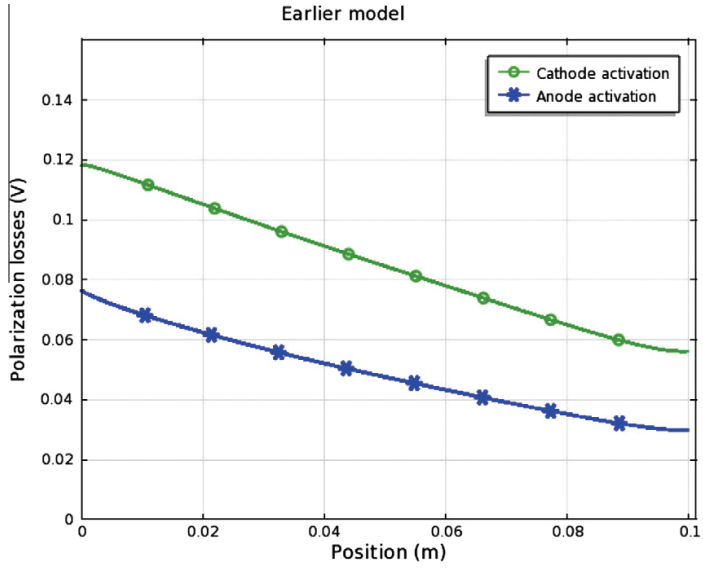


**Fig. 7.** Activation polarization along the flow direction in the anode and cathode predicted by an earlier model [8] (the electrochemical reactions defined as interface conditions).

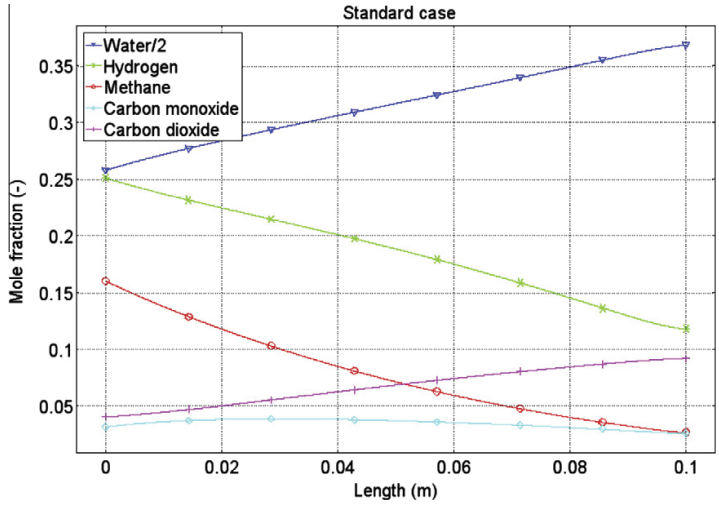


**Fig. 8.** Profiles for mole fractions for water, hydrogen, methane, carbon monoxide and carbon dioxide at the fuel channel-anode interface, along the flow direction. Note that the scales on the *y*-axis are different and the value should be multiplied with 2 for water.

back through the anode to the fuel channel, and further flows out of the cell with the exhaust fuel stream. Only a small mole fraction gradient can be seen through the anode (Fig. 9). For methane a clear mole fraction gradient can be observed through the anode (Fig. 9), and the lowest mole fraction is found at the TPB close to the gas outlet (Figs. 8 and 9). Note that not all the methane is converted to hydrogen and carbon monoxide, because of a relatively intermediate operating temperature (for the standard case) and a high activation energy for the MSR (according to the Klein kinetics). The fuel stream outlet concentration of methane can be decreased by recirculation of part of the fuel gas. However, such an investigation is outside the scope of this study.

As a parameter study, the inlet temperature of the fuel- and air flow streams is increased by 25 K (to 1035 K) to investigate its influence on the cell performance. The fuel- and air flow rates are kept constant, i.e., the fuel- and air utilizations vary, as compared to the standard case above. The temperature distribution for the case with an increased inlet temperature is shown in Fig. 10. The difference between the inlet and outlet temperatures is 49 °C, compared to 35 °C for the standard case (Fig. 3). An increased inlet temperature means an increased reaction rate, both for the internal steam reforming reactions (i.e., a faster conversion of methane) and for the electrochemical reactions (i.e., a higher current density). Note that the internal reforming reactions

Please cite this article in press as: M. Andersson et al., SOFC modeling considering electrochemical reactions at the active three phase boundaries, Int. J. Heat Mass Transfer (2011), doi:10.1016/j.ijheatmasstransfer.2011.10.032

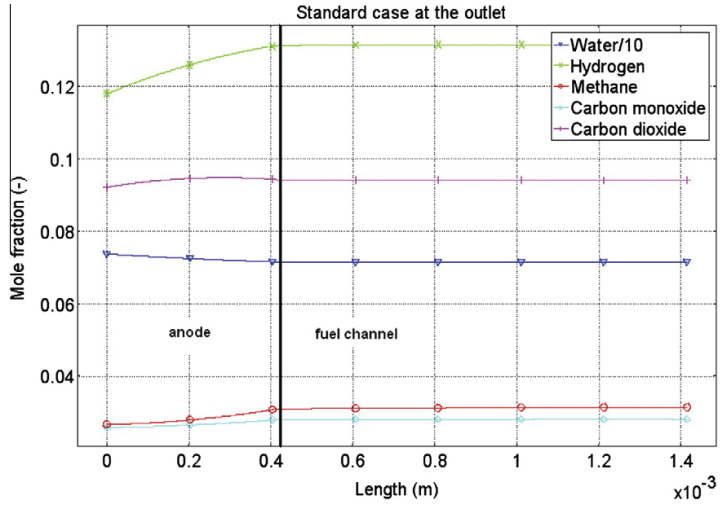


**Fig. 9.** Mole fractions for water, hydrogen, methane, carbon monoxide and carbon dioxide in the anode and fuel channel at the outlet, normal to the flow direction. Note that the scales on the *y*-axis are different and the value should be multiplied with 10 for water.

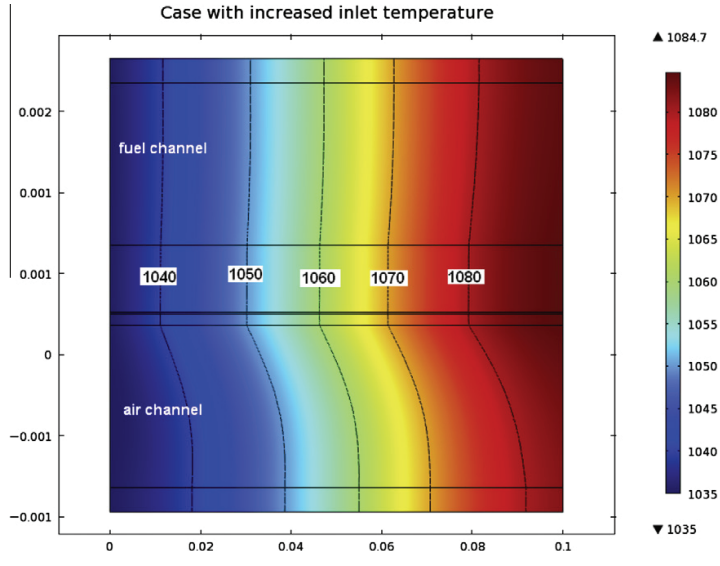


**Fig. 10.** Temperature distribution along the flow direction for the case with increased inlet temperatures (1035 K).

consume net heat and the electrochemical reactions generate heat globally. The polarizations decrease due to an increased local temperature. However, the increased current densities also cause an increase of the polarizations.

Fig. 11 shows the mole fraction distributions of the gas species at the fuel channel-anode interface along the flow direction. A higher inlet temperature means a higher MSR reaction rate and more methane is converted to hydrogen and carbon monoxide, and consequently a lower methane concentration is found close to the exit. A higher concentration of hydrogen in the inlet region results in a higher ideal voltage and also a higher cell current density. The fuel utilization is around 85% for this case, compared to 70% for the standard case (note that the inlet flow rates are kept constant while the cell inlet temperature is increased). The fuel utilizations are evaluated by comparing the fuel gas content at the inlet and at the outlet, where each mole of methane corresponds to 4 moles of hydrogen and each mole of carbon monoxide to 1 mol of hydrogen. The MSR kinetics depend on the activation energy, which is high for the material characteristics in this study, as further discussed in [3,6,25]. An anode catalytic material composition with the low activation energy will result in a higher reaction rate and also a steeper temperature gradient. A disadvantage with an increased temperature gradient is the increased thermal stresses, which can lead to a decreased life time for the operating cell.

The ion current density (in Fig. 12) increases as the inlet temperature increases, with a maximum value of around 3950 A/m$^2$ at the inlet and 3750 A/m$^2$ at the outlet. For the standard case

Please cite this article in press as: M. Andersson et al., SOFC modeling considering electrochemical reactions at the active three phase boundaries, Int. J. Heat Mass Transfer (2011), doi:10.1016/j.ijheatmasstransfer.2011.10.032

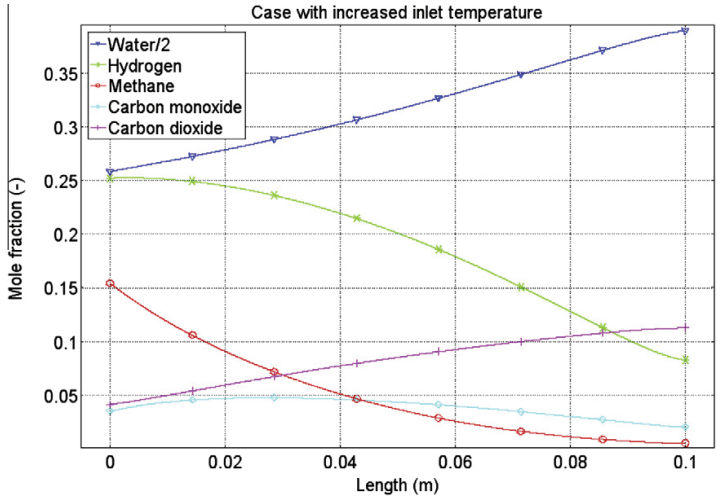


**Fig. 11.** Mole fractions along the flow direction at the fuel channel-anode interface for the case with increased inlet temperatures (1035 K). Note that the scale on the *y*-axis differs for water, as explained in Fig. 8.

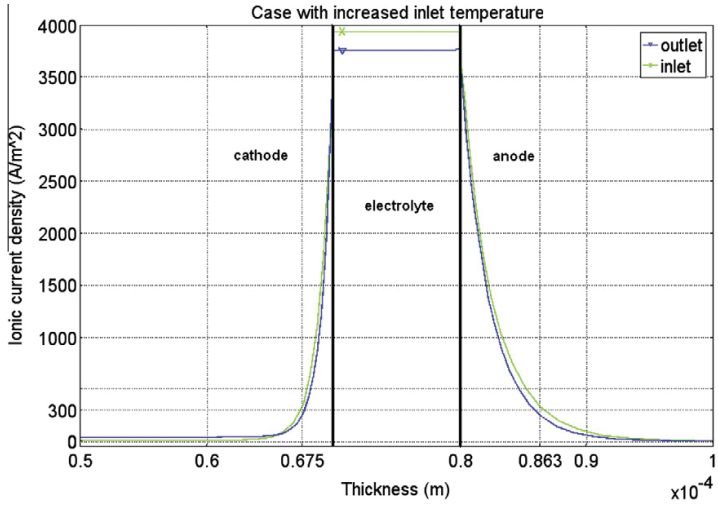


**Fig. 12.** Ion current density (A/m$^2$) for the case with increased inlet temperatures (1035 K).

the maximum value is around 3000 A/m$^2$ at the inlet and 3200 A/m$^2$ at the outlet. The increase in the ion current density is due to the decreased polarizations and the increased hydrogen concentration, mostly from the MSR by an initially higher hydrogen production. The lower ion current density at the outlet, compared to that at the inlet, is due to a lower concentration of hydrogen at the outlet. The depth of the electrochemically active zones increases slightly to 2.5 μm and 6.3 μm for the cathode and anode, respectively. The corresponding values are 2.4 μm and 6.2 μm for the standard case. It should be noted that the reaction zone is slightly thicker at the inlet compared to the one at the outlet, and the values mentioned here are the averaged ones.

Normally the air flow rate is adjusted to make sure that the cell receives sufficient cooling to keep a specific temperature. The air flow rate is, in this study, reduced by 20% to examine the impact on the temperature distribution (*x*- and *y*-directions), the mole fraction variations (*x*-direction) and the ion current density variations (*y*-direction). Decreased air flow rates mean decreased cooling and may cause a higher outlet temperature, as shown in Fig. 13. The difference between the inlet and outlet temperatures is 50 °C, compared to 35 °C for the standard case in Fig. 3. A higher temperature within the cell means a faster consumption of methane and also higher production of carbon monoxide and hydrogen. A higher temperature gradient in the flow direction may decrease the life time for the cell material.

Fig. 14 shows the mole fraction distributions of various gas species along the flow direction for the case with a decreased air flow rate. The fuel utilization reaches 75%, compared to 70% for the standard case. The increase in fuel utilization is due to a higher methane conversion, despite the outlet concentrations of hydrogen

Please cite this article in press as: M. Andersson et al., SOFC modeling considering electrochemical reactions at the active three phase boundaries, Int. J. Heat Mass Transfer (2011), doi:10.1016/j.ijheatmasstransfer.2011.10.032

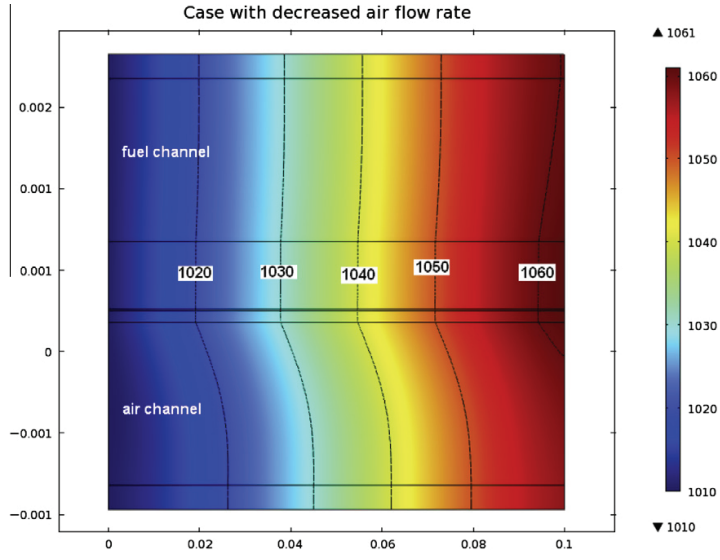


**Fig. 13.** Temperature distribution along the main flow direction for the case with decreased air flow rate.

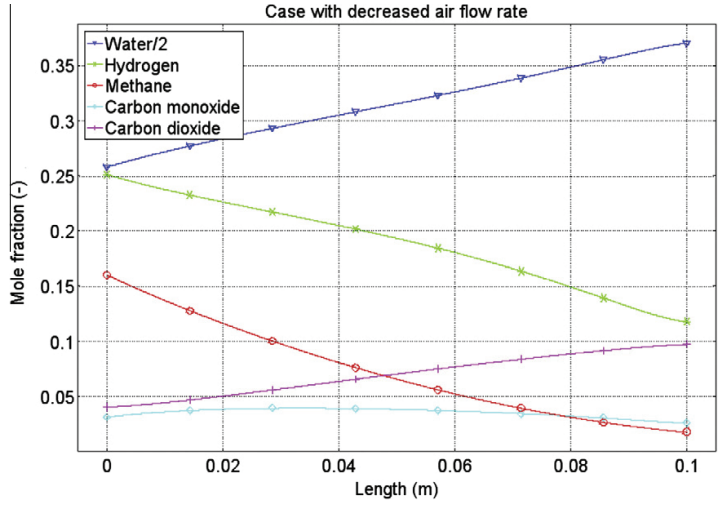


**Fig. 14.** Mole fraction distributions along the flow direction for the case with a decreased air flow rate. Note that the scale on the *y*-axis for water differs, as explained in Fig. 8.

and carbon monoxide are similar to those in the standard case (in Fig. 8). The outlet concentration of carbon dioxide is increased compared to the standard case, due to the higher conversion rate of methane. The air utilization is 23% compared to 18% for the standard case. The ion current density close to the outlet increases (with a maximum value of around 3600 A/m$^2$), as shown in Fig. 15 compared to the standard case (with a maximum value of 3200 A/m$^2$) in Fig. 4. This is mainly due to an increased outlet temperature. It should be mentioned that the current density at the inlet is the same as for the standard case. Also the depth of the electrochemically active zones is the same as for the standard case, i.e., 2.4 μm and 6.2 μm for the cathode and anode, respectively.

The ionic tortuosities within the anode and cathode are decreased from 10 for the standard case to 5 to study the influence on the current density and the temperature distributions within the cell. Note that the air- and fuel flow rates are kept constant, i.e., the air- and fuel utilizations are not specified explicitly. The electrochemical reaction zones increase to 3.8 μm on the cathode side and 9.5 μm on the anode side (as shown in Fig. 16). For the standard case these are 2.4 μm and 6.2 μm, respectively. Thus the active zone available for the electrochemical reactions increases. A lower ionic tortuosity means a decreased ionic resistance in the electrode. The maximum current density at the inlet is about 4050 A/m$^2$, compared to 3000 A/m$^2$ for the standard case (Fig. 4), and at the outlet 3500 A/m$^2$ (compared to 3200 A/m$^2$). The current density at the outlet is lower, than at the inlet, because the fuel utilization increases to 82% (compared to 70% for the standard case) and the mole fraction of hydrogen is lower close

Please cite this article in press as: M. Andersson et al., SOFC modeling considering electrochemical reactions at the active three phase boundaries, Int. J. Heat Mass Transfer (2011), doi:10.1016/j.ijheatmasstransfer.2011.10.032

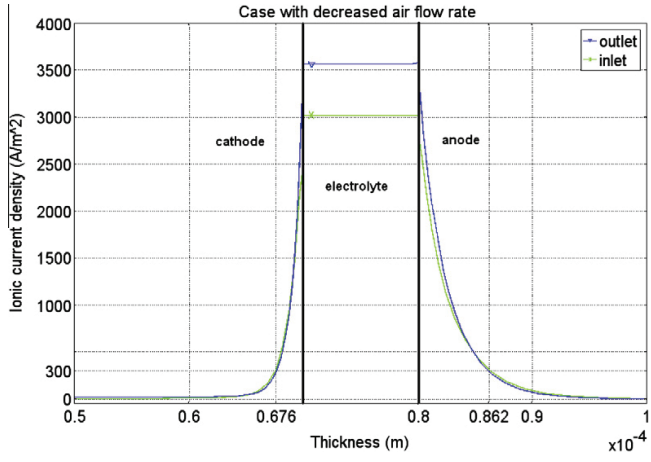


**Fig. 15.** Ion current density (A/m$^2$) for the case with a decreased air flow rate. Note that the scale for the thickness, ($y$)-direction, defines "zero" at the air channel-cathode interface.

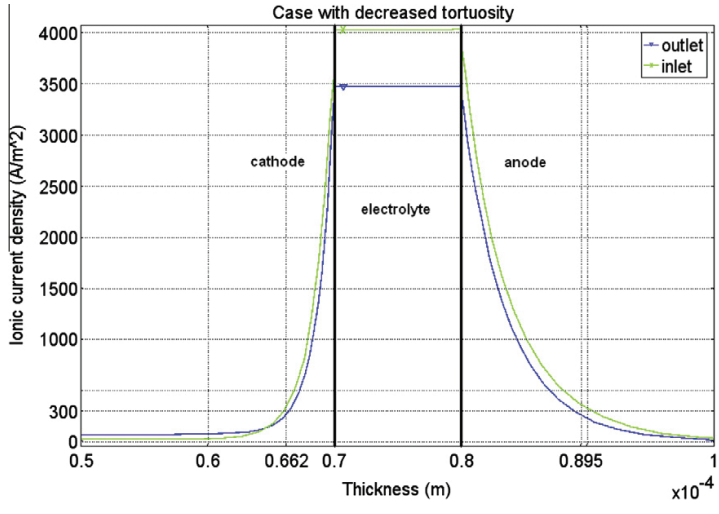


**Fig. 16.** Ion current density (A/m$^2$) for the case with decreased ionic tortuosity. Note that the scale for the thickness, ($y$)-direction, defines "zero" at the air channel-cathode interface.

to the outlet (the minimum value reaches 0.06 compared to 0.12 for the standard case). The outlet temperature is increased due to a higher current density, and it reaches 1052 K (Fig. 17) compared to 1045 K for the standard case (Fig. 3), even at the same inlet temperature. The temperature gradient close to the inlet is higher as for the standard case, due to large heat generation from the high current density close to the inlet.

## 5. Conclusions

A CFD approach is developed and implemented to analyze various chemical and physical phenomena, which take place inside a single cell anode-supported SOFC. Equations for mass-, heat-, momentum-, ion- and electron transport are solved simultaneously and coupling with kinetic expressions for electrochemical and internal steam reforming reactions appearing in various domains is considered. The model includes correlations for a more realistic description of the transport of the ions and the electrons generated within the anode and the cathode. The ion/electron transport pathways are evaluated by accounting for the volume fractions of the specific materials- and pores, as well as the ionic/electronic tortuosities. The electrochemical reactions are defined in a finite region close to the interface and implemented as various source terms in the relevant governing transport equations. This is an extension of a previous model, where the electrochemical reactions were defined at indefinitely thin TPBs.

The internal reforming and the electrochemical reaction rates are dependent on the local microscopic structure, temperature and the gas-phase concentrations. The local temperature depends on the reaction rates, the flow rates of the air and fuel streams, the gas-phase concentrations as well as the different polarizations. The gas-phase concentration distribution depends on the temperature, the flow rates of the air and fuel streams as well as the

Please cite this article in press as: M. Andersson et al., SOFC modeling considering electrochemical reactions at the active three phase boundaries, Int. J. Heat Mass Transfer (2011), doi:10.1016/j.ijheatmasstransfer.2011.10.032

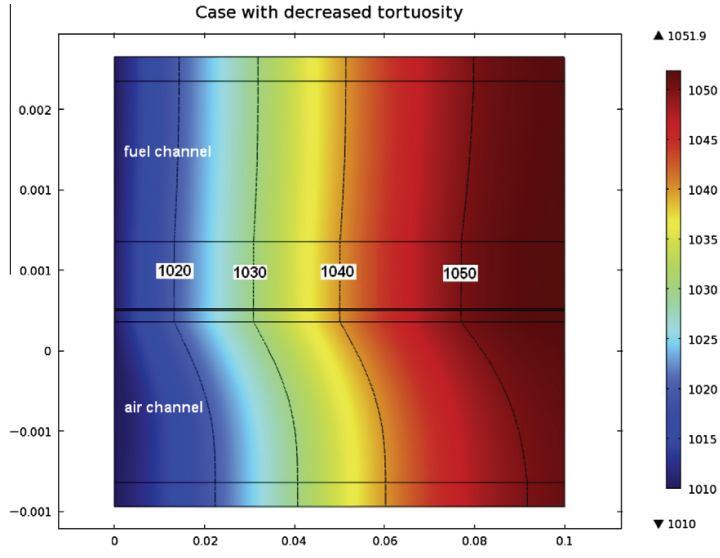


**Fig. 17.** Temperature distribution along the flow direction for the case with decreased ionic tortuosity.

reactions in the electrode porous structure. The ion and electron distributions are affected by the local temperature, the gas-phase concentrations and also the porous material structure. The different polarizations depend on temperature, gas-phase concentrations and porous material structure/design. The above mentioned relationships between the physical parameters/phenomena within a fuel cell show the importance of the couplings between them, i.e., the reason why CFD calculations are necessary and needed to understand the physical phenomena within fuel cells and for improving the fuel cell overall performance, with the overall purpose to reduce the cost and promote commercialization.

Most of the operating parameters are kept constant, while the inlet temperature, air flow rate or the ionic tortuosity are varied for a parameter study. A decreased ionic tortuosity will enable a higher cell current density. In this study the electrons are transported in Ni or LSM and the ions in YSZ. However, other materials are possible for future SOFC designs. This study reveals that the electrochemical reactions occur within only a few micro meters from the electrode-electrolyte interface, e.g., for the standard case 90% of the electrochemical reactions occur within 2.4 μm in the cathode and 6.2 μm in the anode from the electrode-electrolyte interface. The predicted current density gradient is steeper on the cathode side, compared to the anode side, and it is found that around 60% of the polarizations occur in the anode, 10% in the electrolyte and 30% in the cathode. This conclusion differs from our previous studies, where the electrochemical reactions were implemented as interface conditions in the governing transport equations, and the activation polarization on the cathode side dominated over that on the anode side. This difference can be explained by different current density per (active TPB) area and variable area-to-volume-ratios for the electrochemical reactions within the anode and cathode, respectively. Note that none of these effects are included in our previous models [3,6,8,25]. The current density and the activation polarization are highest at the electrolyte–electrode interface and decreases rapidly within the electrodes as the distance from the interface increases. However, ohmic polarization by ion transfer increases for the positions away from the interface. The current model includes and covers the major transport and reaction phenomena, such as charge transfer, various polarizations, and electrochemical reactions at the TPBs. To increase the knowledge related to these phenomena microscale modeling technique is promising for the future study.

The heat, which is generated within the cell, can be used for the internal steam reforming reaction within the anode and/or outside the cell for external reforming and pre-heating of the fuel and air. The cell current density can be increased by increasing the operating temperature, however, a too high maximum temperature or temperature gradient decreases the cell life time. It is possible to increase the inlet temperature if the air flow rate is also increased, i.e., the maximum temperature is kept constant. As a result, a higher current can be withdrawn from the cell, with a constant voltage. However, some extra energy is needed for the air-pump because the flow rate of air is increased.

## Acknowledgments

The financial support from the Swedish Research Council (VR-621-2010-4581) and the European Research Council (ERC-226238-MMFCs) is gratefully acknowledged. The Chinese Academy of Engineering (CAE) and the Royal Swedish Academy of Engineering Sciences (IVA) have supported the first author for a three month research visit to NIMTE, Chinese Academy of Sciences (CAS) in Ningbo, China.

## References

[1] J. Staniforth, M. Ormerod, Implications for using biogas as a fuel source for solid oxide fuel cells: internal dry reforming in a small tubular solid oxide fuel cell, Catal. Lett. 81 (2002) 19–23.
[2] M. Peksen, R. Peters, L. Blum, D. Stolten, Numerical modelling and experimental validation of a planar type pre-reformer in SOFC technology, Int. J. Hydrogen Energy 34 (2009) 6425–6436.
[3] M. Andersson, SOFC Modeling Considering Mass and Heat Transfer, Fluid Flow with Internal Reforming Reactions, Licentiate Thesis, ISRN:LUTMDN/TMHP-09/7063-SE, Department of Energy Sciences, Lund University, Sweden, 2009.
[4] K. Wang, D. Hissel, M.C. Péra, N. Steiner, D. Marra, M. Sorrentino, C. Pianese, M. Monteverde, P. Cardone, J. Saarinen, A review on solid oxide fuel cell models, Int. J. Hydrogen Energy (2011) 7212–7228.
[5] S. Kakac, A. Pramuanjaroenkij, X. Zhou, A review of numerical modeling of solid oxide fuel cells, Int. J. Hydrogen Energy 32 (2007) 761–786.

Please cite this article in press as: M. Andersson et al., SOFC modeling considering electrochemical reactions at the active three phase boundaries, Int. J. Heat Mass Transfer (2011), doi:10.1016/j.ijheatmasstransfer.2011.10.032

[6] M. Andersson, J. Yuan, B. Sundén, Review on modeling development for multiscale chemical reactions coupled transport phenomena in SOFCs, J. Appl. Energy 87 (2010) 1461–1476.
[7] J. Yuan, Y. Huang, B. Sundén, W.G. Wang, Analysis of parameter effects on chemical coupled transport phenomena in SOFC anodes, Heat Mass Transfer 45 (2009) 471–484.
[8] M. Andersson, J. Yuan, B. Sundén, T.S. Li, W.G. Wang, Modeling validation and simulation of an anode supported SOFC including mass and heat transport, fluid flow and chemical reactions, ESFuelCell2011-54006, in: Proceedings of the ASME 9th International Fuel Cell Science, Engineering and Technology Conference, Washington, DC, USA, 2011.
[9] K. Tseronis, I.K. Kookos, C. Theodoropoulos, Modeling mass transport in solid oxide fuel cell anodes: a case for a multidimensional dusty gas-based model, Chem. Eng. Sci. 63 (2006) 5626–5638.
[10] J. Shi, X. Xue, CFD analysis of a symmetrical planar SOFC with heterogeneous electrode properties, Electrochim. Acta 55 (2010) 5263–5273.
[11] M. Ni, M.K.H. Leung, D.Y.C. Leung, Micro-scale modeling of solid oxide fuel cells with micro-structurally grades electrodes, J. Power Sources 168 (2007) 369–378.
[12] Y. Shi, N. Cai, C. Li, Numerical modeling of an anode-supported SOFC button cell considering anodic surface diffusion, J. Power Sources 164 (2007) 639–648.
[13] D. Kanno, N. Shikazono, N. Takagi, K. Matsuzaki, N. Kasagi, Evaluation of SOFC anode polarization simulation using three-dimensional microstructures reconstructed by FIB tomography, Electochim. Acta 56 (2011) 4015–4021.
[14] H. Iwai, N. Shikazono, T. Matsui, H. Teshima, M. Kishimoto, R. Kishida, D. Hayashi, K. Matsuzaki, D. Kanno, M. Saito, H. Muroyama, K. Eguchi, N. Kasagi, H. Yoshida, Quantification of SOFC anode microstructure based on dual beam FIM-SEM technique, J. Power Sources 195 (2010) 955–961.
[15] S.H. Chan, K.A. Khor, Z.T. Xia, A complete polarization model of a solid oxide fuel cell and its sensitivity to change of cell component thickness, J. Power Sources 93 (2001) 130–140.
[16] Y. Patcharavorachot, A. Arpornwichanop, A. Chuachuebsuk, Electrochemical study of a planar solid oxide fuel cell: role of support structures, J. Power Sources 177 (2008) 254–261.
[17] W.G. Bessler, M. Vogler, H. Störmer, D. Gerthsen, A. Utz, A. Weber, E. Ivers-Tiffée, Model anodes and anode models for understanding the mechanism of hydrogen oxidation in solid oxide fuel cells, Phys. Chem. Chem. Phys. 12 (2010) 13888–13903.
[18] W.G. Bessler, S. Gewies, M. Vogler, A new framework for physically based modeling of solid oxide fuel cells, Electrochim. Acta 53 (2007) 1782–1800.
[19] S.A. Hajimolana, M.A. Hussain, W.M.A.W. Daud, M. Soroush, A. Shamiri, Mathematical modeling of solid oxide fuel cells: a review, Renew. Sustain. Energy Rev. 15 (2011) 1893–1917.
[20] D. Mogensen, J.-D. Grunwaldt, P.V. Hendriksen, K. Dam-Johansen, J.U. Nielsen, Internal steam reforming in solid oxide fuel cells: status and opportunities of kinetic studies and their impact on modelling, J. Power Sources 196 (2011) 25–38.
[21] E. Vakouftsi, G.E. Marnellos, C. Anthansiou, F. Coutelieris, CFD modelling of a biogas fuelled SOFC, Solid State Ionics 192 (2010) 458–463.
[22] F. Nagel, T. Schildhauer, S. Biollaz, S. Stucki, Charge, mass and heat transfer interactions in solid oxide fuel cells operated with different fuel gases – a sensitivity analysis, J. Power Sources 184 (2008) 129–142.
[23] P. Aguiar, C.S. Adjiman, N.P. Brandon, Anode-supported intermediate temperature direct internal reforming solid oxide fuel cell. I: Model-based steady-state performance, J. Power Sources 138 (2004) 120–136.
[24] V. Janardhanan, O. Deutschmann, CFD analysis of a solid oxide fuel cell with internal reforming: coupled interactions of transport, heterogeneous catalysis and electrochemical processes, J. Power Sources 162 (2006) 1192–1202.
[25] M. Andersson, H. Paradis, J. Yuan, B. Sundén, Modeling analysis of different renewable fuels in an anode supported SOFC, J. Fuel Cell Sci. Technol. 8 (2011) 031013.
[26] B. Todd, J.B. Young, Thermodynamic and transport properties of gases for use in solid oxide fuel cell modeling, J. Power Sources 110 (2002) 86–200.
[27] W.G. Bessler, J. Warnatz, D.G. Goodwin, The influence of equilibrium potential on the hydrogen oxidation kinetics of SOFC anodes, Solid State Ionics 177 (2007) 3371–3383.
[28] D.Y. Murzin, T. Salmi, Catalytic Kinetics, Elsevier Science, The Netherlands, 2005.
[29] R.C. Reid, J.M. Prausnitz, B.E. Poling, The Properties of Gases and Liquids, fourth ed., R.R. Donnelley & Sons Company, USA, 1986.
[30] COMSOL Multiphysics 4.1 User Guide, Stockholm, Sweden, 2010.
[31] J.R. Ferguson, J.M. Fiard, R. Herbin, Three dimensional numerical simulation for various geometries of solid oxide fuel cells, J. Power Sources 58 (1996) 109–122.
[32] N. Vivet, S. Chupin, E. Estrade, T. Piquero, P.L. Pommier, D. Rochais, E. Bruneton, 3D microstructure characterization of a solid oxide fuel cell anode reconstructed by focused ion beam tomography, J. Power Sources 196 (2011) 7541–7549.
[33] Fuel Cell Handbook, seventh ed., United States Department of Energy, Morgantown, West Virginia, USA, 2004.
[34] M. Kemm, Dynamic Solid Oxide Fuel Cell Modelling for Non-steady State Simulation of System Applications, Doctoral Thesis, Department of Energy Sciences, Lund University, Sweden, 2006, ISBN: 91-628-6981-7.
[35] W. Winkler, P. Nehter, Thermodynamics of fuel cells, Fuel Cells Hydrogen Energy 1 (2008) 15–50.
[36] P. Hofmann, K.D. Panopoulos, L.E. Fryda, E. Kakaras, Comparison between two methane reforming models applied to a quasi-two-dimensional planar solid oxide fuel cell model, Energy 34 (2008) 2151–2157.
[37] N. Akhtar, S.P. Decent, K. Kendall, Numerical modelling of methane-powered micro-tubular, single-chamber solid oxide fuel cell, J. Power Sources 195 (2010) 7796–7807.
[38] Y. Shi, N. Cai, C. Li, C. Bao, E. Croiset, J. Qian, Q. Hu, S. Wang, Modeling of an anode-supported Ni-YSZ|Ni-ScSZ|ScSZ|LSM-ScSZ multiple layers SOFC cell. Part I. Experiments, model development and validation, J. Power Sources 172 (2007) 235–245.
[39] A.V. Akkaya, Electrochemical model for performance analysis of a tubular SOFC, Int. J. Energy Res. 31 (2007) 79–98.
[40] A. Konno, H. Iwai, K. Inuyama, A. Kuroyanagi, M. Saito, H. Yoshida, K. Kodani, K. Yoshikata, Mesoscale-structure control at anode/electrolyte interface in solid oxide fuel cell, J. Power Sources 196 (2011) 98–109.
[41] S. Sohn, J.H. Nam, D.H. Jeon, C.J. Kim, A micro/macroscale model for intermediate temperature solid oxide fuel cells with prescribed fully-developed axial velocity profile in gas channels, Int. J. Hydrogen Energy 35 (2010) 11890–11907.
[42] H. Xiao, T.L. Reitz, M.A. Rottmayer, Polarization measurements of anode-supported solid oxide fuel cells studied by incorporation of a reference electrode, J. Power Sources 183 (2008) 46–54.
[43] J.-M. Klein, Y. Bultel, S. Georges, M. Pons, Modeling of a SOFC fuelled by methane: from direct internal reforming to gradual internal reforming, Chem. Eng. Sci. 62 (2007) 1636–1649.
[44] B.A. Haberman, J.B. Young, Three-dimensional simulation of chemically reacting gas flows in the porous support structure of an integrated-plannar solid oxide fuel cell, Int. J. Heat Mass Transfer 47 (2004) 3617–3629.
[45] V.A. Danilov, M.O. Tade, A CFD-based model of a planar SOFC for anode flow field design, Int. J. Hydrogen Energy 34 (2009) 8998–9006.
[46] S.T. Aruna, M. Muthuraman, K.C. Patil, Synthesis and properties of Ni-YSZ cermet: anode materials for solid oxide fuel cells, Solid State Ionics 111 (1998) 45–51.
[47] M. Mamak, N. Coombs, G.A. Ozin, Practical solid oxide fuel cells with anodes derived from self-assembled mesoporous-NiO-YSZ, Chem. Commun. 20 (2002) 2300–2301.

Please cite this article in press as: M. Andersson et al., SOFC modeling considering electrochemical reactions at the active three phase boundaries, Int. J. Heat Mass Transfer (2011), doi:10.1016/j.ijheatmasstransfer.2011.10.032